THEORY OF NONLINEAR PROPAGATION OF HIGH HARMONICS GENERATED IN A GASEOUS MEDIUM

by

CHENG JIN

B.S., Northwest Normal University, China, 2003
M.S., Northwest Normal University, China, 2006

AN ABSTRACT OF A DISSERTATION

submitted in partial fulfillment of the
requirements for the degree

DOCTOR OF PHILOSOPHY

Department of Physics
College of Arts and Sciences

KANSAS STATE UNIVERSITY
Manhattan, Kansas
2012

ABSTRACT

In this thesis, we establish the theoretical tools to investigate high-order harmonic generation (HHG) by intense infrared lasers in a gaseous medium. The macroscopic propagation of both the fundamental and the harmonic fields is taken into account by solving Maxwell's wave equations, while the single-atom (or single-molecule) response is obtained by quantitative rescattering theory. The initial spatial mode of the fundamental laser is assumed either a Gaussian or a truncated Bessel beam. On the examples of Ar, N_2 and CO_2, we demonstrate that the available experimental HHG spectra with isotropic and aligned target media can be accurately reproduced theoretically even though the HHG spectra are sensitive to the experimental conditions. We show that the macroscopic HHG can be expressed as a product of a macroscopic wave packet and a photorecombination cross section, where the former depends on laser and experimental conditions while the latter is the property of the target only. The factorization makes it possible to retrieve the single-atom or single-molecule structure information from experimental HHG spectra. As for the multiple molecular orbital contribution in HHG, it causes the disappearance of the minimum in the HHG spectrum of aligned N_2 with the increase of laser intensity, and the position of minimum in HHG spectrum of aligned CO_2 depending on many factors is also attributed to it, which could explain why the minima observed in different laboratories may differ. For an important application of HHG as ultrashort light source, we show that measured continuous harmonic spectrum of Xe due to the reshaping of the fundamental laser field can be used to produce an isolated attosecond pulse by spectral and spatial filtering in the far field. For on-going application of using HHG to ionize aligned molecules, we present the photoelectron angular distribution from aligned N_2 and CO_2 in the laboratory frame, which can be compared directly with future experiments.

THEORY OF NONLINEAR PROPAGATION OF HIGH HARMONICS GENERATED IN A GASEOUS MEDIUM

by

CHENG JIN

B.S., Northwest Normal University, China, 2003
M.S., Northwest Normal University, China, 2006

A DISSERTATION

submitted in partial fulfillment of the
requirements for the degree

DOCTOR OF PHILOSOPHY

Department of Physics
College of Arts and Sciences

KANSAS STATE UNIVERSITY
Manhattan, Kansas
2012

Approved by:

Major Professor
Chii-Dong Lin

Copyright

ABSTRACT

In this thesis, we establish the theoretical tools to investigate high-order harmonic generation (HHG) by intense infrared lasers in a gaseous medium. The macroscopic propagation of both the fundamental and the harmonic fields is taken into account by solving Maxwell's wave equations, while the single-atom (or single-molecule) response is obtained by quantitative rescattering theory. The initial spatial mode of the fundamental laser is assumed either a Gaussian or a truncated Bessel beam. On the examples of Ar, N_2 and CO_2, we demonstrate that the available experimental HHG spectra with isotropic and aligned target media can be accurately reproduced theoretically even though the HHG spectra are sensitive to the experimental conditions. We show that the macroscopic HHG can be expressed as a product of a macroscopic wave packet and a photorecombination cross section, where the former depends on laser and experimental conditions while the latter is the property of the target only. The factorization makes it possible to retrieve the single-atom or single-molecule structure information from experimental HHG spectra. As for the multiple molecular orbital contribution in HHG, it causes the disappearance of the minimum in the HHG spectrum of aligned N_2 with the increase of laser intensity, and the position of minimum in HHG spectrum of aligned CO_2 depending on many factors is also attributed to it, which could explain why the minima observed in different laboratories may differ. For an important application of HHG as ultrashort light source, we show that measured continuous harmonic spectrum of Xe due to the reshaping of the fundamental laser field can be used to produce an isolated attosecond pulse by spectral and spatial filtering in the far field. For on-going application of using HHG to ionize aligned molecules, we present the photoelectron angular distribution from aligned N_2 and CO_2 in the laboratory frame, which can be compared directly with future experiments.

TABLE OF CONTENTS

LIST OF FIGURES

LIST OF TABLES

Acknowledgments

First, I would like to sincerely thank my advisor, Dr. Chii-Dong Lin for his guidance, encouragement and support all through my Ph.D. study. I am really grateful that he brings me to this exciting research field, constantly motivates me and gives me invaluable advice. I still remember the most difficult time in my project. The propagation code was working at the low gas pressure, however, it didn't work at the high gas pressure. I could not figure out the problems for a few months, and even wanted to give up. His patience and encouragement helped me going through that time. I also have learned a lot from my advisor about how to conduct effective research and how to grab a hot topic in the field. This valuable experience will be helpful for my future life.

I would like to thank Dr. Anh-Thu Le for his continuous help since I first joined Professor Lin's group. I have learned from him to run and write some computation programmes, which soon became an essential part in my project. He is always available for stimulated discussions, and helping me understand every concept in the field.

Next I would like to give my appreciations to other members, former and current, in Professor Lin's group. Dr. Rui-Hua Xie, with whom I was closely working in the very beginning of my project, taught me step by step to do programming and build up basic research tools. Dr. Turker Topcu initiated the propagation project, and nicely shared with me his experience gathered from successful and unsuccessful attempts. This was really useful and important for me to start a new project. Dr. Zhangjin Chen had been helping me in both research and life for many years. Dr. Toru Morishita gave me the permit to use his TDSE code, and helped me in numerical algorithm. Dr. Song-Feng Zhao had been my collaborator in the project of tunneling ionization of molecules, which is an important part in my project. He kindly provided me with necessary data for my project. And we had a lot of good discussions in many interesting issues. I also have collaborated with Dr. Guoli Wang in the propagation project. I have been benefited from his efforts to investigate

propagation effects under some extreme conditions, such as high intensity and high pressure. I appreciate my class fellow Junliang Xu, who is an intelligent and careful researcher, for his help and collaboration in course studies. Dr. Wei-Chun Chu and Dr. Allison Harris discussed with me about some interesting problems. I really enjoyed these discussions.

I also want to thank Dr. Carlos A. Trallero-Herrrero for stimulating the project of attosecond pulse generation, useful discussions and nice collaboration, and thank Dr. Lew Cocke and Wei Cao for sharing their ideas and stimulated discussions in the project of harmonic spectral splitting.

Then I would like to acknowledge my collaboration with people from other institutes. I really thank Dr. Hans J. Wörner, Julien B. Bertrand, Dr. Paul B. Corkum, and Dr. David M. Villeneuve from National Research Council (NRC) in Canada for providing the experimental data and valuable communications. Without their efforts in experiments, I could not make a complete and convincing story. Dr. Valer Tosa from National Institute for R&D in Isotopic and Molecular Technologies in Romania, discussed with me a lot of technique details about macroscopic propagation, and finally helped me setting up the propagation code. Dr. Robert R. Lucchese from Texas A&M University provided me with photoionization code for molecular calculations and gave me an opportunity to visit him. I am grateful to them.

I also want to thank all of my Ph.D. committee members and outside chair: Dr. Uwe Thumm, Dr. Brian Washburn, Dr. Viktor Chikan and Dr. Naiqian Zhang for serving on my committee and carefully reading my thesis. I thank the Physics Department for taking good care of my study life and broadening my experience with various seminars and meetings. I thank all my friends in K-State for their friendship and their help in all aspects.

Finally I want to express my gratitude to people who are so important in my life. First, I would like to thank Professor Xiao-Xin Zhou for stimulating my interest in research and providing me an opportunity to pursue my dream in the USA. Next I want to thank my dear, Jinping Fu, my parents and my brother for their endless support and love.

Chapter 1

Introduction to high-order harmonic generation

1.1 Background

The laser (light amplification by stimulated emission of radiation), invented in 1960, has opened up new research areas in atomic and molecular physics. Based on this technology, Franken *et al.* [1] first demonstrated the frequency doubling in a crystal in 1961, New and Ward [2] observed the third-harmonic generation in gases in 1967, and a few years later Reintjes *et al.* [3] generated higher-order harmonic such as the fifth order. These harmonics were all in the perturbative region, which could be understood in the framework of n-photon excitation. The probability of absorbing n photons decreases exponentially with n, explaining the rapid decrease in the harmonic intensity with the order. Meanwhile, pulsed lasers were developed towards increasing peak powers, increasing repetition rates and decreasing pulse durations. The character of laser-atom interaction also evolved from being essentially pertubative for laser intensities below 10^{13} W/cm^2 to strongly nonperturbative for higher intensities. When the pulsed laser intensity reaches about 10^{14} W/cm^2, the electric field from the laser becomes comparable to the Coulomb field, and a dramatically nonlinear process of high-order harmonic generation (HHG) can occur, in which an intense ultrafast laser pulse at a given frequency is converted to integer multiples of this fundamental frequency in a conversion medium. The first observations of HHG date back to the late

1980's. Indeed, efficient photon emission in the extreme ultraviolet (XUV) range (from 10 eV up to 124 eV, corresponding to 124 nm to 10 nm, respectively), in the form of high-order harmonics was observed in Chicago (17th harmonic of a KrF laser, 1987) [4] and in Saclay (33rd harmonic of a Nd:YAG laser, 1988) [5]. Different from perturbative harmonics, the high-harmonic spectra start with a rapid decrease in efficiency for low-order harmonics consistent with the perturbation theory, followed by a broad plateau of nearly constant efficiency, and then an abrupt cutoff as shown in Fig. 1.1. Most of the early work concentrated on the extension of the plateau, i.e., to obtain the harmonics of higher frequency and shorter wavelength. Today, HHG produced with short and intense laser pulses has been extended to the water window (below the carbon K-edge at 4.4 nm) [6, 7].

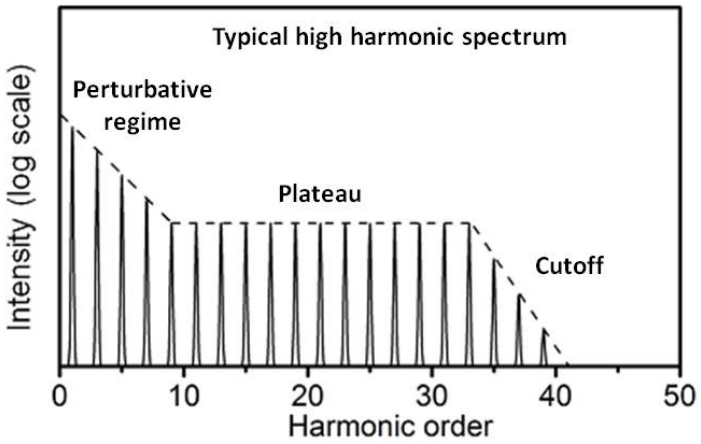

Figure 1.1: *Typical high harmonic spectrum. The spectrum has three parts: the perturbative regime for low orders, the plateau for intermediate orders, and the cutoff at the highest orders.*

Since there was a broad plateau range with comparable harmonic efficiency, another mechanism instead of the pertubative theory was needed to explain HHG phenomenon. A breakthough in the theoretical understanding was initiated in 1992-1993 by Krause *et al.* [8] and Corkum [9], presenting a semiclassical theory, which reproduced the plateau behavior in the observed HHG spectra. According to these works, in the strong ultrafast laser field, an outmost electron is tunnel ionized through a barrier formed by the electric field and atomic

potential when the electric field strength of the laser is close to its peak during an optical cycle, and is driven away from the nucleus. When the oscillating laser field changes its sign (about a quarter of an optical cycle later), the electron first decelerates, and then starts to re-accelerate back towards the parent ion. Therefore, the electron can gain a significant amount of kinetic energy, much larger than the fundamental photon energy. If the returning electron recombines with its parent ion, this kinetic energy plus the ionization potential can be released in the form of high energy photon. This model has been named a "three-step model" because there are three steps involved: ionization, propagation in the laser field and recombination (see Fig. 1.2), or "simple-man's model" due to its striking simplicity. Krause *et al.* [8] also showed that the cutoff position in the HHG spectrum followed a universal law of $I_p + 3.17U_p$, where I_p is the ionization potential, and $U_p = e^2E_0^2/4m_e\omega_0^2$ ponderomotive energy, i.e., the mean kinetic energy acquired by an electron oscillating in the laser field. Here, e is the electron charge, m_e its mass, and E_0 and ω_0 laser electric field and its frequency, respectively. This quasiclassical theory was shortly confirmed by a quantum-mechanical treatment also including quantum effects, such as the depletion of the ground state, wave packet spreading and interference based on a strong-field approximation (SFA) by Lewenstein *et al.* [10] and Antoine *et al.* [11]. Such a highly nonlinear process as high harmonic generation can be accurately treated in a microscopic aspect with these simple models.

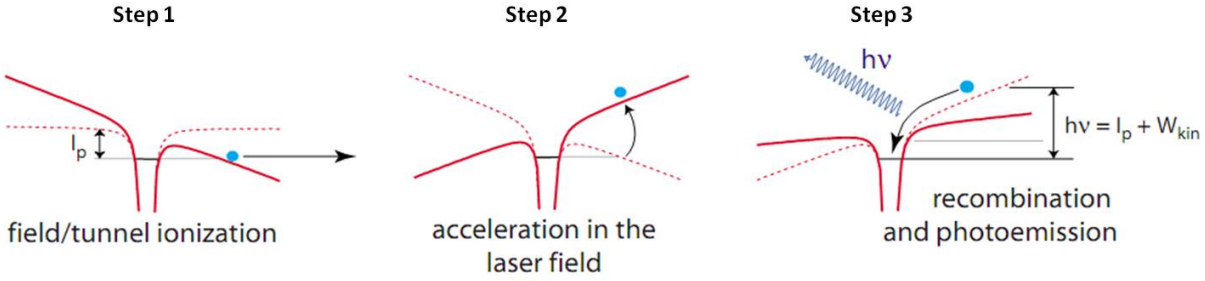

Figure 1.2: *Schematic drawing of the three-step model for HHG. Adapted from [12].*

However, HHG is a process involving not only the response from a single atom outlined

above but also the response from a large ensemble of atoms, molecules or their ions, coherently stimulated by the laser, i.e., the response of the whole medium [12–15]. Both the laser and the generated harmonic fields propagate in a gaseous medium, influenced by the nonlinear effects, such as dispersion, absorption, plasma, and ionization. Harmonic generation will be efficient only if the good phase-matching is achieved, requiring that the generated field to be in phase with the nonlinear polarization over the medium's length. The geometries widely used for generating HHG include that laser is focused in a gas jet or a cell, and laser is guided in a hollow-core fiber or a waveguide filled with gas. Moreover, the high laser intensity used may induce a strong ionization of the nonlinear medium. The resulting spatio- and temporal-dependent free-electron dispersion has important consequences on the propagation of both laser and harmonic fields [16].

1.2 Single-atom response

1.2.1 Three-step model

The intuitive picture mentioned in Sec. 1.1 for harmonic generation from a single atom (or the microscopic process) includes three steps: ionization, propagation and recombination. Each of them will be discussed in detail as follows:

Step 1: Ionization.

In an intense laser field the electron motion is governed by the oscillating electric field of laser pulse once it is freed. Firstly, the electron has to escape the binding potential of an atom in the presence of an intense laser pulse. In 1965 Keldysh [17] suggested an alternative mechanism for ionization could occur under certain conditions. At modest laser intensities ($<10^{14}$ W/cm^2), if the ionization potential is low compared with the frequency of the light and large compared with the electric field of the laser, the normal multiphoton excitation route for ionization via intermediate states applies as shown in Fig. 1.3(a). If the incident field is strong enough, and the atomic potential is significantly distorted to such an extent

that a potential barrier is formed. If the frequency of light is low enough such that the electron can respond to this changing potential, within a quasi-stationary approximation, the electron can tunnel out through a static potential barrier as shown in Fig. 1.3(b). As the laser field strength is high enough, the barrier is completely suppressed and the electron will be classically "ripped off". This is known as barrier-suppressed ionization in Fig. 1.3(c). The critical field is obtained by equating the maximum induced by the field in the atomic potential to the binding energy:

$$F = \frac{\kappa^4}{16 Z_c}, \tag{1.1}$$

where $\kappa = \sqrt{2I_p}$ with I_p being the ionization energy, and Z_c is the charge seen by the active electron. Keldysh also introduced a parameter γ, now well known as "Keldysh parameter" to determine whether the atom is ionized in the tunneling ($\gamma \ll 1$) or the multiphoton regime ($\gamma \gg 1$), which was defined as:

$$\gamma = \sqrt{\frac{I_p}{2U_p}}, \tag{1.2}$$

where U_p is the ponderomotive energy as defined in Sec. 1.1. This can be understood in a qualitative way: the laser-distorted Coulomb potential oscillates with the laser frequency. For higher frequency (larger γ), the electron does not have enough time to accommodate the fast changes in the potential and the quasi-static approximation is not valid. The motion of the electron is governed by an average over many cycles of the laser field. For tunneling (smaller γ), its time, which depends on laser intensity and ionization potential is larger than the optical period, so it occurs in a single cycle. In the multiphoton regime, the steady nonlinear interaction with the laser field (absorption of many photons) leads to an electronic state with an energy larger than zero, thus a free electron. In the opposite limiting case (much smaller γ), the laser field is high enough to fully suppress the barrier. The tunneling ionization model is an essential element in the theory of high harmonic generation, in which the electric field can be regarded as quasi-static one. In 1986, Ammosov, Delone and Krainov [18] gave a generalized analytical theory, which is well known as "ADK theory", to calculate

the ionization rate for arbitrary atoms and initial electronic states. In 2002 Tong and Lin extended the atomic ADK theory to diatomic molecules by considering the symmetry property and the asymptotic behavior of the molecular electronic wave function. They also tabulated the structure parameters of several molecules for calculating the ionization rates. This approach is usually called molecular ADK theory, or MO-ADK theory [19].

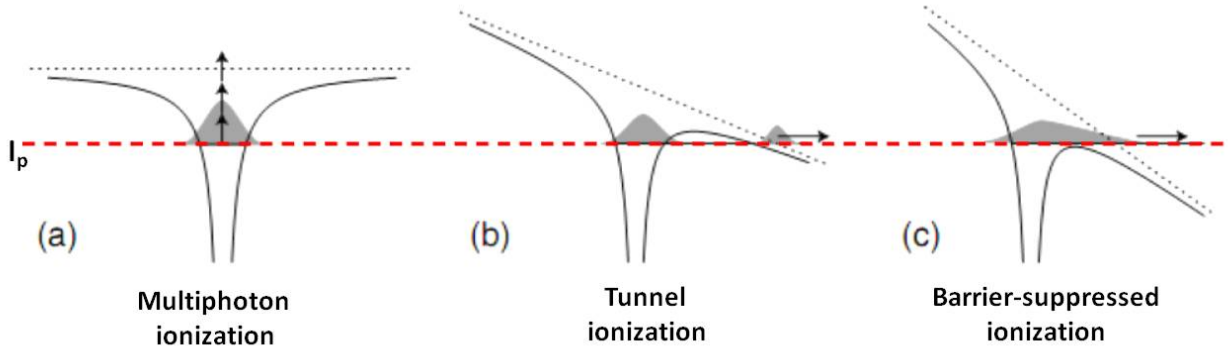

Figure 1.3: *Schematic diagram of three ionization mechanisms. Modified from [15].*

Step 2: Propagation.

After an electron is ionized, it is driven away from the atomic core by a laser field $E(t) = E_0 \cos\omega_0 t$. But at later time, the laser field reverses its direction and the electron is then accelerated back towards the atomic core. Based on the Newton's law of motion, the electron displacement, x, from the core obeys [13]

$$\begin{aligned} \frac{d^2x}{dt^2} &= \frac{eE_0}{m}\cos\omega_0 t, \\ \frac{dx}{dt} &= v = \frac{eE_0}{m\omega_0}\sin\omega_0 t + v_i, \\ x &= -\frac{eE_0}{m\omega_0^2}\cos\omega_0 t + v_i t + x_i, \end{aligned} \tag{1.3}$$

where v_i and x_i are the initial velocity and position. Assuming the conditions $v(t_0)$=$x(t_0)$=0 at the moment of ionization, $t = t_0$, the different classes of electron trajectories during propagation in the laser field are plotted in Fig. 1.4. Electrons starting from the atomic core

located at (0,0), can return to the core at position 0 depending on the initial phase $\phi = \omega_0 t_0$. The final kinetic energies of electrons at the moment of recombination are determined by the intersection with the velocity axis. If the electron ionized at a phase of $\phi = 17°$ along the cutoff trajectory b has the highest kinetic energy of $3.17U_p$ upon it returns to the core. Electrons ionized at the peak of the electric field ($\phi = 0°$) return to the core with zero kinetic energy (can be seen in trajectory d). However, most electrons are produced at unfavorable phases of the electric field and never return to the core (for example, trajectory e). There are "short" and "long" trajectories, leading to the same final energy for the harmonics in the plateau, for example, trajectories a ($\phi = 45°$) and c ($\phi = 3°$), respectively. Only the first two encounters of the electron with the ion (as shown in Fig. 1.4) lead to significant photon emission because of the quantum-mechanical nature of the electron, which suffers from dispersion (spreading of the wave function, thus the overlap with an atom becomes smaller) as soon as it is not bound to a potential.

Step 3: Recombination.

When an electron recombines with the parent ion, the photon energy is determined by the sum of the ionization potential I_p and the momentary kinetic energy W_{kin} of the electron depending on the phase ϕ at the moment of ionization (as shown in Fig. 1.5):

$$\hbar\omega = I_p + W_{kin}, \tag{1.4}$$

where $\hbar$ is the reduced Plank constant (or Dirac constant) and ω is the angular frequency of high harmonic. The maximum kinetic energy is $3.17U_p$ as the phase is 17°, this determines the "cutoff" law of $I_p + 3.17U_p$ for high harmonic generation [8] as mentioned in Sec. 1.1. The recombination step is either replaced by the radiationless transition to the autoionizing state or relaxation with XUV emission to describe the enhancement of the generation efficiency for the harmonic resonant with the transition between the ground and autoionizing state of the generating ion [20], or modified such that a returning electron can promote a lower-lying electron into the valance band and then recombine to the vacancy in the lower-lying state

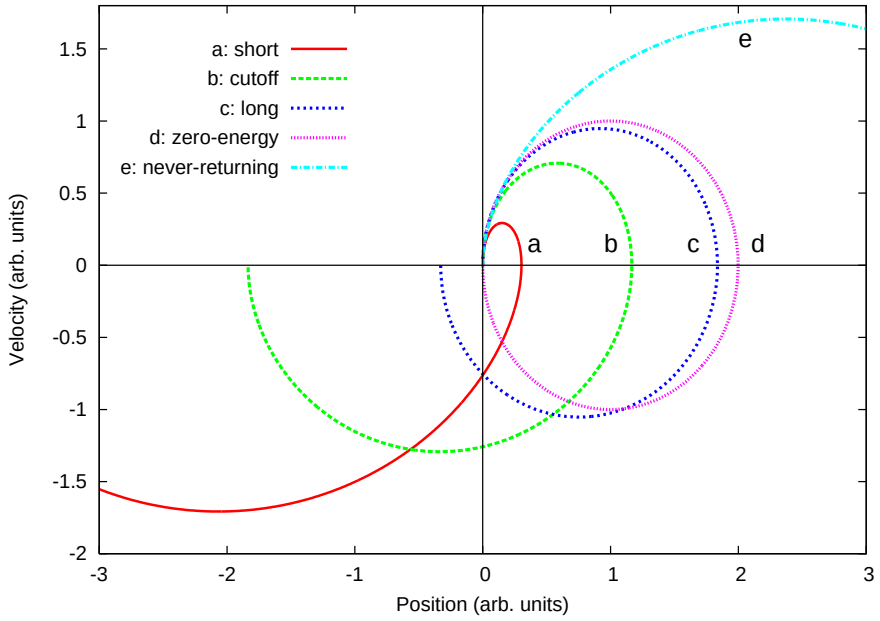

Figure 1.4: *Different classes of electron trajectories during the propagation phase of high harmonic generation, plotted in the position-velocity plane. Reproduced from [12].*

to probe the multi-electron dynamics with high-harmonic spectroscopy [21].

HHG is only one of the strong-field nonlinear processes in the frame of the three-step model. Other important processes are high-energy above-threshold ionization (HATI) [22, 23] and nonsequential double ionization (NSDI) [24, 25]. HATI originates from the elastic scattering of the returning electron with the atomic ion in the backward direction. The electron gains energy in excess of its initial energy in integer multiples of the fundamental laser frequency. A typical photoelectron spectrum shows a characteristic plateau of electron peaks, separated by one fundamental photon energy, with a sharp drop around $2U_p$ and a cutoff of $10U_p$. When an inelastic collision of the electron with its parent ion occurs, another electron can be ionized so that in the end the atom is doubly ionized. This process is called "NSDI". In NSDI, a characteristic intensity dependence of doubly ionized atomic ions is followed the intensity dependence of single ionization. A "knee" was observed in the

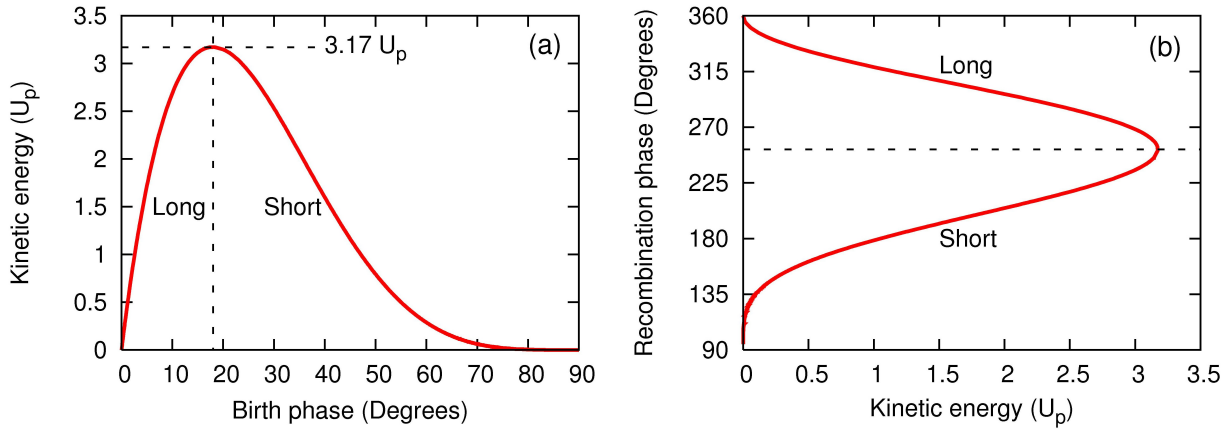

Figure 1.5: *(a) A variation of the kinetic energy of the returning electron as a function of the birth phase (i.e., the phase of the electric field at which the electron is born by tunneling ionization). (b) Plot of the recombination phase (or recombination time) changing with the final kinetic energy. The kinetic energy reaches the maximum (or cutoff) of 3.17 U_p at the birth phase of 17 degrees. Below the cutoff, two trajectories (short and long) lead to the same final kinetic energy.*

intensity dependence at the point where single ionization saturated, indicating that the two processes are coupled. There are two mechanisms for the removal of the second electron by the returning electron: one is through electron-impact ionization, i.e., the (e, $2e$) process, and the other is electron-impact excitation followed by laser tunnel ionization [26].

1.2.2 Wavelength scaling of harmonic efficiency and attochirp

One of the main interests in the study of HHG is to produce bright tabletop XUV or soft X-ray sources, or intense attosecond pulses. The single-atom harmonic cutoff energy is proportional to the square of the wavelength λ_0 of the laser and laser intensity I_0. One approach to extend the cutoff energy is to increase the laser intensity. Unfortunately, due to the depletion of the ground state there is a practical limit beyond which the intensity can be increased. An alternate way is to use longer-wavelength lasers. However, semiclassical strong-filed approximation [10] predicts that the HHG yield from a single atom scales as λ_0^{-3}, which was partially supported by an experiment [27]. A simple physical interpretation for this scaling law is that λ_0^{-2} originates from the wave packet spreading (spending much

more time in the continuum as the wavelength of the laser increases) while an additional λ_0^{-1} factor arises from the conversion from photon number to energy. This is only valid for a single harmonic with both I_p/ω_0 and U_p/ω_0 constant [28]. Quantum-mechanics calculations suggested that single-atom HHG yield drops even more dramatically with laser wavelengths and scales as $\lambda_0^{-5.5}$ for the fixed laser intensity and for a same photon energy interval [29–31]. Later on, this unfavorable scaling law was partially confirmed by experimentally measured scaling laws of $\lambda_0^{-6.3\pm1.1}$ in Xe and $\lambda_0^{-6.5\pm1.1}$ in Kr at constant laser intensity (somewhat worse than the theoretical predictions) [32]. Actually, macroscopic dispersive effects (such as electronic, geometric, dispersion and induced dipole phase) generally result in a more rapid decrease of the HHG scaling with increasing wavelength, this will be discussed in detail in Sec. 3.6.

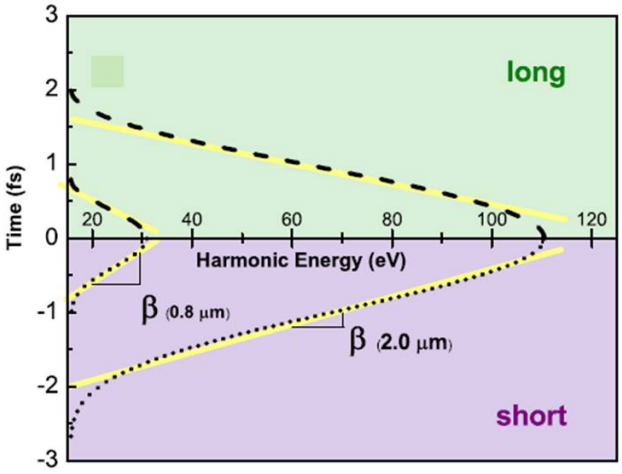

Figure 1.6: *Representation of short and long trajectories predicted by the semiclassical model similar to Fig. 1.5(b). Short trajectories are emitted first, and exhibit a positive chirp β. Increasing the wavelength lowers the attochirp as evidenced by the decrease in slope. Adapted from [33].*

HHG can also be described in an effective way based on classical trajectories. A bound electron freed by intense field ionization is accelerated for approximately half an optical cycle, and then it can recombine with the parent ion to emit an attosecond burst of light. Since the emission process occurs twice per optical cycle, it corresponds to a comb of odd-

order harmonics of the fundamental driving laser field in the frequency domain. The often used quantum mechanical treatment based on SFA [10] neglects the influence of the Coulomb potential on the motion of the free electron in the laser field. Those quantum paths whose quasi-classical action is stationary contribute mostly to the single-atom induced dipole. Consequently, classical mechanics as mentioned in Sec. 1.2.1 is a good approximation to describe the motion of the electron in the continuum, and the semiclassical model predicts a dispersion of the recombination times [as shown in Fig. 1.5(b)], which corresponds to a spectral group delay dispersion (GDD) of the emitted harmonics (attochirp) [33]. The attochirp is the main intrinsic limitation to the duration of Fourier-synthesized attosecond pulses. In attosecond generation, the consecutive harmonics do not emit simultaneously due to the attochirp, and the ordering of the frequencies defines the sign of the attochirp. Consequently, for the production of the shortest attosecond burst there exists an optimal bandwidth (Fourier transform limited pulse duration), beyond which the pulse broadens as dispersion dominates. This attochirp can be partially compensated by propagating the pulses in a suitable dispersive medium [34, 35]. In Fig. 1.6, the attochirp is given by the derivative of the curve of HHG emission times as a function of harmonic photon energy. For a given class of trajectories (either "short" or "long" trajectory), the attochirp is almost constant. It also follows that the attochirp is proportional to the ratio of the fundamental laser period to the harmonic cutoff energy [33] as shown in Fig. 1.6. Since the cutoff energy scales linearly with the laser intensity, one can reduce the attochirp by increasing the peak intensity. However, this is limited to a maximum laser intensity due to the depletion of the ground state as mentioned before. Another better way to reduce the attochirp consists in exploiting the wavelength scaling. Since the laser period is proportional to λ_0 and the cutoff energy scales as λ_0^2, and thus the attochirp (their ratio) should scale as λ_0^{-1}. As mentioned previously, increasing the fundamental wavelength at constant intensity can avoid the problems related to the ionization, so, this method, coupled with the strong enhancement of cutoff energy, would allow a better path towards shorter attosecond pulses centered at

higher photon energies.

1.3 Macroscopic propagation effects

1.3.1 Phase matching conditions

Phase matching is the matching of the phase front of the generated harmonic field to the phase front of the fundamental laser field. In laser-matter interaction, this phase matching could be complicated spatially and temporally due to the spatiotemporal variation of laser intensity. The phase mismatch relation for the qth harmonic can be written as [36, 37]

$$\begin{aligned} \Delta k_q &= (k_q - qk_0) - K_{q,dip} \\ &= \Delta k_{q,geo} + \Delta k_{q,el} + \Delta k_{q,at} - K_{q,dip}. \end{aligned} \tag{1.5}$$

Here k_q and k_0 are the wave vectors of harmonic and fundamental laser fields. The coherence length is proportional to the inverse of the phase mismatch. For the efficient generation of harmonics, the phase mismatch should be small. Each contribution to the phase mismatch will be discussed in more detail.

Geometric dispersion. To drive the HHG process, we need to use a laser with high enough intensity, usually obtained by confining (or focusing) a laser pulse to a small region in space, or guiding the laser beam in a waveguide. This introduces the geometric phase (it is more generally called as "Gouy" phase) for the fundamental laser and the generated harmonics, and the phase mismatch can be written as

$$\Delta k_{q,geo} = k_{q,geo}(r,z) - qk_{0,geo}(r,z). \tag{1.6}$$

There are two main geometries in practice. One is to focus a laser beam in the free space. The most general mode is a Hermite-Gaussian beam. A Gaussian TEM_{00} mode is the lowest Hermite-Gaussian mode whose radial intensity distribution is Gaussian. The Gaussian beams emitted by many lasers are usually refracted by a lens to create a converging beam, and then a Gaussian laser beam is transformed into another Gaussian beam (characterized

by a different set of parameters). However, the focal spot size of a Gaussian beam is only sustained over approximately one Rayleigh length $z_R = \pi w_0^2/\lambda_0$, where w_0 is the beam waist. After that the beam size increases approximately linearly with propagation distance z. (See details in Appendix D.1.) The truncated Bessel beam is a general model for a few-cycle pulse (as discussed in Appendix D.2). The other one is to guide a laser beam in the hollow waveguide to maintain high intensity over an extended propagation length. When a laser pulse is focused into a capillary, the beam radius remains constant over the length of the capillary, due to reflection of the light at the boundaries. The wave vectors of the laser and the generated harmonic fields are all affected due to the particular conditions at the capillary walls. The modification of the wave vector is larger if the diameter of the waveguide is smaller.

Induced dipole phase. For the HHG in the strong-field regime, it is shown that the single-atom induced dipole phase strongly depends on the laser intensity, so the spatial variation of the focused laser beam results in longitudinal and transverse gradients of this phase. The contribution to the phase mismatch is

$$K_{q,dip} = \nabla \varphi_{q,dip}. \tag{1.7}$$

Here the intrinsic dipole phase $\varphi_{q,dip}$ is the action accumulated by an electron during its excursion in the laser field along the trajectory leading to the emission of the qth harmonic. It can be expressed as (in the first-order approximation)

$$\varphi_{q,dip} = -\alpha_i^q I, \tag{1.8}$$

where I is the instantaneous laser intensity. The proportional constant $\alpha_{i=S,L}$ depends on "short" (S) or "long" (L) trajectory. When the harmonics are in the plateau region, $\alpha_{i=S}^q \approx 1{\times}10^{-14}$ rad cm^2/W and $\alpha_{i=L}^q \approx 24{\times}10^{-14}$ rad cm^2/W [38–41]. In the cut-off region, these two trajectories merge into one, and $\alpha_{i=S,L}^q \approx 13.7{\times}10^{-14}$ rad cm^2/W. The intensity dependence of the dipole phase is different for "short" and "long" trajectories, so good phase-matching conditions are different for the two trajectories. This dipole phase is

also responsible for the spectral broadening of high harmonics because the intensity variation $I(t)$ in time causes a frequency chirp $\Delta\omega_q(t) = -\partial\varphi_{q,dip}(t)/\partial t$.

Plasma (electronic) dispersion. The first step of the HHG process is ionization. Actually, only a small portion of electrons freed by the laser field could recombine with the parent ion to emit high-energy photons. The rest miss the core and become free for a long time compared with the laser duration. This would finally cause the modification in the refractive index. The phase mismatch due to free electrons is

$$\begin{aligned} \Delta k_{q,el} &= k_{q,el}(r,z,t) - qk_{0,el}(r,z,t) \\ &\approx \frac{e^2 n_e(r,z,t)}{4\pi\varepsilon_0 m_e c^2} q\lambda_0 = qr_0 n_e(r,z,t)\lambda_0, \end{aligned} \tag{1.9}$$

where $n_e(r,z,t)$ is the spatiotemporal dependent electron density, e, m_e and r_0 are the charge, the mass and the classical radius of an electron, respectively. Here the free-electron dispersion for the harmonic field is neglected because the frequencies of high harmonics are much higher than the plasma frequency.

Neutral (atomic) dispersion. Any conversion media for HHG exhibit dispersion, which is a refractive index depending on the frequency (or wavelength) of the light. The phase mismatch due to neutral atom dispersion is

$$\Delta k_{q,at} = k_{q,at}(r,z,t) - qk_{0,at}(r,z,t). \tag{1.10}$$

The spatiotemporal dependence may be involved due to the ionization of the medium. For the fundamental laser pulse, the Sellmeier equations with coefficients that are specific for a particular medium can be applied to obtain the refractive index, where the wavelength region is not too close to a resonance. For the harmonics in the XUV regime, the refractive index is generally smaller than 1. For an intense ultrafast laser, the intensity dependent modification in the refractive index caused by the third-order susceptibility (usually called as "Kerr effect") may become important in some parts of the pulse close to the laser peak.

1.3.2 Absorption effect

For most conversion media used for HHG process in the photon-energy region of 10 - 100 eV, the photoionization cross section σ, as well as the absorption of the photons is large. So the reabsorption is a limiting factor to phase-matched harmonics in the soft X-ray and XUV spectral region. One can define an absorption length $L_{abs} = 1/\rho\sigma$ as the length over which the intensity of XUV light propagating in an absorbing medium drops to 1/e, where ρ denotes the gas density. The harmonics are generated as the driving laser propagates along the direction z through the medium. The earlier generated harmonics are added to the newly generated ones coherently, and they are also affected by absorption. Based on a one-dimensional model, one can obtain the qth harmonic yield [42, 43]

$$I_q \propto |\int_0^{L_{med}} \rho A_q(z) \exp(-\frac{L_{med}-z}{2L_{abs}}) \exp[i\varphi_q(z)]dz|^2, \tag{1.11}$$

where $A_q(z)$ is the amplitude of the single-atom response, and $\varphi_q(z)$ is its phase at the exit of the medium. For the loose focusing or guiding laser beam, $A_q(z)$ can be assumed independent of z, Eq. (1.11) becomes

$$I_q \propto \rho^2 A_q^2 \frac{4L_{abs}^2}{1+4\pi^2(L_{abs}^2/L_{coh}^2)}[1+\exp(-\frac{L_{med}}{L_{abs}}) - 2\cos(\frac{\pi L_{med}}{L_{coh}})\exp(-\frac{L_{med}}{2L_{abs}})], \tag{1.12}$$

where $L_{coh} = \pi/\Delta k_q$ is the coherence length, which can be calculated by phase mismatch Δk_q in Sec. 1.3.1. The evolution of I_q as a function of the medium length for different ratios of L_{coh}/L_{abs} is plotted in Fig. 1.7. To generate about half the asymptotic harmonic yield for a long coherence and propagation length, the following conditions need to fulfill [42, 43]:

$$L_{med} > 3L_{abs}, L_{coh} > 5L_{abs}. \tag{1.13}$$

Under these conditions, one can generate close to the maximum of harmonic yield, for example, the harmonic yield reaches approximately 90% of the asymptotic value when L_{med} is about $6L_{abs}$. Another important feature from this analysis is that the asymptotic value increases as $|A_q/\rho|^2$, independent of the gas density. It requires to maximize A_q/ρ and fulfill Eq. (1.11) simultaneously to optimize the HHG yield. These optimizing conditions are time dependent and strongly influenced by ionization.

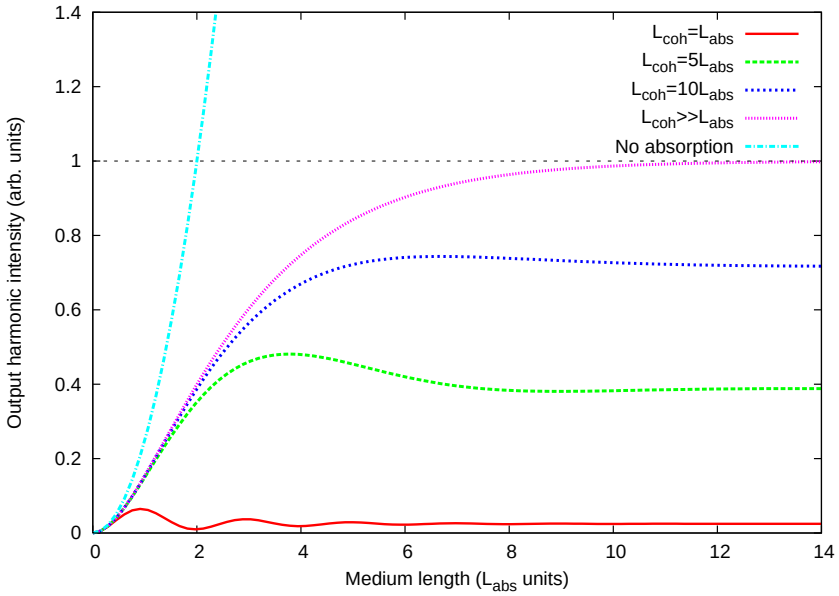

Figure 1.7: *Reabsorption of the generated HHG light in the nonlinear medium. The harmonic intensity increases quadratically with the medium length in the absence of absorption. If absorption is included, there is an asymptotic limit of the HHG intensity as a function of the medium length. Reproduced from [42].*

1.3.3 Spatiotemporal dynamics of laser pulse

As discussed above, most free electrons resulted from ionization could not recombine with the parent ions, and they create a plasma environment for laser propagation in a gaseous medium. This plasma effect contributes to the refractive index as a negative value: $-e^2 n_e(r,z,t)/(2\omega_0^2 \varepsilon_0 m_e)$ with electron density n_e [44] and other parameters defined before. The strong dependence of the ionization on the laser intensity leads to the strong spatiotemporal electron density, and spatiotemporal dynamics for a focused laser beam propagating in a relatively dense medium [16]. Consequently, the generated harmonics which are driven by the distorted laser pulse are greatly affected and shown to be good candidates for producing an isolated attosecond pulse after spatial and spectral filtering in the far field (see Publication [7]).

Defocusing. Laser focusing leads to quite different spatial distribution of the intensity

(or ionization). In the beginning part of the medium, the ionization probability is highest on axis and decreases with r because of the radial laser intensity variation, and the resulting radial variation of the electron density (or refractive index) acts like a negative lens which rapidly defocuses the laser beam [16]. However, the resulting lower intensity in turn slows down the defocusing process. The most changes to the spatial profile occur in the first half of the medium where the laser intensity is still high (also the high ionization). When the ionization probability becomes lower (typically a few percent), the spatial profile does not significantly change its shape and the beam diverges slowly. Finally the profile of laser close to the propagation axis is changed dramatically compared to the assumed one propagating in the vacuum (usually considered as a Gaussian beam).

Blue shift. The ultrafast laser pulse also makes laser intensity change rapidly in time. The time dependent refractive index, through the variation of the electron density, leads to a time dependent phase of the electric field and therefore a frequency chirp. During the evolution of the pulse, there are two cases for the time-dependent electron density [16]. One is that it either increases (when the intensity is high enough to induce the considerable ionization), or stays constant (when the intensity is low). The other is that the intensity is sufficiently high to saturate the ionization probability, the electron density initially increases and then saturates and stays constant. The central frequency of laser field in both cases is blue shifted because the number of the free electron is increased as a function of time, and the blue shift also has time dependence. Thus the fundamental laser field at the exit of the medium is reshaped both spatially and temporally [45]. The outgoing beam is much broader and more divergent than the incoming beam, and has a lower peak intensity. The peak of the pulse may shift to off-axis position in space, it may occur earlier in time and the effective duration of the pulse may be shorter than the incoming pulse.

1.4 Applications of high-order harmonic generation

1.4.1 Generation of attosecond pulse train and isolated attosecond pulse

One of the most attractive goals in nonlinear optics is to generate short-wavelength pulses with ultrashort duration [46]. Due to some unique properties, such as ultrashort duration, high brightness, and good coherence, HHG becomes a candidate source for this purpose. The harmonic emission can be understood intuitively as ultrashort bursts emitted at each recollision of the electron with the parent ion, which takes place during every half optical cycle (linearly polarized laser is assumed). Each emission consists of contributions of two electron trajectories with the shortest return times. Furthermore, either phase matching in the medium, or spatial filtering in the far field, selects contribution of only one of these trajectories. As a result, harmonic radiation consists of a train (called as "attosecond pulse train" – APT) of sharp short-wavelength pulses with sub-femtosecond duration, with only one pulse per half cycle. Experimentally, an APT with duration of 250 as was demonstrated by Paul *et al.* [47] firstly, which corresponds to the coherent superposition of harmonics 11-19 generated in argon. To characterize attosecond pulses, they introduced the RABITT (reconstruction of attosecond beating by interference of two-photon transitions) technique, in which side bands involving adjacent harmonics were measured to determine their phase relationship.

An APT is suitable for a number of specialized applications, however, for many other applications an isolated attosecond pulse (IAP) is required to offer the unique time resolution on the attosecond timescale. Indeed, there was a plethora of techniques developed for the production of IAP, with the idea that harmonics can be limited to generate only from half an optical cycle in a few-cycle or multi-cycle infrared laser pulse. Conceptually, spectral filtering of high harmonics by a few-cycle driving pulse is the simplest scheme for producing an IAP. Generally, the harmonics in the cutoff region are emitted during one half-cycle only (will be continuous spectrum) if the driving pulse is short enough (typically two optical cycles or

less) and has appropriately stabilized carrier-envelope phase (CEP). Using this method, an IAP as short as 80 attoseconds has been generated [48]. Based on the strong sensitivity of the HHG process to the polarization (ellipticity) of the driving laser, the harmonic emission can be localized to the time interval in which the laser is linearly polarized. Using this polarization gating technique, an isolated 130 as pulse has been produced [49, 50]. The advantage of this technique is that in principle a much larger range of frequencies in the harmonic spectrum are emitted during a short time (not only the frequencies in the cutoff region), allowing for potentially much shorter attosecond pulses with higher yields. Other methods for IAP generation include spatiotemporal gating, two-color control, quasi-phase matching, and so on. In a tight-focusing geometry, different phase-matching can be achieved for different photon-energy regions. The good phase matching on axis is only for harmonic radiation within one half cycle of the driving field, an IAP could be temporally selected by applying a spatial and spectral filter in the far field [51, 52]. The polarization gating method above is based on the use of two color fields with the orthogonal polarizations, and the two-color field co-polarized is also used for IAP generation. The presence of the second field with different frequency and intensity breaks the half-cycle periodicity of the electron dynamics and offers an additional time gating. To improve the yield of harmonics, as well as the intensity of attosecond pulses, quasi-phase matching method has been used with the idea that only the constructive build-up of the harmonic radiation was allowed. The newly generated harmonics interferes with earlier ones during the propagation in the medium, while the destructive inference regions can be minimized either by modulating the generating light (for example, using counter-propagating light), or by modulating the generating material (for example, using modulated wave guides) [53–56]. Meanwhile, an IAP can be characterized using an attosecond streak camera technique pioneered by Krausz and coworkers [57, 58] reling on the use of an intense (10^{13} - 10^{14} W/cm^2) infrared laser field that exchanges many photons with the electron after it has been set free in the continuum by the attosecond pulses.

The availability of APT and IAP makes it capable of performing pump-probe experiments with APT or IAP as a pump pulse and infrared (IR) laser as a probe pulse (usually written as "APT+IR" or "IAP+IR") [59–61]. Such experiments have the advantage that the time delay between the APT (or IAP) and the IR can be controlled with high precision at the level of attoseconds. The pump pulse can create an attosecond wave packet evolving in time, and the probe pulse can be applied at different time delays. It is of interest to observe how the results of the probe changes with the time delay, and then using these results to retrieve the information on the dynamic system after the pump pulse. The availability of attosecond pulses may also allow one to perform attosecond pump-probe experiments [62] where a first XUV pulse electronically excites an atomic, molecular, or condensed phase system of interest, thereby initiates an ultrafast electronic process, and a second, time-delayed XUV pulse extracts a signal from the system containing information about the time evolution that has taken place. Both pulses have a duration that is short compared to the typical timescale of the electron dynamics under investigation. Few attempts include that Hu and Collins [63] calculated two-color ionization of He using a sequence of two ultrashort XUV pulses and Yudin *et al.* [64] analyzed the ionization of a set of coherently coupled states using an attoscond pulse.

1.4.2 Probing electronic structure and dynamics of atoms and molecules

HHG itself has also become a tool to obtain the structural and dynamical information of atoms and molecules. Because single-atom (or single-molecule) harmonic emission results from interference of the re-collision electron with the ground-state wave function (Step 3 as discussed in Sec. 1.2.1), the electronic structure of molecular orbitals, or electron-electron interaction is imprinted on the HHG spectrum. In a recent experiment Shiner *et al.* [21] recorded high-harmonic spectra of several atoms (Kr, Xe and Ar) for the photon energy up to 160 eV using a few-cycle 1.8-μm laser. They showed that these spectra can be related to differential photoionization cross sections measured with synchrotron sources, and

these spectra contain features due to collective multi-electron effects involving inner-shell electrons, in particular the giant resonance in Xe. In addition, harmonic interferometry has been used to probe the multi-electron dynamics in molecules by Smirnova *et al.* [65]. They measured the phases and amplitudes of CO_2 harmonics, and revealed features of multiple orbitals and the underlying attosecond multi-electron dynamics, including the dynamics of electron rearrangement upon ionization. In another pioneering experiment, Itatani *et al.* [66] demonstrated the so-called tomographic imaging of molecular orbitals, where the highest-occupied molecular-orbital (HOMO) of N_2 molecule can be retrieved by measuring HHG spectra at a range of alignment angles of the molecular axis with respect to the polarization of the driving laser. This approach has recently been applied to reconstruct the HOMO of CO_2 using harmonic spectroscopy [67].

HHG process can provide access to the molecular structure as well. Following the two-center interference model by Lein *et al.* [68], Kanai *et al.* [69] observed the constructive and destructive interference occurred for selected harmonics subject to a Bragg condition for the returning electron. Since then one can deduce the internuclear distances in the molecule by using the harmonic order where constructive or destructive interference occurs. Single-molecule harmonics can be viewed as from an electron-ion recollision process, where the electron recollides with the positive ion predominantly during a small fraction of the optical cycle of the driving laser, implying that the electron probes the ion with attosecond time resolution. In an experiment on D_2^+ dissociation, one could thus map the first few femtoseconds of the molecular dissociation by using a wavelength-tunable ionization laser, where variation of the wavelength translates into a variable recollision time [70]. In another experiment, Baker *et al.* [71] demonstrated a method that could probe nuclear dynamics and structural rearrangement on a sub-femtosecond time scale using HHG in molecules. The chirped nature of the electron wave packet produced by laser ionization in a strong field gave rise to a similar chirp in the photons emitted upon electron-ion recombination, and this chirp in the emitted light allowed one to obtain information about nuclear dynamics

with 100-as temporal resolution, from excitation by an 8-fs pulse, in a single laser shot.

In the experiments above the nuclear and electronic dynamics were induced by the same laser pulse, one can also apply another probe laser, which subsequently resolves time-delayed processes of electronic and nuclear configuration of the molecule.

1.4.3 Single-photon ionization of aligned molecules

The chemical reactions and biology transformations occur on a time scale of picoseconds or less, where the time evolution of molecules can be commonly probed by exploiting the relation between the structure of a molecule and its photoabsorption spectrum [72]. The interpretation of these experiments often relies on the existing knowledge about the molecular spectroscopy. Therefore X-ray (or XUV) diffraction and electron diffraction are the conventional approaches, which severed well to image the molecular structure. In electron diffraction experiments, the wavelength of the electrons is small compared to the relevant inter-nuclear distances, inducing diffraction that enables one to resolve structures with sub-nanometer resolution. However, the creation of electron bunches shorter than 100 fs is a major challenge. Alternatively, one can use the diffraction of electrons generated within a molecule through photoionization by an XUV or X-ray pulse.

Photoionization is the basic physical process that provides the most direct investigation of molecular structure. The ejected photoelectrons contain information on the molecular orbitals from which they are removed. The outgoing electrons also experience the surrounding atoms in the molecule as scattering centers, endowing the photoelectron angular distribution (PAD) with sensitivity to the underlying molecular structure. It is possible to extract the detailed information on orbitals and/or structure if the PAD is measured in the molecular frame. However, almost all earlier experimental measurements were performed from an ensemble of randomly distributed molecules. Thus the rich dynamical structure of PAD for fixed-in-space molecules still remains largely unexplored. This challenge can be met by measuring photoelectrons and fragment ions formed from the same parent molecule

in coincidence. Using molecular alignment and orientation techniques, it can avoid the requirement of a rapid dissociation accompanied by an axial recoil of the fragment ions. These techniques allow active control of the angular distribution of a parent molecule before ionization takes place using either adiabatic or nonadiabatic methods with infrared lasers [73–75].

Photoionization of aligned molecules has previously been explored with UV/near-infrared radiation [76–78]. However, the kinetic energy of the ejected photoelectron is very low, i.e., the de Broglie wavelength of the electron is much larger than the inter-atomic spacings, which is not suitable for obtaining the structural information. An alternative approach is provided by the HHG source served as XUV or X-ray light, which makes it possible to perform single-photon ionization experiments of aligned molecules. In a few recent experiments, Thomann *et al.* [79] reported the angular dependence of single-photon ionization of aligned N_2 and CO_2 molecules, Kelkensberg *et al.* [80] measured electron angular distribution of CO_2 molecules which were aligned using a near-infrared laser and ionized using XUV pulses, and they revealed the contributions from four orbitals and the onset of the influence of the molecular structure.

1.5 Thesis outline

In this thesis, our main focus is to develop a macroscopic propagation model to quantitatively describe HHG spectra of gaseous atoms and molecules measured in experiments. To make a complete story of HHG, we investigate some of its important applications, i.e., probing the electronic structure of atoms and molecules, producing an isolated attosecond pulse, and ionizing the aligned molecules.

In Chapter 2, we describe a complete theory for HHG in a macroscopic atomic and molecular medium. The theory is divided into two parts: the single-atom (or single-molecule) induced dipole obtained by solving time-dependent Schrödinger equation, and the macroscopic response of the medium by solving Maxwell's wave equation for the fundamental laser

field and harmonic field.

In Chapter 3, we apply our propagation model to simulate the measured HHG spectra by using a multi-cycle laser pulse, and establish a separable approximation for macroscopic HHG. In Chapter 4, we extend our model to incorporate the truncated Bessel beam as an incident laser beam, which is the general case for a few-cycle laser pulse. Our focus in these two chapters is Ar. We especially take a close look of the Cooper minimum in the HHG spectrum.

In Chapter 5, we investigate multi-electron effect and continuum structure in the measured HHG spectrum of Xe. The reshaping of the fundamental laser field plays an important role to form the continuum harmonics, and these harmonics will be proven theoretically to produce an isolated attosecond pulse.

In Chapter 6, we simulate the HHG spectra of molecular targets by taking into account of macroscopic propagation in the medium, which can be quantitatively compared to measurements directly. For two examples, N_2 and CO_2 molecules, we also discuss the multiple orbital contributes to the HHG spectrum.

In Chapter 7, we study another important application of HHG, i.e., single-photon ionization. We use the well-established photoionization theory to calculate the photoelectron angular distribution in the laboratory frame, which can be compared to the future experiments.

Finally, we summarize this thesis in Chapter 8.

Chapter 2

Theoretical tools

2.1 Introduction

Our focus in this thesis is high-order harmonic generation (HHG) by an intense laser field. In considering the interaction of an atom (or a molecule) with radiation, there are three basic processes [81]: spontaneous emission in which an atom is treated as a classical oscillating charge that can make a spontaneous transition from an excited state to a state of lower energy, emitting a photon; absorption in which an atom absorbs a photon from an external radiation field, making a transition from a state of lower to a state of higher energy; and stimulated emission in which an atom can also emit a photon under the influence of an external radiation field. To describe the interaction of an atom (or a molecule) with an intense laser field, there are generally three approaches: classical theory; semiclassical theory; and theory of quantum electrodynamics. In classical theory, atoms (or molecules) can be modeled as a group of classical harmonic oscillators, and the laser field is simply treated as a classical electromagnetic field. In the semiclassical theory, the intense laser field is still treated classically by using Maxwell's wave equations, while the atomic (or molecular) system is described by using quantum mechanics. The influence of the atom on the external field is also neglected in this theory. Since only one-photon transition process is involved in the spontaneous emission, the semiclassical theory cannot explain it. In the theory of quantum electrodynamics, both the intense laser field and atoms are treated quan-

tum mechanically, and it can describe all phenomena involving charged particles interaction by means of exchange of photons.

As discussed in Chapter 1, the process of HHG involves the collective effect of many atoms (or molecules) in the medium interacting with a laser field. This means that a full description of the observed HHG spectra requires not only the treatment of the microscopic nonlinear laser-atom (or -molecule) interaction, but also the macroscopic propagation of harmonic radiation in the medium. Experimentally the harmonics are usually measured far away from the generating medium, the harmonic radiation from the exit of the medium needs to propagate and diverge further in the vacuum. The individual time-dependent dipole induced by the strong oscillating laser field can be obtained by semiclassical theory, and then the fundamental laser field and harmonic field are treated classically as electromagnetic fields propagating in the medium and in the vacuum. A typical HHG study thus consists of three parts: first, the calculation of the single-atom (or -molecule) response by solving the time-dependent Schrödinger equation; second, the propagation of fundamental and harmonic fields by solving the three-dimensional Maxwell's wave equations; third, the further propagation of harmonics in the vacuum (probably involving the complicated optical system) by constructing an optical $ABCD$ matrix. Each part will be discussed in detail in the following.

2.2 Time-dependent Schrödinger equation

In this section, we are only concerned with constructing the time-dependent Schrödinger equation (TDSE) of an atom. Two approximate approaches, strong-field approximation (SFA) and quantitative rescattering (QRS) theory, are applied to solve it. The formulation of TDSE for a molecular target is beyond the scope of this thesis, and we only present the approximated solution of TDSE based on SFA and QRS theory. In this thesis we limit ourselves to linearly polarized light only.

2.2.1 Semiclassical theory

The classical electromagnetic field is described by Maxwell's wave equations. The vector potential of a monochromatic electromagnetic field (with linear polarization) is

$$\vec{A}(\vec{r},t) = \vec{\varepsilon}A_0 \sin(\vec{k}\cdot\vec{r} - \omega_0 t), \tag{2.1}$$

where $\vec{k}$ is the wave vector. And the angular frequency ω_0 and the wave number k (the magnitude of $\vec{k}$) are related by

$$\omega_0 = kc, \tag{2.2}$$

where c is the speed of light. The vector potential $\vec{A}$ in the direction specified by the unit vector $\vec{\varepsilon}$ (polarization vector) has an amplitude $|A_0|$. The wavelength of the laser field is much larger than the size of an atom, characterized by Bohr radius, a_0, thus $k \cdot a_0 << 1$, and then the dipole approximation is applied here. Eq. (2.1) can be written as

$$\vec{A}(t) = \vec{\varepsilon}A_0 \sin(\omega_0 t). \tag{2.3}$$

Using single-active electron (SAE) approximation [8, 82], i.e., all the electrons in an atom are bound except the valence electron, the time-dependent Schrödinger equation of the valence electron in a laser field can be written as

$$\begin{aligned} i\hbar\frac{\partial}{\partial t}\psi(\vec{r},t) &= \left[\frac{1}{2m_e}(\vec{p} - \frac{e}{c}\vec{A})^2 + V(\vec{r})\right]\psi(\vec{r},t) \\ &= \left[\frac{1}{2m_e}(p^2 - \frac{e}{c}\vec{p}\cdot\vec{A} - \frac{e}{c}\vec{A}\cdot\vec{p} + \frac{e^2}{c^2}A^2) + V(\vec{r})\right]\psi(\vec{r},t), \end{aligned} \tag{2.4}$$

where $V(\vec{r})$ is the atomic potential. To obtain Eq. (2.4), we adopt the Coulomb gauge defined in the following:

$$\nabla\cdot\vec{A}(t) = 0, \tag{2.5}$$

and take the scalar potential ϕ=0. The momentum operator $\vec{p}$ is

$$\vec{p} = -i\hbar\nabla. \tag{2.6}$$

Using the commutation relation between $\vec{p}$ and $\vec{A}$:

$$\vec{p}\cdot\vec{A}-\vec{A}\cdot\vec{p}=-i\hbar\nabla\cdot\vec{A}, \tag{2.7}$$

Eq. (2.4) can be written as

$$i\hbar\frac{\partial}{\partial t}\psi(\vec{r},t)=\left[-\frac{\hbar^2}{2m_e}\nabla^2-\frac{e}{cm_e}\vec{A}\cdot\vec{p}+\frac{e^2}{2m_ec^2}A^2+V(\vec{r})\right]\psi(\vec{r},t). \tag{2.8}$$

Under the dipole approximation, $\vec{A}(t)$ only depends on time, so the term with A^2 also depends on time only, which could be eliminated from Eq. (2.8) in terms of the unitary transformation:

$$\Psi_V(\vec{r},t)=\exp\left(\frac{e^2}{2i\hbar m_ec^2}\int_0^t A^2(t')dt'\right)\psi(\vec{r},t). \tag{2.9}$$

And then Eq. (2.8) can be simplified as

$$i\hbar\frac{\partial}{\partial t}\Psi_V(\vec{r},t)=\left[-\frac{\hbar^2}{2m_e}\nabla^2-\frac{e}{cm_e}\vec{A}\cdot\vec{p}+V(\vec{r})\right]\Psi_V(\vec{r},t). \tag{2.10}$$

Eq. (2.10) is the time-dependent Schrödinger equation of an atom in the velocity gauge.

Actually the TDSE in the length gauge is more preferred. We introduce a unitary transformation

$$\Psi_V(\vec{r},t)=\exp\left(\frac{ie}{c\hbar}\vec{A}\cdot\vec{r}\right)\Psi_L(\vec{r},t), \tag{2.11}$$

Eq. (2.10) can be expressed as

$$i\hbar\frac{\partial}{\partial t}\Psi_L(\vec{r},t)=\left[-\frac{\hbar^2}{2m_e}\nabla^2+\frac{e^2}{2m_ec^2}A^2+\frac{e}{c}\frac{\partial\vec{A}}{\partial t}\cdot\vec{r}+V(\vec{r})\right]\Psi_L(\vec{r},t). \tag{2.12}$$

Using the transformation in Eq. (2.9), the term including A^2 could be eliminated. Because the effect of an electron with a magnetic field is much weaker compared to an electric field, the effect of the magnetic field can be neglected. The strength of the electric field $\vec{E}(t)$ is related to the vector potential $\vec{A}(t)$ by

$$\vec{E}(t)=-\frac{1}{c}\frac{\partial\vec{A}(t)}{\partial t}. \tag{2.13}$$

Eq. (2.12) can be further simplified as

$$i\hbar\frac{\partial}{\partial t}\Psi_L(\vec{r},t) = \left[-\frac{\hbar^2}{2m_e}\nabla^2 + V(\vec{r}) - e\vec{r}\cdot\vec{E}(t)\right]\Psi_L(\vec{r},t). \tag{2.14}$$

Eq. (2.14) is the time-dependent Schrödinger equation of an atom in the length gauge. This is the equation used to study the microscopic nonlinear laser-atom interaction for harmonic radiation, and we use "$\Psi(\vec{r},t)$" without "L" to note the time-dependent wave function in the length gauge for simplicity.

Eq. (2.14) can be solved by expanding the $\Psi(\vec{r},t)$ in terms of eigenfunctions, $R_{nl}Y_{lm}(\hat{r})$, of the laser-free Hamiltonian, within the box of $r \in [0, r_{max}]$,

$$\Psi(\vec{r},t) = \sum_{nl} c_{nl}(t)R_{nl}(r)Y_{lm}(\hat{r}), \tag{2.15}$$

where radial functions $R_{nl}(r)$ are expanded in a discrete variable representation (DVR) basis set [83] associated with Legendre polynomials, while c_{nl} are calculated using the split-operator method [84].

2.2.2 Strong-field approximation

Based on strong-field approximation (SFA), Lewenstein *et al.* [10] proposed an analytic form to solve the time-dependent Schrödinger equation of an atom in a low-frequency laser field in 1994. Their theory can recovers the semiclassical interpretation of high-order harmonic generation by Krause *et al.* [8] and Corkum [9] as discussed in Sec. 1.2.1. This approach will be called either "Lewenstein model" or "SFA" interchangeably in this thesis. SFA has also been applied to study the characteristics of HHG from molecular targets [85–92]. In the following we derive the Lewenstein model for an atomic target in detail, and then it is extended for a molecular target straightforwardly.

There are two main assumptions in this model: (i) all the bound states in an atom are neglected excepted for the ground state; (ii) the electron in the continuum state is treated as a free particle without the influence of the Coulomb potential. The depletion of the ground state was neglected initially, and later on added by Antoine *et al.* [11].

We consider an atom in the SAE approximation under the influence of a laser field $E(t)$ with linear polarization in the x direction, which satisfies Eq. (2.14). The time-dependent wave function can be expanded as (atomic units are used):

$$|\Psi(t)\rangle = e^{iI_p t}\left[a(t)|0\rangle + \int d^3\vec{v}\, b(\vec{v},t)|\vec{v}\rangle\right], \tag{2.16}$$

where $a(t) \approx 1$ is the ground-state amplitude, $|0\rangle$ denotes the wave function of the ground state, and $b(\vec{v},t)$ are the amplitudes of the corresponding continuum states. The Schrödinger equation for $b(\vec{v},t)$ can be written as

$$\dot{b}(\vec{v},t) = -i\left(\frac{\vec{v}^{\,2}}{2} + I_p\right)b(\vec{v},t) - E(t)\frac{\partial b(\vec{v},t)}{\partial v_x} + iE(t)d_x(\vec{v}). \tag{2.17}$$

Here $\vec{d}(\vec{v}) = \langle\vec{v}|\vec{x}|0\rangle$ is the transition dipole matrix element from the bound to free state, and $d_x(\vec{v})$ is the component parallel to the polarization axis. Eq. (2.17) can be solved exactly and $b(\vec{v},t)$ can be written in the closed form,

$$\begin{aligned} b(\vec{v},t) &= i\int_0^t dt' E(t') d_x(\vec{v} + \vec{A}(t) - \vec{A}(t')) \\ &\times \exp\{-i\int_{t'}^t dt''\big[(\vec{v} + \vec{A}(t) - \vec{A}(t''))^2/2 + I_p\big]\}, \end{aligned} \tag{2.18}$$

where $\vec{A}(t)$ is the vector potential of the laser field, which is defined in Eq. (2.13).

To calculate the parallel component (with respect to laser polarization) of time-dependent dipole moment, we need to evaluate $D(t) = \langle\Psi(t)|\vec{x}|\Psi(t)\rangle$. Using Eqs. (2.16) and (2.18), we obtain

$$D(t) = \int d^3\vec{v}\, d_x^*(\vec{v}) b(\vec{v},t) + c.c.. \tag{2.19}$$

In the above formula, only the transition back to the ground state is considered, and the contribution from continuum to continuum part is neglected. The velocity operator is defined as follows

$$\vec{v} = \vec{p} - \vec{A}(t), \tag{2.20}$$

the final expression of Eq. (2.19) is

$$D(t) = i \int_0^t dt' \int d^3\vec{p} d_x^*(\vec{p} - \vec{A}(t)) \exp[-iS(\vec{p}, t, t')] E(t') d_x(\vec{p} - \vec{A}(t')) + c.c., \tag{2.21}$$

where

$$S(\vec{p}, t, t') = \int_{t'}^t dt'' \{[\vec{p} - \vec{A}(t'')]^2/2 + I_p\}. \tag{2.22}$$

Eq. (2.21) has a clear physical interpretation, and it is actually a sum of probability amplitudes for the following processes: $E(t')d_x(\vec{p}-\vec{A}(t'))$ is the probability for an electron to make the transition to the continuum at time t' with the canonical momentum $\vec{p}$; $\exp[-iS(\vec{p}, t, t')]$ is a phase factor when the electronic wave function is propagated from time t' until t, where $S(\vec{p}, t, t')$ is the quasi-classical action; $d_x^*(\vec{p}-\vec{A}(t))$ is a transition amplitude when the electron recombines to the parent ion at time t.

The major contribution to the integral over $\vec{p}$ in Eq. (2.21) is from the stationary points of the classical action,

$$\nabla_{\vec{p}} S(\vec{p}, t, t') = 0, \tag{2.23}$$

so the integral over $\vec{p}$ could be performed using a saddle-point method. Defining the electron return (or excursion) time $\tau = t - t'$, Eq. (2.21) is written as

$$\begin{aligned} D(t) &= i \int_0^\infty d\tau \left[\frac{\pi}{\epsilon + i\tau/2}\right]^{3/2} d_x^*(\vec{p}_{st} - \vec{A}(t)) \exp[-iS(\vec{p}_{st}, t, \tau)] \\ &\times E(t-\tau) d_x(\vec{p}_{st} - \vec{A}(t-\tau)) + c.c., \end{aligned} \tag{2.24}$$

where

$$\vec{p}_{st} = \int_{t-\tau}^t dt'' \vec{A}(t'')/\tau, \tag{2.25}$$

$$S(\vec{p}_{st}, t, \tau) = I_p \tau - \frac{1}{2}\vec{p}_{st}^2 \tau + \frac{1}{2}\int_{t-\tau}^t \vec{A}^2(t'') a t''. \tag{2.26}$$

Here the small positive constant of ϵ comes from the regularized Gaussian integration over $\vec{p}$ around the saddle-point.

It is straightforward to put the depletion of the ground state in Eq. (2.24), it becomes as

$$\begin{aligned} D(t) &= i\int_0^\infty d\tau\left[\frac{\pi}{\epsilon+i\tau/2}\right]^{3/2} d_x^*(\vec{p}_{st}-\vec{A}(t))a^*(t)\exp[-iS(\vec{p}_{st},t,\tau)] \\ &\times E(t-\tau)d_x(\vec{p}_{st}-\vec{A}(t-\tau))a(t-\tau)+c.c.. \end{aligned} \tag{2.27}$$

The ground-state amplitude $a(t)$ can be expressed as [11, 85]

$$a(t)=\exp\left(-\int_0^t\frac{\gamma(t')}{2}dt'\right). \tag{2.28}$$

Here $\gamma(t')$ is the ionization rate.

Eq. (2.27) is the generally used formula of Lewenstein model to calculate the single-atom harmonic radiation induced by an intense laser field. For a single-molecule HHG, we assume that the molecules are aligned along the x axis, while the laser field $E(t)$ is linearly polarized on the x-y plane with an angle θ with respect to the molecular axis. The parallel component of the time-dependent dipole moment can be expressed as

$$\begin{aligned} D_\parallel(t) &= i\int_0^\infty d\tau\left[\frac{\pi}{\epsilon+i\tau/2}\right]^{3/2}[\cos\theta d_x^*(t)+\sin\theta d_y^*(t)]a^*(t) \\ &\times [\cos\theta d_x(t-\tau)+\sin\theta d_y(t-\tau)]a(t-\tau)E(t-\tau) \\ &\times \exp[-iS(\vec{p}_{st},t,\tau)+c.c., \end{aligned} \tag{2.29}$$

where $\vec{d}(t)=\vec{d}\left[\vec{p}_{st}(t,\tau)-\vec{A}(t)\right]$ and $\vec{d}(t-\tau)=\vec{d}\left[\vec{p}_{st}(t,\tau)-\vec{A}(t-\tau)\right]$ are the transition dipole matrix elements. The perpendicular component $D_\perp(t)$ can be given in a similar formula with $[\cos\theta d_x^*(t)+\sin\theta d_y^*(t)]$ replaced by $[\sin\theta d_x^*(t)-\cos\theta d_y^*(t)]$ in Eq. (2.29). In the calculation, the ground-state electronic wave function of a molecule is obtained using the quantum chemistry codes such as GAMESS or GAUSSIAN [93].

Eq. (2.29) is the extended formula of Lewenstein model to calculate the single-molecule HHG induced by an intense laser field. In the SFA, the transition dipole moment $\vec{d}(\vec{p})$ is given by $\langle\vec{p}|\vec{r}|0\rangle$ with the continuum state approximated by a plane wave $|\vec{p}\rangle$. For hydrogenlike atoms, the dipole matrix element for transition from the ground state to a continuum state

is given in the form

$$d(p) = i\frac{2^{7/2}(2I_p)^{5/4}}{\pi}\frac{p}{(p^2+2I_p)^3}. \tag{2.30}$$

For other atoms and molecules, $\vec{d}(\vec{p})$ is calculated numerically with the known wave function of the ground state.

2.2.3 Quantitative rescattering theory

The Lewenstein model is well-known to give good results for the harmonics with high-photon energy, especially for cutoff harmonics, but it fails to predict the harmonics in the lower plateau region since the effect of Coulomb potential is not included. To improve the SFA, the quantitative rescattering (QRS) theory has been developed in Lin's group [94]. QRS theory states that single-atom (or -molecule) HHG can be expressed as a product of a returning electron wave packet and the photorecombination cross section (PRCS) of the laser-free continuum electron back to the initial bound state. Based on the Lewenstein model, each step in the three-step model (see Sec. 1.2.1) can be quantified [see Eq. (2.21)]. The last step, i.e., recombination, is not described precisely due to a plane-wave approximation, but the motion of an electron after tunneling ionization governed mostly by the laser field has been well taken into account in the SFA. One can extract an accurate returning electron wave packet by using SFA. The PRCS as the other integral part in the QRS theory is only determined by the structure of an atomic (or molecular) target, and it can be accurately calculated by solving the stationary Schrödinger equation. Eqs. (2.27) and (2.29) for calculating HHG are expressed in the time domain, while QRS theory deals with the induced dipole moment in the frequency domain. A detailed discussion of QRS theory for HHG is given in Ref. [95]. In the following we describe the QRS theory for atoms and molecules separately.

1. Atomic target

According to the QRS, the induced dipole moment $D(\omega)$ can be written as [96]

$$D(\omega) = W(\omega)d(\omega), \tag{2.31}$$

where $d(\omega)$ is the complex photorecombination (PR) transition dipole matrix element, and $W(\omega)$ is the complex microscopic wave packet. $|W(\omega)|^2$ describes the flux of the returning electrons and is the property of the laser only. The QRS replaces the plane wave used in the SFA by an accurate scattering wave in the calculation of PR transition dipole matrix elements, while the returning microscopic wave packet is the same as that in the SFA. The harmonic frequency ω is related to the electron momentum p by

$$\hbar\omega = \frac{p^2}{2m_e} + I_p. \tag{2.32}$$

In practical applications, the QRS obtains the induced dipole moment by

$$D^{\mathrm{QRS}}(\omega) = D^{\mathrm{SFA}}(\omega)\frac{d^{\mathrm{QRS}}(\omega)}{d^{\mathrm{SFA}}(\omega)}, \tag{2.33}$$

where both $D^{\mathrm{SFA}}(\omega)$ and $d^{\mathrm{QRS}}(\omega)$ are complex numbers, while $d^{\mathrm{SFA}}(\omega)$ is either a pure real or pure imaginary number. Within the SAE approximation, we calculate $d^{\mathrm{QRS}}(\omega)$ using "exact" numerical wave functions for the bound and continuum states. For Ar, we use the model potential given by Müller [97],

$$V(r) = -[1 + Ae^{-r} + (17 - A)e^{-Cr}]/r, \tag{2.34}$$

with A=5.4 and C=3.682. In this model, spin-orbit interaction is neglected. The parameters have been chosen such that the minimum in the photoionization (or photorecombination) cross section is reproduced correctly. Tong and Lin [98] also proposed a model potential for rare atoms,

$$V(r) = -\frac{Z_c + a_1e^{-a_2r} + a_3re^{-a_4r} + a_5e^{-a_6r}}{r}, \tag{2.35}$$

where Z_c is the charge seen by the active electron asymptotically, and $a_1, ..., a_6$ are parameters obtained by fitting $V(r)$ to the numerical potential from self-interaction free density functional theory. Note that in principle the parameters in Eq. (2.33) can be generalized to many-electron wave functions if needed.

2. Molecular target

Within the QRS theory, the induced dipole moment $D(\omega, \theta)$ for a fixed-in-space molecule is given explicitly by

$$D(\omega, \theta) = N(\theta)^{1/2} W(\omega) d(\omega, \theta), \tag{2.36}$$

where $N(\theta)$ is the alignment-dependent ionization probability, $W(\omega)$ is the microscopic wave packet, and $d(\omega, \theta)$ is the alignment-dependent transition dipole (complex in general). Here θ is angle between the molecular axis with respect to the laser's polarization. We limit ourselves to linear molecules here, and consider the parallel component of HHG with respect to the laser polarization only. Thus only the parallel component of the transition dipole $d(\omega, \theta)$ is needed in the calculation. Note that $W(\omega)$ does not depend on the alignment angle θ.

The wave packet $W(\omega)$ can actually be calculated in two ways. First, it can be calculated formally as

$$W(\omega) = \frac{D(\omega, \theta)}{N(\theta)^{1/2} d(\omega, \theta)}. \tag{2.37}$$

Here $D(\omega, \theta)$ for a fixed alignment angle θ can be calculated using Eq. (2.29). And then $N(\theta)$ and $d(\omega, \theta)$ are also calculated in the frame of SFA, where the continuum waves are replaced by plane waves. Since the wave packet $W(\omega)$ is independent of the alignment angle θ, it needs to be calculated only once for a given angle θ. The second approach of obtaining the wave packet is to use a reference atom with a similar ionization potential. For the reference atom, we can perform either TDSE or SFA to calculate the induced dipole

moment $D(\omega)$, and then following Eq. (2.31) the wave packet can be expressed as

$$W(\omega) = \frac{D_{ref}(\omega)}{d_{ref}(\omega)}. \tag{2.38}$$

In the QRS, the single-molecule induced dipole moment is then obtained from Eq. (2.36) by combining the electron wave packet with the accurate $d(\omega, \theta)$ obtained from quantum chemistry code [99, 100] and the tunneling ionization rate $N(\theta)$ obtained from the MO-ADK theory [19].

It has been well documented that QRS results are nearly as accurate as those obtained from TDSE whenever accurate results from the latter can be obtained, i.e., including the atom in the SAE approximation [96] and the H_2^+ molecular ion [101]. Applications of the QRS for HHG from single molecules have been investigated in Refs. [95, 102, 103].

2.3 Maxwell's wave equation

2.3.1 Fundamental laser field

In a dense and ionizing gaseous medium, the propagation of a fundamental driving laser pulse is affected by refraction, nonlinear self-focusing, ionization, and plasma defocusing. The pulse evolution in such a medium is described by a three-dimensional (3-D) Maxwell's wave equation [44, 104, 105]:

$$\nabla^2 E_1(r,z,t) - \frac{1}{c^2}\frac{\partial^2 E_1(r,z,t)}{\partial t^2} = \mu_0 \frac{\partial J_{\text{abs}}(r,z,t)}{\partial t} + \frac{\omega_0^2}{c^2}(1-\eta_{\text{eff}}^2)E_1(r,z,t), \tag{2.39}$$

where $E_1(r,z,t)$ is the transverse electric field of the fundamental laser pulse with angular frequency ω_0. In cylindrical coordinates, $\nabla^2 = \nabla_\perp^2 + \partial^2/\partial z^2$, where z is the axial propagation direction. The effective refractive index η_{eff} of the gas medium can be written as

$$\eta_{\text{eff}}(r,z,t) = \eta_0(r,z,t) + \eta_2 I(r,z,t) - \frac{\omega_{\text{p}}^2(r,z,t)}{2\omega_0^2}. \tag{2.40}$$

The first term $\eta_0 = 1 + \delta_1 - i\beta_1$ takes into account of refraction (δ_1) and absorption (β_1) effects of the neutral atoms, the second term accounts for the optical Kerr nonlinearity,

which depends on laser intensity $I(t)$, and the third term is from free electrons, which contains the plasma frequency $\omega_{\rm p} = [e^2 n_{\rm e}(t)/(\varepsilon_0 m_{\rm e})]^{1/2}$, where $m_{\rm e}$ and e are the mass and charge of an electron, respectively, and $n_{\rm e}(t)$ is the density of free electrons. The absorption term $J_{\rm abs}(t)$ due to the ionization of the medium is expressed as [16, 106]

$$J_{\rm abs}(t) = \frac{\gamma(t) n_{\rm e}(t) I_{\rm p} E_1(t)}{|E_1(t)|^2}, \tag{2.41}$$

where $\gamma(t)$ is the ionization rate, and $I_{\rm p}$ is the ionization potential. This term is usually small under the conditions for high harmonic generation [16, 106].

The absorption effect (β_1) on the fundamental laser field caused by neutral atoms is in general small, so it is neglected. We only keep the real terms in the refractive index $\eta_{\rm eff}$, and Eq. (2.39) can be written as

$$\begin{aligned} \nabla^2 E_1(r,z,t) - \frac{1}{c^2}\frac{\partial^2 E_1(r,z,t)}{\partial t^2} &= \mu_0 \frac{\partial J_{\rm abs}(r,z,t)}{\partial t} \\ &+ \frac{\omega_{\rm p}^2}{c^2} E_1(r,z,t) - 2\frac{\omega_0^2}{c^2}(\delta_1 + \eta_2 I) E_1(r,z,t). \end{aligned} \tag{2.42}$$

By going to a moving coordinate frame ($z' = z$ and $t' = t - z/c$) and neglecting $\partial^2 E_1/\partial z'^2$ since the z' dependence of the electric field is very slow, we obtain [107]

$$\begin{aligned} \nabla_\perp^2 E_1(r,z',t') - \frac{2}{c}\frac{\partial^2 E_1(r,z',t')}{\partial z' \partial t'} &= \mu_0 \frac{\partial J_{\rm abs}(r,z',t')}{\partial t'} \\ &+ \frac{\omega_{\rm p}^2}{c^2} E_1(r,z',t') - 2\frac{\omega_0^2}{c^2}(\delta_1 + \eta_2 I) E_1(r,z',t'). \end{aligned} \tag{2.43}$$

The temporal derivative in Eq. (2.43) can be eliminated by a Fourier transform, yielding the equation

$$\nabla_\perp^2 \tilde{E}_1(r,z',\omega) - \frac{2i\omega}{c}\frac{\partial \tilde{E}_1(r,z',\omega)}{\partial z'} = \tilde{G}(r,z',\omega), \tag{2.44}$$

where

$$\tilde{E}_1(r,z',\omega) = \hat{F}[E_1(r,z',t')], \tag{2.45}$$

and

$$\tilde{G}(r,z',\omega) = \hat{F}\{\mu_0\frac{\partial J_{\rm abs}(r,z',t')}{\partial t'} + \frac{\omega_{\rm p}^2}{c^2}E_1(r,z',t') \\ -2\frac{\omega_0^2}{c^2}[\delta_1+\eta_2 I(r,z',t')]E_1(r,z',t')\}, \tag{2.46}$$

where $\hat{F}$ is the Fourier transform operator acting on the temporal coordinate.

The plasma frequency $\omega_{\rm p}(r,z',t')$ is determined by the free-electron density $n_{\rm e}(t')$, and $n_{\rm e}(t')$ can be calculated as following

$$n_{\rm e}(r,z',t') = n_0\{1-\exp[-\int_0^{t'}\gamma(r,z',\tau)d\tau]\}, \tag{2.47}$$

where n_0 is the neutral atom density, and $\gamma(r,z',\tau)$ is the ionization rate calculated from Ammosov-Delone-Krainov (ADK) theory [18, 19, 98]. The refraction coefficient δ_1, depending on the pressure and temperature of the gas medium, is obtained from the Sellmeier equation [108, 109]. The nonlinear refractive index η_2, also depending on pressure of the gas medium, can be calculated through third-order susceptibility $\chi^{(3)}$, which can be measured from experiments [110, 111]. Note that the relationship between η_2 and $\chi^{(3)}$ in Koga *et al.* [112] differs from that in Boyd [113] since the latter is derived by using time-averaged intensity of the optical field.

At the entrance of a gas jet ($z'=z_{\rm in}$), the fundamental laser field is assumed to be either Gaussian or truncated Bessel in space, and in time it has a Gaussian or cosine square envelop (see Appendix D for details). These will be specified whenever we present the calculated results. The pressure is assumed constant within the gas jet.

2.3.2 High-harmonic field of atoms

The 3-D propagation equation of the harmonic field is described by [16, 107, 114]

$$\nabla^2 E_{\rm h}(r,z,t) - \frac{1}{c^2}\frac{\partial^2 E_{\rm h}(r,z,t)}{\partial t^2} = \mu_0\frac{\partial^2 P(r,z,t)}{\partial t^2}, \tag{2.48}$$

where $P(r,z,t)$ is the polarization depending upon the applied optical field $E_1(r,z,t)$. In this equation, the free-electron dispersion is neglected because the frequencies of high harmonics

are much higher than the plasma frequency. Again going to a moving coordinate frame and neglecting $\partial^2 E_\mathrm{h}/\partial z'^2$, Eq. (2.48) becomes

$$\nabla_\perp^2 E_\mathrm{h}(r,z',t') - \frac{2}{c}\frac{\partial^2 E_\mathrm{h}(r,z',t')}{\partial z'\partial t'} = \mu_0 \frac{\partial^2 P(r,z',t')}{\partial t'^2}. \tag{2.49}$$

We eliminate the temporal derivative by a Fourier transform, obtaining the equation

$$\nabla_\perp^2 \tilde{E}_\mathrm{h}(r,z',\omega) - \frac{2i\omega}{c}\frac{\partial \tilde{E}_\mathrm{h}(r,z',\omega)}{\partial z'} = -\omega^2\mu_0 \tilde{P}(r,z',\omega), \tag{2.50}$$

where

$$\tilde{E}_\mathrm{h}(r,z',\omega) = \hat{F}[E_\mathrm{h}(r,z',t')], \tag{2.51}$$

and

$$\tilde{P}(r,z',\omega) = \hat{F}[P(r,z',t')]. \tag{2.52}$$

The source term on the right-hand side of Eq. (2.50) describes the response of the medium to the laser field and includes both linear and nonlinear terms. It is convenient to separate the polarization into linear and nonlinear components as: $\tilde{P}(r,z',\omega) = \chi^{(1)}(\omega)\tilde{E}_\mathrm{h}(r,z',\omega) + \tilde{P}_\mathrm{nl}(r,z',\omega)$, where the linear susceptibility $\chi^{(1)}(\omega)$ includes both linear dispersion and absorption through its real and imaginary parts, respectively. The nonlinear polarization term $\tilde{P}_\mathrm{nl}(r,z',\omega)$ can be expressed as

$$\tilde{P}_\mathrm{nl}(r,z',\omega) = \hat{F}\{[n_0 - n_\mathrm{e}(r,z',t')]D(r,z',t')\}, \tag{2.53}$$

where $n_\mathrm{e}(r,z',t')$ is calculated from Eq. (2.59), and $D(r,z',t')$ is the single-atom induced dipole moment caused by the fundamental driving laser field.

The refractive index $n(\omega) = \sqrt{1+\chi^{(1)}(\omega)/\varepsilon_0}$ [113] (which is valid only off resonance or for small absorption) is related to atomic scattering factors by

$$n(\omega) = 1 - \delta_\mathrm{h}(\omega) - i\beta_\mathrm{h}(\omega) = 1 - \frac{1}{2\pi} n_0 r_0 \lambda^2 (f_1 + i f_2), \tag{2.54}$$

where r_0 is the classical electron radius, λ is the wavelength of harmonic, n_0 is again the neutral atom density, and f_1 and f_2 are atomic scattering factors which can be obtained

from Refs. [115, 116]. Note that $\delta_{\rm h}(\omega)$ and $\beta_{\rm h}(\omega)$ account for the dispersion and absorption of the medium on the harmonics, respectively. Finally Eq. (2.50) can be written as

$$\nabla_{\perp}^2 \tilde{E}_{\rm h}(r,z',\omega) - \frac{2i\omega}{c}\frac{\partial \tilde{E}_{\rm h}(r,z',\omega)}{\partial z'} - \frac{2\omega^2}{c^2}(\delta_{\rm h}+i\beta_{\rm h})\tilde{E}_{\rm h}(r,z',\omega) = -\omega^2\mu_0\tilde{P}_{\rm nl}(r,z',\omega), \tag{2.55}$$

where the nonlinear polarization as the source of the harmonic field is explicitly given. After the propagation in the medium, we obtain the near-field harmonics at the exit face of the gas jet ($z' = z_{\rm out}$).

2.3.3 High-harmonic field of aligned molecules

In general both the fundamental laser field and the harmonic field are modified when they copropagate through a macroscopic medium. If both the pressure and laser intensity are low, the effects of dispersion, Kerr nonlinearity, and plasma defocusing on the fundamental laser field can be neglected. In other words, the source term in Eq. (2.39) can be taken as zero, the fundamental field is not modified through the medium. Under these conditions the profile of the fundamental laser field in space (in the vacuum) can be expressed in an analytical form. If it can be considered as a Gaussian beam, its spatial and temporal dependence is given approximately in Appendix D.3. For the harmonic field, the dispersion and absorption effects from the medium, which are explicitly expressed as a dispersion-absorption term in Eq. (2.55) are not included when the pressure is low. These effects would become important if the gas pressure is high. For molecular targets, we will limit ourselves to experiments carried out under the conditions of low laser intensity and low gas pressure, and only include the induced dipoles for the generated harmonic field.

The 3-D Maxwell's wave equation for the harmonics in a molecular gas medium is

$$\nabla^2 E_{\rm h}^{\parallel}(r,z,t,\alpha) - \frac{1}{c}\frac{\partial^2 E_{\rm h}^{\parallel}(r,z,t,\alpha)}{\partial^2 t} = \mu_0 \frac{\partial^2 P_{\rm nl}^{\parallel}(r,z,t,\alpha)}{\partial^2 t}. \tag{2.56}$$

Here $E_{\rm h}^{\parallel}(r,z,t,\alpha)$ and $P_{\rm nl}^{\parallel}(r,z,t,\alpha)$ are the parallel components (with respect to the polarization direction of the generating laser) of the electric field of the harmonic and the nonlinear

polarization caused by the fundamental laser, respectively. α is the pump-probe angle, i.e., the angle between the aligning (pump) and the generating (probe) laser polarizations.

The nonlinear polarization term can be expressed as

$$P_{\mathrm{nl}}^{\parallel}(r,z,t,\alpha) = [n_0 - n_{\mathrm{e}}(r,z,t,\alpha)]D^{\parallel,\mathrm{tot}}(r,z,t,\alpha), \tag{2.57}$$

where $n_0 - n_{\mathrm{e}}(r,z,t,\alpha)$ gives the density of the remaining neutral molecules, and $D^{\parallel,\mathrm{tot}}(t,\alpha)$ is the parallel component of the induced single-molecule dipole over a number of active electrons (including the effects from outermost and the inner molecular orbitals). And $n_{\mathrm{e}}(t,\alpha)$ is the free-electron density, which can be calculated as follows

$$n_{\mathrm{e}}(t,\alpha) = \int_0^{\pi} n_{\mathrm{e}}(t,\theta')\rho(\theta',\alpha)\sin\theta' d\theta'. \tag{2.58}$$

Here $n_{\mathrm{e}}(t,\theta')$ is the alignment-dependent free-electron density, obtained from

$$n_{\mathrm{e}}(t,\theta) = n_0\{1 - \exp[-\int_{-\infty}^{t} \gamma(\tau,\theta)d\tau]\}, \tag{2.59}$$

where $\gamma(\tau,\theta)$ is the alignment-dependent ionization rate, which can be calculated by MO-ADK theory [19] for different molecular orbitals. In Eq. (2.58), θ' is the alignment angle with respect to the polarization direction of the probe laser, and $\rho(\theta',\alpha)$ is the alignment distribution with pump-probe angle α [95, 117] (see Appendix B).

By going to a moving coordinate frame again, Eq. (2.56) can be written in the frequency domain as

$$\nabla_{\perp}^2 \tilde{E}_{\mathrm{h}}^{\parallel}(r,z',\omega,\alpha) - \frac{2i\omega}{c}\frac{\partial \tilde{E}_{\mathrm{h}}^{\parallel}(r,z',\omega,\alpha)}{\partial z'} = -\omega^2\mu_0\tilde{P}_{\mathrm{nl}}^{\parallel}(r,z',\omega,\alpha), \tag{2.60}$$

where

$$\tilde{E}_{\mathrm{h}}^{\parallel}(r,z',\omega,\alpha) = \hat{F}[E_{\mathrm{h}}^{\parallel}(r,z',t',\alpha)], \tag{2.61}$$

and

$$\tilde{P}_{\mathrm{nl}}^{\parallel}(r,z',\omega,\alpha) = \hat{F}[P_{\mathrm{nl}}^{\parallel}(r,z',t',\alpha)]. \tag{2.62}$$

After the propagation in the medium, we obtain the parallel component of near-field harmonics on the exit face of the gas jet ($z' = z_{\rm out}$). For isotropically distributed molecules and partially aligned molecules with $\alpha = 0°$ or $90°$, by symmetry there are only parallel harmonic components. The perpendicular components, which are usually much smaller, would appear for partially aligned molecules and the harmonics will be elliptically polarized in general [118]. Generalization of Eq. (2.60) to the perpendicular component is straightforward, but we restrict ourselves to the parallel component in this thesis only.

Note that Eqs. (2.44), (2.55), and (2.60) are solved using a Crank-Nicholson routine for each value of ω. Typical parameters used in the calculations are $200 \sim 400$ grid points along the radial direction r and 400 grid points along the longitudinal direction z for a 1-mm wide gas jet.

In the calculation, the induced dipole moments included in nonlinear polarizations of Eqs. (2.53) and (2.57) are mostly obtained by QRS theory in this thesis. For an atomic target, we can use Eq. (2.33) to calculate the single-atom induced dipole in frequency domain, and then transfer it back to time domain by the Fourier transform. For a linear molecular target, it can only be partially aligned if it is placed in a short laser field (pump laser). The intensity of the aligning laser is usually weak and not tightly focused such that it can be assumed to be constant within the gas medium. In other words, the degree of molecular alignment is not varied in the medium at one fixed pump-probe time delay. The averaged induced dipole from the partially aligned molecules at each point in the gas medium is then obtained by coherently averaging induced dipole moment of a fixed-in-space molecule in Eq. (2.36) over the molecular angular distribution, i.e.,

$$D^{\parallel,\rm avg}(\omega,\alpha) = \int_0^\pi D^{\parallel}(\omega,\theta')\rho(\theta',\alpha)\sin\theta' d\theta', \tag{2.63}$$

where $\rho(\theta',\alpha)$ is the angular (or alignment) distribution of the molecules again. Eq. (2.63) is only for one particular molecular orbital. The total laser induced dipole over a number

of active electrons can be written as [119, 120]

$$D^{\parallel,\mathrm{tot}}(\omega,\alpha)=\sum_{j,n}D_{j,n}^{\parallel,\mathrm{avg}}(\omega,\alpha), \tag{2.64}$$

where index j refers to the different molecular orbital, and n is an index to account for degeneracy in each molecular orbital. In the end Eq. (2.64) is transferred into time domain, and put back into Eq. (2.57).

2.4 Far-field harmonic emission

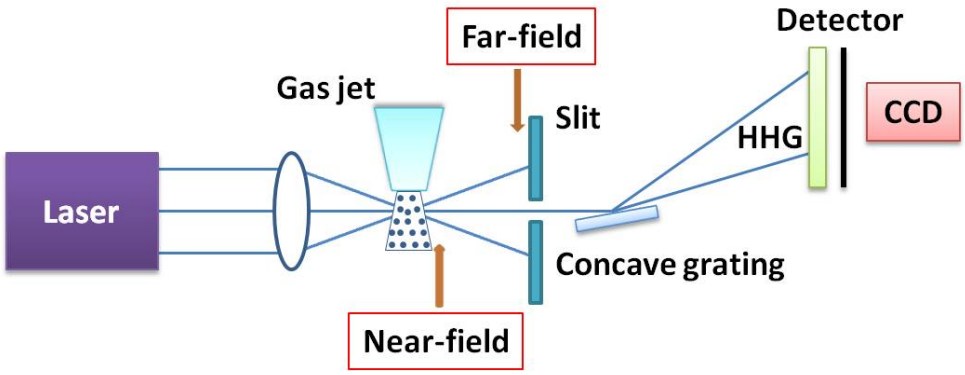

Figure 2.1: *Typical configuration for measuring HHG in the far field. Adapted from Publication [8].*

Once the harmonics are emitted at the exit plane of an atomic or molecular (probably aligned) gas medium (called near-field harmonics), as shown in Fig. 2.1, they will propagate further in the vacuum until they are detected by the spectrometer. In this process, harmonics may go through a slit, an iris or a pinhole, or be reflected by a mirror or more complicated optical system before they reach the detector (called far-field harmonics). In an axial-symmetric optical system, the complex electric field on the initial plane (near field) is related to the final plane (far field) by an $ABCD$ ray matrix, and AD-BC=1 for a lossless system. Here we only consider the simplest configuration shown in Fig. 2.1 without any additional optics (or within free space propagation) between near field and far field, and A=1, B=1, C=0 and D=1 in the $ABCD$ matrix. For constructing the more complicated

$ABCD$ matrix, see Appendix D.2. According to the diffraction theory in the paraxial approximation, the far-field harmonics can be obtained by using near-field harmonics through a Hankel transformation [121–123]

$$E_{\mathrm{h}}^{\mathrm{f}}(r_{\mathrm{f}}, z_{\mathrm{f}}, \omega) = -ik \int \frac{\tilde{E}_{\mathrm{h}}(r, z', \omega)}{z_{\mathrm{f}} - z'} J_0(\frac{krr_{\mathrm{f}}}{z_{\mathrm{f}} - z'}) \exp[\frac{ik(r^2 + r_{\mathrm{f}}^2)}{2(z_{\mathrm{f}} - z')}] r dr, \tag{2.65}$$

where J_0 is the zero-order Bessel function, z_{f} is the far-field position from the laser focus, r_{f} is the transverse coordinate in the far field, and the wave vector k is given by $k = \omega/c$. Note the elements of an $ABCD$ matrix are not expressed explicitly in Eq. (2.65), but the explicit expression can be found in Appendix D.2. For a case of molecules, $\tilde{E}_{\mathrm{h}}(r, z', \omega)$ is replaced by the electric field in Eq. (2.60), which also depends on pump-probe angle α, and is parallel or perpendicular to the polarization of harmonic generating laser.

Suppose the harmonics in the far field are collected from an extended area. By integrating harmonic yield over this area, the power spectrum of the macroscopic harmonics is obtained:

$$S_{\mathrm{h}}(\omega) \propto \int \int |E_{\mathrm{h}}^{\mathrm{f}}(x_{\mathrm{f}}, y_{\mathrm{f}}, z_{\mathrm{f}}, \omega)|^2 dx_{\mathrm{f}} dy_{\mathrm{f}}, \tag{2.66}$$

where x_{f} and y_{f} are the Cartesian coordinates on the plane perpendicular to the propagation direction, and $r_{\mathrm{f}} = \sqrt{x_{\mathrm{f}}^2 + y_{\mathrm{f}}^2}$.

Note in Eq (2.66), the detailed information on the experimental setup is involved. To simulate experimental HHG spectra quantitatively, besides the general used laser parameters, such as intensity, duration, wavelength, spot size, and so on, we need more parameters about the experiment (for example, the size and location of a slit).

Chapter 3

Medium propagation effects in high-order harmonic generation of Ar

Most of figures and paragraphs in this chapter are adapted from Publication [8], [11] and [17].

3.1 Introduction

High-order harmonic generation (HHG) is an extreme nonlinear optical process in which an intense ultrafast infrared laser light is efficiently converted to an ultrafast coherent extreme ultraviolet (XUV) or soft X-ray light. As discussed in Chapter 1, HHG has been widely studied for its potential as a short-wavelength light source [6], or the production of ultrashort light pulses [46]. It has also been shown to extract information of the atomic structure [21] or to image molecular structure with sub-Angstrom precision in space and sub-femtosecond precision in time [65, 66, 124, 125]. HHG process in single-atom response level can be intuitively understood in terms of the semiclassical "three-step" model [8, 9]. However, the laser field interacts with a macroscopic medium, and the harmonics from all atoms are generated coherently, a full description of the experimentally observed HHG spectra requires the treatment of the nonlinear propagation of the fundamental laser beam together with the harmonics in the medium. As discussed in Chapter 2, the most accurate way to obtain the microscopic laser induced dipole of an atom is to solve the time-dependent Schrödinger

equation (TDSE) numerically. Since this approach is quite time consuming and the calculations have to be carried out for hundreds of laser peak intensities in order to describe the nonuniform laser distribution inside a focused laser beam, this is rarely done in existing studies including macroscopic propagation effect of HHG [45]. Instead, the much simpler strong-field approximation (SFA) [10] is often used to calculate the single-atom induced dipole. Despite of this limitation, the temporal and spatial properties of HHG observed experimentally have been reasonably understood from such SFA-based calculations. On the other hand, in a few examples, macroscopic HHG spectra obtained using TSDE-calculated induced dipoles do show significant quantitative discrepancies compared to SFA-based calculations [16, 41], and such studies have been limited to a few atomic gases only.

In this chapter, we demonstrate an accurate and efficient method for calculating the HHG spectrum from an atomic gaseous medium. This method is based on the recently developed quantitative rescattering (QRS) theory [26, 94, 95], which allows us to calculate laser induced dipole of an atom with accuracy comparable to that obtained from solving TDSE, yet with computing time comparable to that by using the SFA. The validity of the QRS, at the single-atom level has been carefully calibrated against TDSE results for one-electron model atoms [96]. Clearly such comparison is incomplete without considering the macroscopic propagation effects. In this chapter, we first consider the situations where the laser intensity and the gas pressure are small such that the fundamental laser field is almost not modified during the propagation (or it can be assumed propagating in the vacuum). This simplification allows us to calculate the macroscopic HHG spectra with TDSE-based single-atom induced dipoles, which can be used to calibrate the spectra with QRS-based induced dipoles. We then extend the theoretical model to the more realistic situations of higher laser intensities and gas pressures, at which the nonlinear propagation of the fundamental field needs to be taken into account. We examine the simulated HHG spectra of Ar and compare them directly with experimental data. Based on the QRS theory, we show that the macroscopic HHG can be expressed as a product of a "macroscopic wave packet" (MWP)

and the photorecombination (PR) cross section of the target. The MWP reflects the effect of the laser and the consequence of propagation in the medium.

In Sec. 3.2, with the single-atom response from TDSE or QRS, we calculate the macroscopic HHG spectra of Ar when a gas jet is put at the generally good phase-matching position. We also show the phase of the calculated macroscopic harmonics with changing gas-jet position. In Sec. 3.3, we simulate HHG spectra of Ar with a 1200- or 1360-nm laser by taking into account the detailed experimental information, the experimental spectra from 30-90 eV can be accurately reproduced theoretically based on the QRS theory. In Sec. 3.4, we show how the width and depth of the well-known Cooper minimum in the HHG spectrum of Ar changes with gas-jet position. In Sec. 3.5, we first show that the macroscopic HHG spectrum can be decomposed as a PR transition dipole (or a PR cross section) and a MWP. We also verify that MWP is a property of laser independent of the target by comparing the wave packets from different targets under the same laser. The harmonics are quite different by varying the experimental conditions, and we find that all the differences can be attributed to the different MWP's. Thus we show the dependence of MWP on the gas-jet position with respect to the laser focus, the degree of phase matching with the change of the gas pressure for individual harmonics. Since phase-matching condition is also dependent on the wavelength of the laser used, we investigate how the macroscopic HHG scales with the laser wavelength in Sec. 3.6. In Sec. 3.7, we give a summary of this chapter.

3.2 Macroscopic HHG spectra: QRS vs TDSE

In the numerical simulation, we take the fundamental laser pulse in space to be a Gaussian beam with cylindrical symmetry, propagating along the z direction. The beam waist at the laser focus is fixed as w_0=25 μm, and a 1-mm long gas jet with constant atom density is placed after or at the laser focus. In the time domain the laser pulse is assumed to have a cosine-squared envelope, and the carrier-envelope phase is taken to be $\varphi_{\mathrm{CE}} = 0$ radian. (see Appendix D.3 for details.)

In the SFA calculation, the ground-state wave function of Ar is obtained numerically by using the quantum chemistry software GAUSSIAN [93]. And for the QRS calculation, we use the model potential in Eq. (2.35), which gives a Cooper minimum occurring near 42 eV instead of 50 eV from the Muller potential [97].

3.2.1 Strength of the harmonics

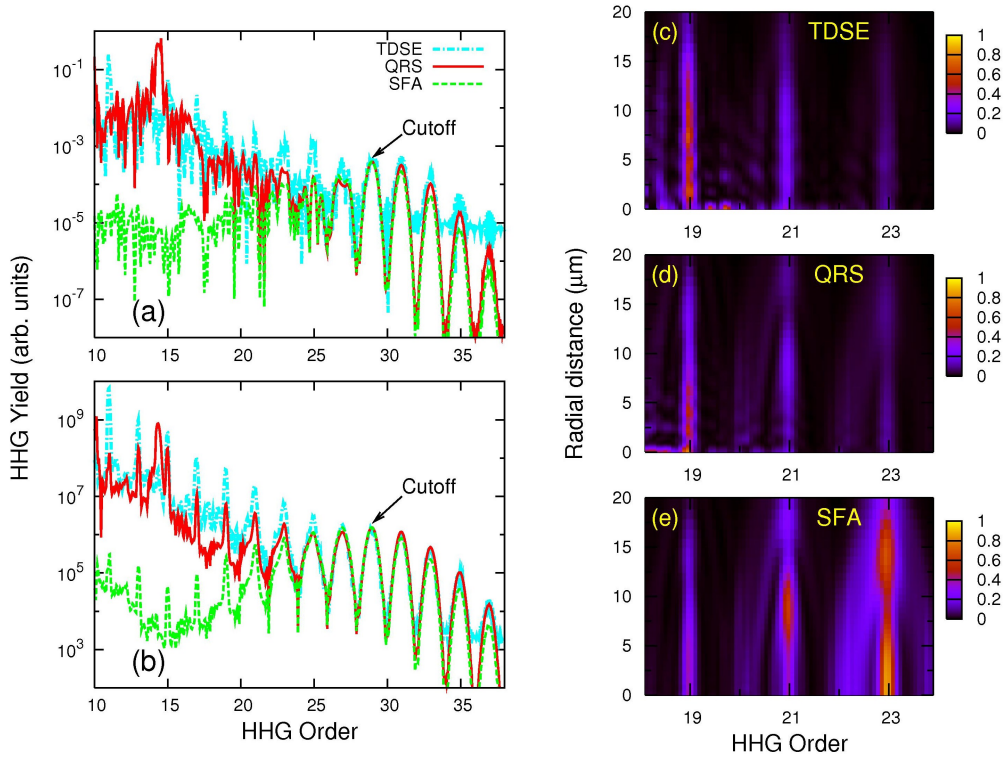

Figure 3.1: *(a) Single-atom and (b) macroscopic harmonic spectra of Ar from the TDSE, QRS and SFA. Spatial distribution of macroscopic harmonic emission at the exit face of gas jet from the (c) TDSE, (d) QRS and (e) SFA. Adapted from Publication [17].*

With the amplitude and phase of single-atom HHG calculated from the TDSE, SFA, and QRS as the source terms for the macroscopic propagation equation of the harmonic field, we calculate and compare the macroscopic HHG spectra from these three different models.

In Fig. 3.1(a), single-atom HHG spectra of Ar exposed to a 19.4 fs (full width at half maximum, FWHM) laser pulse with peak intensity of 1.5×10^{14} W/cm^2 and central wave-

length of 800 nm are shown. The spectra from QRS and SFA are normalized to that from the TDSE near the cutoff. We can see that HHG spectra in the plateau region are very noisy, with no clear peaks at odd harmonics except in the cutoff region. It also shows that SFA agrees with TDSE only for harmonics close to the cutoff, while in the plateau region there are large discrepancies. For the QRS, on the other hand, it is in a good agreement with the TDSE except for a sharp spike near harmonic 14 (or H14). The abnormal spike near H14 can be easily traced to zero of the PR cross section of Ar in the plane wave approximation.

In Fig. 3.1(b), we show the macroscopic HHG spectra of Ar when gas jet is placed 2 mm after the focus and laser peak intensity at the center of the gas jet is 1.5×10^{14} W/cm^2. The pulse duration and wavelength are the same as those in Fig. 3.1(a). The HHG signal after propagation is collected at the exit of the gas jet (near field). The macroscopic HHG spectra from QRS and SFA are again normalized to that from TDSE in the cutoff region. Several general features of the spectra are presented: sharp drop of the spectra beyond the cutoff; well-resolved odd harmonics are observed across the whole plateau; spectral widths are smaller in the plateau and increase with the harmonic order; the cutoff location of the spectrum is about the same as that in single-atom response. In comparison with single-atom HHG spectrum, the propagation greatly cleans up the spectrum between odd harmonics. The relative intensity of odd harmonics do not change too much even after propagation. If we only look at the cutoff region, the SFA gives the correct prediction with the TDSE. Obviously, it fails for the lower plateau spectrum. The QRS model, after the propagation, gives a much better agreement with the one obtained from the TDSE over the whole spectral region. This result shows that the QRS is capable of improving the SFA quite significantly, but with computational effort close to the SFA. Again the spike in the propagated spectra near H14 is caused by the same reason as in the single-atom case.

In Fig. 3.1(b), only the total HHG signal at the exit face of gas jet has been displayed. An interesting question is how the QRS model improves over the SFA in comparison with the TDSE for the harmonic field intensity in different region of the exit face (which has

cylindrical symmetry). In Figs. 3.1(c)-(e), the strength $|\widetilde{E}_h(r, z', \omega)|^2$ versus the radial distance for H19 to H23 are shown based on the three models. Again, the TDSE and the QRS show the good overall agreement. This comparison also offers a good reason for adopting QRS-based single-atom response for the macroscopic propagation of HHG.

3.2.2 Phase of the harmonics

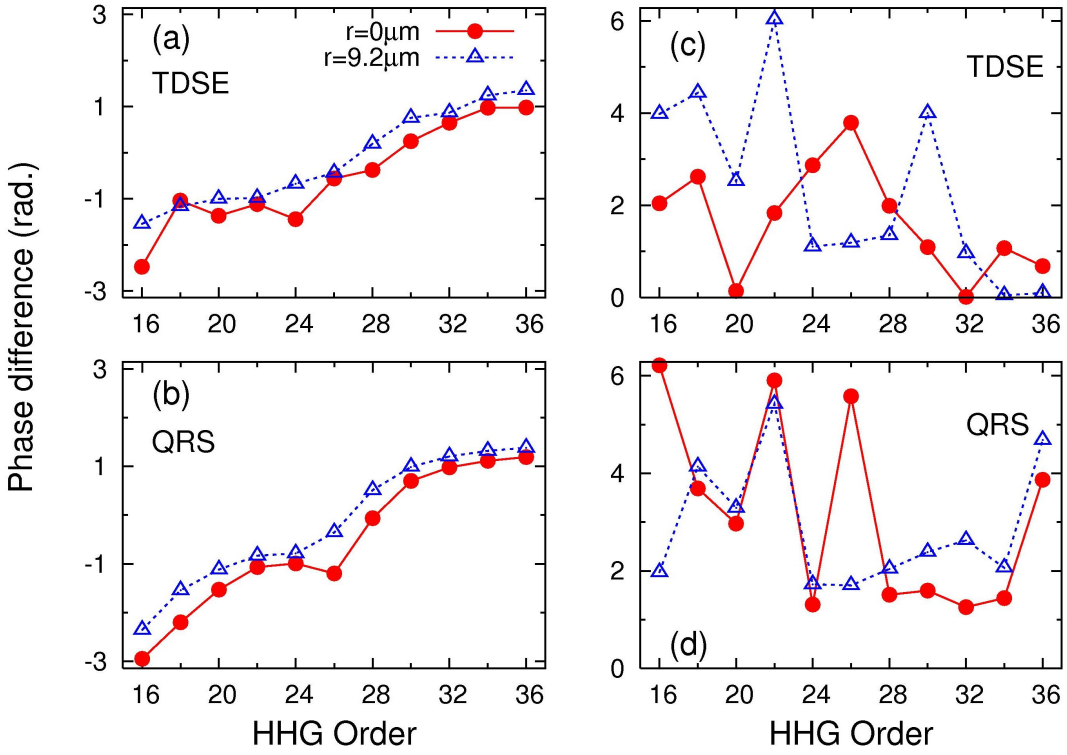

Figure 3.2: *Phase difference of macroscopic harmonics from the TDSE and the QRS, which is calculated for r=0 μm or r=9.2 μm at the exit of gas jet. [(a) and (b)] Gas jet is put 2 mm after the focus. [(c) and (d)] Gas jet is put at the focus. Laser intensity in the center of gas jet is always kept as 1.5×10^{14} W/cm^2; laser duration and wavelength are the same as in Fig. 3.1. Adapted from Publication [17].*

The phase of HHG is crucial for attosecond pulse generation. According to Eq. (2.31), the phase of harmonics gets contribution from the returning wave packet as well as from the complex PR transition dipole moment. How is the harmonic phase affected by the macroscopic propagation? This question also demands a proper way to present the phase of

harmonics. According to the semiclassical theory, the phase difference between successive odd harmonics reveals the harmonic emission time [35]. Since the phase difference between consecutive odd harmonics can be measured using the RABITT technique [47] experimentally, we choose to study the phase difference as defined by

$$\Delta\phi_{2n} = \phi_{2n+1} - \phi_{2n-1}. \tag{3.1}$$

In Figs. 3.2(a) and (b), we show the phase difference of macroscopic HHG for Ar from TDSE and QRS, where the spectral strength has been shown in Fig. 3.1(b). Define the phase difference in the interval [-π, π], we show the successive phase difference at two different positions r=0 μm and r=9.2 μm at the exit face of gas jet. Since harmonic fields emitted at different radial positions finally are added up incoherently when a few odd harmonics are combined to generate attosecond pulses [11, 126], it is meaningful to observe phase behavior of harmonics in different positions separately. From Fig. 3.2(a) the phase difference increases almost linearly with the harmonic order (linear chirp [35]) with the same slope for both r=0 μm and r=9.2 μm due to phase-matching, but the curve for r=9.2 μm is shifted up in comparison with r=0 μm. In these two cases the absolute phase increases quadratically with the harmonic order. In Fig. 3.2(b), the QRS gives the same phase behavior as the TDSE in Fig. 3.2(a). Again, this shows the validity of the QRS in studying the macroscopic response.

In order to understand the mechanism of HHG phase behavior after the propagation, we move the gas jet into the laser focus, fix the laser peak intensity at its center to be 1.5×10^{14} W/cm^2, and keep other laser parameters the same as in Figs. 3.2(a) and (b). Phase difference of macroscopic HHG for Ar from TDSE and QRS are shown in Figs. 3.2(c) and (d). Whether r=0 μm or r=9.2 μm, both the TDSE and the QRS give random-like phase differences, and are similar to single-atom HHG. Note that our observation of this phase behavior agrees with Gaarde *et al.*'s TDSE calculation [126] (see their Fig. 3).

3.3 Macroscopic HHG spectra: theory vs experiment

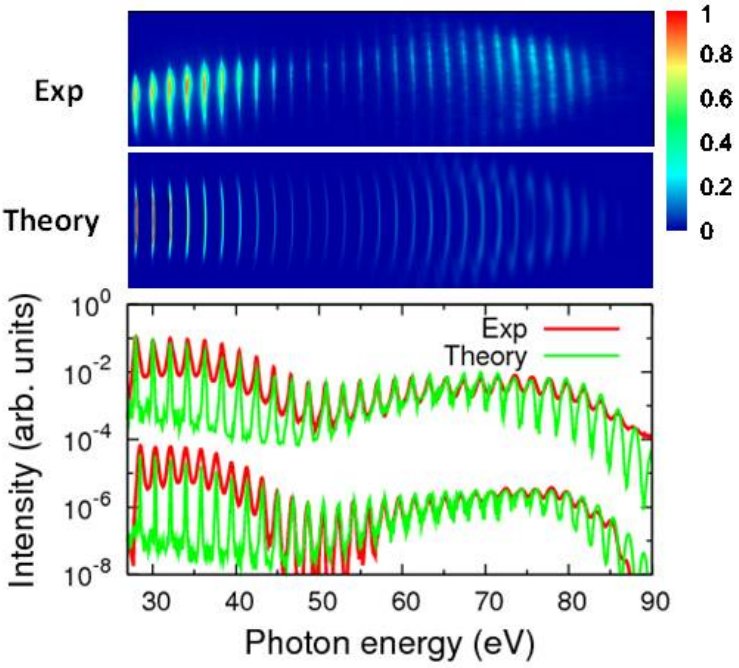

Figure 3.3: *HHG spectra of Ar generated by a 1200-nm laser. Upper frame: Spatial distribution of harmonic emission vs photon energy in the far field. Lower frame: Comparison of theoretical (green lines) and experimental (red lines) HHG yield integrated over the vertical dimension for 1200-nm (upper curves) and 1360-nm (lower curves) lasers. Other laser parameters are given in the text. Adapted from Publication [8].*

To compare with the experimental HHG measurements, we carry out the propagation for both fundamental and harmonic fields in the medium, and take into account the further propagation of the harmonics in the vacuum, i.e., the information of the detecting system. The spatial beam mode of the fundamental field at the entrance of the gas medium is assumed as Gaussian one. In the QRS calculation, we use the Muller potential in Eq. (2.34) to obtain the PR cross section of Ar, and the returning electron wave packet is obtained from SFA, where Ar is assumed as a hydrogenlike atom in Eq. (2.30).

Fig. 3.3 shows the measured and simulated HHG spectra of Ar. Experimentally, a 0.5-mm-long gas jet was placed few mm's after the laser focus. A vertical slit with a width of 100 μm was placed 24 cm after the gas jet. For a 1200- (1360-) nm laser used in the experiment,

the beam waist at the focus is 47.5 (52.5) μm, and the pulse duration is $\sim$ 40 ($\sim$ 50) fs. The laser intensity and gas pressure in the simulations are adjusted until the best overall fit is achieved with the experimental data. For the 1200-nm laser, the peak intensity for experiment (theory) is 1.6 (1.5)$\times 10^{14}$ W/cm^2, and the gas pressure is 28 (84) Torr. For the 1360-nm laser, the corresponding intensity and pressure are 1.25 (1.15)$\times 10^{14}$ W/cm^2, and 28 (56) Torr, respectively. In the upper frame of Fig. 3.3, the horizontal axis is the photon energy, and the vertical axis is the transverse spatial dimension. The experimental and theoretical spectra, generated by the 1200-nm laser, are normalized at harmonic 75 (H75), or at photon energy of 77 eV. We can see the general agreement between the two spectra except for the "up-down" asymmetry in the experimental spectra, which is due to asymmetry in the laser beam profile. The "famous" Cooper minimum is clearly seen in both experimental and theoretical spectra. The harmonic yields integrated over the vertical dimension are compared in the lower frame in Fig. 3.3. The HHG spectra with a 1360-nm laser is also shown. In both cases, we can see a good agreement (in envelope of HHG spectrum) between theory and experiment over the 30-90 eV region covered. A careful examination of Fig. 3.3 reveals that there are still small discrepancies between the experimental data and the simulations by QRS despite various attempts using somewhat different laser parameters. The harmonic width (or harmonic chirp) in the simulation is narrower than that in the experimental measurement. The harmonic width is mainly determined by laser intensity, pulse duration, and gas pressure. In the experiments, parameters such as pressure of the gas jet and laser intensity and its spatial distribution cannot be measured precisely. Other factors, such as the use of the slit and the position of the detector, can also influence the HHG spectra. All of these uncertainties can contribute to the discrepancy between the simulation and the measured HHG spectrum.

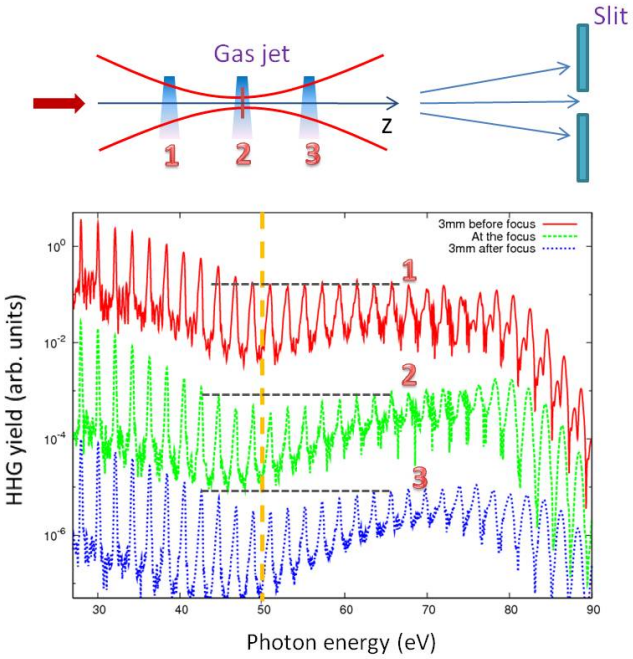

Figure 3.4: *Variation of width and depth of the Cooper minimum in HHG spectrum of Ar using a 1200-nm laser. Upper frame: the sketch of experimental setup where the gas jet is put at different positions with respect to the laser focus. Lower frame: calculated HHG spectra of Ar at three different gas-jet positions. Yellow dashed line indicates the position of Cooper minimum using the Muller potential [97]. Laser intensity in the gas jet is* 1.6×10^{14} *W/cm*^{2}*, gas pressure is 56 Torr. Other parameters are the same as those in Fig. 3.3.*

3.4 Disappearance of Cooper minimum in the HHG spectra of Ar

The Cooper minimum (CM) in the HHG spectra of Ar has been studied intensively by using the traditional 800-nm lasers [127–129], or longer-wavelength lasers [130, 131]. This minimum always occurs in the single-atom HHG spectrum of Ar based on the QRS theory, however, it is not necessary to appear in the macroscopic spectrum. The position of the CM can change or even disappear under different experimental conditions. Experiments have shown that the CM may disappear in the HHG spectrum by changing the gas pressure [128] or by changing the gas-jet position with respect to the laser focus [129].

To make this point clear, we also carry out calculations for different experimental con-

ditions as shown in the upper frame of Fig. 3.4. In the lower frame of Fig. 3.4, we show the calculated HHG spectra of Ar in the far field with changing the gas-jet position. In case 3, the CM is wide and deep in the spectra. With moving the gas jet close to the laser focus, the CM becomes shallow in case 2, and the harmonics around 70 eV do not show the clean peak structures indicating that the phase matching conditions become poor. If we place the gas jet before the laser focus as shown in case 1, the phase matching conditions are greatly changed since the geometric phase of fundamental laser changes its sign. The CM disappears in the spectrum, and some of the high-energy harmonics show the noisy structures. This example once again tells us that the CM in the macroscopic HHG spectra can be washed out easily by changing the macroscopic experimental conditions. The change of the experimental conditions can also be reflected by the "macroscopic wave packet", which will be discussed in Sec. 3.5.

3.5 Macroscopic wave packet

Based on the QRS theory, the macroscopic HHG spectrum in the near field or in the far field for atomic targets can be expressed as

$$S_{\mathrm{h}}(\omega) \propto \omega^4 |W'(\omega)|^2 |d(\omega)|^2, \tag{3.2}$$

where $W'(\omega)$ (the complex amplitude) is called a "macroscopic wave packet" (MWP), and $d(\omega)$ is the PR transition dipole moment. The MWP can be considered as the collective effect of the microscopic wave packet for the returning electrons, which is mostly governed by the fundamental laser field. And the MWP can be calculated by solving Maxwell's propagation equation. In other words, the laser, gas medium, and experimental setup effects are all incorporated into MWP. While the structure information of the target is included in PR transition dipole. In this chapter, only the amplitude of MWP is considered.

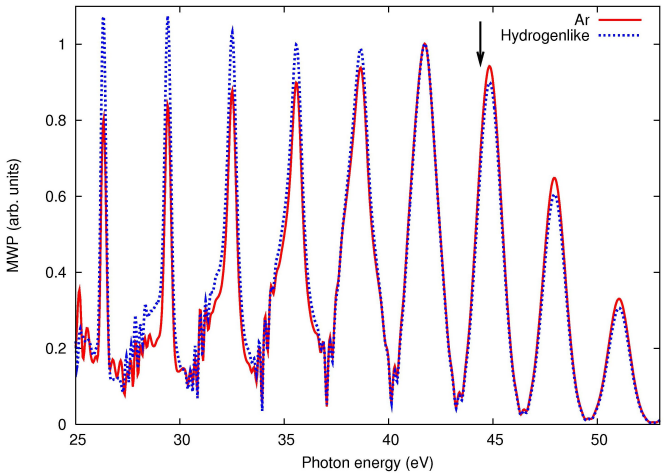

Figure 3.5: *Macroscopic wave packets extracted from macroscopic HHG spectra based on the QRS using Ar and hydrogenlike atom. Gas jet is at 2 mm after the laser focus. Laser intensity is* 1.5×10^{14} W/cm^2. *The arrow indicates the cutoff position determined by the classical model. Adapted from Publication [17].*

3.5.1 Independence of wave packet on targets

To extract the PR transition dipole (or PR cross section) from the macroscopic HHG spectrum, we need to rely on the MWP in Eq. (3.2). The question is how to obtain the MWP, which is only a property of laser and experimental setup. We answer this question in a different way. Taking Ar target as an example, we can use the QRS to generate single-atom induced dipole moment and then carry out the propagation to obtain the macroscopic HHG. Recall that in this case the single-atom returning wave packet is calculated from SFA using the ground state wave function of Ar, and the MWP is extracted by using Eq. (3.2). In Fig. 3.5, we show the resulting MWP $|W'(\omega)|$ of Ar (solid line) from HHG spectra in Fig. 3.1(b). Using laser parameters and focusing condition the same as those in Fig. 3.1(b), we also show another MWP calculated from a hydrogenlike atom in Fig. 3.5, where the effective nuclear charge has been adjusted such that its $1s$ binding energy is the same as the $3p$ ground state energy of Ar. By normalizing the two MWPs at the cutoff energy (marked by an arrow and estimated from the laser peak intensity at the center of gas jet) we see that they agree relatively well. These results indeed show that MWPs from different targets with

the same I_p agree with each other reasonably well under the same laser condition. (More examples can be found in Publication [17].) These results have important implications. Since atomic PR transition dipole is generally well known, by taking the HHG spectra of an atomic target and a molecular one with nearly identical binding energy in the same laser field, one can extract the transition dipole of the molecule from the ratio of the HHG yields of the two targets and the known PR transition dipole of the atomic target. This model has been assumed in Itatani *et al.* [66] and in Levesque *et al.* [132]. Our results confirm the validity of their assumptions.

3.5.2 Separation of target structure information from HHG spectra

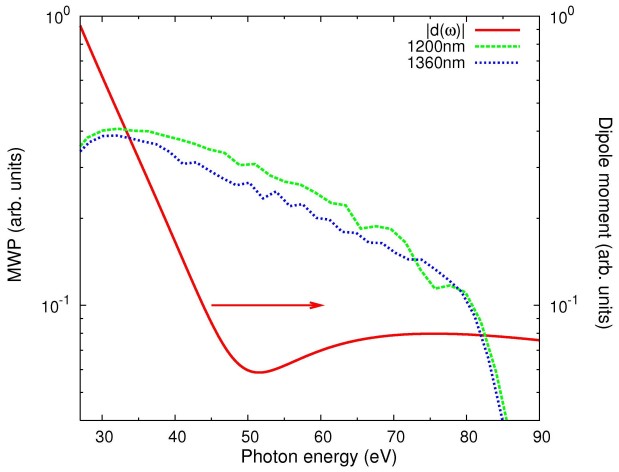

Figure 3.6: *Macroscopic wave packet extracted from HHG spectra of Ar for 1200- and 1360-nm lasers in Fig. 3.3. Calculated photorecombination transition dipole moment using the Muller potential [97] is also shown. Adapted from Publication [8].*

According to Eq. (3.2), the HHG spectra in the lower frame of Fig. 3.3 can be decomposed as MWPs and PR transition dipole moment in Fig. 3.6. The two wave packets derived from 1200-nm and 1360-nm lasers are quite similar, but they only have slight different slopes near 50 eV. The PR transition dipole, however, shows a clear and broad CM around 50 eV. Thus, we can conclude that the broad CM in the HHG spectra shown in Fig. 3.3 is caused by the

minimum in the PR transition dipole (or PR cross section). The precise position of CM in the HHG spectra is somewhat influenced by the MWP. As an example shown in Fig. 3.6, due to the difference in MWP, the position of CM with the 1200-nm laser in Fig. 3.3 is slightly different from that with the 1360-nm laser. This could explain that the measured position of CM of Ar varies from one laboratory to another due to the sensitivity of MWP to the experimental conditions.

3.5.3 Dependence of wave packet on experimental conditions

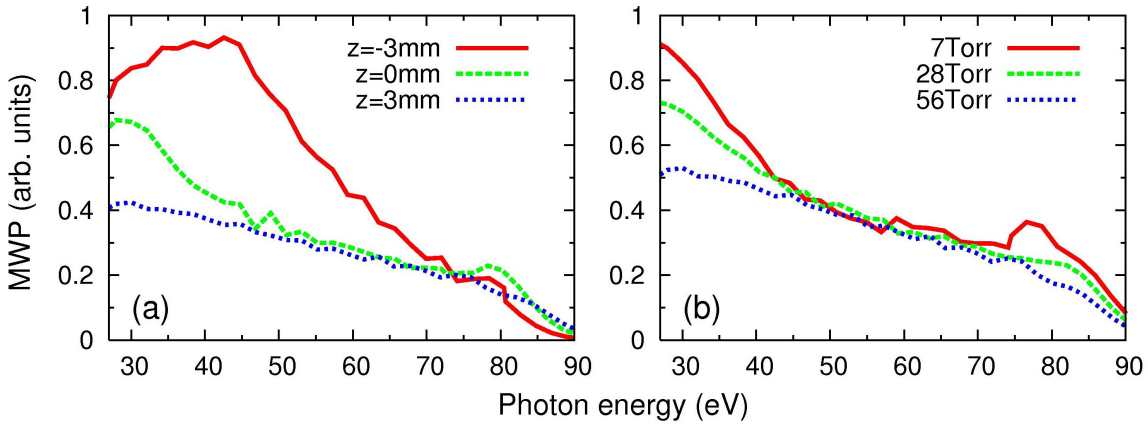

Figure 3.7: *(a) Dependence of macroscopic wave packet $|W'(\omega)|$ on the position of the Ar gas jet with respect to the laser focus, and (b) on gas pressure. Adapted from Publication [8].*

The MWP is a characteristic, which doesn't depend on the PR transition dipole of the target. In other words, the macroscopic conditions only affect HHG through its modifications on the MWP. Thus, we can only study the macroscopic propagation effect on HHG by investigating how the MWP varies with the laser and experimental conditions.

In Fig. 3.7(a), we show the MWPs for three gas-jet positions, which are at z=-3 mm (gas jet before laser focus), z=0 mm (at), and z=3 mm (after). The three curves are extracted from HHG spectra in Fig. 3.4. For easy visualization, we only show the smooth envelope of $|W'(\omega)|$. Among the three curves, the "after" curve is very flat since good phase-matching is favored for this arrangement as the single-atom harmonic phase is partially compensated

by the geometric phase from the focused laser. If the gas jet is placed before the laser focus, the MWP changes rapidly, especially near photon energy around 50 eV. Such strong energy dependence can wash out the CM in the HHG spectrum in Fig. 3.4.

In Fig. 3.7(b) we investigate how the MWP depends on the gas pressure for the focusing condition of z=3 mm. Laser and other experimental parameters are the same as Fig. 3.7(a). The MWP has been normalized by the ratio of the pressure. The three curves would be on top of each other if a complete phase-matching condition had been fullfilled. The curve for higher pressure is slightly lower indicates that full phase matching is not reached, especially for the lower harmonics. With the increase of pressure, the MWP is much smoother vs energy. In fact, increasing the gas pressure tends to smooth out the harmonics. These results also indicate that the harmonic energy increases quadratically with the gas pressure, which is in agreement with measurements reported in Ref. [32].

3.6 Wavelength scaling of harmonic efficiency

One of the main interests in the study of HHG is to improve the harmonic efficiency, thus producing bright tabletop XUV or soft X-ray sources, or intense attosecond pulses. Since the single-atom harmonic cutoff energy is proportional to the square of the wavelength of the driving laser, HHG generated by mid-infrared (MIR) lasers can efficiently reach high-energy photons, but the yield is less favorable. It is of interest to study how the HHG yield scales with the laser wavelength. In the single-atom response level, there have been a few theoretical calculations [29, 31, 133–135]. Macroscopic propagation effect has to be included in order to compare with experimental HHG spectra. A few investigations on the wavelength scaling of HHG experimentally [32, 130, 136] have been reported. However, theoretical analysis is still rather scarce.

To study wavelength scaling of the HHG yield, one has to fix all other parameters that may affect the efficiency of HHG. One also has to decide if it is the total HHG yield or only the HHG yield within a given photon energy region. In single-atom HHG simulations, the

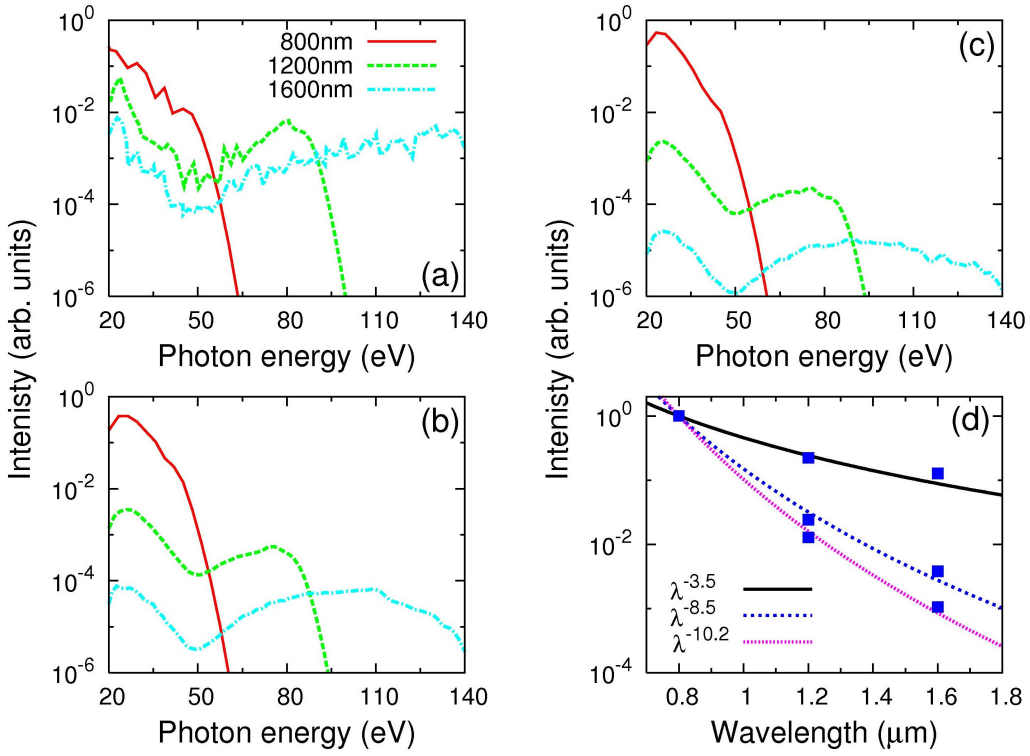

Figure 3.8: *(a) Single-atom HHG spectra, and macroscopic HHG spectra without (b) and with (c) the slit for 800 nm (solid lines), 1200 nm (dashed lines) and 1600 nm (dot-dashed lines) lasers. The laser parameters are given in the text. (d) Wavelength dependence of the total integrated HHG yields above 20 eV. The integrated HHG yields in (a), (b) and (c) follow* $\lambda^{-3.5\pm0.5}$, $\lambda^{-8.5\pm0.5}$ *and* $\lambda^{-10.2\pm0.2}$, *respectively. Adapted from Publication [11].*

laser parameters can be easily fixed, but this is not the case in experiments. Theoretical simulations including macroscopic propagation effect are few [137, 138]. Since the resulting HHG spectra depend on so many other parameters, any wavelength scaling laws derived are likely to depend on the experimental parameters used. In spite of this limitation, it is still of interest to take a look at the wavelength scaling by using the present QRS model. For this purpose, we will define a parameter that describes the efficiency of harmonic generation. This is the ratio between the output energy (total harmonic energy) with respect to the input energy (fundamental laser energy) for different laser wavelengths. The input pulse energy can be calculated using Eq. (D.14) if the laser beam has a Gaussian distribution in time and space. The output energy can be obtained by integrating the harmonic intensity

over a photon-energy region:

$$E_{\text{out}} = \int_{\omega_{\min}}^{\omega_{\max}} \int\int |E_{\text{h}}(x, y, \omega)|^2 dx dy d\omega. \tag{3.3}$$

.

In Fig. 3.8(a) we show the single-atom HHG spectra calculated for three wavelengths. Only the envelope of each spectra is shown. In the calculation, the laser intensity and duration are kept as 1.6×10^{14} W/cm^2 and 40 fs, respectively. In Fig. 3.8(b) the HHG spectra obtained after including macroscopic propagation are shown. In the calculation, the beam waist at the focus is kept as 47.5 μm, a 0.5 mm-long gas jet is placed at 3 mm after the laser focus, and gas pressure is kept at 56 Torr. The yield of each harmonic is obtained by integrating over the whole plane perpendicular to the propagation axis. In Fig. 3.8(c), the HHG yields are recorded after they have passed a slit (the slit with a width of 100 μm is placed at 24 cm after the gas jet). From Figs. 3.8(b) and 3.8(c), we calculate the HHG efficiencies per atom vs the wavelength.

In Fig. 3.8(a), the ratio of input energy is 1:1:1 for 800 nm, 1200 nm, and 1600 nm lasers. If we integrate the HHG yields above 20 eV as the output energy. The resulting energy follows $\lambda^{-3.5\pm0.5}$ shown in Fig. 3.8(d). If we integrate the HHG yields between 20 eV and 50 eV, which would give a scaling rule of λ^{-5}. In Tate *et al.* [29], the laser intensity and the number of optical cycles were fixed for 800 nm and 2000 nm lasers. According to our approach, the ratio of input energy is 1:2.5 for the 800 nm and 2000 nm lasers. And their scaling rules at constant intensity of $\lambda^{-(5-6)}$ would be modified as $\lambda^{-(6-7)}$ at a constant input energy.

When propagation effect is considered it is generally known [27, 29] that phase-matching condition is more difficult to meet for longer-wavelength lasers, thus the HHG efficiency decreases with increasing wavelength. Here we consider the total HHG yields for the lasers used in Fig. 3.8(b) in which the gas jet is placed at z=3 mm. Since the laser intensity is fixed at the center of the thin gas jet, we calculate that the intensities at the laser focus are 1.78×10^{14} W/cm^2, 2.01×10^{14} W/cm^2, and 2.33×10^{14} W/cm^2, for 800 nm, 1200 nm, and

1600 nm lasers, respectively, thus the input energies have the ratios of 1:1.13:1.31. We find that HHG yields integrated from 20 eV up scale like $\lambda^{-8.5\pm0.5}$, as shown in Fig. 3.8(d). If we only integrate the harmonics between 20-50 eV, then the scaling rule is $\lambda^{-10.5}$.

Experimentally, Colosimo *et al.* [130] reported that the HHG yields between 35-50 eV for 2000 nm lasers are about 1000 times smaller than that for 800 nm lasers, for experimental conditions that were kept "as fixed as possible". This would give a λ^{-9} dependence in this narrow energy region which is not too far off from our scaling of $\lambda^{-10.5}$. In addition, Shiner *et al.* [32] reported a scaling rule of $\lambda^{-6.3\pm1.1}$ for the HHG of Xe with a fixed laser intensity. By assuming perfect phase-matching condition for all the laser wavelengths used, they derived scaling law of $\lambda^{-6.3\pm1.1}$ that was to be compared to the scaling law derived from the single-atom response. We cannot compare their results with our simulations. They used a truncated Bessel beam (instead of Gaussian beam) in the experiment and the gas jet was located at the laser focus. Since the HHG yields depend on so many experimental parameters, it is clear that any simple scaling laws derived should be taken with caution. In Fig. 3.8(d), we also show the scaling law for the case where the HHG yields are collected after the slit. We integrate the HHG signals above 20 eV and obtain the $\lambda^{-10.2\pm0.2}$ scaling. In general, good phase-matching condition becomes more difficult to meet with increasing laser wavelength. Even if the gas jet is placed after the laser focus, the short trajectories are not selected efficiently for longer-wavelength lasers. A slit is usually used to select contributions from short trajectories in the far field. By blocking out contributions [see Fig. 3.8(c)] from the long trajectories the harmonic efficiency becomes worse.

Based on the above analysis, the HHG yields for long-wavelength driving lasers under the same experimental conditions appear quite unfavorable. On the other hand, for practical purpose, experimentally high harmonics are to be generated with optimized conditions. In Colosimo *et al.* [130] it was reported that the HHG yields between 35-50 eV generated by using 2000 nm lasers can be as high as 50% of that from 800 nm lasers if the experimental conditions were optimized independently. Furthermore, Chen *et al.* [139] demonstrated that

it was possible to use much higher pressure to generate HHG for long-wavelength lasers, thus achieving usable photon yields even in the water-window region. Clearly additional theoretical analysis of macroscopic propagation effects on HHG for long-wavelength driving lasers under different experimental conditions is desirable.

3.7 Conclusion

In the past two decades HHG by infrared laser pulses with atoms has been widely investigated both experimentally and theoretically. Since the HHG is generated from a macroscopic medium, theoretically we need to deal with both the microscopic laser-atom interaction, and macroscopic propagation of laser and harmonic fields. In this chapter, we first showed that the calculated macroscopic HHG spectrum obtained from the QRS-based atomic dipoles was in much better agreement with the TDSE than that from the SFA. For the TDSE being carried out efficiently, in these comparisons we only limited ourselves in the conditions of low-intensity lasers and low-density gas medium where the fundamental field can be considered as propagating in the vacuum. Then we extended our model to the higher laser intensities and gas pressures at which the nonlinear propagation of the fundamental laser field was also considered with the inclusion of dispersion, plasma, and Kerr effects, and simulated the HHG spectra of Ar with 1200- and 1360-nm lasers by considering the detailed experimental information. The experimental HHG spectra have been successfully reproduced by theory. The most pronounced structure in the measured spectra of Ar, i.e., the Cooper minimum, has also been reproduced. Specifically, we investigated how the Cooper minimum was washed out by changing the experimental conditions.

We showed that the macroscopic HHG spectrum can be expressed as a product of a MWP and a single-atom photorecombination transition dipole moment. The MWP has been shown to be largely independent of the target if the ionization potential is nearly the same for the two targets. The study of HHG spectra with the macroscopic conditions can be simplified as the study of MWPs only, which can be easily obtained by solving the Maxwell's

equation with the SFA-based induced dipoles. The concept of MWP also implies that one can extract the photorecombination transition dipole of an unknown atom or molecule from one for which the photorecombination transition dipole moment is known by comparing their measured HHG spectra in the same laser pulse.

It is always an obstacle to improve the harmonic efficiency if the long-wavelength laser is applied to obtain the high-energy photons. Tate *et al.* [29] suggested that the harmonic yield followed a $\lambda^{-(5-6)}$ scaling at constant intensity theoretically. However, this scaling law was obtained by the calculation of the single-atom response. It is generally known that the macroscopic propagation of the HHG makes this scaling law even worse. In this chapter, we showed the scaling law with wavelength in the single-atom response first based on the QRS theory. And then we fixed the input pulse energy, and showed how this scaling law was varied with the macroscopic conditions. This study also implies that the scaling law can be improved by changing the experimental conditions, such as increasing gas pressure, increasing input energy, optimizing the detecting system, and so on.

Chapter 4

Comparison of high-order harmonic generation of Ar using a truncated Bessel or a Gaussian beam

Figures and most paragraphs in this chapter are adapted from Publication [2].

4.1 Introduction

As discussed in Chapter 3, a full quantitative description of high-order harmonic generation (HHG) in a macroscopic medium requires the inclusion of the propagation of the fundamental laser field and the generated harmonic field. The QRS theory has been successfully incorporated into the well-established macroscopic propagation theory such that the simulated HHG spectra can be compared directly with experimental measurements in Fig. 3.3, where experimental conditions have been well specified. The harmonics in these studies were generated with multi-cycle (FWHM, ~ 10 optical cycles) laser pulses. And these simulations were based on the assumption that the initial fundamental laser pulse at the entrance of the gas medium is a Gaussian beam. Few-cycle laser pulses are also widely used to produce the high harmonics, and they are usually obtained by gas-filled hollow-core fiber compression technique [140]. In this method, an incident laser beam can be dominantly coupled into the fundamental EH_{11} hybrid mode by proper mode matching. At the exit of the fiber a truncated Bessel (TB) beam is produced instead of a Gaussian beam. Nisoli *et al.* [141] have

shown that the spatial properties (divergence and brightness) of the harmonics were greatly improved using a TB beam as the driving laser pulse. To simulate harmonics generated by few-cycle pulses we generalize the propagation code to include situations where the spatial distribution of the generating laser pulse is a TB beam.

In this chapter, using the spatial TB beam we first want to check if we can simulate the high-harmonic spectra of Ar reported by Wörner *et al.* [127], which were carried out with a few-cycle laser at relatively high intensities (Fig. 1 of their paper). Our second goal is to establish the general conditions where the generated harmonic spectra are insensitive to whether the generating beam is a Gaussian or a TB beam.

We modify the numerical code by changing the initial condition in which the input beam is a TB beam. A TB beam exiting from the hollow-core fiber is usually refocused through lens and mirrors before entering the harmonic-generating gas medium. In the Appendix D.2, we describe two types of TB beams. In TB-1 (Type-1 Bessel), a tight focusing beam was used by Nisoli *et al.* [141]. In TB-2 (Type-2 Bessel), for the case of a loosely focused TB beam, was used by Wörner *et al.* [127] and Shiner *et al.* [21]. In Sec. 4.2 we show the calculated HHG spectra of Ar with a TB beam or a Gaussian beam using a 780-nm laser and setup parameters as close as those in Wörner *et al.*'s [127]. Even with the TB-2 beam, we still have not been able to reproduce the observed deep Cooper minimum (CM) reported in the experiment. However, we are able to reproduce the HHG spectra of Ar reported in Shiner *et al.*'s [21] where the harmonic spectra were generated using 1800-nm mid-infrared lasers. We then turn to study the detailed harmonic growth maps in space for TB-1 and TB-2 beams in terms of phase matching conditions. In Sec. 4.3, we investigate how these maps change with the gas-jet position. In Sec. 4.4, we specifically study the pressure induced phase mismatch by analyzing the harmonic growth map for different gas pressures. We then draw the conclusion that for TB-2 beam, the HHG spectra are generally close to those generated from a Gaussian beam with the similar beam waist. A summary in Sec. 4.5 concludes this chapter.

4.2 Simulation of HHG spectrum of Ar

4.2.1 Few-cycle 780-nm laser

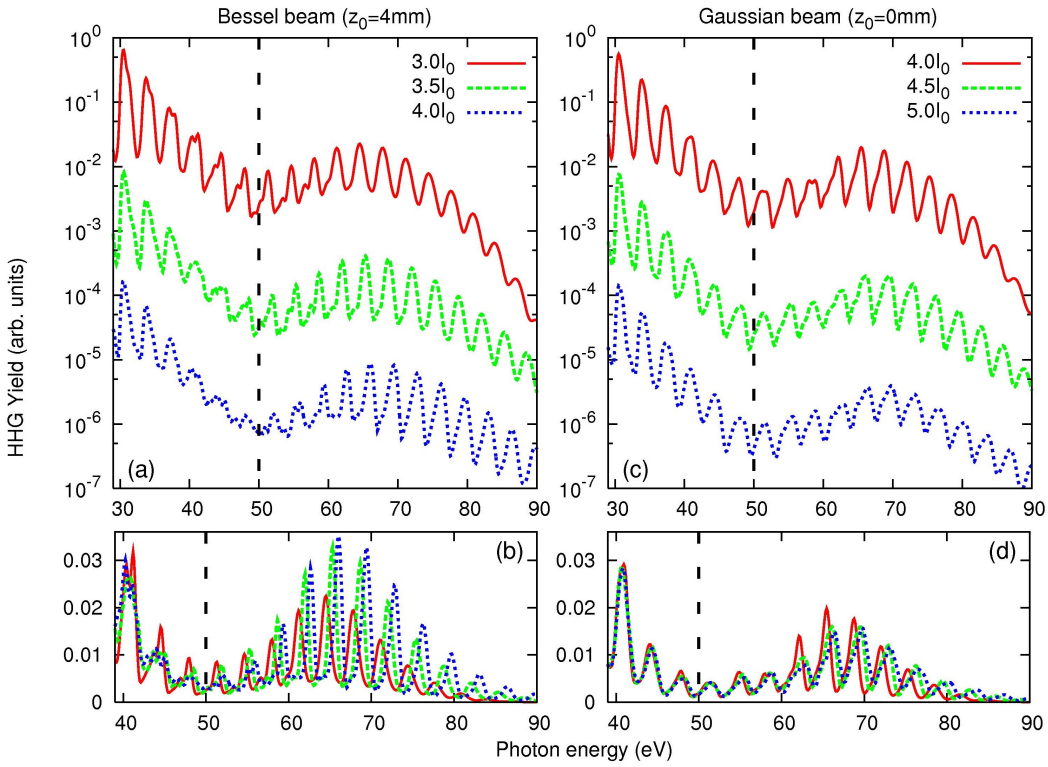

Figure 4.1: *Calculated HHG spectra (CEP averaged) of Ar assuming the initial laser pulse is a truncated Bessel beam (Type 2 in Fig. D.5) [(a) and (b)], or a Gaussian beam (beam waist w_0=50 μm) [(c) and (d)]. z_0 is the position of the gas jet with respect to the laser focus, and laser intensity (at the focus, z=0 mm) is given in units of $I_0=10^{14}$ W/cm^2. Dashed lines indicate the position of the Cooper minimum. Laser wavelength is 780 nm. See text for additional laser parameters. This figure should be compared with Fig. 1 in Ref. [127] and Fig. 4.2(b) below. Adapted from Publication [2].*

It is well-known that photoionization cross section (PICS) of Ar has a minimum [142], called Cooper minimum (CM), at photon energy near 51 eV. The Cooper minimum also appears in the harmonic spectrum of Ar, and has been reported in many measurements [21, 127–131] using different laser intensities and different laser wavelengths. To observe clear CM, the cutoff of the HHG spectrum should lie well above 51 eV. In experiments with typical 800-nm Ti:sapphire lasers, this would require a high laser intensity. On the other

hand, at high intensities saturation occurs. Thus in earlier experiments with 800-nm lasers, the CM in the HHG spectrum of Ar was not clearly located. To avoid saturation effect, in Wörner *et al.* [127] few-cycle laser pulses were used and clear CM has been reported. In this experiment, a hollow-core fibre filled with Ar gas was used to achieve self-phase modulation for the laser pulse, subsequently, using chirped mirrors it was compressed to a few-cycle pulse ($\sim$ 3 optical cycles). The most prominent feature of the experimental result was the appearance of a clear deep CM at 53$\pm$3 eV, which didn't not shift with laser intensity. Wörner *et al.*'s [127] measurements appear to be consistent with the general prediction of the QRS theory, in that the position of the CM is at about 51 eV, and the position does not change with laser intensity. However, the width and depth of the CM appear to contradict the QRS theory. (The CM observed in the PICS of Ar is not as deep [142].) We have carried out simulations with experimental parameters by assuming that the incident laser pulses were Gaussian beams, but were unable to reproduce the broad and deep Cooper minimum reported in the experiment. We thus decide to investigate whether the limitation is due to the use of a Gaussian beam in the simulation. Here we show the results from simulations using a truncated Bessel beam.

In the simulation, both the fundamental and harmonic field are propagated in the medium, and the single-atom induced dipole is obtained by using the QRS theory. Laser wavelength is 780 nm, and duration is 3 cycles (FWHM). The gas jet is 1-mm wide in the interaction region and the gas pressure is assumed to be a constant at 30 Torr, and a slit with a width of 100 μm is placed at 24 cm after the gas jet to select the harmonics in the far field. These parameters are close to those in Wörner *et al.* [127]. The laser peak intensity at the focus (in the vacuum) was adjusted as indicated in Fig. 4.1 to obtain the correct experimental cut-off position.

We first assume that the laser pulse is a Gaussian beam with waist w_0=50 μm and the center of the gas jet is at the laser focus (z_0=0 mm). The HHG spectra after CEP averaged are shown in Fig. 4.1(c). For clarity, the spectra have been shifted for different intensities.

In Fig. 4.1(d), we show the spectra for three intensities in linear scale. The CM appears at about 50 eV. Beyond 4×10^{14} W/cm^2, the laser field reaches saturation and higher harmonics show blue shift. The ratio of the maximum yield near the cutoff with respect to the lowest yield at the CM is about a factor of 3 - 6 in the simulation, but the same ratio is close to 100 in the experiment of Wörner *et al.* [127] [also see Fig. 4.2(b) below]. We have varied the position of the gas jet (z_0) with respect to the laser focus, but the harmonic spectra remain nearly the same as those in Fig. 4.1(c).

We next assume that the incident beam is a TB-2 pulse, and the center of the gas jet is located at 4 mm after the laser focus (i.e., z_0=4 mm). The HHG spectra after CEP averaged are shown in Figs. 4.1(a) and (b). The laser intensities indicated are the ones at the laser focus (z=0 mm), so the on-axis intensities at z=4 mm are almost the same as those in the Gaussian pulses (at z=0 mm) in Fig. 4.1(c). The high-harmonic spectra shown in Fig. 4.1(a) do not differ significantly from those in Fig. 4.1(c), with the CM appearing near 50 eV. From Fig. 4.1(b), we find that with the TB-2 beam, the HHG spectra are stronger for the higher harmonics, such that the previous maximum/minimum ratio rises by about 50%, but still much smaller than the ratio seen in Wörner *et al.* [127]. We have also changed z_0 (not shown), the CM was always seen, but the depth of the CM reported in the experiment still cannot be reproduced. Thus the origin of the discrepancy remains unexplained.

4.2.2 Few-cycle 1800-nm laser

As shown in Eq. (1.4), the cutoff energy can be extended with the increase of laser wavelength since the ponderomotive energy is proportional to the square of the wavelength of a driving laser.Iit is preferable to study the CM in HHG spectra of Ar using near-infrared (NIR) lasers. Indeed, such measurements have been reported by Jin *et al.* (Publication [8]) using 1.2- and 1.36-μm lasers and by Higuet *et al.* [131] with 1.8- to 2.0- μm and 50-fs NIR lasers. None of these experiments reported the CM as deep as shown in Wörner *et al.* [127]. In fact, the experimental data reported in Jin *et al.* (Publication [8]) were well reproduced

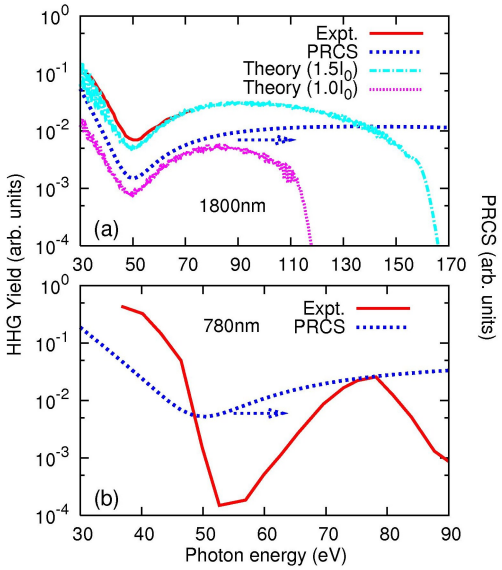

Figure 4.2: *(a) Comparison of experimental (envelope only) [21] and theoretical HHG spectra using an 1800-nm laser. Laser intensity used in the simulation is indicated in units of I_0=10^{14} W/cm^2. See text for additional parameters. Experimental data are shown only from 30 to 75 eV due to constraint from the filter. (b) Experimental HHG spectra (envelope only) [127] using a 780-nm laser with intensity of 2.9×10^{14} W/cm^2. Calculated photorecombination cross section (PRCS) using the Muller potential [97] is also shown in (a) and (b). Adapted from Publication [2].*

by our simulations using an incident Gaussian beam spatially. Recently, Shiner *et al.* [21] also reported the measurements of Ar HHG spectra using a few-cycle ($\sim$ 2 optical cycles) 1800-nm laser (see Fig. 9 in the supplementary information). We show their experimental spectrum in Fig. 4.2(a). We carry out the simulation with an 1800-nm, 11-fs laser pulse. A gas jet (0.5 mm wide) is located at the laser focus, gas pressure is 6 Torr, and a slit with a width of 190 μm is placed at 45.5 cm after the gas jet. Only the harmonics after the slit are detected. The initial laser beam is assumed as a Gaussian one with w_0=100 μm. The calculated HHG spectra (CEP averaged) with two intensities are shown in Fig. 4.2(a). We can see that the experimental spectrum agrees very well with the theoretical one (laser intensity is 1.5×10^{14} W/cm^2). These spectra also agree well with the calculated PRCS of Ar using the Muller potential [97]. With decreasing laser intensity, the general spectral shape and the depth of the Cooper minimum don't change much except that the cut-off position

moves to lower photon energy. This also shows that a Gaussian beam can be used to model the experiment of Shiner *et al.* [21]. In other words, the general HHG spectra obtained from loose focusing TB beam and Gaussian beam do not differ significantly.

Based on the above simulations, we conclude that the deep Cooper minimum in the HHG spectra [see Fig. 4.2(b)] reported in Wörner *et al.* [127] remains not reproduced by simulations. On the other hand, the very deep minimum was not observed in other experiments using NIR lasers [21]. Our simulations can reproduce these latter observations.

4.3 Phase matching conditions at the low gas pressure

Nisoli *et al.* [141] have shown that the characteristics of HHG using a truncated Bessel beam and Gaussian beam were quite different. Our results in Sec. 4.2 seem to contradict with their conclusions. It turns out that in Nisoli *et al.* [141] they used a tightly focused truncated Bessel beam (or TB-1), while in Sec. 4.2, a loosely focused truncated Bessel beam (or TB-2) was applied. In Appendix D.2 we summarize how the two types of the TB beams are constructed, together with their typical spatial intensity distributions. In this section, we present a systematic comparison of phase matching conditions for the TB-1, TB-2, and Gaussian beams. In the calculation, the *ab initio* macroscopic propagation and the QRS theory for the single-atom response are applied, the laser intensity (at the focus, as shown in Figs. D.3 and D.5), wavelength, duration (FWHM), and CEP are fixed at 3×10^{14} W/cm^2, 780 nm, 3 cycles, and 0, respectively.

As discussed in Sec. 1.3.1, phase matching is a pre-requisite for efficient generation of high harmonics. The phase mismatch for the q-th harmonic in Eq. (1.5) includes four terms [12, 15, 16, 36, 37]. Each term has been discussed in detail in Sec. 1.3.1. Here we only give a brief review. The first term of the phase mismatch is due to the geometry of laser focusing. The second term is from the dispersion by free electrons that are present in the gas medium, i.e., free electron or plasma dispersion. The third term is from neutral atom dispersion where the index of refraction changes with wavelength. The last term is due to

laser-induced atomic dipole phase which depends strongly on laser intensity. The dipole phase mismatch is given by $K_{q,dip} = \nabla\varphi_{q,dip}$, where $\varphi_{q,dip}$ is the action accumulated by an electron during its excursion in the laser field. This phase depends on whether the q-th harmonic is emitted by electrons that take the "long" or "short" trajectories.

4.3.1 Phase-matching map at low gas pressure

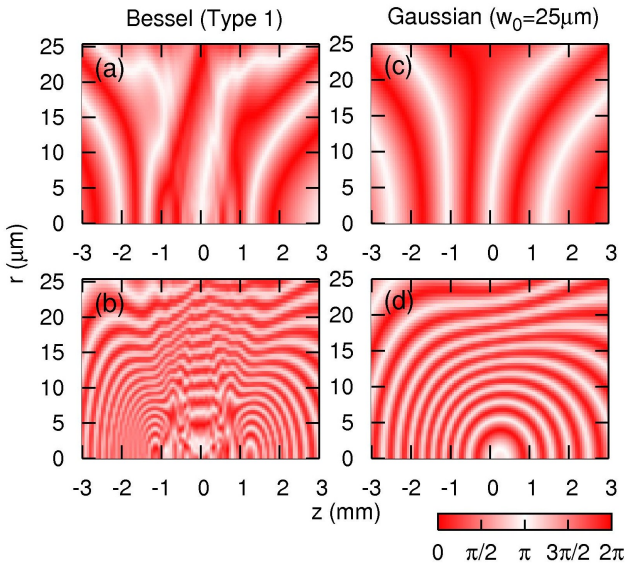

Figure 4.3: *Phase matching map for H15 of the interplay between the geometric phase $\varphi_{q,geo}(r,z)$ and induced dipole phase $\varphi_{q,dip}(r,z)$ for Type-1 Bessel and Gaussian (w_0=25 μm) beams. Upper row: "short" trajectory; lower row: "long" trajectory. Note that $\Delta\varphi_q(r,z)$=$\varphi_{q,geo}(r,z)$-$\varphi_{q,dip}(r,z)$ modulo 2π is plotted, and the phase change between two neighboring white regions is 2π. Adapted from Publication [2].*

We first set the gas pressure very low (0.1 Torr) such that pressure effect can be ignored. In this case, the phase matching conditions are only determined by the interplay between the geometric phase $\varphi_{q,geo}(r,z)$ and the induced dipole phase $\varphi_{q,dip}(r,z)$ in Eq. (1.8). We plot $\Delta\varphi_q(r,z)$=$\varphi_{q,geo}(r,z)$ - $\varphi_{q,dip}(r,z)$, modulo 2π, in Fig. 4.3 for the 15th harmonic (H15) in contrast to the generally used contour map for the coherence length [36, 143]. The color coding is chosen such that it is bright (or white) when $\Delta\varphi_q$ is near π, and dark (or red) when near 0 and 2π (such that no color changes at the two boundaries). Note that the

length scale is in *mm* along the z-axis and in μm along the r-axis. In Fig. 4.3, the phase between two neighboring white regions is 2π. For good phase matching, this region is large (such that the gradient is small). From the figure we can see in general it is easier to achieve good phase matching for "short" (upper row) than for "long" (lower row) trajectories.

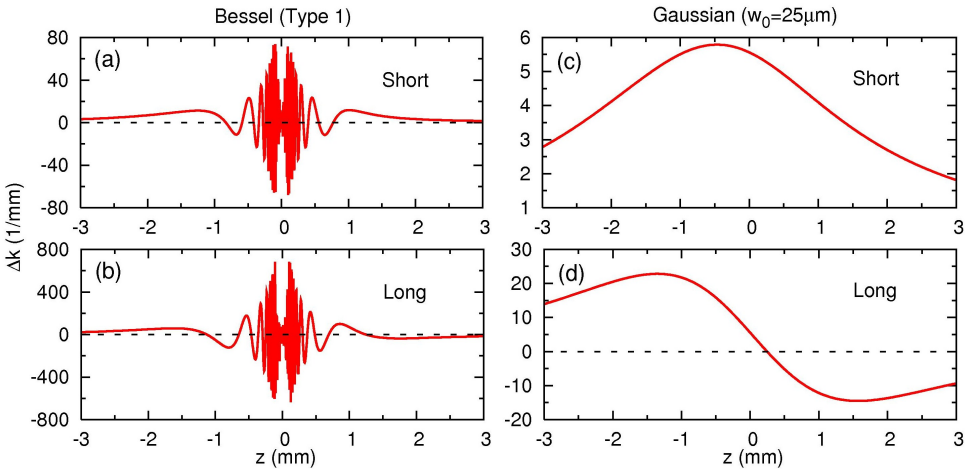

Figure 4.4: *On-axis phase mismatch* $\Delta k_q(z) = (\partial/\partial z)[\Delta\varphi_q(0,z)]$ *for the phase shown in Fig. 4.3 with Type-1 Bessel and Gaussian* (w_0*=25* μm*) beams.* q*=15. Upper row: "short" trajectory; lower row: "long" trajectory. Dashed lines indicate the zero values of the phase mismatch. Note that the values of* $\Delta k_q(z)$ *from z=-0.2 to 0.2 mm in (a) and (b) are probably not precise numerically due to the dramatic phase oscillation along z direction. Adapted from Publication [2].*

Using the phases in Fig. 4.3 we can calculate the phase mismatch by taking the gradient. In Figs. 4.4(c) and (d) we show the phase mismatch $\Delta k_q(z)$ for H15 along the propagation axis z for a Gaussian beam. It is much smaller for the "short"-trajectory component than for the "long"-trajectory one. Furthermore, phase matching is better after the focus. Since laser intensity decreases quickly away from the focus, thus a gas jet located at z=2 mm is about near the optimum condition for HHG generation for a Gaussian beam. In Figs. 4.4(a) and (b) the phase mismatch $\Delta k_q(z)$ for a TB beam along the propagation axis z is shown. Again the phase mismatch is much larger for "long"-trajectory component than for the "short"-trajectory one. Although the phase oscillates widely near z=0 mm, spatial average over a small volume would result in a small phase mismatch. Thus for TB beams a broad

good phase-matching region close to the axis from z=-1.5 to 1.5 mm for "short"-trajectory harmonics can be achieved. This conclusion is consistent with the experimental results of Nisoli *et al.* [141]. For the typical gas-jet length ($\sim$ 1 mm), the phase matching conditions should depend strongly on the position of the gas jet, and for whether it is Type-1 Bessel or Gaussian (w_0=25 μm) beams.

For harmonics generated away from the axis, the phase mismatch has components parallel and perpendicular to the axis. For a Gaussian beam, the distance between two white regions (where phase changes by 2π) is larger along the z-axis than along the r-axis, see Figs. 4.3(c) and (d), thus phase matching (by taking the gradient of the phase) is still favorable, even not as good as the on-axis region (also see Fig. 4 in [36]). From Fig. 4.3, in general, "long"-trajectory harmonics tend to have off-axis phase matching and the harmonics are more divergent.

We next consider loosely focused laser beams. From Eqs. (D.4) and (D.5), we note that for a Gaussian beam, if we scale z by the confocal parameter b and scale r by the beam waist w_0, the intensity and phase stay the same. Thus for the loosely focused Gaussian beam the phase matched volume will increase (by b or w_0 in each direction). For a typical fixed gas-jet length, we expect that good phase-matching conditions are more easily achieved. This is also true for TB beams. We have checked (not shown) that the phase map for TB-2 and Gaussian (w_0=50 μm) beams were very similar to those shown for TB-1 and Gaussian (w_0=25 μm) beams in the scaled coordinates (for H15). Thus for loosely focused TB-2 beams the phase matching conditions do not differ much from the loosely focused Gaussian beam. In Sec. 4.3.2, we will show that in this case the HHG spectra generated by TB-2 beam and by Gaussian beam are very similar.

4.3.2 Dependence of harmonic yield on gas-jet position

Fig. 4.5 shows the intensity distributions of the plateau harmonic H15 and cutoff harmonic H35, under tight-focusing conditions at two different gas-jet (1-mm width) positions, for

Table 4.1: *Phase mismatch $\Delta k_{q,geo}(0,z)$ and $K_{q,dip}(0,z)$ (mm^{-1}) derived from Eqs. (1.6) and (1.8) for a Gaussian beam. Here z=1 mm and I_0=3×10^{14} W/cm^2.*

Harmonic order		H15				H35			
Confocal parameter b (mm)		5	3	20	15	5	3	20	15
$\Delta k_{q,geo}$		4.83	6.46	1.39	1.83	11.72	15.69	3.37	4.45
$K_{q,dip}$	Short ("S")	0.71	1.28	0.059	0.103	< 9.77	< 17.51	< 0.81	< 1.41
	Long ("L")	17.12	30.67	1.41	2.47	> 9.77	> 17.51	> 0.81	> 1.41

a TB-1 beam and a Gaussian beam. The other laser parameters are given in the figure caption. To understand these results, we examine the phase mismatch [see Eq. (1.5)] values in units of 1/mm. On-axis phase mismatch $\Delta k_{q,geo}(0,z)$ and $K_{q,dip}(0,z)$ for a Gaussian beam are written as [16, 37]

$$\Delta k_{q,geo}(0,z) \approx \frac{2}{b}(q-1)\frac{1}{1+(2z/b)^2}, \tag{4.1}$$

$$K_{q,dip}(0,z) = \frac{8z}{b^2}\frac{1}{[1+(2z/b)^2]^2}\alpha_i^q I_0. \tag{4.2}$$

Here α_i^q is defined in Eq. (1.8), and other parameters can be found in Appendix D. In Table 4.1, we show the typical values of $\Delta k_{q,geo}(0,z)$ and $K_{q,dip}(0,z)$ calculated by using Eqs. (4.1) and (4.2) at z=1 mm on the axis (r=0). [We caution that the value of $K_{q,dip}(0,z)$ calculated using α_i^q in the cut-off region in Eq. (1.8) may not be very accurate.] Since the gas pressure is very low (0.1 Torr), there is no laser defocusing. For b=5 mm (w_0=25 μm), clearly from Table 4.1, the "short" trajectory is favored for good phase matching. The coherence length is $l_{coh}=\pi/\Delta k_q$, where $\Delta k_q = \Delta k_{q,geo} - K_{q,dip}$ is calculated to be about 1 mm for both H15 [also see Fig. 4.4(c)] and H35. This large coherence length allows the harmonic intensity to grow steadily along the propagation axis z, as seen in Figs. 4.5(f) and (h). If the gas jet is placed before the laser focus (z_0=-1 mm), $K_{q,dip}$ changes its sign while $\Delta k_{q,geo}$ remains the same as that at z=1 mm. Thus the coherence length l_{coh} (no matter "short" or "long" trajectory) becomes much smaller. In Figs. 4.5(e) and (g), we see that

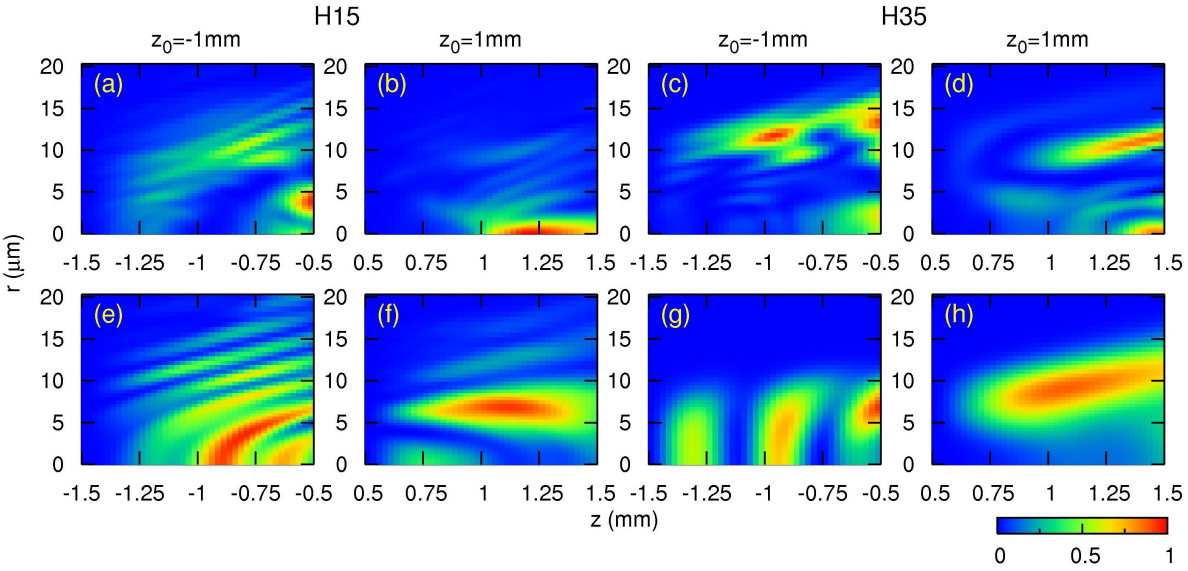

Figure 4.5: *Spatial distributions (normalized) of harmonic intensity for H15 and H35 using tight focusing laser beams. z_0 is the position of the gas-jet center with respect to the laser focus, i.e., $z_0 > 0$ means the gas jet (1-mm wide) is placed after the laser focus. Gas pressure: 0.1 Torr (i.e., the fundamental laser field is not modified through propagating in the medium). Upper row: Type-1 Bessel beam; lower row: Gaussian beam (w_0=25 μm). Adapted from Publication [2].*

the buildup of the harmonic along z is not monotonic. The small coherence length results in destructive interference such that the harmonic yield vanishes, followed by buildup and then destruction, as z increases. Thus gas-jet position z_0=-1 mm is not favorable for phase matching for the generation of harmonics. For Type-1 Bessel beam, as shown in Figs. 4.5(a)-(d), the harmonic spatial distribution is quite different from the Gaussian beam, but the strong gas-jet position dependence is similar, i.e., the coherence length is shorter for negative z_0 than for positive z_0.

The same analysis can be done for a loosely focused Gaussian beam (b=20 mm, w_0=50 μm). At z=1 mm, l_{coh} is $\sim$ 2 mm (H15) or $\sim$ 1 mm (H35), and l_{coh} becomes $\sim$ 1 mm at z=-2 mm. The large coherence length allows steadily monotonic buildup of the harmonics as z is increased, as confirmed by numerical results shown in Figs. 4.6(e)-(h). For Type-2 Bessel in Figs. 4.6(a)-(d), the harmonic spatial distribution is very similar to the Gaussian

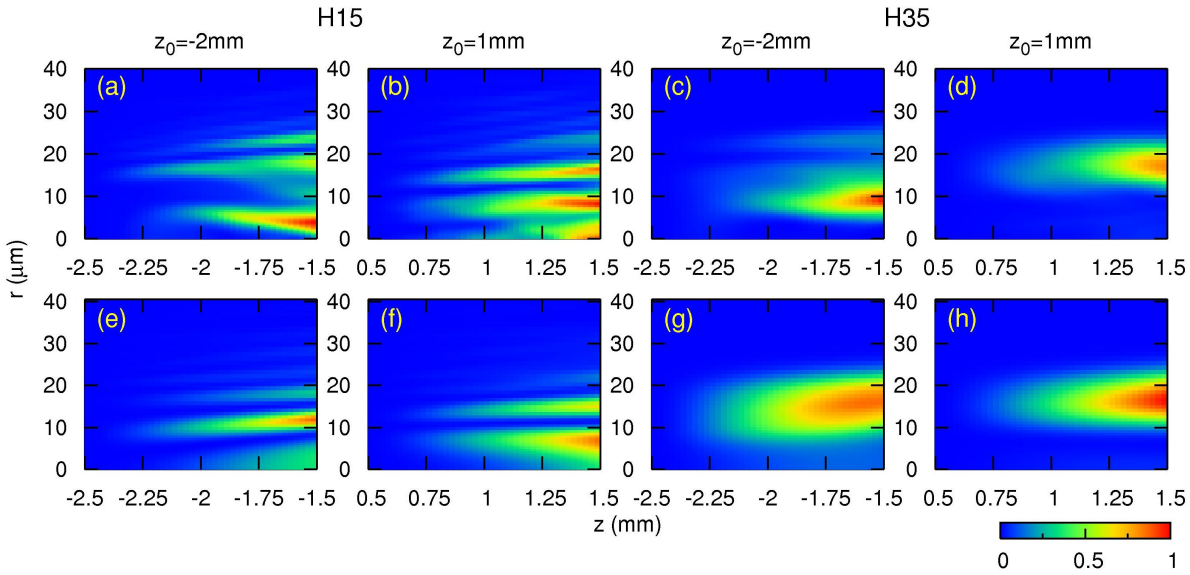

Figure 4.6: *Same as Fig. 4.5 except for loosely focused laser beams. Upper row: Type-2 Bessel beam; lower row: Gaussian beam (w_0=50 μm). Adapted from Publication [2].*

beam. These confirm that for loosely focused Gaussian and Bessel beams the generated harmonic spectra are expected to be quite similar for the same gas-jet positions and the results are less sensitive to their positions with respect to the laser focus as discussed in Sec. 4.2.

4.4 Pressure induced phase mismatch

The phase mismatch $\Delta k_{q,el}$ in Eq. (1.9) due to free electrons and $\Delta k_{q,at}$ in Eq. (1.10) due to neutral atom dispersion explicitly depend on pressure [144]. $\Delta k_{q,el}$ is always positive, and $\Delta k_{q,at}$ usually is negative for high-energy photons. The two terms can compensate, i.e., add up to near zero, at very low ionization level (about 6% for H15, and 4% for H35) if a 780-nm, 3-cycle (FWHM) laser is applied. On the other hand, gas pressure also induces laser defocusing and blue-shift, thus changes the geometric phase mismatch $\Delta k_{q,geo}$ in Eq. (1.6) and $K_{q,dip}$ in Eq. (1.7). It is difficult to quantify the variations of these values since the laser field undergoes complicated spatial and temporal variation in the medium. In the following, we only illustrate the effect of laser defocusing by changing the confocal parameter b for a

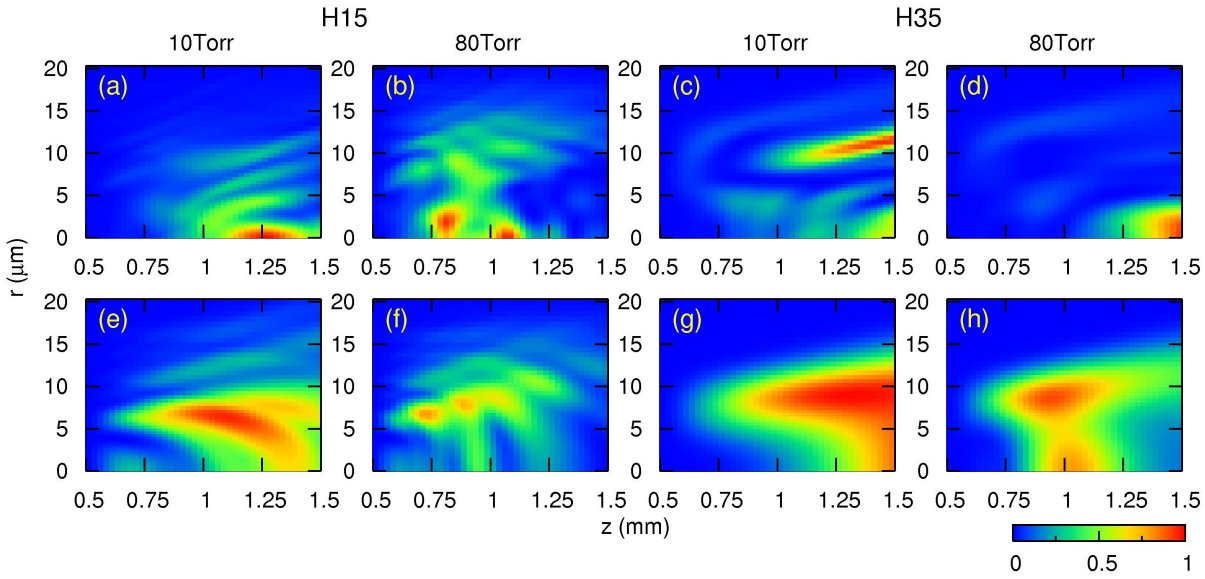

Figure 4.7: *Spatial distributions (normalized) of the harmonic intensity under different pressures (10 Torr and 80 Torr) using tight focusing laser beams. z_0=1 mm (can be read from the z-coordinate). Gas jet is 1-mm wide, and harmonic order is indicated. Upper row: Type-1 Bessel beam; lower row: Gaussian beam (w_0=25 μm). Adapted from Publication [2].*

Gaussian beam.

We first give a rough estimate of phase mismatch caused by the pressure, i.e., $\Delta k_{q,el}+\Delta k_{q,at}$, and $\Delta k_{q,geo} - K_{q,dip}$ due to the laser defocusing. For the tight focusing Gaussian beam, the ionization level (in the end of the laser pulse) is about 12%, thus the values of $\Delta k_{q,el}+\Delta k_{q,at}$ are about 0.5 and 2 mm^{-1} at 10 Torr for H15 and H35, respectively. These values increase to 4 and 16 mm^{-1} at 80 Torr. On the other hand, pressure could induce laser defocusing, i.e., making the confocal parameter b smaller. In Table 4.1, we show $\Delta k_{q,geo}$ and $K_{q,dip}$ as b changes to 3 mm. We can see at 10 Torr, the phase mismatch caused by the laser focusing is dominant, and then becomes comparable to $\Delta k_{q,el}+\Delta k_{q,at}$ at 80 Torr. For Type-1 Bessel and Gaussian beams, the geometric phase and induced dipole phase between the two beams have been shown to be quite different (see Fig. 4.3). With the increase in pressure, their differences still prevail so the harmonic spatial distributions for the two beams behave differently at higher pressure as well. Fig. 4.7 shows the spatial harmonic emissions for Type-1 Bessel and Gaussian beams at two pressures, and they are quite different for the two tightly

focused beams.

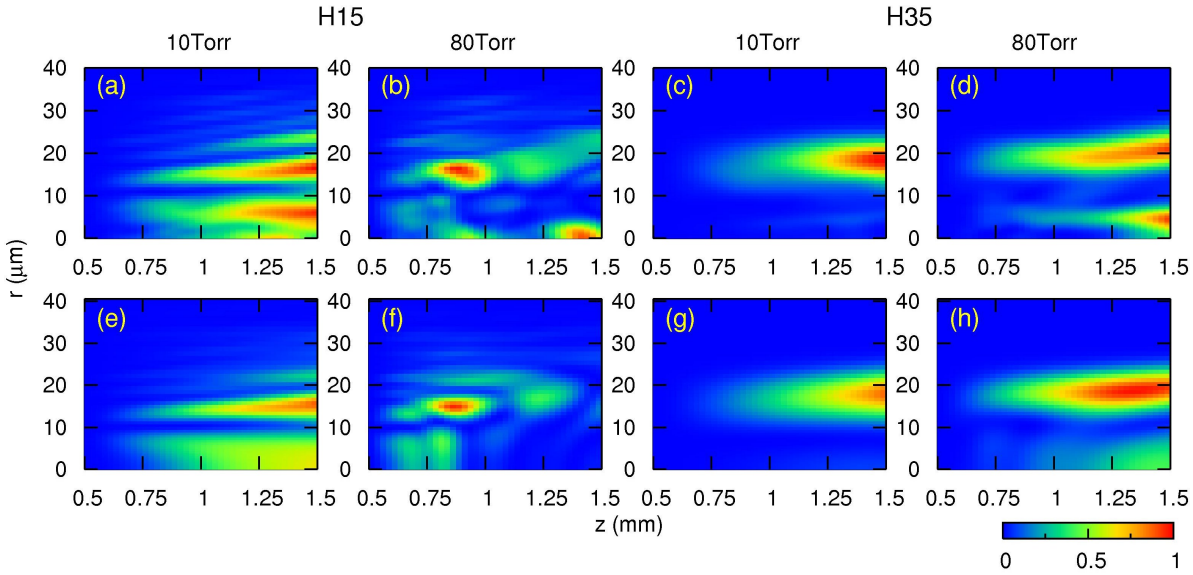

Figure 4.8: *Same as Fig. 4.7 except for the loose focusing laser beams. Upper row: Type-2 Bessel beam; lower row: Gaussian beam (w_0=50 μm). Adapted from Publication [2].*

We carry out a similar analysis for the loosely focused laser beams. The ionization level is found to be about 15% for the loose focusing Gaussian beam, so the values of $\Delta k_{q,el}+\Delta k_{q,at}$ are about 1 and 3.5 mm^{-1} at 10 Torr for H15 and H35, respectively. These values increase to 8 and 28 mm^{-1} at 80 Torr. In Table 4.1, changing b to 15 mm for the Gaussian beam does not change the phase mismatch much. $\Delta k_{q,geo} - K_{q,dip}$ is comparable with $\Delta k_{q,el}+\Delta k_{q,at}$ at 10 Torr, and then $\Delta k_{q,el}+\Delta k_{q,at}$ becomes dominant as the pressure is increased. Fig. 4.8 shows that the spatial harmonic emissions for Type-2 Bessel and Gaussian beams are similar even at moderate pressures.

4.5 Conclusion

In this chapter, we have examined the generation of harmonics in the gas medium for incident intense lasers that have Gaussian or truncated Bessel spatial profiles. We have investigated how the generated harmonic emissions (with the inclusion of propagation effect) depend on the gas-jet position and gas pressure, for tightly and loosely focused Bessel and Gaussian

beams. First we simulated the HHG spectra of Ar reported in Wörner *et al.* [127] using the 780-nm few-cycle pulses. We were unable to reproduce the deep and broad Cooper minimum in the observed HHG spectra of Ar, whether we assumed that the spatial profile was a truncated Bessel beam or a Gaussian beam. However, our simulation was able to reproduce the observed HHG spectra of Ar generated using 1800-nm lasers in Shiner *et al.* [21]. We suggested that additional experiments might be needed to clarify the existing discrepancy for the 780-nm data.

We have also analyzed phase matching conditions for tightly and loosely focused Bessel and Gaussian beams, and have varied the gas-jet position and gas pressure. We have demonstrated that for loosely focused Bessel or Gaussian beams the harmonic growth maps were very similar thus resulting in nearly identical harmonic spectra. For tightly focused beams, the harmonic growth maps were different for Bessel and Gaussian beams, and the resulting HHG spectra differed from each other as well. At higher pressure and/or intensity, phase matching analysis is complicated due to laser defocusing and blue shift as the laser intensity changes in the gas medium. To probe atomic or molecular electronic structure using HHG, harmonics generated from loosely focused beams are preferable since the spectra would be less sensitive to gas-jet location and other experimental parameters. For tightly focused beams the harmonic spectra are very sensitive to experimental conditions such that the comparison of theoretical simulation with experiment is less straightforward since experimental parameters are not all generally well specified.

Chapter 5

Generation of an isolated attosecond pulse in the far field by spatial filtering with an intense few-cycle mid-infrared laser

Figures and most paragraphs in this chapter are adapted from Publication [7].

5.1 Introduction

As discussed in Sec. 1.4.1, high-order harmonic generation (HHG) has been widely used for the production of attosecond pulses in the extreme ultraviolet (XUV) [16, 46, 145]. Due to its great potential for probing ultrafast electronic processes, there is a plethora of techniques for the production of an isolated attosecond pulse (IAP), with the idea that harmonics be generated from half an optical cycle only in a few- or multi-cycle infrared laser pulse as discussed in Sec. 1.4.1. Since the harmonic field generated by all atoms within the laser focus co-propagates with the fundamental laser field in the gas medium, as well as possible further propagation in the free space depending on the experimental setup, any methods using HHG to generate the IAP also need to take into account the effects of macroscopic propagation of fundamental and harmonic fields. As demonstrated in Chapters 3 and 4, these effects have been well taken care by using the well-established propagation theory with the quantitative rescattering (QRS)-based single-atom induced dipoles, the phase of the

harmonics which is inevitably involved in the propagated harmonic field plays an essential role for the attosecond pulse generation. In this chapter, we will focus on the generation of the attosecond pulses, which allows us to test the phase of harmonics in the previous studies as well.

Recently, Xe has become a favorite candidate for generating an intense IAP [146], studying phase-matching effects in the generation of high-energy photons [147], and probing the multi-electron dynamics with high-harmonic spectroscopy [21]. Ferrari *et al.* [146] reported the generation of a high-energy 160-as IAP using low-order harmonics of Xe from a CEP-stabilized laser. They used very high laser intensity and very dilute gas so that the fundamental field was not severely distorted, but the ground state of atom was depleted very quickly in the leading edge of the laser pulse. Only low-order harmonics emitted within one half cycle were used to obtain an IAP. Shiner *et al.* [21] used a 1.8-μm laser with a duration of less than two optical cycles to obtain the HHG spectra of Xe up to the photon energy of 160 eV. They have shown that HHG spectra exhibited strong enhancement above about 90 eV. This enhancement is well-known in photoionization (PI) of Xe due to the presence of a strong shape resonance from the $4d$ shell which, through the channel coupling, modifies the partial PI cross section of the $5p$ shell of Xe – a feature attributed to many-electron effects. According to QRS theory, such enhancement is anticipated since partial photorecombination (PR) cross section (related to photoionization) enters directly in the laser-induced dipole. To simulate HHG spectra at high-photon energies, multi-electron effects on the laser-induced dipoles thus have to be included. Using such dipoles in the QRS model, we simulate the HHG spectra of Xe generated by 1.8-μm lasers by including the macroscopic propagation effects.

In this chapter, mostly we aim at understanding the HHG spectra of Xe observed experimentally in Publication [5], which show nearly continuous photon energy distributions (to be called continuum structure) at high laser intensities. Such continuum spectra have also been observed in molecules, like NO (see Publication [5]). From our simulation, we wish

to demonstrate whether IAPs are generated by these harmonics. For this, we demonstrate how to select different ranges of harmonics to synthesize an IAP by using a spatial filter in the far field. This approach is different from that in Ferrari *et al.* [146], but similar to the analysis in Gaarde *et al.* [148]. In Sec. 5.2, we briefly summarize the QRS theory including multi-electron effects and present the calculated HHG spectra of Xe with a mid-infrared laser. In Sec. 5.3, we show the spatiotemporal electric field of fundamental laser pulse. In Sec. 5.4, we first give the wavelet theory for the time-frequency analysis, and then plot the near- and far-field harmonics in time domain using this technique. In Sec. 5.5, we demonstrate the IAP generation in the far field by synthesizing harmonic orders from 40 to 80 (H40-H80) and H90-H130. A study of carrier-envelope phase (CEP) dependence of IAP presented in Sec. 5.6 concludes that it is still possible to obtain an IAP even by using a laser where the CEP is not stabilized. We also compare attosecond pulses calculated using the QRS and the SFA in Sec. 5.7. A short summary in Sec. 5.8 concludes this chapter.

5.2 Macroscopic HHG spectra of Xe using an 1825-nm few-cycle laser

5.2.1 Photorecombination dipole moment of Xe in QRS theory

The single-atom induced dipole moment $D(t)$ in Eq. (2.53) is obtained by the QRS theory. In energy (or frequency) domain, $D(\omega) = W(\omega)d(\omega)$, where $d(\omega)$ is the PR transition dipole moment and $W(\omega)$ is the microscopic wave packet. In QRS theory, $W(\omega)$ is determined by the laser field and can be accurately calculated based on the strong-field approximation (SFA), and $d(\omega)$ is the transition dipole between the initial and final states of PR or PI. When the multi-electron effect is not important, $d(\omega)$ can be calculated using the single-active electron (SAE) approximation. However, the transition dipole is easily generalized to include many-electron effects, as routinely done in PI theory of atoms and molecules. Thus to include many-electron effects in $d(\omega)$, multi-channel calculations such as many-body perturbation theory, close-coupling method, R-matrix method, random-phase approximation, and many

others can all be employed for such purpose. Since PI of Xe has been well studied, we obtain $d(\omega)$ in this chapter semi-empirically. The major many-body effect for PI of Xe from $5p$ shell occurs at photon energy where $4d$ shell is open. Thus below about 60 eV, the transition dipole from $5p$ can be obtained from a single-electron model. This gives the magnitude and phase of the transition dipole. At higher energies, the effect from the $4d$ shell on the transition dipole of $5p$ becomes important since PI cross section of Xe from $4d$ has a large and broad shape resonance around 100 eV. The inter-shell coupling will enhance $d(\omega)$ for $5p$ near and above 90 eV. Such enhancement has been calculated in Kutzner *et al.* [149] using the relativistic random-phase approximation (RRPA). In our calculation, the phase of $d(\omega)$ is taken from the $5p$ shell under the SAE approximation while the magnitude is taken from Ref. [149]. This approximation does not change the temporal structure of attosecond pulses (will be shown in Sec. 5.7) since the phase of $D(\omega)$ is dominated by the phase of the wave packet $W(\omega)$. We comment that in QRS the induced dipole is given in the energy domain, thus the calculation is similar to the time independent theory used in PI which has been well-established in the last 30 years.

5.2.2 Macroscopic HHG spectra of Xe at low and high intensities

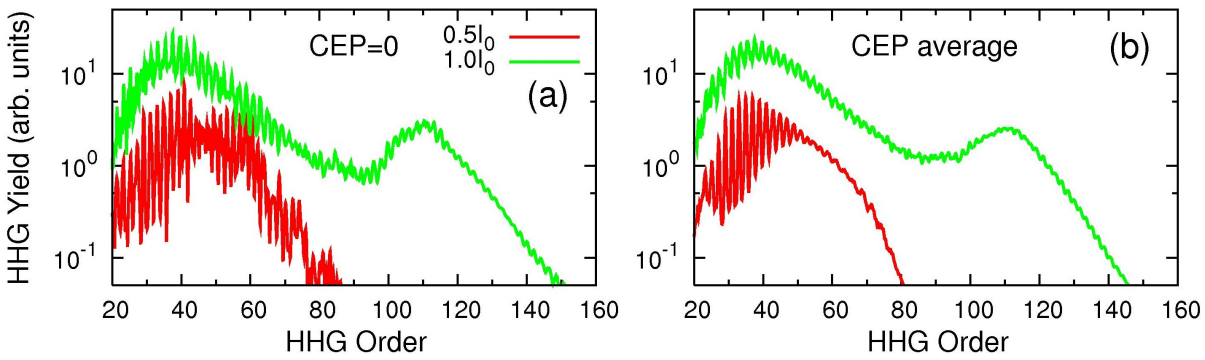

Figure 5.1: *Macroscopic HHG spectra of Xe in an 1825-nm laser, for (a) CEP=0 and (b) CEP averaged. Laser intensities are indicated in units of I_0=10^{14} W/cm^2. See text for additional laser parameters and the experimental arrangement. Adapted from Publication [7].*

HHG spectra of Xe extended to the photon energy of over one hundred electron volts using 1.8-μm lasers with the pulse duration of few optical cycles have been reported recently [21] (also see Publication [5]).

In Fig. 5.1, we show the calculated HHG spectra of Xe exposed to a 14-fs (FWHM), 1825-nm laser. The laser beam waist is 100 μm. A 1-mm-long gas jet with the pressure of 30 Torr is placed at the laser focus. The harmonics are detected after a slit with a width of 190 μm and placed 455 mm behind the focus. These parameters are chosen to be close to those in the experiment of Trallero-Herrero *et al.* (see Publication [5]). For the present purpose we analyze HHG spectra obtained from our theoretical simulations at two laser peak intensities 0.5×10^{14} W/cm^2 and 1.0×10^{14} W/cm^2, which are below and above the critical intensity for Xe at $\sim 0.87\times10^{14}$ W/cm^2 [98], respectively. Here the critical intensity is defined with respect to the static electric field where an electron can escape over the top of the field-induced potential barrier classically.

We show the macroscopic HHG spectra for CEP=0 in Fig. 5.1(a). The two laser intensities present different characteristics of harmonics. For the low intensity, the harmonics are very sharp, i.e., the valley between the neighboring odd harmonics is very deep. At high intensity, the valley is very shallow, i.e., the spectrum shows a continuum structure. Furthermore, the harmonics are not exactly at odd orders due to the blue shift of the fundamental field. Note that the spectrum rises above about H90 is due to the inter-shell or many-electron effects discussed in Sec. 5.2.1. Since a few-cycle laser pulse is applied, the HHG spectra have a strong CEP dependence. In Fig. 5.1(b), we show the CEP averaged HHG spectra. The main characteristics of harmonics remain the same except that the harmonic spectra are much smoother. The CEP is fixed at zero in the following sections unless otherwise stated.

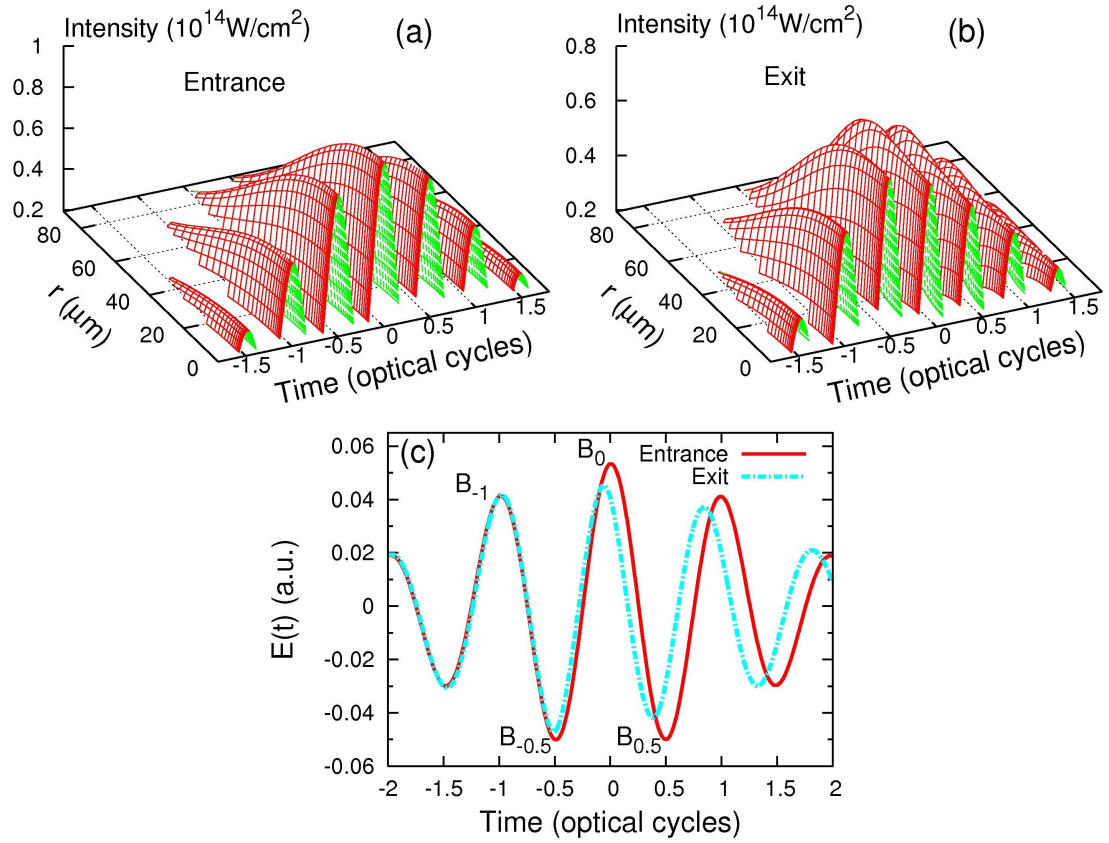

Figure 5.2: *Spatiotemporal intensity profile of the fundamental laser pulse at (a) the entrance and (b) the exit of Xe gas jet. Laser intensity at the focus is 1.0×10^{14} W/cm^2 (assumed in the vacuum) and CEP=0. (c) Evolution of the on-axis electric field at the entrance (solid line) and the exit (dot-dashed line). The laser field becomes chirped during the propagation. For sub-cycle dynamics analysis, we use the label B_t, with t=-1, -0.5, 0, and 0.5 (in units of optical cycles) to indicate the approximate half-cycle where the electron is born. Note that t is defined within the half cycle only. Adapted from Publication [7].*

5.3 Spatiotemporal evolution of fundamental laser field

To understand the different spectral features in Fig. 5.1, we inspect the fundamental field in the ionizing medium. The spatiotemporal intensity profile and on-axis electric fields of the laser pulse at the entrance and the exit of the gas jet are shown in Fig. 5.2. The laser peak intensity is 1.0×10^{14} W/cm^2, which would give an ionization probability of $\sim$ 35% at the end of laser pulse for Xe according to an empirical ADK formula in barrier-suppression regime [98]. While the electric field at the entrance has a good Gaussian shape both in time and

space, it is strongly reshaped during the propagation in the ionizing medium. At the exit it shows positive chirp in time (blue shift in frequency) [see Fig. 5.2(c)] and defocusing in space [see Fig. 5.2(b)]. We have also checked the fundamental field with laser peak intensity of 0.5×10^{14} W/cm^2. It always maintains Gaussian spatial distribution and there is no blue shift because the ionization probability is very low. The reshaping of the fundamental field at high intensity is responsible for the continuum structure in the HHG spectra in Fig. 5.1. Note that similar results have been obtained by Gaarde *et al.* [45] using a 750-nm laser interacting with Ne gas.

5.4 Time-frequency representation of high harmonics

5.4.1 Wavelet analysis of attosecond pulses

A time-frequency representation (TFR) (or spectrogram) of the harmonic field $E_{\rm h}(t)$ is a simultaneous representation of the temporal and spectral characteristics of the harmonics. We perform the time-frequency analysis in terms of the wavelet transform of the harmonic field [150–153]:

$$A(t,\omega) = \int E_{\rm h}(t')w_{t,\omega}(t')dt', \tag{5.1}$$

with the wavelet kernel $w_{t,\omega}(t') = \sqrt{\omega}W[\omega(t'-t)]$. We choose the Morlet wavelet [150]:

$$W(x) = (1/\sqrt{\tau})e^{ix}e^{-x^2/2\tau^2}. \tag{5.2}$$

The width of the window function in the wavelet transform varies as the frequency changes, but the number of oscillations (proportional to τ) within the window is held constant. The dependence of $A(t,\omega)$ on the parameter τ has been tested. The absolute value of $A(t,\omega)$ depends on τ, but the general temporal pattern does not change much. In this chapter, we choose $\tau = 15$ to perform the wavelet transform.

Harmonics emitted at the exit plane (near field) of the medium act as a source for the far-field harmonics. In order to avoid the complexity of the harmonic spatial distribution in

the near field (see Fig. 4 in Publication [11]), we calculate $A(t,\omega)$ for each radial point in the near field and then integrate over the radial coordinate [152]:

$$|A_{\text{near}}(t,\omega)|^2 = \int_0^\infty 2\pi r dr \left| \int E_{\text{h}}(r,t')w_{t,\omega}(t')dt' \right|^2. \tag{5.3}$$

To demonstrate the divergence of harmonics, we preform the TFR for each radial point in the far field.

The spectral filter used to select a range of harmonics (ω_1 - ω_2) could affect the generation of attosecond pulse trains (APTs) or IAPs. Theoretically we can obtain the total intensity of an APT or an IAP in the near field as following [11]:

$$I_{\text{near}}(t) = \int_0^\infty 2\pi r dr \left| \int_{\omega_1}^{\omega_2} E_{\text{h}}(r,\omega)e^{i\omega t}d\omega \right|^2. \tag{5.4}$$

In the far field, a spatial filter is used to select the harmonics in a prescribed area. In this chapter, we assume that the filter is circular with a radius r_0, and is perpendicular to the propagation direction of harmonics. The intensity of an APT or an IAP in the far field is

$$I_{\text{far}}(t) = \int_0^{r_0} 2\pi r dr \left| \int_{\omega_1}^{\omega_2} E^{\text{f}}_{\text{h}}(r,\omega)e^{i\omega t}d\omega \right|^2. \tag{5.5}$$

5.4.2 Time-frequency analysis of harmonics in near and far fields

As shown in Eq. (1.8), for each harmonic order q, the phase can be expressed as $\varphi_i^q(r,z,t) = -\alpha_i^q I(r,z,t)$, where $I(r,z,t)$ is the spatiotemporal intensity of the fundamental laser field. The proportional constant $\alpha_{i=S,\ L}$ depends on "short" (S) or "long" (L) trajectories. The phase can also be expressed in terms of the ponderomotive energy U_p and the electron excursion time τ_i^q: $\varphi_i^q \approx -\beta_i U_p \tau_i^q$ [154], where the coefficient β_i for the "short" trajectory is much smaller than for the "long" trajectory. The electron excursion times for the two trajectories are $\tau_S^q \approx T/2$ and $\tau_L^q \approx T$ (T is the laser period) [38]. It shows that the phase grows with the cubic power of the wavelength. The curvature of the phase front caused by the radial variation $\partial\varphi_i^q(r)/\partial r$ makes the harmonic beam divergent. The divergence of "short"- or "long"-trajectory harmonic is determined by either $\Delta\alpha_i^q$ or $\Delta I(r)$.

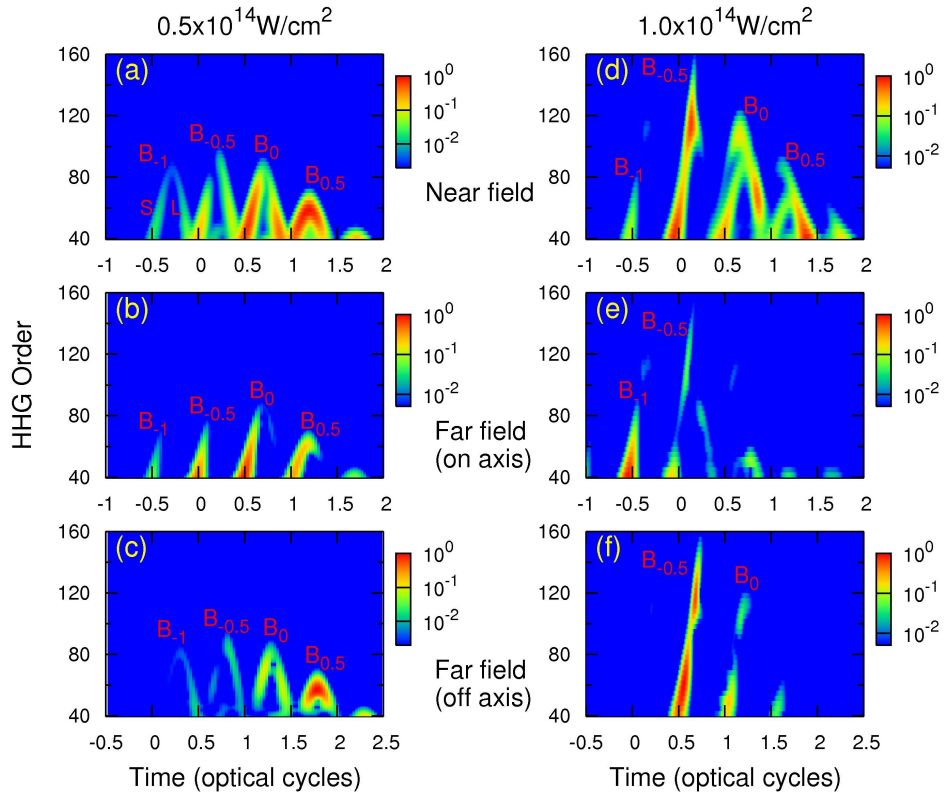

Figure 5.3: *Top row: Time-frequency representation (TFR) of harmonics in the near field. Middle row: TFR for on-axis (r=0 mm, divergence: 0 mrad) harmonics in the far field. Bottom row: TFR for off-axis (r=1 mm, divergence: 2.2 mrad) harmonics in the far field. Far-field position is at z=455 mm, and laser intensity (CEP=0) along each column is indicated. Electrons are released at each half cycle, labeled by B_t, with t=-1, -0.5, 0 and 0.5 as in Fig. 5.2. For each B_t, electrons can follow a "short" (S) or "long" (L) trajectory to recombine with the ion to emit harmonics. For each harmonic, the emission time can be read from the time axis. For each B_t, the emission time for each off-axis harmonic is delayed with respect to the corresponding on-axis harmonic, e.g., compare (b) vs (c), and (e) vs (f). All the TFRs have been normalized. Adapted from Publication [7].*

1. Harmonics in the near field

The TFR, $|A_{\rm near}(t,\omega)|^2$, calculated from Eq. (5.3), are shown in Figs. 5.3(a) and (d) for harmonics above H40 at two laser intensities, collected at the exit face of the gas jet (near field). In Fig. 5.3(a), the symbols S and L are used to indicate the first (earliest) group of harmonics generated. Here S (L) stands for "short" ("long")-trajectory harmonics that have positive (negative) chirp. These harmonics are from electrons born at t=-1 (in units of

optical cycles), i.e., B_{-1} to indicate born time at t=-1, in the leading edge of the pulse [see Fig. 5.2(c)]. In the following, the electron born time t (in units of optical cycles) is indicated by B_t in the figure, while the harmonic emission time is read off from the horizontal axis of the figure, one for the "short", and the other for the "long" trajectory. In this chapter the time is always defined in moving coordinate frame (also see Publication [11]). At the low intensity in Fig. 5.3(a), we can see that both S and L contribute to harmonics generated from electrons born at t=-1, -0.5, 0 and 0.5. In other words, harmonics are generated by electrons born over four half cycles. Note that Tate *et al.* [29] have shown that harmonics generated by mid-infrared lasers had large contributions from electron trajectories even longer than the "long" trajectories in single-atom response, which has also been confirmed in our calculation (not shown). But these trajectories are all eliminated during the propagation in the medium since their phases are very large. For low intensity, the propagation in the medium cannot eliminate contributions from "long" trajectories.

The same TFR analysis for the high intensity is shown in Fig. 5.3(d). Higher harmonic cutoff from each burst is easily seen since the intensity is twice higher. Comparing to Fig. 5.3(a), there are no contributions to the harmonics from the "long" trajectories for electrons born at t=-1 and -0.5, i.e., from the leading edge of the pulse. Since the laser intensity is twice higher, the phase of each harmonic is also twice higher (also see Fig. 17 in Ref. [155] and Fig. 1(A) in Ref. [35]), thus resulting in cancelation of contributions from the "long" trajectories. For electrons born at the falling edge of the pulse, due to the blue shift (thus shorter wavelength) and reshaping (thus lower intensity) the phases of harmonics due to the "long" trajectories are smaller and they can survive after propagation in the medium, for example, for electrons born at t=0, and 0.5, see Fig. 5.3(d).

2. On-axis harmonics in the far field

In Fig. 5.3(b), the TFR is shown for r=0 mm in the far field (455 mm after the laser focus). At low intensity, the emission from "short" trajectories born at different times have the similar small divergence, and after propagation in free space they all survive along the axis

in the far field. Interference between "short"-trajectory harmonics from each half cycle leads to enhancement in odd harmonics and suppression in even harmonics (see Fig. 18 in Ref. [13]), and resulting in a big contrast between an odd harmonic and neighboring harmonics shown in Fig. 5.1(a) for the spectra obtained with a slit. At high intensity, only harmonics from the "short"-trajectory electrons born at t=-1 survive (the next one at t=-0.5 is much weaker), see Fig. 5.3(e). This would result in a nearly continuum spectra and a potential for generating an isolated attosecond pulse.

3. Off-axis harmonics in the far field

In Figs. 5.3(c) and (f), the TFR is shown for r=1 mm (divergence: 2.2 mrad) in the far field. Each off-axis burst has an obvious time delay with respect to the on-axis burst because it travels a longer distance in free space. At low intensity, harmonics from "long" trajectories appear on each burst since they have large divergence [see Fig. 5.3(c)]. At high intensity, the "short" trajectories contribute to bursts $B_{-0.5}$ and B_0 [see Fig. 5.3(f)]. They appear to come from the pulse reshaping, see Fig. 5.2(b) showing laser peak intensity shifting to region away from the propagation axis. They experience larger $\Delta I(r)$ with respect to "short"-trajectory electrons born at B_{-1} at the leading edge. Fig. 5.3(f) shows that a continuum spectra from a "short" trajectory is generated for electrons born at t=-0.5.

Note that attochirp (emission time varying with harmonic order) [35, 156] of "short"- or "long"-trajectory harmonics exists even after propagation. They may be compensated using a "plasma compressor" [35] because free electrons induce a negative group velocity dispersion, or by thin filters with linear negative group velocity dispersion [34]. But attochirp is inversely proportional to laser wavelength [33]. This implies that one can select a broad range of harmonics to synthesize a short attosecond pulse using an 1825-nm laser (will be shown next). The harmonic emission of "short" trajectory in the far field in Figs. 5.3(e) and (f) varies with time or radial distance. This provides the possibilities to generate IAPs using the different ranges of harmonics on or off axis. We will only show the spectral and spatial filters applied on axis in the far field in the following.

5.5 Spectral and spatial filtering in generation of attosecond pulses

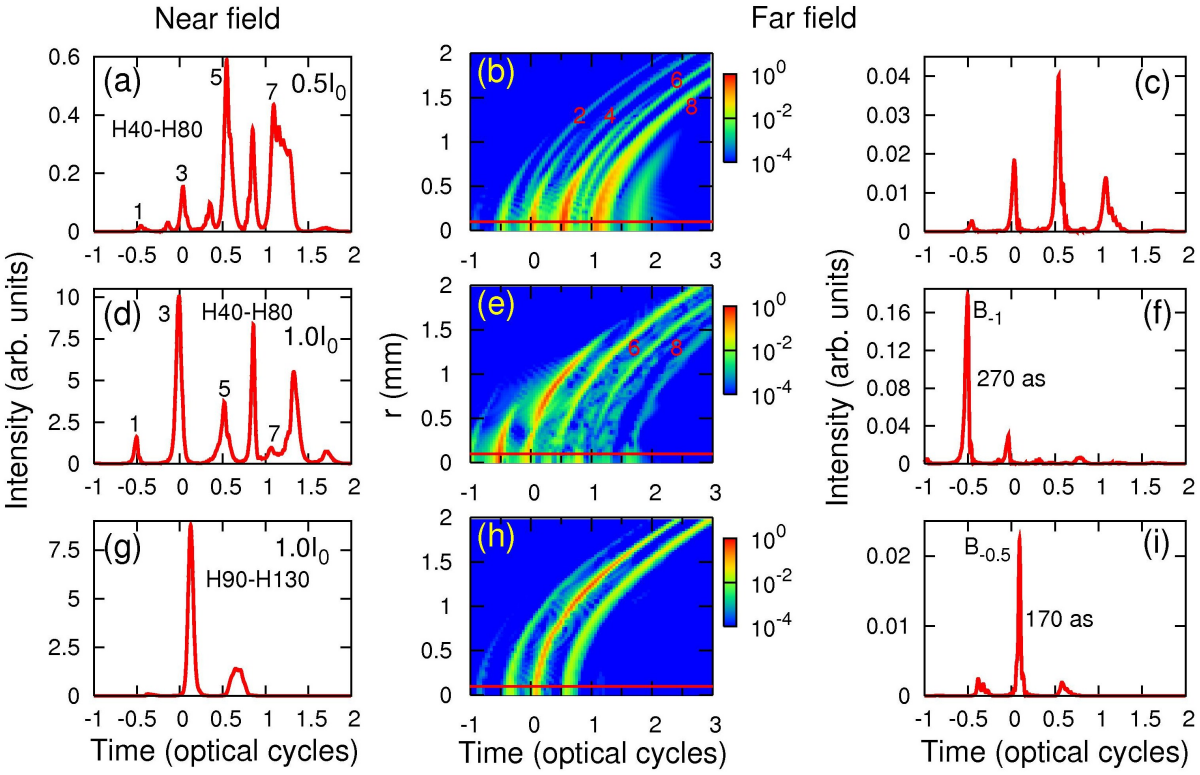

Figure 5.4: *First column: Intensity (or envelope) of attosecond pulses in the near field, synthesized from the harmonics and the laser intensity shown in each frame. Laser intensities are given in units of I_0=10^{14} W/cm^2. In (a) and (d), odd bursts ("short" trajectories) are labeled. Even bursts due to "long" trajectories are not labeled for brevity. Middle column: Spatial distribution (normalized) of attosecond pulses in the far field (z=455 mm). Notice that even bursts ("long" trajectories) have large divergence, or at large r. The odd bursts (not labeled) have smaller divergence. There is a time delay between off-axis attosecond pulses compared to on-axis ones. Last column: Intensity of attosecond pulses in the far field using a spatial filter with a radius r_0=100 μm (shown by the solid line in red in each middle-column frame). Adapted from Publication [7].*

A spectral filter is usually used to synthesize attosecond pulses. In this section we also study how the attosecond pulses are manipulated through spatial filtering. Fig. 5.4(a) displays the intensity profile of an XUV light by synthesizing H40-H80 at the near field generated by laser intensity of 0.5×10^{14} W/cm^2. The intensity of the attosecond pulses

$I_{near}(t)$ is calculated by using Eq. (5.4). The time-frequency analysis of these harmonics has been given in Fig. 5.3(a). Besides attosecond bursts occurring at each half optical cycles, which can be attributed to harmonics resulting from "short" trajectories, we observe other pulses in between which are attributed to contributions from "long" trajectories. The main peaks from the "short" trajectories are labeled by 1, 3, 5 and 7 in the figure, while those in between (2, 4, 6 and 8 are not labeled) are from "long" trajectories. The attosecond pulses thus generated show a poor periodicity in time, see Fig. 5.4(a).

If the XUV light is synthesized at the far field, in particular, by introducing a spatial filter, then it may be possible to remove harmonics resulting from the "long" trajectories. In Fig. 5.4(b), the intensity distributions of the synthesized light in space in the far field are shown. They are obtained from the near-field harmonics by further propagation in free space. The peaks 2, 4, 6 and 8 [not shown in Fig. 5.4(a) explicitly] are attributed to "long" trajectories. They are indicated in Fig. 5.4(b) showing that they are distributed far from the propagation axis. By using a spatial filter (indicated by a solid line in red, with a radius r_0=100 μm) to select harmonics generated near the axis only, as shown in Fig. 5.4(c) by using Eq. (5.5) to calculate $I_{far}(t)$, well-behaved APTs are then obtained. We comment that the time delay between off-axis and on-axis harmonics leads to the curved spatial distribution in Fig. 5.4(b), and it can be understood mathematically since each harmonic behaves like a Gaussian beam, and the geometric phase of each harmonic is proportional to r^2 along the transverse direction (see Fig. 4 in Publication [11]). The traveling distance of off-axis harmonics can be compensated using a reflecting mirror to refocus the harmonic beam or by a detector with a curved surface. In principle, this compensation becomes important to reduce the duration of attosecond pulses when a spatial filter with a large radius is applied. In this chapter, the radius of the spatial filter is chosen to be small enough to avoid this curvature effect.

Next we use the same range of harmonics (H40-H80) generated by the laser intensity of 1.0×10^{14} W/cm^2 to synthesize attosecond pulses in the near field. Referring to Fig. 5.3(b),

the "short" trajectories dominate the harmonic generation in the leading edge of the laser, while the "long" trajectories dominate the harmonic generation in the falling edge. The synthesized XUV light, shown in Fig. 5.4(d) indeed reflects this point where the first two peaks occur at multiples of half optical cycles, while the last four peaks are not. In Fig. 5.4(e), the spatial distribution of the synthesized XUV light in the far field indeed supports this description. By using a spatial filter (indicated by a solid line in red, with a radius r_0=100 μm) to select only "short" trajectories, as shown in Fig. 5.4(f), a nice IAP with a duration of 270 as is obtained, accompanied by a weak sub-pulse with a much weaker intensity. This demonstrates the generation of IAPs using spatial filtering. A similar mechanism of IAP generation has been proposed by Strelkov *et al.* [157, 158] using the harmonics in the plateau region generated by the Ar gas with very high pressure.

The TFR in Fig. 5.3(e) shows considerable on-axis emission above H80 at burst $B_{-0.5}$. We use H90-H130 to generate attosecond pulses in the near field in Fig. 5.4(g). Both bursts have considerable contributions from "short" trajectories. In the far field [see Fig. 5.4(h)], they show different divergences as discussed before. Finally, we obtain an IAP with a duration of about 170 as in Fig. 5.4(i) with a spatial filter. The intensity of the IAP is about 1/8 as that in Fig. 5.4(f) due, not only to the larger divergence of "short"-trajectory harmonics born at $B_{-0.5}$ than at B_{-1}, but also the lower harmonic intensity of H90-H130 than that of H40-H80. On the other hand, the duration of the IAP is decreased. Similar mechanism of IAP generation has been proposed by Gaarde *et al.* [45, 148] using harmonics in the cutoff region by a 750-nm laser exposed on Ne gas.

5.6 CEP dependence of isolated attosecond pulses

The selection of an IAP by a spatial filter in the far field discussed above is only for a single CEP, and thus only useful if the laser is CEP-stabilized (has not been achieved for 1.8-μm lasers yet). To check if the method can be used for lasers that are not CEP-stabilized, we investigate the CEP dependence of the IAP generation.

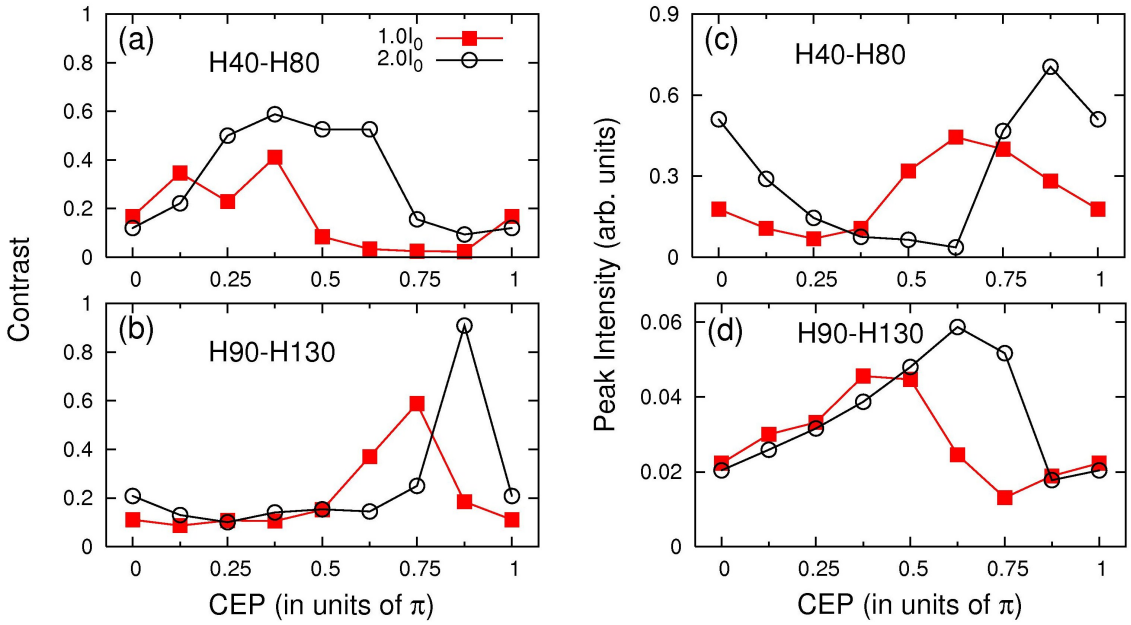

Figure 5.5: *(a) and (b): The contrast ratio between intensities of the strongest satellite and the main attosecond burst, (c) and (d): The peak intensity of the main attosecond burst as a function of CEP. Laser intensities are shown in units of* I_0*=*10^{14} *W/cm*^{2}*. Harmonics used to generate an IAP are labeled. Far-field position: z=455 mm, and the radius of the spatial filter:* r_0*=100 μm. Adapted from Publication [7].*

In Figs. 5.5(a) and (b), we show the contrast ratio between the intensities of the strongest satellite and the strongest attosecond burst, and in Figs. 5.5(c) and (d), we show the peak intensity of the strongest attosecond burst, as the CEP is varied, for the two laser intensities indicated. A good IAP is to have high peak intensity for the main peak and weak satellites. From Figs. 5.5(c) and (d), we note that at the CEP's where the strongest attosecond bursts have high peak values, the contrast ratios shown in Figs. 5.5(a) and (b) at these CEP's are always small. In the meanwhile, when the contrast ratio is large, the strongest attosecond burst is always weak. Thus it is possible to generate single attosecond pulses even when the CEP of the driving laser is not stabilized. This explains the success why the first single attosecond pulses were generated using few-cycle laser pulses that were not phase-stabilized [159].

5.7 Comparison between QRS and SFA in modeling propagation effects

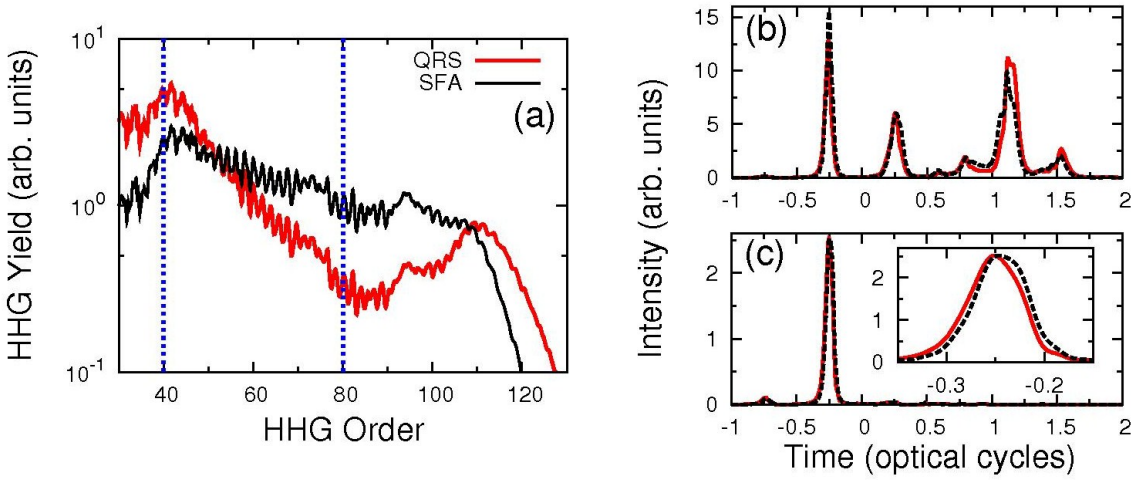

Figure 5.6: *Comparison of HHG spectra and attosecond pulses calculated using QRS and SFA for single-atom induced dipoles. (a) Macroscopic HHG spectra (total spectra without using a slit) of Xe by QRS [red (dark gray) line] and SFA [black (light gray) line]. Laser parameters: I=1.0×10^{14} W/cm^2 and CEP=$\pi/2$. Intensity of attosecond pulses (b) in the near field, and (c) in the far field (z=455 mm) using a spatial filter with a radius r_0=300 μm: QRS [red (solid) lines] vs SFA [black (dashed) lines]. Inset in (c): enlarged temporal structure of an IAP. The spectra are normalized at the peak intensities in (c). The same normalization factor is used in (a) and (b). H40-H80 are used to synthesize attosecond pulses. Adapted from Publication [7].*

In the last two decades, the strong-field approximation (SFA), which is in the frame of the SAE approximation, has been widely used to predict the temporal structure of attosecond pulses even though SFA is unable to explain the observed harmonic spectra precisely in general. In the present calculation, we use QRS in the propagation calculation. For single-atom response, QRS has been tested against TDSE, both for the magnitude and phase, as documented in Le *et al.* [96], for example. In QRS, the wave packet is obtained from SFA, including the phase. The transition dipole $d(\omega)$ also introduces a phase. In SFA, this phase is a constant, either real or pure imaginary (depending on the symmetry of the ground state) and independent of the harmonic order. In QRS, the transition dipole moment is a

complex number in general. From PI theory, however, it is known that the phase of the transition dipole does not change much with the photon energy. Thus the phases of the harmonics calculated from QRS and SFA do not differ significantly. Since the phases of the harmonics are much more important in synthesizing attosecond pulses [41], this explains why propagation theory based on SFA has been so successful in explaining the generation of attosecond pulses, in spite of its failure in predicting or explaining the observed harmonic spectra. In this section, we support this analysis with actual results from simulations.

In Fig. 5.6(a) the HHG spectra of Xe obtained from SFA (within the SAE approximation) and QRS (including multi-electron effects) using the laser parameters given in the captions are shown. Clearly the spectra differ greatly. In Figs. 5.6(b) and (c) the synthesized (H40-H80) attosecond pulses at the near field and the far field are shown. Clearly the results from the two calculations are essentially identical (after an overall normalization), in spite of the large differences in the harmonic spectra. We have checked some other cases and found that the temporal structures of the attosecond pulses from the two theories were always very similar. Larger differences than those shown in Figs. 5.6(b) and (c) are expected if a wider range of harmonics are used or if the spectra from the two theories differ much more, but the general conclusion is correct.

5.8 Conclusion

In this chapter, we have studied the generation of isolated attosecond pulses (IAPs) using few-cycle mid-infrared lasers at high intensities near and above the critical intensity of Xe. The calculations are based on the QRS theory where many-electron effects are included in the single-atom induced dipole moment; specifically, by including the coupling of the inner $4d$ shell of Xe in the partial $5p$ photorecombination transition dipole matrix element. The effect of the medium on the fundamental and harmonic fields is obtained by solving the Maxwell's wave equations. The modification (or reshaping in space and time) of the fundamental field is due to its nonlinear interaction with the medium includes dispersion,

plasma effect, and Kerr nonlinearity. We have investigated the spatiotemporal evolution of the fundamental laser field in detail, and found that its reshaping is responsible for the continuum structure in the HHG spectra. This conclusion is carried out in terms of the time-frequency analysis of harmonics in the near and far fields.

Since the divergence of harmonic emission from different half cycles is varied due to the blue shift and defocusing of the fundamental laser pulse (or complicated reshaping), we have shown that isolated attosecond pulses can be generated by synthesizing H40-H80 or H90-H130, selected by a spatial filter centered on the propagation axis in the far field. The mechanism of IAP generation in this chapter could be called as "ionization gating". It works for a loosely focused laser at high laser intensity (above the critical intensity), which is reshaped as it propagates through the medium with a moderate gas pressure. A similar approach has been discussed by Gaarde *et al.* [45, 148] using a 750-nm laser interacting with 135-Torr Ne gas. Our studies have shown that it could reshape the fundamental laser field using a long-wavelength laser with a moderate gas pressure ($\sim$ 30 Torr). The extended harmonic cutoff of Xe leads to a broad range of harmonics available for IAP generation. This approach is also different from Ferrari *et al.* [146] where low harmonics ($\sim$ 30 eV, which is equivalent to H40 in this chapter) are used to generate the IAP. In addition, we have shown that the method is very robust and an IAP can be generated even if the laser CEP is not stabilized.

Chapter 6

Effects of macroscopic propagation and multiple molecular orbitals on the high-order harmonic generation of aligned N_2 and CO_2 molecules

Figures and most paragraphs in this chapter are adapted from Publication [4], [8] and [9].

6.1 Introduction

As discussed in Sec. 1.4.2, high-order harmonic generation (HHG) has been employed to probe the electronic structure of molecules on an ultrafast time scale recently [65, 66, 102, 124, 160]. Actually the last step in the HHG process - "recombination" is the inverse of photoionization. Any spectral features in the photoionization cross section (PICS) would thus be embodied in the HHG spectrum as well. Since molecules can be impulsively aligned by a laser field [73], the observation of HHG from aligned molecules further offers the opportunity for probing PICSs from aligned molecules that are not generally possible with synchrotron radiation experiments. In addition, the first step of HHG is a highly nonlinear tunneling ionization process which is very selective with respect to the ionization energy of the molecular orbital from which the electron is removed. Thus HHG in general is dominated by the recombination to the highest-occupied molecular-orbital (HOMO). In contrast, direct photoionization of a molecule is a linear process, where PICSs from the next or next few inner

orbitals could be of comparable importance. For example, for N_2, the HOMO is a σ_g orbital. The next more tightly bound orbital, the HOMO-1, is a π_u orbital with an ionization energy 1.3 eV higher. The HOMO-2, is a σ_u orbital and is 3.2 eV more tightly bound than the HOMO. Calculations by Lucchese *et al.* [99] and experimental results [161, 162] show that for photon energy from the threshold at 15 eV to about 40 eV, the PICS from the HOMO-2 is negligible, but the HOMO-1 PICS is actually comparable with that of the HOMO. The HOMO has a shape resonance that peaks near the photon energy of 29 eV. These are predictions and measurements made on randomly oriented N_2 molecules. How do these features depend on the alignment of molecules? Today the rich structure in PICSs from fixed-in-space molecules predicted by the theory remains mostly unexplored experimentally. Can high-harmonic spectra generated by laser pulses from aligned molecules provide new information that are not yet directly available from photoionization measurements? The answer is yes. McFarland *et al.* [163] reported that HHG from the HOMO-1 dominates over that from the HOMO when the molecules are perpendicularly aligned with respect to the laser polarization. Mairesse *et al.* [164] performed harmonic spectroscopy to characterize the attosecond dynamics of multielectron rearrangement during strong-field ionization.

Among the molecules, CO_2 is another most extensively studied system so far [165–168]. Initially the interest was focused on the observation of the minimum in the HHG spectrum of CO_2 [65, 169, 170]. The positions of the minima from different experiments, however, are often vastly different. For fixed-in-space CO_2 molecules the PICSs of HOMO indeed exhibit minima at small alignment angles. If HHG is generated from HOMO only, then one expects that the position of the minimum does not significantly change with laser intensity. Indeed, strong field ionization depends exponentially on the ionization potential I_p. The HOMO-1 and HOMO-2 orbitals in CO_2 are 4 and 4.4 eV more deeply bound than the HOMO, thus they are not expected to contribute significantly to the HHG spectra. However, it is also well known that tunneling ionization rates depend sensitively on the symmetry of the molecular orbital [171]. The HOMO is a π_g orbital. It means that at small alignment angles the ion-

ization rates are small. For HOMO-2, on the other hand, it is a σ_g orbital, thus it has large ionization rate when CO_2 molecules are parallel aligned. Thus for small alignment angles, HOMO-2 may become important even though it is bound 4.4 eV deeper than the HOMO. (HOMO-1 is a π_u orbital and thus not expected to contribute significantly to the HHG.) The alignment dependence of tunneling ionization rate is usually calculated using molecular Ammosov-Delone-Krainov (MO-ADK) theory [19] (also see Publication [14]) or SFA. For most molecules that have been studied the two models give nearly identical alignment dependence (after normalization). However, this is not the case for CO_2. Experimentally, the alignment dependence of CO_2 ionization reported by Pavičić *et al.* [172] is very narrowly peaked near alignment angle of 46°. It differs significantly from the predictions of MO-ADK and SFA (see Publication [18]). In fact, so far all theoretical attempts [173–176] (also see Publication [16]) have not been able to confirm the sharp alignment dependence reported in the experiment. Furthermore, the observed HHG spectra from aligned molecules are inconsistent with the reported experimental alignment dependence of ionization [103, 118].

Earlier attempts to extract structure information from HHG spectra were based on the two-center interference model [68] and the strong-field approximation (SFA) [85, 86]. Subsequently, a quantitative rescattering (QRS) theory [26, 94, 95] was developed which established that HHG spectra from an isolated molecule can be expressed as the product of a returning electron wave packet with a photorecombination cross section (PRCS). The QRS asserts that the PRCS is independent of the laser parameters, including the wavelength, intensity, and pulse duration. The latter affect the returning electron wave packet only. In the meanwhile, Smirnova *et al.* [65] studied HHG from aligned CO_2 molecules and emphasized the importance of hole dynamics with including multiple orbitals. Within the QRS theory, multiple orbitals can be easily incorporated into the theory and it was first used by Le *et al.* [103] to explain the HHG data by McFarland *et al.* [163]. These theoretical studies were all based on single-molecule calculations. To extract structure information of individual molecules, e.g., the amplitude and phase of photorecombination (PR) transition

dipole from the measured HHG, the propagation effect in the medium should be investigated. For molecular targets, this has not been performed so far. Instead, it was often assumed that HHG was measured under the perfect phase-matching conditions and that the observed harmonics were directly proportional to the harmonics from a single molecule. While such assumptions may be inadequate if accurate structure information of individual molecules is to be extracted from the observed HHG spectra.

In this chapter, we will simulate the measured HHG spectra of random and aligned N_2 molecules, and revisit the issue about the importance of the HOMO-1 contribution raised in Refs. [103, 163, 177]. And then we will check how the famous shape resonance in HOMO PICS of N_2 present in the HHG spectrum. Finally we will simulate the measured HHG spectra of random and aligned CO_2 molecules, and investigate the factors which would change the position of the minimum in the HHG spectra. So far there have been no other theoretical attempts to simulate HHG spectra of molecular targets, which can be compared with measured ones directly. This chapter is organized as follows. In Sec. 6.2, we will show the calculated HHG spectra against measured ones for N_2 molecules being randomly distributed or aligned with pump-probe angle as 0 degree, and the macroscopic wave packet extracted from calculated HHG spectra. In Sec. 6.3, we will discuss how the HOMO-1 contribution present in the HHG spectrum of aligned N_2 molecules with pump-probe angle as 90 degree as laser intensity varies. In Sec. 6.4, we will show the PICS of N_2 from well-established theory, and the shape resonance in the HHG spectra at small alignment angles. In Sec. 6.5, we will simulate the existing HHG spectra of CO_2 molecules, and discuss the origin of the minimum for the aligned cases. In Sec. 6.6, we will investigate carefully how the minimum in the HHG spectrum of aligned CO_2 shifts its position. A short summary in Sec. 6.7 concludes this chapter. Note that in this chapter we are only concerned of the parallel component of HHG along the polarization direction of generating laser.

6.2 HOMO contribution in HHG of random and aligned N_2 molecules

6.2.1 Macroscopic HHG spectra of random and aligned N_2: theory vs experiment

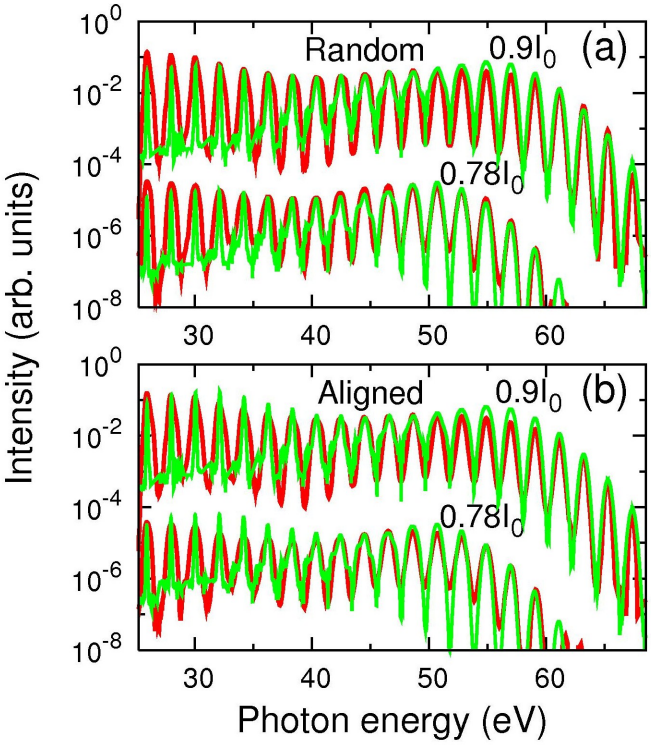

Figure 6.1: *Comparison of HHG spectra from theory (green curves) and experiment (red curves) of Ref. [178], (a) for randomly distributed N_2 and (b) for N_2 aligned along the polarization direction of the generating laser, i.e., pump-probe angle α=0°. The laser intensities are indicated where I_0=10^{14} W/cm^2. See text for additional laser parameters. Adapted from Publication [8].*

HHG spectra from molecules by 1200-nm lasers have been reported for randomly distributed and aligned N_2 recently by Wörner *et al.* [178]. In this section, we report our simulated results for N_2 molecules, at the two peak laser intensities, 0.9 and 1.1×10^{14} W/cm^2, reported in [178]. Experimentally, the laser duration (full width at half maximum, FWHM) is ∼ 44 fs, the beam waist at the focus is ∼ 40 μm, and the length of gas jet is ∼ 1 mm, which is located 3 mm after the laser focus. A vertical slit with a width of 100 μm is placed 24 cm

after the gas jet. To achieve good agreement in the cutoff positions, the intensities (in the center of the gas jet) used in the theory are 0.78 and 0.9×10^{14} W/cm^2 instead, respectively. Since the experiment was carried out at low laser intensity and low gas pressure, the harmonics are propagated without absorption and dispersion effects from the medium, and the fundamental laser field is not modified through the medium as discussed in Sec. 2.3.3. In the theoretical simulation, we first obtain induced dipoles of fixed-in-space molecules using QRS theory (as discussed in Sec. 2.2.3) for different laser peak intensities. The induced dipoles are averaged coherently according to the alignment distribution [see Eq. (2.63)] and then fed into the Maxwell's wave equations.

Fig. 6.1 shows the good overall agreement between the measured and the simulated spectra, for both randomly distributed and aligned N_2. By examining the experimental HHG spectra more carefully, they reveal a shallow minimum at 38 $\pm$ 2 eV (low intensity) and at 41 $\pm$ 2 eV (high intensity) for both aligned and unaligned molecules. The theory also predicts a minimum: for unaligned molecules, the minimum is at $\sim$ 39 eV for low intensity and $\sim$ 40 eV for high intensity. For aligned molecules, the minimum is at $\sim$ 42 eV for low intensity and $\sim$ 44 eV for high intensity. In the experiment, the degree of alignment was estimated to be $\langle\cos^2\theta\rangle$=0.6 - 0.65. In the simulation, an alignment distribution of $\cos^4\theta$ is used. Note that only HOMO is included in the calculation. We believe that this is the first time that HHG spectra from molecules have been calculated including the propagation effect in the medium and the simulated results have been compared directly to the measured spectra.

6.2.2 Separation of photorecombination transition dipole from HHG spectrum

As shown in Sec. 3.5, the macroscopic HHG spectrum for atomic targets can be expressed as

$$S_{\rm h}(\omega) \propto \omega^4 |W'(\omega)|^2 |d(\omega)|^2, \tag{6.1}$$

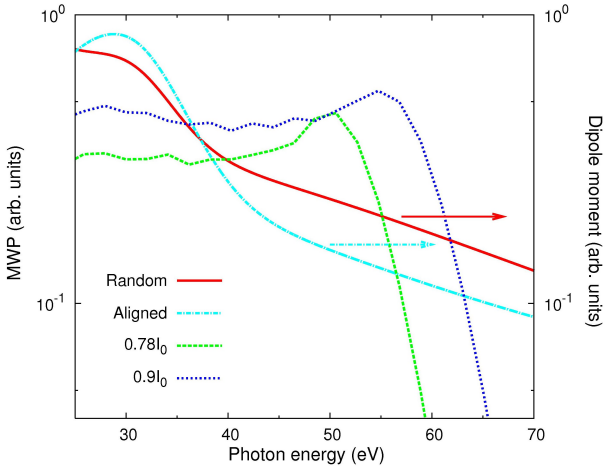

Figure 6.2: *Macroscopic wave packets (MWPs) for two different laser intensities, and averaged PR transition dipoles are for random and aligned N_2 molecules. MWPs are extracted from HHG spectra in Fig. 6.1 according to Eq. (6.1). Adapted from Publication [8].*

where $W'(\omega)$ is called a "macroscopic wave packet" (MWP), and $d(\omega)$ is the PR transition dipole moment. For the macroscopic HHG spectrum of partially aligned molecules, this equation is still valid with $d(\omega)$ being replaced by coherently averaged PR transition dipole:

$$d^{\text{avg}}(\omega,\alpha) = \int_0^{\pi} N(\theta')^{1/2} d(\omega,\theta')\rho(\theta',\alpha)\sin\theta' d\theta', \tag{6.2}$$

where $N(\theta')$ is the alignment-dependent ionization probability, $\rho(\theta',\alpha)$ the alignment distribution, and $d(\omega,\theta')$ the parallel component of the alignment-dependent PR transition dipole. Here θ' is the alignment angle with respect to the polarization direction of the probe laser, and α is the pump-probe angle. From Eq. (6.1), the target structure is reflected in the PR transition dipole, the propagation effect of the harmonics, in the meanwhile, is incorporated into the MWP. The two properties are well separated. The MWP represents the cumulative effect of the returning electron wave packet (or microscopic wave packet) after propagation in the medium and in the free space. The validity of Eq. (6.1) forms the basis of extracting molecular structure information from the experimentally measured HHG spectra.

For the HHG spectra shown in Fig. 6.1, we can separate the averaged PR transition dipoles and MWPs according to Eq. (6.1), see Fig. 6.2. The averaged PR transition dipole

indeed shows a rapid drop near 40 eV, which is due to the presence of a shape resonance of N_2 in the lower energy, and the rapid drop is more pronounced for aligned molecules than for random ones (see Fig. 6.5). For the MWP, under the same laser intensity, we have checked that they are the same for randomly distributed and aligned molecules. Thus it explains why the HHG from single-molecule response can be used to interpret how the intensity of each harmonic changes with pump-probe time delay in Le *et al.* [102]. However, the MWP changes more rapidly with laser intensity, especially for the longer wavelength laser used here. We note that the two MWPs in Fig. 6.2 have somewhat different slopes near 40 eV. The multiplication of the MWP and the PR transition dipole results in a weak minimum in the observed HHG spectra. The minimum would be more clearly seen if the molecules were better aligned. From Le *et al.* [95], the minimum in PR transition dipole changes rapidly with the alignment angle and the effect is severely averaged out when molecules are not well aligned. We further mention that the MWPs in Figs. 3.6 and 6.2 are rather different. They are due to the large difference in the laser peak intensities used. In the future, it is desirable that predictions such as those in Figs. 3.6 and 6.2 be checked experimentally.

6.3 Intensity dependence of multiple orbital contributions in HHG of aligned N_2 molecules

6.3.1 Macroscopic HHG spectra: theory vs experiment

In Sec. 6.2, we have simulated the HHG spectra of aligned N_2 molecules with the pump-probe angle $\alpha = 0°$. In this section, we present new measurements for aligned N_2 molecules at a time delay corresponding to the maximal alignment while the HHG-generating laser is perpendicular to the aligning one. The degree of alignment is estimated to be $\langle\cos^2\theta\rangle$=0.60±0.05.

Fig. 6.3 shows the HHG spectra of aligned N_2 molecules generated by a 1200-nm laser which is perpendicular to the aligning laser. Experimental conditions are the same as those in Sec. 6.2. The intensities (in the center of the gas jet) used in the theory are adjusted to coincide with experimental HHG cutoff position. In Figs. 6.3(a)- 6.3(c), the

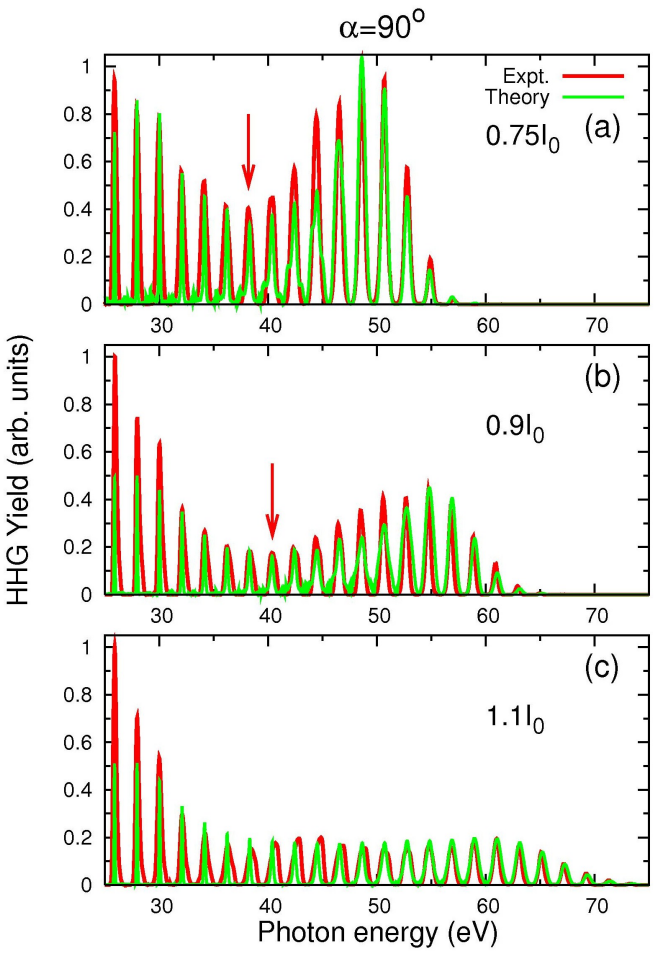

Figure 6.3: *Comparison of experimental [red (dark gray) lines] and theoretical [green (light gray) lines] HHG spectra of aligned N_2 in a 1200-nm generating laser where the pump-probe angle α=90°. Laser intensities in the simulations are indicated where I_0=10^{14} W/cm^2. Degree of alignment is $\langle\cos^2\theta\rangle$=0.60 by the aligning laser. See text for additional laser parameters. Only σ orbital is included in the simulations in (a) and (b), and both σ and π orbitals are included in the simulation in (c). Arrows indicate the positions of minima. Adapted from Publication [4].*

laser intensities in theory (experiment) are 0.75 (0.65), 0.9 (1.1), and 1.1 (1.3), in units of 10^{14} W/cm^2, respectively. We use the degree of alignment $\langle\cos^2\theta\rangle$=0.60 (see Appendix B for the quantum calculation of the molecular alignment) and keep other parameters close to experimental ones in the simulation. The HHG spectra from the experiment and theory are normalized at the cutoff.

The main features in the spectra are the deep minima at 38.2 eV and 40.4 eV, at the two lower intensities in Figs. 6.3(a) and 6.3(b), respectively. The minimum disappears at the higher intensity in Fig. 6.3(c). To simulate the spectra at the two low intensities, we include the HOMO (σ orbital) only. The simulation reproduces not only the correct shape of the spectra, but also the precise positions of the minima in the spectra in Figs. 6.3(a) and 6.3(b). For the higher intensity in Figs. 6.3(c), when we only included the σ orbital the theory could not reproduce the correct spectral shape. It also predicted a minimum in the spectrum which was not seen in the experiment [see Fig. 6.4(a)]. We then included both σ and π (HOMO-1) orbitals. A very good agreement between theory and experiment (correct shape and no minimum in the spectrum) in Fig. 6.3(c) is then achieved.

6.3.2 Single HOMO orbital contribution at low laser intensity

We now take a careful examination of the spectral features in Figs. 6.3(a) and 6.3(b). The deep minimum is related to the σ orbital. This minimum has been observed in many experiments, either in unaligned or aligned N_2 [170, 178–180]. The minimum shifts only slightly when the laser intensity is changed. This behavior is similar to the well-known Cooper minimum in Ar [127, 128]. The same behavior with laser intensity has been observed by Wörner *et al.* [178] (see their Fig. 1) and Farrell *et al.* [180] (see their Fig. 7) when α=0°. This can be understood as proposed in Sec. 6.2. When only one molecular orbital is contributing to the HHG spectra, the harmonic yield is given in Eq. (6.1). In Fig. 6.4 we show that there is a fast drop-off in the averaged PR transition dipole (shown is the square of the magnitude multiplied by ω^2) of the σ orbital around 38 eV [see Fig. 6.4(b)], which causes the pronounced minimum in the HHG spectra. For different laser intensities, the slope of the averaged PR transition dipole does not change, but the MWP ($\omega^2|W'(\omega)|^2$) increases monotonically with photon energy. Since the spatial distribution of the infrared (IR) laser intensity is different when the peak intensity at the focus is increased, the wave packet is modified differently as it propagates through the medium (see Fig. 6.2). This

makes the minimum in the HHG spectra shift slightly with laser intensity. Using only one molecular orbital, our theoretical simulation can reproduce the position of the minimum close to the experimental one.

6.3.3 Multiple orbital contributions (HOMO and HOMO-1) at higher laser intensity

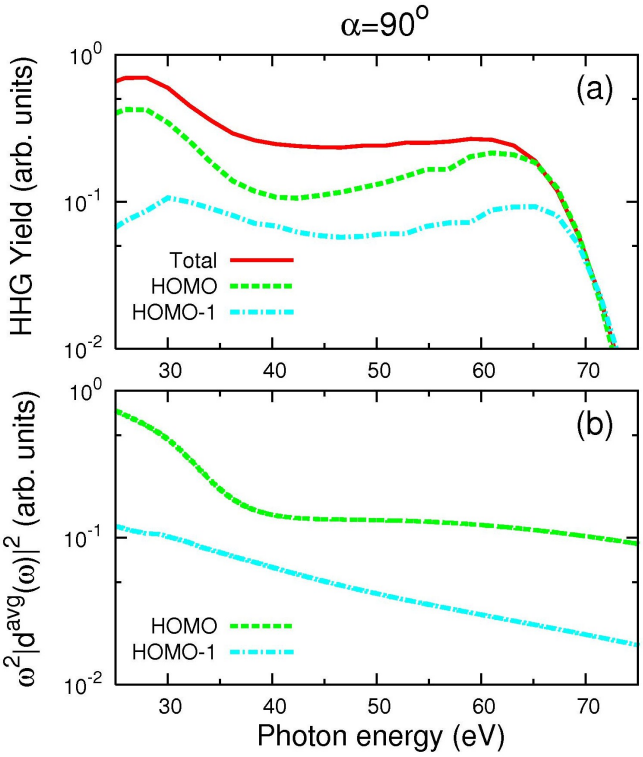

Figure 6.4: *(a) Calculated macroscopic HHG spectra (envelope only) corresponding to Fig. 6.3(c). Total (HOMO and HOMO-1 together) spectra and individual HOMO and HOMO-1 spectra. (b) Averaged photorecombination transition dipoles (parallel component, the square of the magnitude multiplied by ω^2) of the HOMO and HOMO-1 corresponding to (a). Laser intensity is 1.1×10^{14} W/cm^2. Degree of alignment is $\langle\cos^2\theta\rangle$=0.60 by the aligning laser. The pump-probe angle α=90°. Adapted from Publication [4].*

We next analyze the spectral features in Fig. 6.3(c). In Fig. 6.4(a), the envelopes of the HHG spectra in Fig. 6.3(c) from the two individual molecular orbitals, and from the total one, are obtained after macroscopic propagation in the gas medium, are shown. Meanwhile, the averaged PR transition dipoles (the square of the magnitude multiplied by ω^2,

degeneracy is not included) of the two orbitals are shown in Fig. 6.4(b).

In Fig. 6.4(a), the σ orbital alone shows a deep minimum, similar to Figs. 6.3(a) and 6.3(b). Since the π orbital shows comparable contributions over the whole spectral region, the interference between σ and π orbitals washes out the minimum in the spectra. From Eq. (6.2), the relative contribution between the two orbitals can be adjusted by the alignment-dependent ionization probabilities $N(\theta')$ and the alignment distribution $\rho(\theta', \alpha)$. For lower intensities, the relative $N(\theta')$ of the π orbital is small, so only the HOMO orbital contributes to the spectra. As the intensity increases, both orbitals contribute and the two amplitudes interfere resulting in a drastic change of the spectra.

As shown in Eq. (6.1), the macroscopic HHG spectra from individual molecular orbitals can be considered as a product of a MWP and an averaged PR transition dipole, based on the QRS theory. Since the ionization potential of the σ orbital (15.6 eV) differs from the π orbital (16.9 eV) only by 1.3 eV, the MWPs of the two orbitals are almost the same under the same IR laser, so the relative contribution between σ and π orbitals to the total HHG spectra is mostly determined by the averaged PR transition dipoles. In Figs. 6.3(a) and 6.3(b), the magnitude of $N(\theta')$ for σ orbital is much larger than the one for the π orbital, thus making the corresponding averaged PR transition dipole also larger. At the higher intensity of Fig. 6.3(c), the averaged transition dipoles between the two orbitals become comparable. Thus by increasing the laser intensity, the total HHG can evolve from single-orbital to multiple-orbital phenomena. Note that the MO-ADK theory [19] (also see Publication [14]) is used to calculate $N(\theta')$. There are also other models in the literature [103, 176, 181] for calculating the ionization rates. Using different ionization rates and different alignment distributions may change the theoretical predictions. We find that the ionization rates obtained from MO-ADK theory is very close to the recent model calculation used by Petretti *et al.* [176] where they solved the time-dependent Schrödinger equation (TDSE) at laser intensity of 1.5×10^{14} W/cm^2.

The contribution of the π orbital to the HHG of N_2 molecules when the pump-probe angle

α=90° has been studied previously [163, 177] using 800-nm pulses at the high intensities of around 2.0×10^{14} W/cm^2. In this case, HOMO-1 was found to be much more pronounced in the cutoff region. Note that the QRS theory has been applied to interpret the results in [163] with the ionization probability obtained from SFA [103] without including the propagation effect. (Note that at the alignment angle of 90°, the ratio of ionization rate between HOMO and HOMO-1 is about 2 from the SFA in comparison with about 5 from the MO-ADK theory [19].) In this study, a 1200-nm laser generates a broad photon energy range even with a low laser intensity and the π orbital contributes not only in the cutoff region, but also in the plateau.

In the future, measurements similar to the present one but with a full range of pump-probe angles may provide a way to determine the relative ionization probabilities of the two orbitals. The pump-probe angle α=90° is much closer to the alignment angle of 90° since the "volume element" $\sin\theta' \mathrm{d}\theta'$ in the angular integration peaks at 90°. To probe the PR transition dipole of the HOMO orbital, HHG spectra taken at low laser intensity with long-wavelength lasers is preferable to avoid multiple orbital contributions. This would make the retrieval of the structure of the target easier. If one wishes to study the π orbital, then a higher laser intensity and better alignment will enhance its contribution to the HHG [163, 177].

6.4 Shape resonance in photoionization and harmonic generation of N_2 molecules

6.4.1 Photoionization cross sections and phases of N_2 from HOMO and HOMO-1 orbitals

The most basic information on photoionization of a fixed-in-space molecule is the parallel and perpendicular transition dipole amplitudes in the body-frame of the molecule. They appear in the differential PICS in the body-fixed frame as shown in Appendix C:

$$\frac{d^2\sigma}{d\Omega_{\hat{k}} d\Omega_{\hat{n}}} = \frac{4\pi^2\omega k}{c} \mid \langle \Psi_i | \vec{r}\cdot\hat{n} | \Psi^{(-)}_{f,\vec{k}} \rangle \mid^2, \tag{6.3}$$

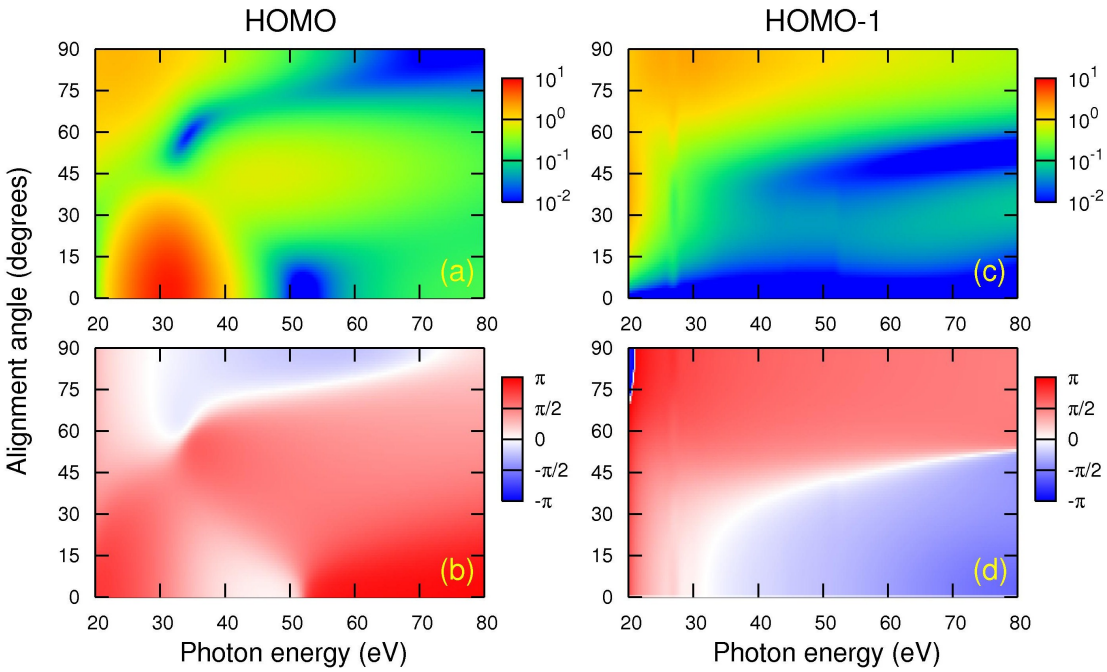

Figure 6.5: *Calculated differential photoionization cross sections [(a) and (c)] and phases [(b) and (d)] of the HOMO and HOMO-1 for N_2 in terms of the alignment angles, respectively. The shape resonance in the HOMO shows up around 30 eV for small alignment angles only. Only the parallel component to the polarization direction of the laser is shown. Adapted from Publication [4].*

where $\hat{n}$ is the polarization direction of the light, $\vec{k}$ the momentum of the photoelectron, and ω the photon energy. We will only focus on the case of $\hat{n} \parallel \vec{k}$ since they are related to the parallel polarized HHG spectra measured from aligned molecules.

In Fig. 6.5 we show the differential PICSs (in units of Mb) and the corresponding phases of the σ and π orbitals of N_2 using the well-established photoionization theory (see Appendix C) for photon energy from 20 to 80 eV. These data have been shown previously for selected photon energies against the alignment angles for the HOMO (see Fig. 5 of [95]) and HOMO-1 (see Fig. 2 of [103]). The observed HHG minima shown in Fig. 6.3 above for α=90° and in Fig. 6.1 for α=0° and for randomly distributed N_2 molecules can all be understood as due to the rapid change of cross section near 40 eV at alignment angles either close to 0° or 90°. Clearly the precise position of the minimum will depend on the degree of alignment. For the HOMO-1, Fig. 6.5 shows that the cross section generally peaks at large alignment

angles. Thus interference of HHG spectra from the σ and π orbitals are only observed close to α=90°. Note that in Fig. 6.5 the PICS for the two orbitals are shown on the same scale. Except for the HOMO shape resonance near 30 eV that will be discussed next, the PICS from HOMO-1 is comparable with that from HOMO over the photon energies covered. This result has been confirmed by the measured electron spectra in photoionization experiments. In HHG, HOMO contribution is always dominant for the randomly distributed N_2. HOMO-1 can become more important only at large alignment angles and higher laser intensities, as discussed earlier.

6.4.2 Shape resonance in HHG of aligned N_2

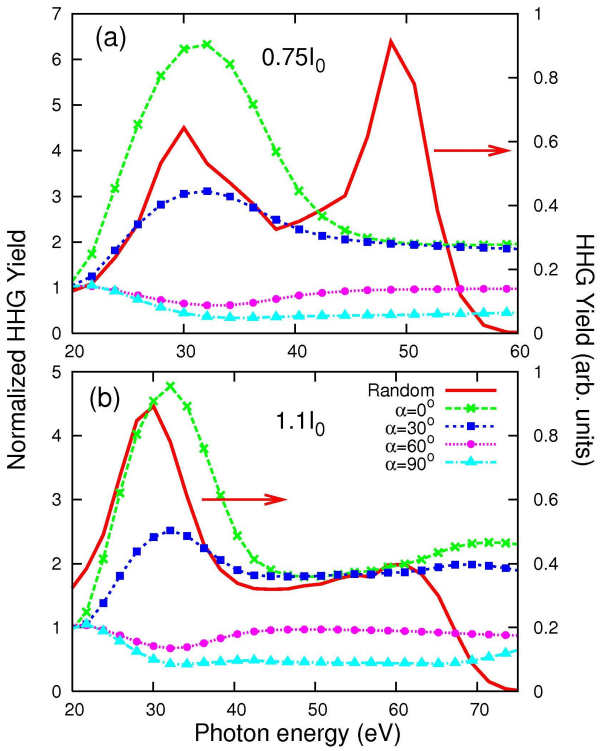

Figure 6.6: *Calculated macroscopic HHG spectra (envelope only) of unaligned N_2 and normalized HHG yields of aligned N_2 with respect to the unaligned ones as a function of the photon energy at the selected pump-probe angle α. Laser intensities are indicated where I_0=10^{14} W/cm^2. Degree of alignment is $\langle\cos^2\theta\rangle$=0.60. Adapted from Publication [4].*

Resonances are very common in photoionization spectra. Most of them are due to

the so-called Feshbach resonances which in general are quite narrow and thus can only be observed using high-resolution spectroscopy. However, broad Feshbach resonances and shape resonances can be observed since they have widths from fractions to a few eV's. In HHG, resonances have been explored in experiment [21] and theory [20, 182, 183] (also see Publication [7]) recently for atomic targets. But shape resonances are rare for common atomic targets. The resonance feature observed in Xe [21] is due to the intershell coupling with the well-known shape resonance that occurs in the $4d$ shell. On the other hand, shape resonances are very common in molecules. For N_2, there is a pronounced shape resonance in the HOMO channel near photon energy of 30 eV. This is due to the $3\sigma_g \rightarrow k\sigma_u$ channel, and for small alignment angles only. We can see a decrease of the phase shift by π for this resonance from 20 to 40 eV in Fig. 6.5(b). There are no other known shape resonances in the covered energy region. Clearly this shape resonance is best observed by selecting ionization from the σ orbital only, by using low laser intensity and for molecules that are aligned nearly parallel to the polarization axis of the probing laser.

In Fig. 6.6, we first show the calculated HHG spectra (envelope only, normalized) of randomly distributed N_2 at two laser intensities. For randomly distributed N_2 molecules, it is known that the σ orbital is the dominant contributor to the HHG spectra. The peak around 30 eV in the HHG spectra is due to the shape resonance in the PICS of σ orbital at small alignment angles. In Fig. 6.6, we also show the normalized yield at selected alignment angles with respect to the randomly distributed one. We take the degree of alignment $\langle\cos^2\theta\rangle$=0.60. The intensity of each odd harmonic q is obtained by integrating over harmonics $q-1$ to $q+1$. For low laser intensity, the shape resonance is very pronounced at $\alpha = 0°$. It decreases as the pump-probe angle is increased, showing that the shape resonance is present only at small aligning angles. For higher laser intensities, the same behavior is seen even though the π orbital is also contributing at large pump-probe angles. We should comment that absorption is not included in the present simulation and it will suppress the shape resonance if the gas pressure is high.

Comparison of this prediction with existing experimental data is far from conclusive. Torres *et al.* [170] have shown high-harmonic data for aligned N_2 using a 1300-nm laser with intensity of 1.3×10^{14} W/cm^2 (see their Fig. 4). The general trend of their data is very close to our prediction, but they used a higher intensity and a higher degree of alignment ($\langle\cos^2\theta\rangle$=0.66), and thus the HOMO-1 channel may contribute to the signal at larger alignment angles. Using 800-nm lasers, Lee *et al.* [177] reported the HHG ratios of aligned vs unaligned N_2 at the selected alignment angles. They did not present data near the resonance region and they used a high intensity of 2.5×10^{14} W/cm^2 [see their Fig. 1(c)]. Our calculation does not reproduce their measured ratios. They also reported that the normalized HHG yields for α=0° and 90° crosses at about harmonic order 39. This is confirmed in our calculation (not shown). The very recent measurement by Kato *et al.* [184] did not extend below 30 eV either. There are other measurements [180, 185, 186] using Ar or α=0° as a reference. Direct comparison with these data are difficult. Thus, it remains to be seen if the shape resonance in N_2 can be seen in the HHG spectra as predicted here. We comment that absorption was not included in our propagation simulation. Absorption may modify the prediction if the gas pressure is too high. Experiments dedicated to address this issue would be of interest.

6.5 Contributions of multiple molecular orbital in HHG of aligned CO_2 molecules

6.5.1 Macroscopic HHG spectra of random and aligned CO_2: theory vs experiment

HHG spectra for isotropically distributed and partially aligned CO_2 molecules by 800-nm and 1200-nm lasers have been reported recently [178]. In this section, we will present the simulated HHG spectra for random and aligned CO_2 separately in the following. SFA is used to calculate the ionization probability in QRS theory in this section and next section, unless otherwise stated.

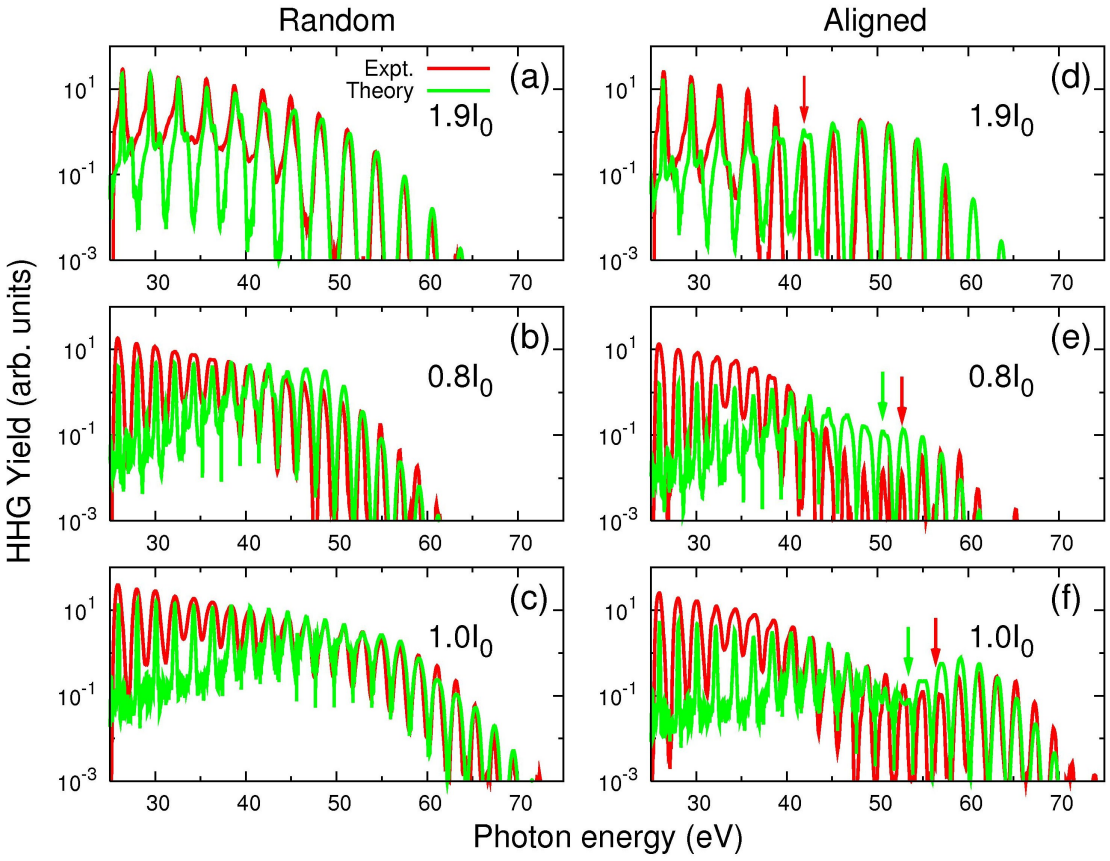

Figure 6.7: *Comparison of theoretical (green -light-lines) and experimental (red -dark-lines) HHG spectra of random and aligned CO_2 molecules, in an 800-nm laser shown in (a) and (d), and in a 1200-nm laser shown in (b), (c), (e) and (f). Laser intensities are indicated where I_0=10^{14} W/cm^2. Experimental data are from Ref. [178]. Arrows indicate the positions of minima. Pump-probe angle α=0°. See text for additional laser parameters and experimental arrangements. Adapted from Publication [9].*

1. HHG spectra of randomly distributed CO_2

In Figs. 6.7(a)-6.7(c), we show the HHG spectra for isotropically distributed CO_2 molecules by 800-nm and 1200-nm lasers. To obtain good agreement between theory and experiment, especially in the cutoff region, the intensity used in the theory is adjusted from the value given in the experiment. In Figs. 6.7(a)-6.7(c), the intensities in theory (experiment) are 1.9 (2.1), 0.8 (1.0), 1.0 (1.2), in units of 10^{14} W/cm^2, respectively. Other parameters used in the simulation are the same as those given in the experiment [178]. The laser parameters

are: pulse duration is $\sim$ 32 fs (800 nm) or $\sim$ 44 fs (1200 nm), beam waist at the focus is $\sim$ 40 μm. A 0.6-mm-wide gas jet is located 3 mm (800 nm) or 3.5 mm (1200 nm) after the laser focus, and a slit with a width of 100 μm is placed at 24 cm after the gas jet.

Figs. 6.7(a)-6.7(c) clearly show the good overall agreement between experiment and theory for randomly distributed CO_2 molecules. We have checked that HOMO is dominant for randomly distributed CO_2, with negligible contributions from inner orbitals. The HHG spectra do not exhibit any minima, as opposed to the spectra of random N_2 molecules (as shown in Fig. 6.1) when they are generated under the same experimental conditions [178]. For randomly distributed CO_2, there was no minimum found in HHG spectra using an 800-nm laser by Vozzi *et al.* [169]. However, for the 1300-nm lasers, the data from Torres *et al.* [170, 187] appear to show a very weak minimum at photon energy near 45 eV. Without more careful study including different intensities and wavelengths, however, this is not conclusive.

2. HHG spectra of aligned CO_2

Experimentally HHG spectra have also be reported from aligned CO_2 molecules. A relatively weak and short laser pulse was used to impulsively align molecules, and the HHG spectra were taken at half-revival ($\sim$ 21.2 ps in CO_2) when the molecules were maximally aligned [178]. The angular distributions of the aligned molecules are obtained by solving the TDSE of rotational wave packet (see Appendix B). The degree of alignment is $\langle\cos^2\theta\rangle$=0.60 in Fig. 6.7(d), and $\langle\cos^2\theta\rangle$=0.50 in Figs. 6.7(e) and 6.7(f). The polarizations of the pump and probe lasers are parallel to each other.

The HHG spectra of partially aligned CO_2 molecules are shown in Figs. 6.7(d)-6.7(f), which are obtained under the same generating lasers and experimental arrangements as those in Figs. 6.7(a)-6.7(c), respectively. The simulation and experimental data agree well with each other in general. In Fig. 6.7(e), the discrepancy is a little bigger, showing the drop near 40 eV is larger in the experiment than in the theory. But we note that in Fig. 6.7(f), the experimental data do not drop as rapidly, in agreement with the theoretical simulation.

The minima in the HHG spectra of CO_2 and their dependence on laser intensity have been

widely discussed in the literature [65, 187]. In Fig. 6.7(d), for an 800-nm laser, experiment gives a strong minimum at 42 ± 2 eV, our simulation predicts a minimum around 42 eV. For the 1200-nm laser, in Fig. 6.7(e), experiment shows a minimum at 51 ± 2 eV, theory predicts a minimum around 50 eV. In Fig. 6.7(f), the experimental minimum is shifted to 57 ± 2 eV, and the theoretical one is moved to around 53.5 eV. Thus our simulation also shows the shift of the minimum from low to high harmonic orders as laser intensity is increased. Below we interpret the origin of the shift.

6.5.2 Origin of minimum in the HHG spectra of aligned CO_2

We next analyze the origin of the minimum in the HHG spectra seen in Figs. 6.7(d)-6.7(f), and consider the dominant contributions from HOMO and HOMO-2 only. The averaged PR transition dipole is defined in Eq. (6.2) for each molecular orbital. This gives a measure of the relative contribution of each molecular orbital to the HHG, which is obtained by averaging over the angular (or alignment) distribution of the partially aligned molecules, weighted by the square root of the tunneling ionization probability. The relative ionization rates between HOMO and HOMO-2 change with laser intensity.

Figs. 6.8(a)-6.8(c) show the envelopes of the HHG spectra from individual molecular orbitals together with the total ones, each obtained after propagation in the medium. In the meanwhile, the averaged PR transition dipoles of HOMO and HOMO-2 under different generating lasers and alignment distributions are shown in Figs. 6.8(d)-6.8(f), respectively.

In Figs. 6.8(a) and 6.8(b), there are no minima in the HHG spectra of HOMO or HOMO-2, but the minimum shows up in the total spectra. This is due to the interference between HOMO and HOMO-2. We call this type I minimum. Clearly the minimum position will change with laser intensity since the relative ionization rates between HOMO and HOMO-2 change with intensity [also see Figs. 6.11(c) and 6.11(d)]. Similar analysis can be found in Ref. [65]. In Fig. 6.8(c), there is a minimum in the HOMO spectra at 52.6 eV. This minimum is shifted to 53.6 eV in the total spectra due to the interference with the HOMO-

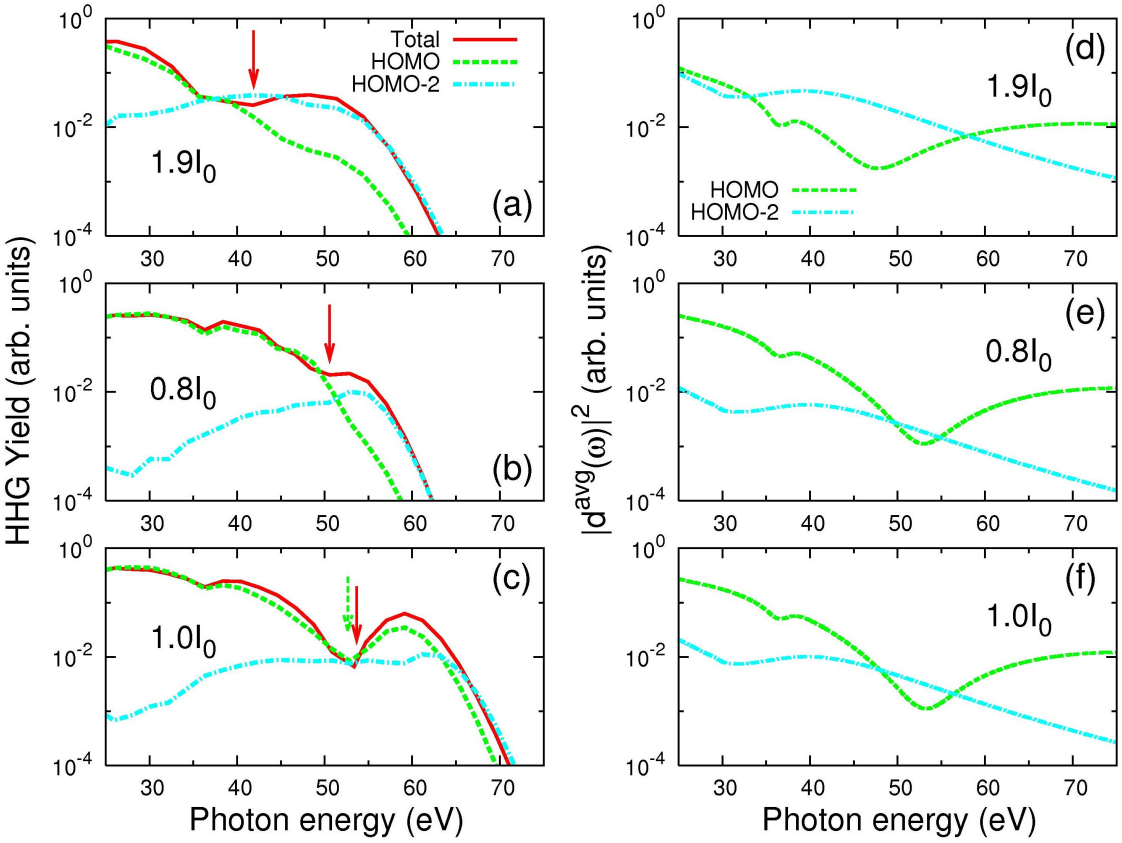

Figure 6.8: *(a)-(c) Macroscopic HHG spectra (envelope only) corresponding to Figs. 6.7(d)-6.7(f), respectively. Total (HOMO and HOMO-2 together) spectra and the spectra of individual HOMO and HOMO-2 are shown. (d)-(f) Averaged photorecombination transition dipoles (parallel component, the square of magnitude) of HOMO and HOMO-2 corresponding to (a), (b) and (c), respectively. Laser intensities are indicated where I_0=10^{14} W/cm^2. Arrows indicate the positions of minima. Pump-probe angle α=0°. Adapted from Publication [9].*

2. This is categorized as type II minimum. Similar analysis of this type can be found in Refs. [187, 188]. The minimum in the HOMO spectra is due to the minimum in the averaged PR transition dipole of HOMO shown in Fig. 6.8(f). But their positions differ due to modification of the "macroscopic wave packet" (MWP). In this connection we mention that the earlier calculations [95, 102] with an 800-nm laser showed minimum in HHG spectra at small pump-probe angles due to the contribution from the HOMO only. These calculations were carried out with a higher degree of alignment and higher laser intensities as compared

to our present study. This is expected as the minimum in the averaged PR transition dipole from HOMO in Fig. 6.8(d) becomes deeper and is slightly shifted away from the cutoff to lower energies with increased degree of alignment [see Fig. 6.8(e) and 6.8(f)]. Furthermore, as shown in Fig. 6.2, the minimum in the HOMO spectra could also result from the multiplication of MWP and averaged PR transition dipole even when neither has minimum. When a minimum occurs in the dominant orbital, its position will not change much if it remains the dominant one when the laser intensity changes. The little bump around 36 eV in the HOMO spectra as well as in the total spectra can be seen due to the bump in the HOMO curves in Figs. 6.8(d)-6.8(f). Its position does not change much since the HOMO-2 remains small.

In Fig. 6.2, we have shown that the macroscopic HHG spectrum is the product of a MWP and an averaged PR transition dipole for each individual molecular orbital. Since the ionization rate for each orbital has been incorporated in the averaged PR transition dipole, the MWP is mostly identical except for the phase due to ionization potential. The averaged PR transition dipole is very sensitive to ionization rates. The relative magnitude changes rapidly with the increase of laser intensity. Thus when two averaged PR transition dipoles are comparable [see Fig. 6.8(d)], the position of the minimum changes rapidly with the laser intensity. The averaged PR transition dipole is also sensitive to alignment distributions [see Figs. 6.8(d)-6.8(f)]. At low laser intensity, HOMO-2 is small, interference often occurs in a narrow region only where the two amplitudes are comparable, see Figs. 6.8(b) and 6.8(c). In comparison, in Smirnova *et al.* [65], HOMO and HOMO-2 tend to interfere over a broad photon-energy region. The ionization rates and transition dipoles used in their calculations are different from ours.

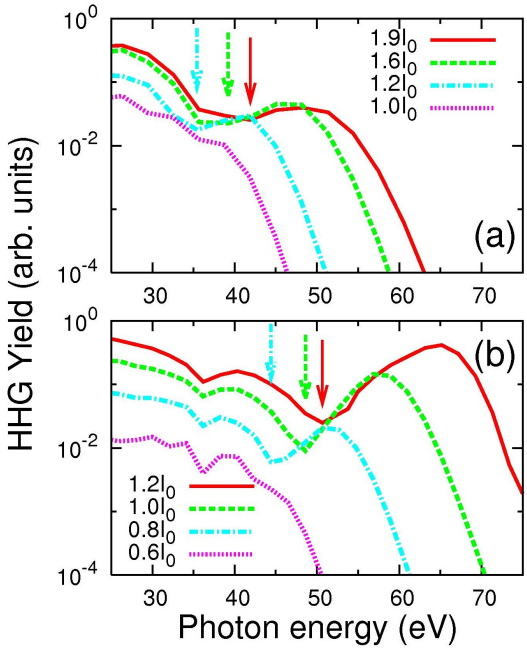

Figure 6.9: *Laser intensity dependence of macroscopic HHG spectra (envelope only) (a) in an 800-nm laser and (b) in a 1200-nm laser. Intensities are shown in units of* I_0=10^{14} *W/cm*^{2}. *Arrows indicate the positions of minima. Degree of alignment:* $\langle\cos^2\theta\rangle$=0.60. *Pump-probe angle* α=0°. *Adapted from Publication [9].*

6.6 Major factors that influence positions of the minima in the HHG spectra of aligned CO_2 molecules

6.6.1 Progression of harmonic minimum versus laser intensity

In Figs. 6.9(a) and 6.9(b) we show the envelope of the calculated HHG spectra for four different peak intensities with an 800-nm laser and a 1200-nm laser, respectively. For the 800-nm spectra, the lowest intensity does not have a minimum. For the higher ones, each spectrum has a type I minimum, with its position shifts to lower photon energy as the laser intensity is decreased. The degree of alignment of molecules used in the calculation is $\langle\cos^2\theta\rangle$=0.60. We find that the shift cannot be attributed to either MWP or the averaged PR transition dipole alone. For the 1200-nm data, also with $\langle\cos^2\theta\rangle$=0.60, which is different from Figs. 6.7(e) and 6.7(f), we find that the minimum is type II, where the averaged PR transition dipole of the HOMO has a minimum. The minimum in the HHG spectra of

the HOMO shifts to higher photon energy as the intensity increases, but the interference with HOMO-2 shifts the minimum to even higher energies. In other words, the shift of the position of the HHG minimum vs intensity cannot be attributed to a single factor alone.

6.6.2 Other factors influencing the precise positions of HHG minima

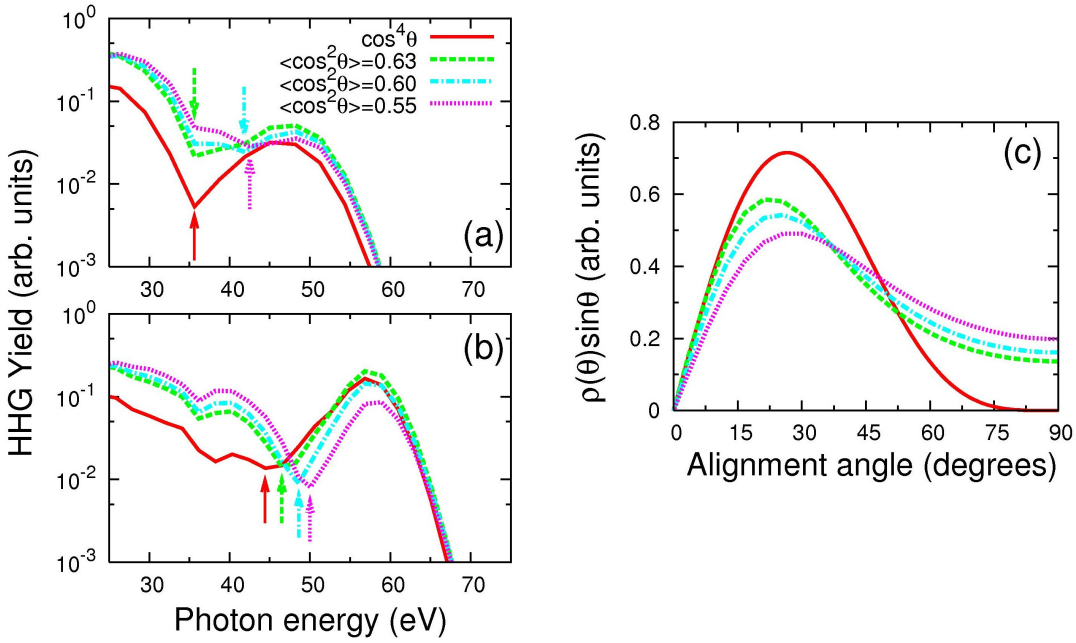

Figure 6.10: *Dependence of macroscopic HHG spectra (envelope only) with degrees of molecular alignment distributions for (a) an 800-nm laser with intensity of 1.8×10^{14} W/cm^2, and (b) a 1200-nm laser with intensity of 1.0×10^{14} W/cm^2. The weighted angular distributions of the molecules are shown in (c). Arrows indicate the positions of minima. Pump-probe angle $\alpha=0°$. Adapted from Publication [9].*

In our analysis, the averaged PR transition dipole is calculated over the angular distribution of the molecules and thus depends on the degree of alignment. Since the latter cannot be accurately measured, we check how sensitive the calculated spectra is with respect to the assumed alignment distribution. In Fig. 6.10(c), four different alignment distributions are shown. The distributions are multiplied by the volume element $\sin\theta$ for easy comparison. Three of them are obtained from the calculated rotational wave packets (see Appendix B),

with $\langle\cos^2\theta\rangle$ as 0.63, 0.60 and 0.55, respectively. The other is the commonly used $\cos^4\theta$ distribution. For 800-nm and 1200-nm lasers, the envelopes of the calculated HHG spectra are shown in Figs. 6.10(a) and 6.10(b), respectively. The precise position of the minimum changes slightly except for the one from the $\cos^4\theta$ distributions. However, change of a couple of eV's is seen.

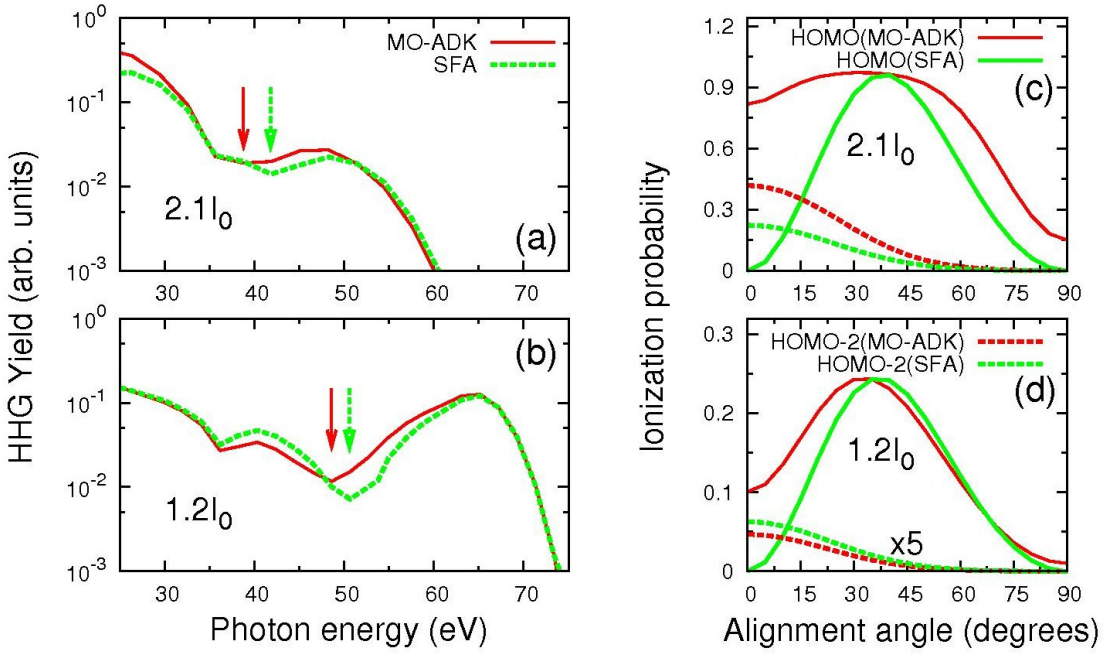

Figure 6.11: *Dependence of macroscopic HHG spectra (envelope only) on the ionization probabilities calculated from MO-ADK or SFA in (a) an 800-nm laser, and (b) a 1200-nm laser. Laser intensities are indicated where I_0=10^{14} W/cm^2. Arrows indicate the positions of minima. Degree of alignment: $\langle\cos^2\theta\rangle$=0.60. Pump-probe angle α=0°. (c) and (d) Alignment-dependent ionization probabilities of HOMO and HOMO-2 calculated using MO-ADK and SFA. Laser parameters are the same as (a) and (b). Ionization probabilities of HOMO-2 in (d) are multiplied by 5. Adapted from Publication [9].*

To precisely determine the minimum in the HHG spectra, accurate alignment-dependent ionization probability $N(\theta)$ for each molecular orbital is needed. For CO_2, even for HOMO, different theories in the literature [65, 172–176] (also see Publication [14] and [18]) show non-negligible differences, and they do not agree with the experimental data [172]. Here we examine how the HHG spectra change with the different ionization rates used. The

ionization rates for both HOMO and HOMO-2 can all be easily calculated from SFA or from MO-ADK theory. Figs. 6.11(a) and 6.11(b) show the HHG spectra calculated using the ionization probabilities shown in Figs. 6.11(c) and 6.11(d). Other laser parameters used in the calculation are given in the figure captions. The difference of the position of the minimum is 3 eV in Fig. 6.11(a) and 2 eV in Fig. 6.11(b). Note that the ionization probabilities from SFA and MO-ADK are normalized at the peak of the HOMO curve. In Fig. 6.11(a) the spectra are normalized at H33 (51 eV) and in Fig. 6.11(b) at H65 (67 eV).

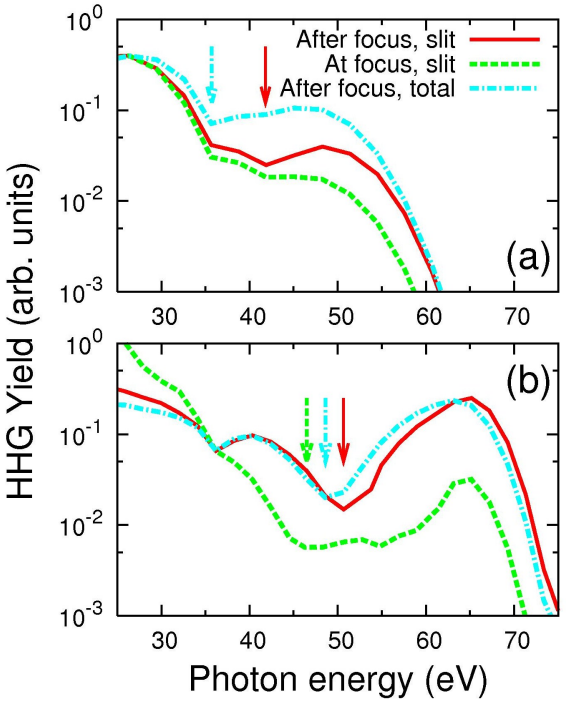

Figure 6.12: *Dependence of macroscopic HHG spectra (envelope only) on experimental arrangements (a) for an 800-nm laser with intensity of 2.1×10^{14} W/cm^2, and (b) for a 1200-nm laser with intensity of 1.2×10^{14} W/cm^2. The arrangements are: (1) gas jet after focus and slit is used (solid lines); (2) gas jet at the focus and slit is used (dashed lines); and (3) gas jet is after the focus but without the slit (dot-dashed lines). Arrows indicate the positions of minima. Degree of alignment: $\langle\cos^2\theta\rangle$=0.60. Pump-probe angle α=0°. Adapted from Publication [9].*

The HHG spectra are also sensitive to the experimental arrangement and thus can also move the position of the HHG minimum. To demonstrate this, we (i) move the gas jet

to the laser focus and collect the signal using a slit; (ii) put the gas jet after the laser focus, and collect HHG signal without slit (total signal). These two will be compared to the arrangement used in this paper: gas jet is after the laser focus and the HHG is collected with a slit. The results are compared in Fig. 6.12. Note that the spectra are normalized at H17 (26 eV) in Fig. 6.12(a) and at H35 (36 eV) in Fig. 6.12(b). Not only the spectra change quite significantly, but also the position of the HHG minimum. This illustrates that it is very difficult to compare the position of the HHG minimum from different experiments. In this comparison, the change of the HHG spectra is due to the change of MWP which depends on the experimental setup. The averaged PR transition dipoles of HOMO and HOMO-2 are the same in the three calculations.

6.7 Conclusion

In this chapter, we have described a complete theory (as discussed in Sec. 2.3.3) for HHG in a macroscopic molecular medium. Our approach is based on the simultaneous solution of the coupled Maxwell's wave equations describing macroscopic propagation of both driving laser pulse and its high harmonic fields together with the microscopic induced dipoles. For the latter we use the recently developed QRS theory. This scheme provides a simple and efficient method for calculating HHG from a macroscopic medium. To our knowledge, this is the first time that theoretically calculated HHG spectra with including the propagation effect can be directly compared with experimentally measured spectra. We summarize this chapter in the following:

(1) We have demonstrated that experimental HHG spectra of random or aligned N_2 and CO_2 molecules can now be accurately reproduced by theory. The contribution of the outmost molecular orbital only or the multiple molecular orbitals is included in the calculation depending on conditions of molecular alignment. If there is only one molecular orbital dominant for the HHG process, we have further shown that the HHG spectrum can be expressed as the product of a macroscopic wave packet and the photorecombination transition

dipole moment. The latter is a property of the target, and is independent of the lasers, not of the propagation effect. This factorization makes it possible to extract target structure information from the experimental HHG spectra. It provides the needed theoretical basis for using HHG as ultrafast probes of excited molecules, such as those demonstrated recently [124].

(2) We have carefully investigated HHG spectra of aligned N_2 at a time delay of the maximal alignment using a 1200-nm laser when the pump-probe angle is set at 90°. The minimum in the HHG spectrum appears at about 38 - 40 eV at two low laser intensities. It disappears at a higher laser intensity. We have carried out theoretical simulations to understand these results, and concluded that the minima in the HHG are associated with the properties of the transition dipole moments for photoionization from the HOMO. At higher intensity, the contribution from HOMO-1 becomes important and interference between the two contributions washes out the minimum.

(3) We have examined the possibility of observing the well-known shape resonance in the photoionization of N_2 in the HHG spectra. While the normalized HHG yield (with respect to randomly distributed molecules) shows clear enhancement at small alignment angles and shape resonance may have been seen in the 1300-nm data [170], no evidence of shape resonance has been observed in the HHG spectra from 800-nm lasers. Further experiments dedicated to resolve this issue will be of great interest.

(4) We have analyzed the multiple orbital contribution to HHG in CO_2 with the inclusion of macroscopic propagation effect. In the past few years, there have been many experimental and theoretical studies on the HHG of CO_2 from many laboratories, using lasers with different wavelengths and intensities, for CO_2 molecules that are randomly distributed or partially aligned. In particular, for CO_2 molecules that are partially aligned along the polarization axis of the probe laser, many experiments have shown that the HHG spectra exhibit minima and the positions of the minima shift with laser intensities [65, 178, 187]. The shift of the minimum position with laser intensities has been attributed to the interference between the

contributions to HHG from the HOMO-2 with the one from the HOMO, despite HOMO-2 lying at 4.4 eV deeper than the HOMO. We have found that although HHG spectra change significantly under different experimental parameters such as degree of alignment, focusing condition, and the use of a slit, the position of the minimum in the HHG spectrum behaves in a similar trend as laser intensity varies. This trend has been found to be consistent with the recent experimental measurements from different groups.

We comment that our theory, i.e., QRS theory (as shown in Sec. 2.2.3 and Sec. 2.3.3), and the earlier one by Smirnova *et al.* [65] both explain the intensity dependence of the change of HHG minima, but the details between the two theories are quite different. The alignment dependence of the ionization rates, the recombination dipole matrix elements and their phases entering the two theories are not the same, for both the HOMO and HOMO-2 taking CO_2 for example. As illustrated in this chapter, these parameters can all affect the position of the predicted interference minimum. Furthermore, in Smirnova *et al.* [65] the interference is attributed to the importance of hole dynamics in the ion core. Our approach is formulated in the time-independent fashion, no hole dynamics is included. Since HHG spectra are taken without explicit observation of electron dynamics, the difference between the two models cannot be settled. Despite these differences, our understanding of the HHG spectra of CO_2 has come a long way since 2005 [69]. With the possibility of including macroscopic propagation effect "routinely" in the HHG theory for molecular targets, further experimental studies should explore the effects of laser focusing condition and gas pressure, for lasers extending to longer wavelengths. Such studies would further our basic understanding of strong-field physics of molecules to the next level, and eliminate the need of introducing extraneous assumptions in the interpretation of experimental data.

Chapter 7

Photoelectron angular distributions in single-photon ionization of aligned N_2 and CO_2 molecules using XUV light

Figures and most paragraphs in this chapter are adapted from Publication [15].

7.1 Introduction

Photoionization (PI) is the basic physical process that allows the most direct investigation of molecular structure [189–192]. Until recently, however, almost all experimental measurements have been performed from an ensemble of randomly distributed molecules. Thus the rich dynamical structure of photoelectron angular distributions (PADs) for fixed-in-space molecules predicted nearly 30 years ago still remains largely unexplored [193]. Molecular frame photoelectron angular distribution (MF-PAD) has been investigated with X-ray or extreme ultraviolet (XUV) photons if the molecular cation dissociates immediately after the absorption of the photon. Using photoion-photoelectron coincidence techniques the molecular axis can be inferred from the direction of motion of the fragmentation products. Clearly this method is not applicable if the cations are stable, and thus it is not applicable to PI from the highest-occupied molecular-orbital (HOMO). In the last decade it has been shown that gas phase molecules can be aligned with infrared (IR) lasers using either adiabatic or nonadiabatic methods [73–75]. To investigate PI of molecules, the nonadiabatic method is

preferable such that PI occurs in field-free conditions.

In a recent experiment, Thomann *et al.* [79] reported the angular dependence of single-photon ionization of aligned N_2 and CO_2 molecules. The molecules were first impulsively aligned by a non-ionizing IR laser pulse impinging on supersonically cooled molecules. These aligned molecules were then ionized by 10 fs soft X-ray pulses, and the photoelectrons were detected in coincidence with the molecular ions. The aligning pulse generated a rotational wave packet, which periodically exhibits macroscopic field-free alignment about the polarization axis of the pump laser. The soft X-ray was from high-order harmonic generation (HHG). Filters were used to select only the 27th harmonic (H27) which has a center energy of 43 eV. The ions and electrons were measured during the first half-revival where the molecular-axis distribution changes from aligned to antialigned. In other words, PI can be investigated from partially aligned molecules to probe molecular frame PI directly. Due to the limited number of soft X-ray photons, this measurement did not report PAD from aligned molecules. Similarly, the energy resolution did not permit different ionic states to be distinguished. In spite of this, the experiment did succeed in establishing clearly that PI yield was maximum when the molecules were aligned perpendicular to the polarization of soft X-ray for both N_2 and CO_2 molecules. This is a strong contrast to strong-field multiphoton ionization where the two molecules show great differences.

In this chapter we will explain the experimental results of Thomann *et al.* [79] using the well established PI theory of molecules [99, 100]. These theories have been widely used to interpret experimental results for randomly distributed molecules. However, the PI theory also predicts much detail that can be measured from aligned molecules, in particular, the angular distributions of photoelectrons from different subshells. Since the technology of HHG is advancing rapidly, we anticipate that PAD from aligned molecules will become available soon. This chapter is organized as follows. In Sec. 7.2, we will examine the alignment dependence of H27 if it is generated by exposing N_2 molecules to intense IR lasers [103]. Since HHG involves a recombination step which is the inverse process of photoionization,

such a comparison is of interest. In Sec. 7.3, we will show the simulated single-photon ionization yield of aligned N_2 and CO_2 molecules in the experiment of Thomann *et al.* [79]. This would also allow us to compare the alignment dependence of single-photon PI by soft X-ray with multiphoton ionization by IR lasers [194, 195]. In Sec. 7.4, we will report the predicted PAD of fixed-in-space N_2 molecules in the laboratory frame. In Sec. 7.5, we will introduce the pump-probe setup similar to Thomann *et al.* [79] and report the predicted PAD for partially aligned N_2 molecules (with different degree of alignment) in the laboratory frame. The predicted angular distributions in the laboratory frame are presented in such a way that they can be compared directly to future experiments. In fact, several such measurements have been reported recently [77, 196]. In Sec. 7.6 we will investigate how the PADs of aligned N_2 molecules change with the photon energy. In Sec. 7.7, we will predict the PAD in the laboratory frame for fixed-in-space and partially aligned CO_2 molecules using the same pump-probe scheme as in Sec. 7.5. The similar measurements for aligned CO_2 molecules have been reported in [80] recently. A summary in Sec. 7.8 concludes this chapter.

7.2 Connection between photoionization and harmonic generation

For aligned molecules, experimentally one can measure the ionization cross section by single photons, say, at 43 eV, by multiphotons with IR lasers, say, at 800 nm (1.55 eV per photon), or by the observation of high-order harmonics, say, H27, at 43 eV. Today field-free molecules can be transiently aligned by lasers only, thus experiments are carried out at intense IR laser facilities. To compare with experimental measurements, theory must perform calculations first on molecules that are fixed in space. Here we compare photoionization cross sections (PICSs) for ionization by a 43 eV photon of N_2 leaving N_2^+ in the $X\ ^2\Sigma_g^+$, $A\ ^2\Pi_u$ and $B\ ^2\Sigma_u^+$ ionic states, corresponding to removing an electron from the HOMO, HOMO-1 and HOMO-2 orbitals of N_2, respectively. In Fig. 7.1(a) we show the alignment dependence of integrated

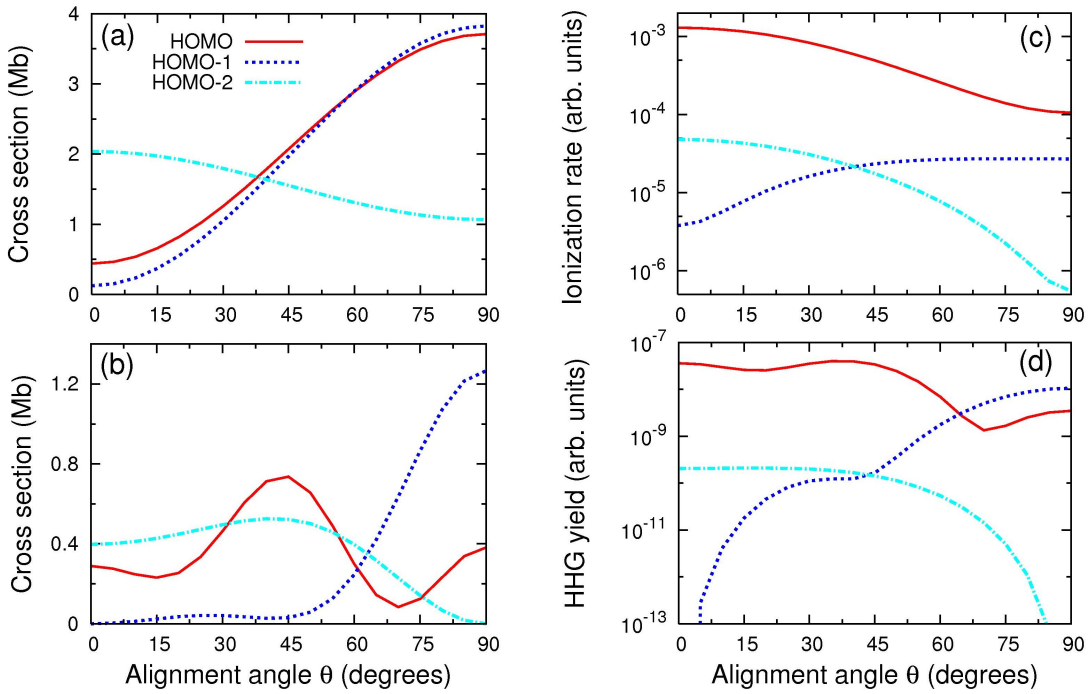

Figure 7.1: *(a) Integrated photoionization cross sections, and (b) doubly differential cross sections for electrons ejected in the polarization direction, for N_2 aligned at an angle θ from the polarization axis, by a single photon at 43 eV. (c) Alignment dependence of the multiphoton ionization rate of N_2 by a laser with intensity of 2×10^{14} W/cm^2. (d) Alignment dependence of the 27th harmonic (43 eV) of N_2 by a laser with intensity of 2×10^{14} W/cm^2, wavelength of 800 nm, and duration (FWHM) of 30 fs. HOMO (solid lines), HOMO-1 (dotted lines) and HOMO-2 (dot dashed lines). Adapted from Publication [15].*

PICS for ionization leading to the X, A and B states of the ion. The polarization axis is fixed and the molecular axis makes an angle θ with respect to it. According to Eq. (C.19), we obtain the asymmetry parameter $\beta_{\hat{n}}$ to be -0.83, -0.95 and 0.47 for X, A and B states, respectively [99].

From Fig. 7.1(a), we note that PICSs are of the same order of magnitude, with the HOMO and HOMO-1 channels having nearly identical θ-dependence even though HOMO is a σ_g orbital and HOMO-1 is a π_u orbital. This is in strong contrast with ionization by intense IR lasers. Fig. 7.1(c) shows the alignment-dependent multiphoton ionization rates of N_2 by intense lasers with peak intensity of 2×10^{14} W/cm^2 calculated with the MO-ADK

theory [19] (or Publication [14]). Note that ionization rates for X, A and B states are quite different since tunneling is the main mechanism for ionization at such high intensities. For the tunneling processes the ionization rate decreases rapidly as the ionization energy increases. The A and B states are higher than the X state (15.6 eV) by 1.3 eV and 3.2 eV, respectively [197]. On the other hand, the alignment dependence of strong field ionization reflects the shape of the charge density of the molecular orbital from which the electron is removed.

Next we consider the alignment dependence of single-molecule HHG. According to the quantitative rescattering (QRS) theory in Eq. (2.36), the HHG yield is proportional to the product of tunneling ionization rate [see Fig. 7.1(c)] and the differential PICS for electrons ejected along the polarization axis [see Fig. 7.1(b)] (the modulus square of photoionization transition dipole is proportional to differential PICS). The resulting alignment dependence of H27 is shown in Fig. 7.1(d). It shows that at the intensity of 2×10^{14} W/cm^2 HOMO-1 overtakes HOMO in contributing to the generation of H27 when molecules are aligned near 90°. Using the QRS theory, Le *et al.* [103] were able to explain these results observed experimentally by McFarland *et al.* [163]. We comment that the HHG contributions from the three orbitals shown in Fig. 7.1(d) should have been added coherently. Coherence can be neglected in regions where there is only one dominant channel as discussed in Sec. 6.2 and Sec. 6.3.

One advantage of studying HHG is that the phase of the dipole transition matrix element can be retrieved from the phase of the harmonics, see Refs. [95, 102, 165, 168]. On the other hand, unlike photoionization, experimental HHG spectra suffer from macroscopic propagation effect as discussed in Chapter 6 and thus care must be taken when drawing conclusions on single molecule HHG spectra from experimental HHG spectra.

7.3 Total photoionization yield from aligned N_2 and CO_2 molecules

Thomann *et al.* [79] employed a state-of-the-art high-harmonic ultrafast soft X-ray to ionize field-free aligned molecules in which the cations are nondissociative. In their experiment, a single harmonic order – H27 at 43 eV – with a width of a few eV's, was selected as the ionizing probe pulse. The ion yield was detected around the first half-revival of 4.2 ps for N_2 and 21.0 ps for CO_2, respectively. The polarization axes for the aligning and ionizing pulses were parallel such that molecular distributions had cylindrical symmetry with respect to the polarization axis. They presented the yields of singly ionized N_2 and CO_2 by 43 eV photons as a function of time delay between the two pulses. In this section, we report the comparison between our theoretical calculations with their experimental results. The formulation for the alignment dependence of integrated PICS is presented in Appendix C.3.

7.3.1 Single-photon ionization yield of aligned N_2 molecules: theory vs experiment

In Fig. 7.2(a), we show the calculated degree of alignment $\langle\cos^2\theta\rangle$ for N_2 vs time delay. In the calculation, the pump laser has wavelength of 800 nm, duration(full width at half maximum, FWHM) of 140 fs, and intensity of 5×10^{12} W/cm^2, taken from Ref. [79]. We choose gas temperature of 20 K to obtain a high degree of alignment. By solving the time-dependent Schrödinger equation of Eq. (B.1), $\langle\cos^2\theta\rangle$ can be calculated from Eq. (B.4). In Fig. 7.2(c) the alignment-dependent PICS (summed over X, A and B ionic states) are shown. Combining with the calculated alignment distribution of molecules, we obtain the photoionization yield vs time delay. The results are shown in Fig. 7.2(b) and compared to experimental data of Ref. [79]. Clearly the theoretical calculations are in good agreement with experiment. It shows that when molecules are aligned mostly perpendicular to the polarization axis the total ionization yield peaks. This is easily understood from Fig. 7.1(a), or from Fig. 7.2(c) which shows the sum of ionization cross sections (normalized at θ=90°)

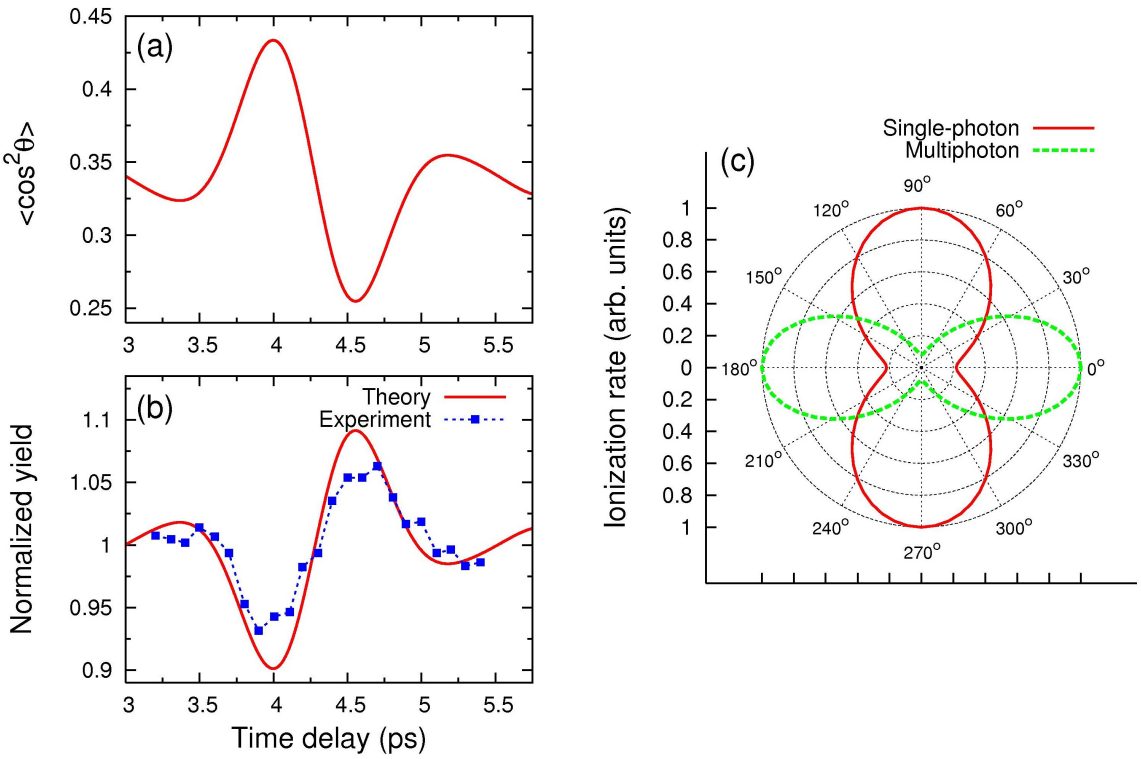

Figure 7.2: *(a) Calculated degree of alignment* $\langle\cos^2\theta\rangle$ *for* N_2 *vs time delay near first half-revival. (b) Single-photon ionization yield from transiently aligned* N_2 *by 43 eV photons vs time delay: theory (solid line) and experiment (solid squares) [79]. (c) Angular dependence of the ionization rate in single-photon (43 eV) ionization (solid line), and by multiphoton ionization by an IR laser with intensity of* 2×10^{14} *W/cm*^{2} *(dashed line). Adapted from Publication [15].*

from the X, A and B ionic states. For comparison, the alignment dependence of multiphoton ionization rates (normalized at θ=0°) by intense IR lasers at peak intensity of 2×10^{14} W/cm^2 are also shown in Fig. 7.2(c). The ionization rate here is calculated by using the MO-ADK theory [19]. In this case, ionization occurs mostly from the X ionic state, i.e., only from the HOMO orbital.

7.3.2 Single-photon ionization yield of aligned CO_2 molecules: theory vs experiment

Similar calculations are carried out for CO_2 molecules. The parameters for the pump laser are wavelength of 800 nm, duration (FWHM) of 140 fs, and intensity of 3.5×10^{12} W/cm^2,

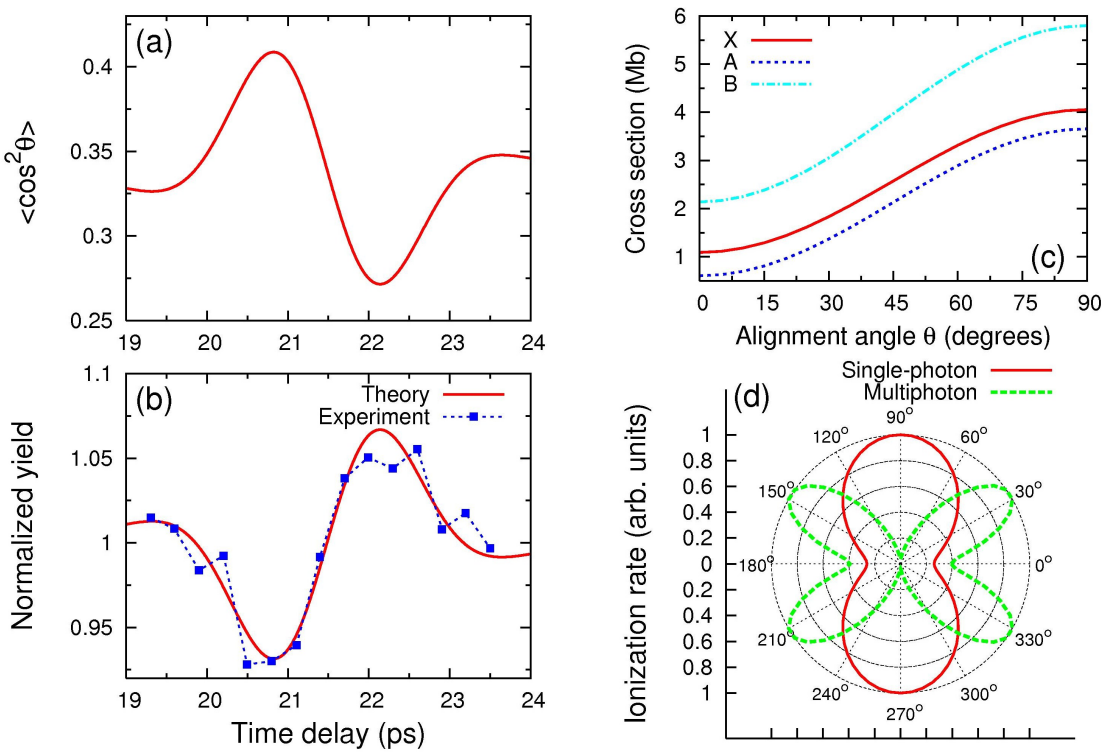

Figure 7.3: *(a) Calculated degree of alignment* $\langle\cos^2\theta\rangle$ *for* CO_2 *vs time delay near first half-revival. (b) Single-photon ionization yield from transiently aligned* CO_2 *by 43 eV photons vs time delay: theory (solid line) and experiment (solid squares) [79]. (c) Integrated photoionization cross section for ionization leading to the X (solid line), A (dotted line) and B (dot dashed line) ionic states of* CO_2^+*, with alignment angle* θ*, by single-photon (43 eV) ionization of* CO_2*. (d) Angular dependence of the ionization rate for single-photon (43 eV) ionization (solid line), and for multiphoton ionization by an infrared laser with intensity of* 1.1×10^{14} *W/cm*^{2} *(dashed line). Adapted from Publication [15].*

taken form [79]. The gas temperature is chosen to be 20 K. PICS at each fixed alignment angle θ for ionization leading to CO_2^+ in the X $^2\Pi_g$, A $^2\Pi_u$ and B $^2\Sigma_u^+$ ionic states are shown in Fig. 7.3(c). The asymmetry parameter $\beta_{\hat{n}}$ extracted from Fig. 7.3(c) are -0.64, -0.77 and -0.53 for the X, A and B states, respectively. And the θ-dependence of the ionization cross sections (summed over X, A and B states, and normalized at θ=90°) are shown in polar plot in Fig. 7.3(d). In Fig. 7.3(d) the total multiphoton ionization rate (normalized at θ=35°) vs θ for an IR laser with intensity of 1.1×10^{14} W/cm^2 is also shown. The latter has the shape of a butterfly, reflecting the angular dependence of the π_g orbital of the HOMO. Note that

in adding up cross sections from different channels, the degeneracy of the molecular orbitals should be included.

The $\langle \cos^2 \theta \rangle$ and the total ionization yield vs time delay for CO_2 are shown in Figs. 7.3(a) and (b), respectively. Both have behavior that is quite similarly to the behavior seen in Figs. 7.2(a) and (b) for N_2. The calculated results in Fig. 7.3(b) are in good agreement with the results from Ref. [79]. Note that the alignment dependence of multiphoton ionization for individual X, A and B ionic states are actually quite different and they have different oribtal symmetries. To obtain tunneling ionization rate from the MO-ADK theory shown in Fig. 7.3(d) the vertical ionization energies are taken from [100, 197] while the molecular parameters are from Zhao *et al.* (see Publication [14]). The similar alignment-dependent multiphoton ionization rates for different laser intensities have been shown in Fig. 6.11 by using MO-ADK theory or strong-field approximation.

7.4 Photoelectron angular distributions (PADs) of fixed-in-space N_2 molecules in the laboratory frame

Experimentally, COLTRIMS (Cold Target Recoil Ion Momentum Spectroscopy) has been used to measure the full momentum vectors of charged particles resulting from the ionization of molecules [198]. For different ionization channels, the detected photoelectron energy $E_{\rm pe}$ is related to photon energy $h\nu$ and vertical ionization energy $E_{\rm ion}$ by $E_{\rm pe} = h\nu - E_{\rm ion}$. The PAD from different ionization channels can be measured. We present the results in the laboratory frame so they can be compared to future measurements. The formulation for the PAD in the laboratory frame in presented in Appendix C.4.

In Fig. 7.4, we show the PAD from fixed-in-space N_2 molecules that make an angle θ with the polarization axis. Photons of 43 eV are used and the ions are left in the X, A and B ionic states after PI. Figs. 7.4(a)-(c) compare the PAD for emission angles from 0° to 90° for several molecular alignments. As the alignment angle changes, the PAD changes rapidly. The PADs for the three channels at a given molecular alignment angle also vary

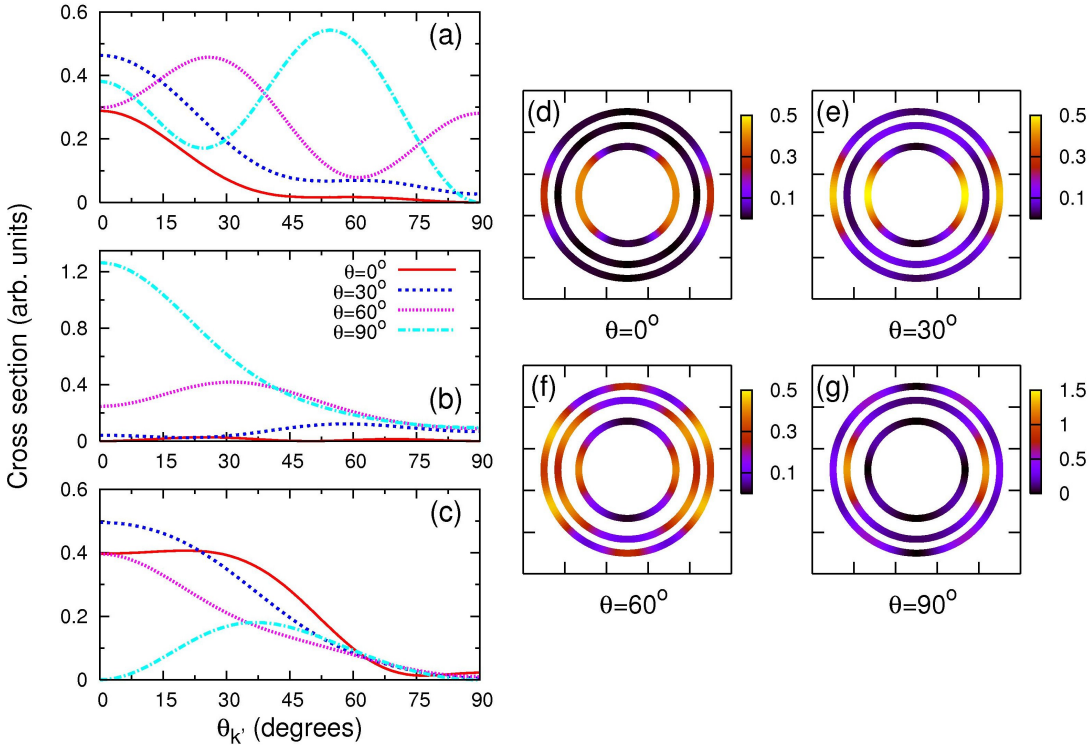

Figure 7.4: *Photoionization cross sections in the laboratory frame for single-photon (43 eV) ionization of fixed-in-space N_2 vs emission angle $\theta_{k'}$ at alignment angles indicated and for ionization leading to N_2^+ in the X, A and B states, shown in panels (a)-(c), respectively. In panels (d)-(g) the same distributions are shown for the X, A and B channels at each fixed-in-space molecular alignment angle. See text. Adapted from Publication [15].*

significantly. For easier comparison of the complicated PAD, false colors are used to present the PAD for each ionic state, see Figs. 7.4(d)-(g). The radius measures the photoelectron energies. Thus the rings, starting from the outermost rings, are for electrons ejected from HOMO, HOMO-1 and HOMO-2, respectively. These complicated variations of the PADs from aligned molecules is in strong contrast with PI from isotropically distributed molecules where the PAD depends on a single β-parameter, and can be expressed as in Eq. (C.25).

7.5 PADs of transiently aligned N_2 molecules in the laboratory frame

7.5.1 PADs of aligned N_2 molecules at the low degree of alignment

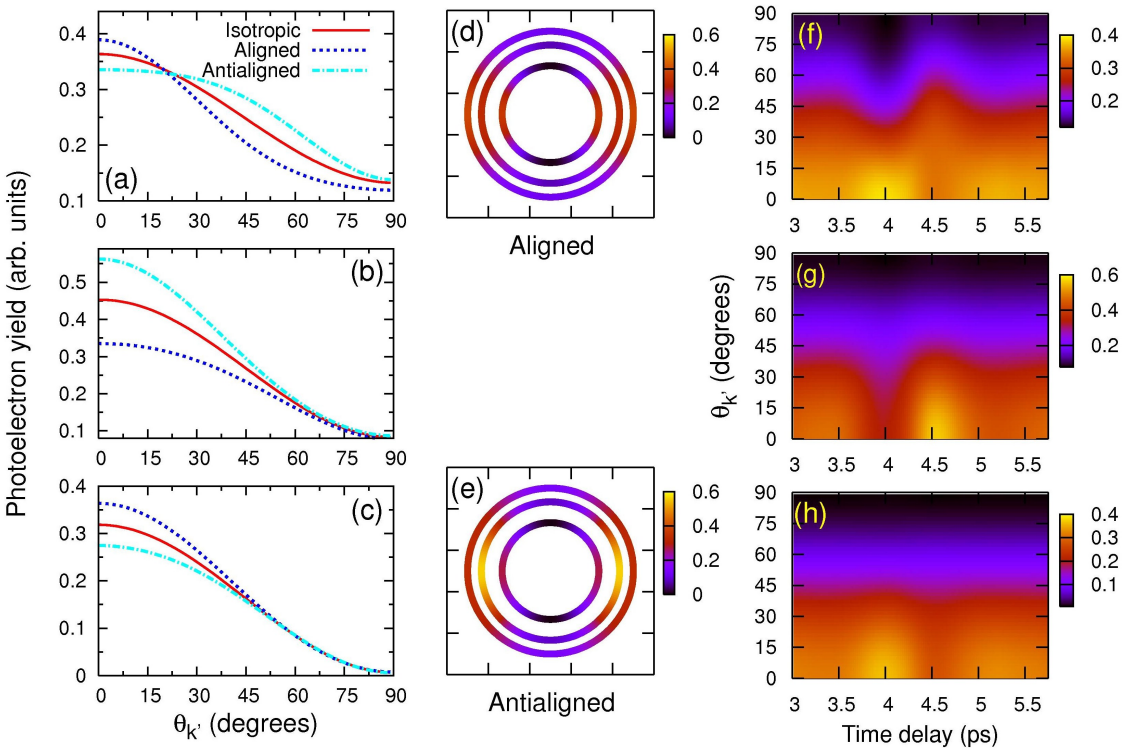

Figure 7.5: *PADs in the laboratory frame for single-photon (43 eV) ionization of N_2 as a function of emission angle $\theta_{k'}$ and pump-probe time delay. (a)-(c): Molecules are maximally aligned (τ=4.00 ps), antialigned (τ=4.55 ps), and isotropically distributed, for ionization leading to N_2^+ ions in X, A and B states, respectively. (d) and (e): The same distributions are compared for maximally aligned and antialigned molecules. (f)-(h): PADs vs time delay for the X, A and B channels, respectively. Adapted from Publication [15].*

For transiently aligned molecules the angular distribution of molecules with respect to laser polarization axis evolves with time delay. To compare with experimental measurements, the PAD for each fixed angle must be averaged over the molecular alignment distributions. In Figs. 7.5(a)-(c), we show the PAD after such averaging for the X, A and B ionic states, respectively, at the two time delays when molecules are maximally aligned or antialigned. Note that the angular averaging has severely smoothed out the structures

compared to the "raw" data shown in Fig. 7.4. In Figs. 7.5(a)-(c) we also show the PAD for molecules that are isotropically distributed for comparison. Using Eq. (C.25), we find the values of $\beta_{\hat{k}'}$ to be 0.74, 1.20 and 1.88 for the X, A and B channels, respectively [99]. In Figs. 7.5(d) and (e) the PAD from the three ionic states are compared together. Such data can be compared directly to future experiments since the PAD has been expressed in the laboratory frame with the fixed polarization axis. Alternatively, the laboratory-fixed PAD for each ionic state vs the time delay can also be measured and they are shown in Figs. 7.5(f)-(h). While the degree of molecular alignment by IR lasers is not very sharp, in the future data like Figs. 7.5(f)-(h) can be de-convoluted to retrieve PAD for fixed molecular alignment angles, and to compare with theoretical calculations shown in Figs. 7.4(a)-(c).

7.5.2 PADs of aligned N_2 molecules at the high degree of alignment

In Fig. 7.5, we assume that the pump laser to align the molecules is the same as that assumed in Fig. 7.2. The maximum degree of alignment is only $\langle\cos^2\theta\rangle$=0.43, such that no striking features are seen. In order to improve the contrast, we assume a pump laser with intensity of 5×10^{13} W/cm^2, duration of 60 fs at temperature of 20 K to align molecules. The maximum degree of alignment achieved is $\langle\cos^2\theta\rangle$=0.71. We show the PAD in the laboratory frame in Fig. 7.6. Molecules are maximally aligned at τ=4.04 ps and antialigned at τ=4.39 ps. In comparison with Fig. 7.5, with the better alignment, we can clearly see the improved contrast and PADs of aligned and antialigned molecules become closer to that for fixed-in-space molecules at θ=0° and 90°, respectively, see Fig. 7.5.

7.6 Photon energy dependence of PADs for aligned N_2 molecules

All the calculations above have been carried out at photon energy of 43 eV. Next we explore the behavior of the alignment dependence of the PAD at photon energies of 20 eV, 30 eV and

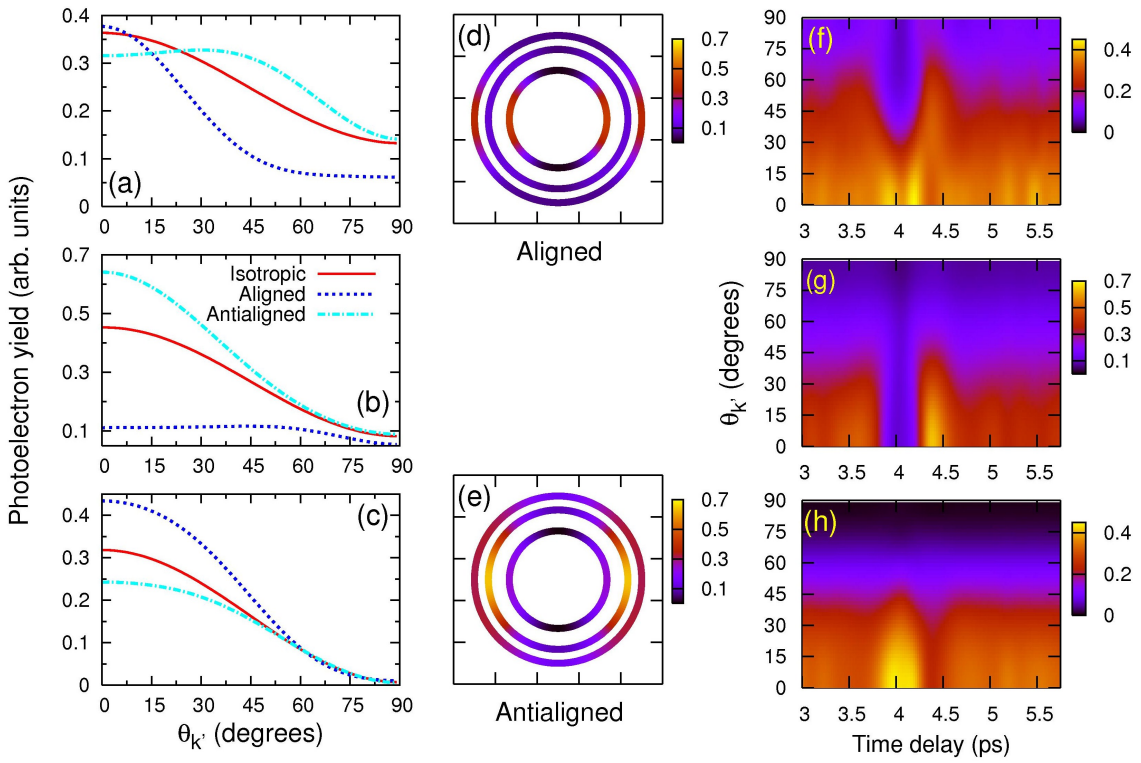

Figure 7.6: *Same as Fig. 7.5 except that a strong aligning pump laser is assumed. See text. Adapted from Publication [15].*

46 eV. In Fig. 7.7 the PAD for the X, A, and B channels are shown for fixed alignment angles of θ=0°, 30°, 60° and 90°, respectively, together with the PAD for isotropically distributed molecules. As the photon energy changes, the PAD also vary substantially at each alignment angle. At 30 eV, as shown in Lucchese *et al.* [99], there is a $3\sigma_g \rightarrow k\sigma_u$ resonance in the HOMO channel. From Fig. 7.7(e), we further demonstrate that this resonance occurs for small alignment angles only. [The same conclusion is obtained in Fig. 6.5(a).] From Fig. 7.7, it is clear that the PAD for aligned molecules are quite complicated. The PAD changes much with photon energy as well as with the alignment angle. Thus in trying to understand the dynamics of a molecule, measurements that do not explore the alignment dependence will tend to miss important features.

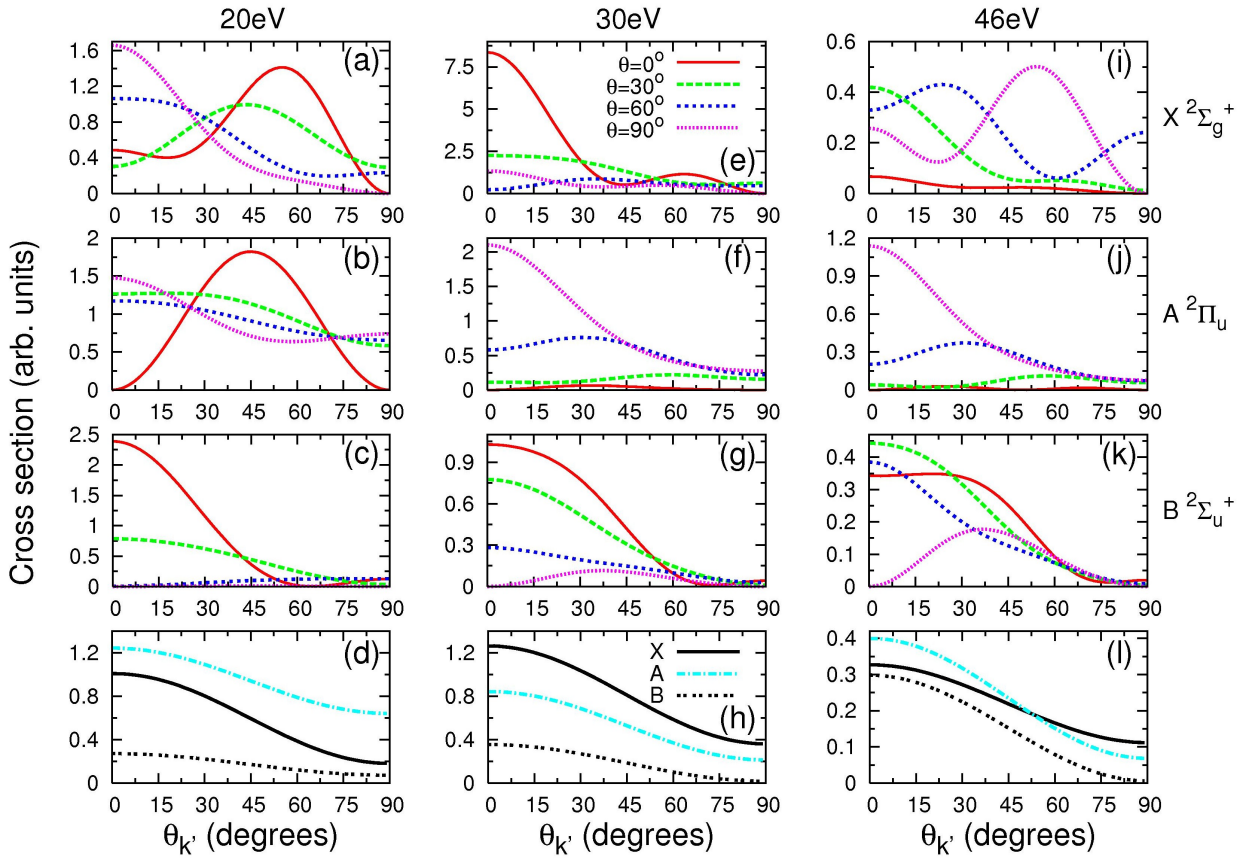

Figure 7.7: *Fixed-in-space photoionization angular distributions (vs $\theta_{k'}$) in the laboratory frame, for photon energies of 20eV, 30eV or 46eV, and the four alignment angles are shown. First row: X-channel. Second row: A-channel. Third row: B-channel. The last row shows that the PAD becomes featureless if the molecules are isotropically distributed. Adapted from Publication [15].*

7.7 PADs of transiently aligned CO_2 molecules in the laboratory frame

7.7.1 PADs of fixed-in-space CO_2 molecules

In Fig. 7.8 we show the PAD in the laboratory frame for CO_2 ionized by a 43 eV photon. The three ionization channels considered are $X\ ^2\Pi_g$, $A\ ^2\Pi_u$ and $B\ ^2\Sigma_u^+$, with ionization potential of 13.8, 17.7 and 18.2 eV, respectively [100, 197]. In Figs. 7.8(a)-(c) the PAD are shown at alignment angles θ=0°, 30°, 60° and 90°, respectively. In Figs. 7.8(d)-(g) the PAD from the three channels are compared together using false colors. The radius of the circle

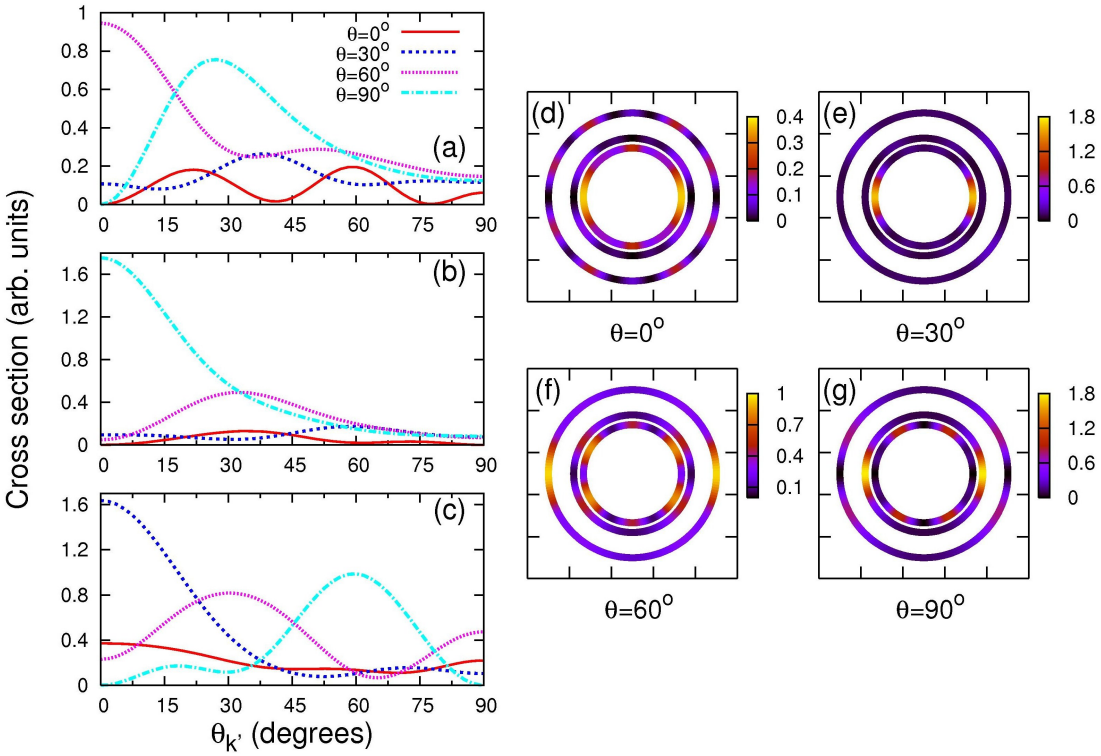

Figure 7.8: *Photoionization cross sections in the laboratory frame for single-photon (43 eV) ionization of fixed-in-space CO_2 vs emission angle $\theta_{k'}$ at alignment angles indicated and for ionization leading to CO_2^+, in panels (a)-(c), in the X, A and B states, respectively. In panels (d)-(g) the same distributions are shown for the X, A and B channels at each fixed-in-space molecular alignment angle. See Text. Adapted from Publication [15].*

is a measure of the energy of the photoelectron.

7.7.2 PADs of aligned CO_2 molecules

In Figs. 7.9 (a)-(c) we show the calculated PAD for CO_2 molecules aligned by a pump laser at the time delay of τ=20.82 ps and 22.14 ps when molecules are aligned and antialigned, as well as when molecules are isotropically distributed. The PAD are compared together in Figs. 7.9(d) and (e), and vs the time delay in Figs. 7.9(f)-(h). The asymmetry parameters, $\beta_{\hat{k}'}$, in Eq. (C.25), can be deduced from Figs. 7.9 (a)-(c), are 0.92, 1.32 and 0.68 for X, A and B states, respectively [100]. Since the angular distribution of molecules can be considered as known, in the future when experimental data similar to Figs. 7.9(f)-(h) become available,

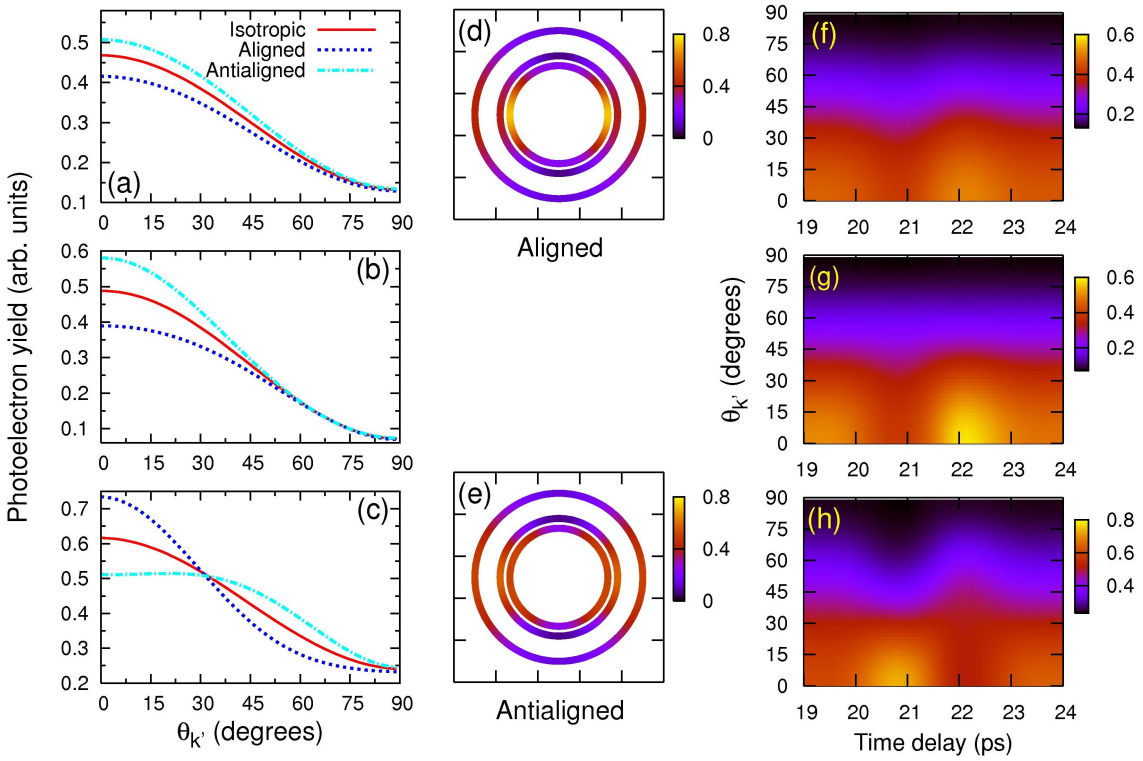

Figure 7.9: *PADs in the laboratory frame for single-photon (43 eV) ionization of CO_2 as a function of emission angle $\theta_{k'}$ and pump-probe time delay. (a)-(c): Molecules are maximally aligned (τ=20.82 ps), antialigned (τ=22.14 ps) and isotropically distributed, for ionization leading to CO_2^+ ions in the X, A and B states, respectively. (d) and (e): The same distributions are compared for maximally aligned and antialigned molecules. (f)-(h): PADs vs time delay for the X, A and B channels, respectively. Adapted from Publication [15].*

one may deconvolute the experimental results to retrieve the alignment dependence of the PAD and compare to the calculated values.

7.8 Conclusion

In this chapter we study photoelectron angular distributions (PADs) from aligned molecules. These data can provide much more details on the molecule than PAD from isotropically distributed molecules [193]. Since field-free molecular alignment can only be achieved by an IR laser, PAD from aligned molecules can be measured only at strong-field IR laser facili-

ties. The IR laser can be used to align molecules, to generate soft X-ray or XUV photons, and to ionize aligned molecules. Experiments have been carried out to determine the total ionization yield from such aligned molecules. With higher intensity of XUV photons or soft X-ray becoming available, one can measure the PAD from aligned molecules. In fact, such measurement has been reported recently [80]. We calculate PADs theoretically for geometries where the PAD can be measured in the future. Using aligned linear molecules such as N_2 and CO_2, we calculate the expected PAD for the removal of one electron from the HOMO, HOMO-1 and HOMO-2 orbitals, by photoionization codes that have been developed. These theoretical predictions often have not been tested except for randomly distributed molecules. In the future, PAD from aligned molecules that are also undergoing changes in the vibrational degrees of freedom can also be measured. In fact, such experiments have been demonstrated by Bisgaard *et al.* [77] and PAD will be able to provide insights on the time-dependent systems. With these possibilities, the well-tested PAD measurements of isotropically distributed molecules are expected to play important roles in structure determination of molecules.

Chapter 8

Summary

High-order harmonic generation (HHG) is a dramatic nonlinear process when atoms or molecules are exposed to an intense infrared laser pulse. In this process, the fundamental laser light is efficiently converted to an extreme ultraviolet (XUV) or soft X-ray light. Its potential has been shown to probe the electronic structure of targets and the time-resolved molecular structure, ionize the aligned molecules, and produce the attosecond pulse train and isolated attosecond pulse. In this thesis, we have established a complete model for HHG in a gaseous medium by incorporating the quantitative rescattering (QRS) theory with the standard macroscopic propagation theory. Here we will summarize the main achievements in this thesis.

1. Numerical modeling the macroscopic HHG.

To describe a HHG process completely, we need to consider both the single-atom (or single-molecule) response and macroscopic response of the medium. The QRS theory is an efficient approach to calculate the single-atom (or single-molecule) induced dipole, which has the comparable accuracy with solving the time-dependent Schrödinger equation (TDSE). It is then fed into the propagation equation of the harmonic field. Meanwhile we include plasma, dispersion, and Kerr effects for the propagation of fundamental laser field in the medium. The further free propagation of harmonics from the exit plane of a gas jet can be handled by Hankel transformation. Two types of spatial beams for the fundamental laser, Gaussian and truncated Bessel beams, are incorporated into propagation model, which are

mainly dealing with the multi-cycle and few-cycle laser pulses, respectively. Our model has been checked against the TDSE results by comparing both the magnitude and phase of macroscopic HHG.

2. Quantitative comparison with measured HHG.

Since the HHG is a coherent process, there are many factors which can influence the HHG spectrum. The direct comparison with measured HHG spectrum for atoms is rare, and it has not been done for molecules as far as our knowledge goes. In the usual studies of single-atom (or single-molecule) HHG, we are mainly concerned about laser intensity, pulse duration, wavelength, and carrier-envelope phase (CEP). Besides these parameters, we also include position and width of the gas jet, gas pressure, spatial beam modes, detecting system, and so on in our model. The more experimental parameters can be specified, the better simulation can be resulted from our model. For a few examples with the well specified experimental conditions, we are able to show the good agreement between the measured HHG spectrum and the simulation over a broad photon-energy region for isotropic and aligned N_2 and CO_2. According to our knowledge, this is the first time that measured HHG spectrum of molecules can be described quantitatively by theory. We also show the good quantitative agreement between measured HHG spectra of Ar and simulations for different wavelengths. For recently measured HHG spectrum of Xe using a mid-infrared laser pulse, our model is able to predict the multi-electron effect and continuum structure.

3. Factorization of macroscopic HHG.

In QRS theory, the HHG from a single atom (or a single molecule) can be separated as an electron returning wave packet and a photorecombination (PR) transition dipole. In this thesis, we have proven numerically that the macroscopic HHG can be written as a product of a "macroscopic wave packet" (MWP) and a PR transition dipole. For a molecular target, the PR transition dipole is replaced by an alignment-averaged one. The PR transition dipole reflects the electronic structure of a target, i.e., the property of a target only. While the laser and medium propagation effects can all be included in MWP. For the same target, all

the variations of HHG spectra by changing experimental conditions can be attributed to the differences in the MWP. This factorization (or separable approximation) of HHG after macroscopic propagation provides a necessary theoretical basis for extracting the electronic structure of molecular orbital from HHG spectrum.

4. Spatial filtering in the far field for isolated attosecond pulse generation.

The continuum harmonics in the spectrum (in the frequency domain) are generally used to produce an isolated attosecond pulse (IAP) (in time domain). However, it is challenged to measure the duration of an IAP experimentally. To make a connection between an IAP and continuum harmonics, alternatively it has to rely on the theoretical model. In this thesis, we have investigated the continuum structure in the HHG spectrum of Xe, measured with a CEP-not-stabilized few-cycle mid-infrared laser pulse. By using the time-frequency (or wavelet) analysis we are able to show that the reshaping of the fundamental laser field is responsible for the continuous harmonics. And then we have suggested an approach to create an IAP by using a filter centered on axis to select the harmonics in the far field with different divergence. This approach has been tested for different CEPs.

5. Multiple orbital contribution in HHG for aligned molecules.

The first step for HHG process is tunneling ionization. Since the tunneling ionization rate depends on the ionization potential exponentially, the electrons are usually ionized from the outmost molecular orbital (or highest-occupied molecular-orbital, HOMO) only. However, the ionization rate also depends on the symmetry of molecular orbital. At some alignment angles, the ionization rate of outmost molecular orbital becomes small, while it becomes large for some inner molecular orbitals. In this case, the HHG process could occur in both the outmost and inner molecular orbitals. There are two mostly studied molecules, N_2 and CO_2. The HOMO-1 contributes to HHG when the laser polarization is perpendicular to the molecular axis of N_2. For CO_2, the contribution of HOMO-2 is presented in HHG when laser polarization is parallel to the molecular axis. In this thesis, we have shown that the HOMO-1 contribution of N_2 in HHG spectrum over a broad region of photon energy can

be controlled by the laser intensity. And the minimum in the HHG spectrum of CO_2 can be easily influenced by many factors due to the interference between HOMO and HOMO-2. This can explain why the minima measured in different laboratories may vary.

In brief, we have established an *ab initio* model to describe the HHG completely. A few interesting issues in the field have been touched in this thesis. All these studies strengthen the theoretical basis for the applications of HHG, and they are also helpful for experimentalists in the future.

Bibliography

[1] P. A. Franken, A. E. Hill, C. W. Peters, and G. Weinreich. Generation of optical harmonics. *Phys. Rev. Lett.*, 7:118–119, 1961.

[2] G. H. C. New and J. F. Ward. Optical third-harmonic generation in gases. *Phys. Rev. Lett.*, 19:556–559, 1967.

[3] J. Reintjes, R. C. Eckardt, C. Y. She, N. E. Karangelen, R. C. Elton, and R. A. Andrews. Generation of coherent radiation at 53.2 nm by fifth-harmonic conversion. *Phys. Rev. Lett.*, 37:1540–1543, 1976.

[4] A. McPherson, G. Gibson, H. Jara, U. Johann, T. S. Luk, I. A. McIntyre, K. Boyer, and C. K. Rhodes. Studies of multiphoton production of vacuum-ultraviolet radiation in the rare gases. *J. Opt. Soc. Am. B*, 4:595–601, 1987.

[5] M. Ferray, A. L'Huillier, X. F. Li, L. A. Lompré, G. Mainfray, and C. Manus. Multiple-harmonic conversion of 1064 nm radiation in rare gases. *J. Phys. B*, 21:L31–L35, 1988.

[6] A. Rundquist, C. G. Durfee III, Z. Chang, C. Herne, S. Backus, M. M. Murnane, and H. C. Kapteyn. Phase-matched generation of coherent soft X-rays. *Science*, 280:1412–1415, 1998.

[7] R. A. Bartels, A. Paul, H. Green, H. C. Kapteyn, M. M. Murnane, S. Backus, I. P. Christov, Y. Liu, D. Attwood, and C. Jacobsen. Generation of spatially coherent light at extreme ultraviolet wavelengths. *Science*, 297:376–378, 2002.

[8] J. L. Krause, K. J. Schafer, and K. C. Kulander. High-order harmonic generation from atoms and ions in the high intensity regime. *Phys. Rev. Lett.*, 68:3535–3538, 1992.

[9] P. B. Corkum. Plasma perspective on strong field multiphoton ionization. *Phys. Rev. Lett.*, 71:1994–1991, 1993.

[10] M. Lewenstein, Ph. Balcou, M. Y. Ivanov, A. L'Huillier, and P. B. Corkum. Theory of high-harmonic generation by low-frequency laser fields. *Phys. Rev. A*, 49:2117–2132, 1994.

[11] P. Antoine, A. L'Huillier, M. Lewenstein, P. Salières, and B. Carré. Theory of high-order harmonic generation by an elliptically polarized laser field. *Phys. Rev. A*, 53:1725–1745, 1996.

[12] C. Winterfeldt, C. Spielmann, and G. Gerber. Colloquium: Optimal control of high-harmonic generation. *Rev. Mod. Phys.*, 80:117–140, 2008.

[13] M. Protopapas, C. H. Keitel, and P. L. Knight. Atomic physics with super-high intensity lasers. *Rep. Prog. Phys.*, 60:389–486, 1997.

[14] P. Salières, A. L'Huillier, P. Antoine, and M. Lewenstein. Study of the spatial and temporal coherence of high-order harmonics. *Adv. At. Mol. Opt. Phys.*, 41:83–142, 1999.

[15] T. Pfeifer, C. Spielmann, and G. Gerber. Femtosecond x-ray science. *Rep. Prog. Phys.*, 69:443–505, 2006.

[16] M. B. Gaarde, J. L. Tate, and K. J. Schafer. Macroscopic aspects of attosecond pulse generation. *J. Phys. B*, 41:132001, 2008.

[17] L. V. Keldysh. Ionization in the field of a strong electromagnetic wave (multiphonon absorption processes and ionization probability for atoms and solids in strong electromagnetic field). *Sov. Phys. - JETP*, 20:1307–1314, 1965.

[18] M. V. Ammosov, N. B. Delone, and V. P. Krainov. Tunnel ionization of complex

atoms and of atomic ions in an alternating electromagnetic field. *Sov. Phys. - JETP*, 64:1191–1194, 1986.

[19] X. M. Tong, Z. X. Zhao, and C. D. Lin. Theory of molecular tunneling ionization. *Phys. Rev. A*, 66:033402, 2002.

[20] V. Strelkov. Role of autoionizing state in resonant high-order harmonic generation and attosecond pulse production. *Phys. Rev. Lett.*, 104:123901, 2010.

[21] A. D. Shiner, B. E. Schmidt, C. Trallero-Herrero, H. J. Wörner, S. Patchkovskii, P. B. Corkum, J.-C. Kieffer, F. Légaré, and D. M. Villeneuve. Probing collective multi-electron dynamics in xenon with high-harmonic spectroscopy. *Nature Phys.*, 7:464–467, 2011.

[22] P. Agostini, F. Fabre, G. Mainfray, G. Petite, and N. K. Rahman. Free-free transitions following six-photon ionization of xenon atoms. *Phys. Rev. Lett.*, 42:1127–1130, 1979.

[23] G. G. Paulus, W. Nicklich, H. Xu, P. Lambropoulos, and H. Walther. Plateau in above threshold ionization spectra. *Phys. Rev. Lett.*, 72:2851–2854, 1994.

[24] D. N. Fittinghoff, P. R. Bolton, B. Chang, and K. C. Kulander. Observation of nonsequential double ionization of helium with optical tunneling. *Phys. Rev. Lett.*, 69:2642–2645, 1992.

[25] B. Walker, B. Sheehy, L. F. DiMauro, P. Agostini, K. J. Schafer, and K. C. Kulander. Precision measurement of strong field double ionization of helium. *Phys. Rev. Lett.*, 73:1227–1230, 1994.

[26] C. D. Lin, A. T. Le, Z. Chen, T. Morishita, and R. Lucchese. Strong-field rescattering physics—self-imaging of a molecule by its own electrons. *J. Phys. B*, 43:122001, 2010.

[27] B. Shan and Z. Chang. Dramatic extension of the high-order harmonic cutoff by using a long-wavelength driving field. *Phys. Rev. A*, 65:11804, 2001.

[28] W. Becker, S. Long, and J. K. McIver. Modeling harmonic generation by a zero-range potential. *Phys. Rev. A*, 50:1540–1560, 1994.

[29] J. Tate, T. Auguste, H. G. Muller, P. Salières, P. Agostini, and L. F. DiMauro. Scaling of wave-packet dynamics in an intense midinfrared field. *Phys. Rev. Lett.*, 98:013901, 2007.

[30] K. Schiessla, K. L. Ishikawab, E. Persson, and J. Burgdörfer. Wavelength dependence of high-harmonic generation from ultrashort pulses. *J. Mod. Opt.*, 55:2617–2630, 2008.

[31] M. V. Frolov, N. L. Manakov, and A. F. Starace. Wavelength scaling of high-harmonic yield: Threshold phenomena and bound state symmetry dependence. *Phys. Rev. Lett.*, 100:173001, 2008.

[32] A. D. Shiner, C. Trallero-Herrero, N. Kajumba, H.-C. Bandulet, D. Comtois, F. Légaré, M. Giguère J.-C. Kieffer, P. B. Corkum, and D. M. Villeneuve. Wavelength scaling of high harmonic generation efficiency. *Phys. Rev. Lett.*, 103:073902, 2009.

[33] G. Doumy, J. Wheeler, C. Roedig, R. Chirla, P. Agostini, and L. F. DiMauro. Attosecond synchronization of high-order harmonics from midinfrared drivers. *Phys. Rev. Lett.*, 102:093002, 2009.

[34] R. López-Martens, K. Varjú, P. Johnsson, J. Mauritsson, Y. Mairesse, P. Salières, M. B. Gaarde, K. J. Schafer, A. Persson, S. Svanberg, C.-G. Wahlström, and A. L'Huillier. Amplitude and phase control of attosecond light pulses. *Phys. Rev. Lett.*, 94:033001, 2005.

[35] Y. Mairesse, A. de Bohan, L. J. Frasinski, H. Merdji, L. C. Dinu, P. Monchicourt, P. Breger, M. Kovačev, R. Taieb, B. Carre, H. G. Muller, P. Agostini, and P. Salières. Attosecond synchronization of high-harmonic soft X-rays. *Science*, 302:1540–1543, 2003.

[36] Ph. Balcou, P. Salières, A. L'Huillier, and M. Lewenstein. Generalized phase-matching conditions for high harmonics: The role of field-gradient forces. *Phys. Rev. A*, 55:32043210, 1997.

[37] H. Dachraoui, T. Auguste, A. Helmstedt, P. Bartz, M. Michelswirth, N. Mueller, W. Pfeiffer, P. Salières, and U. Heinzmann. Interplay between absorption, dispersion and refraction in high-order harmonic generation. *J. Phys. B*, 42:175402, 2009.

[38] M. Lewenstein, P. Salières, and A. L'Huillier. Phase of the atomic polarization in high-order harmonic generation. *Phys. Rev. A*, 52:47474754, 1995.

[39] Ph. Balcou, A. S. Dederichs, M. B. Gaarde, and A. L'Huillier. Quantum-path analysis and phase matching of high-order harmonic generation and high-order frequency mixing processes in strong laser fields. *J. Phys. B*, 32:2973–2989, 1999.

[40] M. B. Gaarde, F. Salin, E. Constant, Ph. Balcou, K. J. Schafer, K. C. Kulander, and A. L'Huillier. Spatiotemporal separation of high harmonic radiation into two quantum path components. *Phys. Rev. A*, 59:13671373, 1999.

[41] M. B. Gaarde and K. J. Schafer. Quantum path distributions for high-order harmonics in rare gas atoms. *Phys. Rev. A*, 65:031406, 2002.

[42] E. Constant, D. Garzella, P. Breger, E. Mevel, C. Dorrer, C. Le Blanc, F. Salin, and P. Agostini. Optimizing high harmonic generation in absorbing gases: Model and experiment. *Phys. Rev. Lett.*, 82:1668–1671, 1999.

[43] C. G. Durfee III, A. R. Rundquist, S. Backus, C. Herne, M. M. Murnane, and H. C. Kapteyn. Phase matching of high-order harmonics in hollow waveguides. *Phys. Rev. Lett.*, 83:2187–2190, 1999.

[44] E. Esarey, P. Sprangle, J. Krall, and A. Ting. Self-focusing and guiding of short laser pulses in ionizing gases and plasmas. *IEEE J. Quantum Electron.*, 33:1879–1914, 1997.

[45] M. B. Gaarde, M. Murakami, and R. Kienberger. Spatial separation of large dynamical blueshift and harmonic generation. *Phys. Rev. A*, 74:053401, 2006.

[46] F. Krausz and M. Ivanov. Attosecond physics. *Rev. Mod. Phys.*, 81:163–234, 2009.

[47] P. M. Paul, E. S. Toma, P. Breger, G. Mullot, F. Augé, Ph. Balcou, H. G. Muller, and P. Agostini. Observation of a train of attosecond pulses from high harmonic generation. *Science*, 292:1689–1692, 2001.

[48] E. Goulielmakis, M. Schultze, M. Hofstetter, V. S. Yakovlev, J. Gagnon, M. Uiberacker, A. L. Aquila, E. M. Gullikson, D. T. Attwood, R. Kienberger, F. Krausz, and U. Kleineberg. Single-cycle nonlinear optics. *Science*, 320:1614–1617, 2008.

[49] G. Sansone, E. Benedetti, F. Calegari, C. Vozzi, L. Avaldi, R. Flammini, L. Poletto, P. Villoresi, C. Altucci, R. Velotta, S. Stagira, S. De Silvestri, and M. Nisoli. Isolated single-cycle attosecond pulses. *Science*, 314:443–446, 2006.

[50] H. Mashiko, S. Gilbertson, C. Li, S. D. Khan, M. M. Shakya, E. Moon, and Z. Chang. Double optical gating of high-order harmonic generation with carrier-envelope phase stabilized lasers. *Phys. Rev. Lett.*, 100:103906, 2008.

[51] C. A. Haworth, L. E. Chipperfield, J. S. Robinson, P. L. Knight, J. P. Marangos, and J. W. G. Tisch. Half-cycle cutoffs in harmonic spectra and robust carrier-envelope phase retrieval. *Nature Phys.*, 3:52–57, 2007.

[52] T. Pfeifer, A. Jullien, M. J. Abel, P. M. Nagel, L. Gallmann, D. M. Neumark, and S. R. Leone. Generating coherent broadband continuum soft-X-ray radiation by attosecond ionization gating. *Opt. Express*, 15:17120–17128, 2007.

[53] I. P. Christov, H. C. Kapteyn, and M. M. Murnane. Quasi-phase matching of high-harmonics and attosecond pulses in modulated waveguides. *Opt. Express*, 7:362–367, 2000.

[54] A. Paul, R. A. Bartels, R. Tobey, H. Green, S. Weiman, I. P. Christov, M. M. Murnane, H. C. Kapteyn, and S. Backus. Quasi-phase-matched generation of coherent extreme-ultraviolet light. *Nature*, 421:51–54, 2003.

[55] O. Cohen, X. Zhang, A. L. Lytle, T. Popmintchev, M. M. Murnane, and H. C. Kapteyn. Grating-assisted phase matching in extreme nonlinear optics. *Phys. Rev. Lett.*, 99:053902, 2007.

[56] X. Zhang, A. L. Lytle, T. Popmintchev, X. Zhou, H. C. Kapteyn, M. M. Murnane, and O. Cohen. Quasi-phase-matching and quantum-path control of high-harmonic generation using counterpropagating light. *Nature Phys.*, 3:270–275, 2007.

[57] J. Itatani, F. Quéré, G. L. Yudin, M. Yu. Ivanov, F. Krausz, and P. B. Corkum. Attosecond streak camera. *Phys. Rev. Lett.*, 88:173903, 2002.

[58] M. Kitzler, N. Milosevic, A. Scrinzi, F. Krausz, and T. Brabec. Quantum theory of attosecond XUV pulse measurement by laser dressed photoionization. *Phys. Rev. Lett.*, 88:173904, 2002.

[59] P. Johnsson, R. López-Martens, S. Kazamias, J. Mauritsson, C. Valentin, T. Remetter, K. Varjú, M. B. Gaarde, Y. Mairesse, H. Wabnitz, P. Salières, Ph. Balcou, K. J. Schafer, and A. L'Huillier. Attosecond electron wave packet dynamics in strong laser fields. *Phys. Rev. Lett.*, 95:013001, 2005.

[60] T. Remetter, P. Johnsson, J. Mauritsson, K. Varjú, Y. Ni, F. Lépine, E. Gustafsson, M. Kling, J. Khan, R. López-Martens, K. J. Schafer, M. J. J. Vrakking, and A. L'Huillier. Attosecond electron wave packet interferometry. *Nature Phys.*, 2:323–326, 2006.

[61] P. Ranitovic, X. M. Tong, B. Gramkow, S. De, B. DePaola, K. P. Singh, W. Cao, M. Magrakvelidze, D. Ray, I. Bocharova, H. Mashiko, A. Sandhu, E. Gagnon, M. M.

Murnane, H. C. Kapteyn, I. Litvinyuk, and C. L. Cocke. IR-assisted ionization of helium by attosecond extreme ultraviolet radiation. *New J. Phys.*, 12:013008, 2010.

[62] M. F. Kling and M. J. J. Vrakking. Attosecond electron dynamics. *Annu. Rev. Phys. Chem.*, 59:463–492, 2008.

[63] S. X. Hu and L. A. Collins. Attosecond pump probe: Exploring ultrafast electron motion inside an atom. *Phys. Rev. Lett.*, 96:073004, 2006.

[64] G. L. Yudin, S. Chelkowski, J. Itatani, A. D. Bandrauk, and P. B. Corkum. Attosecond photoionization of coherently coupled electronic states. *Phys. Rev. A*, 72:051401, 2005.

[65] O. Smirnova, Y. Mairesse, S. Patchkovskii, N. Dudovich, D. Villeneuve, P. Corkum, and M. Yu. Ivanov. High harmonic interferometry of multi-electron dynamics in molecules. *Nature*, 460:972–977, 2009.

[66] J. Itatani, J. Levesque, D. Zeidler, H. Niikura, H. Pépin, J. C. Kieffer, P. B. Corkum, and D. M. Villeneuve. Tomographic imaging of molecular orbitals. *Nature*, 432:867–871, 2004.

[67] C. Vozzi, M. Negro, F. Calegari, G. Sansone, M. Nisoli, S. De Silvestri, and S. Stagira. Generalized molecular orbital tomography. *Nature Phys.*, 7:822–826, 2011.

[68] M. Lein, N. Hay, R. Velotta, J. P. Marangos, and P. L. Knight. Role of the intramolecular phase in high-harmonic generation. *Phys. Rev. Lett.*, 88:183903, 2002.

[69] T. Kanai, S. Minemoto, and H. Sakai. Quantum interference during high-order harmonic generation from aligned molecules. *Nature*, 435:470–474, 2005.

[70] H. Niikura, F. Légaré, R. Hasbani, M. Yu. Ivanov, D. M. Villeneuve, and P. B. Corkum. Probing molecular dynamics with attosecond resolution using correlated wave packet pairs. *Nature*, 421:826–829, 2003.

[71] S. Baker, J. S. Robinson, C. A. Haworth, H. Teng, R. A. Smith, C. C. Chirilă, M. Lein, J. W. G. Tisch, and J. P. Marango. Probing proton dynamics in molecules on an attosecond time scale. *Science*, 312:424–427, 2006.

[72] A. H. Zewail. Femtochemistry: Atomic-scale dynamics of the chemical bond using ultrafast lasers (Nobel lecture). *Angew. Chem. Int. Ed. Engl.*, 39:2586–2631, 2000.

[73] H. Stapelfeldt and T. Seideman. Colloquium: Aligning molecules with strong laser pulses. *Rev. Mod. Phys.*, 75:543–557, 2003.

[74] B. Friedrich and D. Herschbach. Alignment and trapping of molecules in intense laser fields. *Phys. Rev. Lett.*, 74:4623–4626, 1995.

[75] F. Rosca-Pruna and M. J. J. Vrakking. Revival structures in picosecond laser-induced alignment of I_2 molecules. I. experimental results. *J. Chem. Phys.*, 116:6567–6578, 2002.

[76] M. Tsubouchi, B. J. Whitaker, L. Wang, H. Kohguchi, and T. Suzuki. Photoelectron imaging on time-dependent molecular alignment created by a femtosecond laser pulse. *Phys. Rev. Lett.*, 86:4500–4503, 2001.

[77] C. Z. Bisgaard, O. J. Clarkin, G. Wu, A. M. D. Lee, O. Geßner, C. C. Hayden, and A. Stolow. Time-resolved molecular frame dynamics of fixed-in-space CS_2 molecules. *Science*, 323:1464–1468, 2009.

[78] Y. Tang, Y.-I. Suzuki, T. Horio, and T. Suzuki. Molecular frame image restoration and partial wave analysis of photoionization dynamics of NO by time-energy mapping of photoelectron angular distribution. *Phys. Rev. Lett.*, 104:073002, 2010.

[79] I. Thomann, R. Lock, V. Sharma, E. Gagnon, S. T. Pratt, H. C. Kapteyn, M. M. Murnane, and W. Li. Direct measurement of the angular dependence of the single-photon ionization of aligned N_2 and CO_2. *J. Phys. Chem. A*, 112:9382–9386, 2008.

[80] F. Kelkensberg, A. Rouzée, W. Siu, G. Gademann, P. Johnsson, M. Lucchini, R. R. Lucchese, and M. J. J. Vrakking. XUV ionization of aligned molecules. *Phys. Rev. A*, 84:051404, 2011.

[81] B. H. Bransden and C. J. Joachain. *Physics of Atoms and Molecules*, volume 2nd Ed. New York: Prentice-Hall, 2003.

[82] K. C. Kulander and B. W. Shore. Calculations of multiple-harmonic conversion of 1064-nm radiation in Xe. *Phys. Rev. Lett.*, 62:524–526, 1989.

[83] J. C. Light, I. P. Hamilton, and J. V. Lill. Generalized discrete variable approximation in quantum mechanics. *J. Chem. Phys.*, 82:1400–1409, 1985.

[84] X. M. Tong and S. I. Chu. Theoretical study of multiple high-order harmonic generation by intense ultrashort pulsed laser fields: A new generalized pseudospectral time-dependent method. *Chem. Phys.*, 217:119–130, 1997.

[85] X. X. Zhou, X. M. Tong, Z. X. Zhao, and C. D. Lin. Role of molecular orbital symmetry on the alignment dependence of high-order harmonic generation with molecules. *Phys. Rev. A*, 71:061801, 2005.

[86] X. X. Zhou, X. M. Tong, Z. X. Zhao, and C. D. Lin. Alignment dependence of high-order harmonic generation from N_2 and O_2 molecules in intense laser fields. *Phys. Rev. A*, 72:033412, 2005.

[87] C. C. Chirilă and M. Lein. Strong-field approximation for harmonic generation in diatomic molecules. *Phys. Rev. A*, 73:023410, 2006.

[88] J. P. Marangos, C. Altucci, R. Velotta, E. Heesel, E. Springate, M. Pascolini, L. Poletto, P. Villoresi, C. Vozzi, G. Sansone, M. Anscombe, J.-P. Caumes, S. Stagira, and M. Nisoli. Molecular orbital dependence of high-order harmonic generation. *J. Mod. Opt.*, 53:97–111, 2006.

[89] A. T. Le, X. M. Tong, and C. D. Lin. Evidence of two-center interference in high-order harmonic generation from CO_2. *Phys. Rev. A*, 73:041402, 2006.

[90] S. Ramakrishna and T. Seideman. Information content of high harmonics generated from aligned molecules. *Phys. Rev. Lett.*, 99:113901, 2007.

[91] S. Odžak and D. B. Milošević. Interference effects in high-order harmonic generation by homonuclear diatomic molecules. *Phys. Rev. A*, 79:023414, 2009.

[92] A. Abdurrouf and F. H. M. Faisal. Theory of intense-field dynamic alignment and high-order harmonic generation from coherently rotating molecules and interpretation of intense-field ultrafast pump-probe experiments. *Phys. Rev. A*, 79:023405, 2009.

[93] M. J. Frisch *et al.*, GAUSSIAN 03, Revision C.02 (Gaussian Inc., Pittsburgh, PA, 2003).

[94] T. Morishita, A. T. Le, Z. Chen, and C. D. Lin. Accurate retrieval of structural information from laser-induced photoelectron and high-order harmonic spectra by few-cycle laser pulses. *Phys. Rev. Lett.*, 100:013903, 2008.

[95] A. T. Le, R. R. Lucchese, S. Tonzani, T. Morishita, and C. D. Lin. Quantitative rescattering theory for high-order harmonic generation from molecules. *Phys. Rev. A*, 80:013401, 2009.

[96] A. T. Le, T. Morishita, and C. D. Lin. Extraction of the species-dependent dipole amplitude and phase from high-order harmonic spectra in rare-gas atoms. *Phys. Rev. A*, 78:023814, 2008.

[97] H. G. Muller. Numerical simulation of high-order above-threshold-ionization enhancement in argon. *Phys. Rev. A*, 60:1341–1350, 1999.

[98] X. M. Tong and C. D. Lin. Empirical formula for static field ionization rates of atoms

and molecules by lasers in the barrier-suppression regime. *J. Phys. B*, 38:2593–2600, 2005.

[99] R. R. Lucchese, G. Raseev, and V. McKoy. Studies of differential and total photoionization cross sections of molecular nitrogen. *Phys. Rev. A*, 25:2572–2587, 1982.

[100] R. R. Lucchese and V. McKoy. Studies of differential and total photoionization cross sections of carbon dioxide. *Phys. Rev. A*, 26:1406–1418, 1982.

[101] A. T. Le, R. D. Picca, P. D. Fainstein, D. A. Telnov, M. Lein, and C. D. Lin. Theory of high-order harmonic generation from molecules with intense laser pulses. *J. Phys. B*, 41:081002, 2008.

[102] A. T. Le, R. R. Lucchese, M. T. lee, and C. D. Lin. Probing molecular frame photoionization via laser generated high-order harmonics from aligned molecules. *Phys. Rev. Lett.*, 102:203001, 2009.

[103] A. T. Le, R. R. Lucchese, and C. D. Lin. Uncovering multiple orbitals influence in high-harmonic generation from aligned N_2. *J. Phys. B*, 42:211001, 2009.

[104] E. Takahashi, V. Tosa, Y. Nabekawa, and K. Midorikawa. Experimental and theoretical analyses of a correlation between pump-pulse propagation and harmonic yield in a long-interaction medium. *Phys. Rev. A*, 68:023808, 2003.

[105] M. Geissler, G. Tempea, A. Scrinzi, M. Schnürer, F. Krausz, and T. Brabec. Light propagation in field-ionizing media: Extreme nonlinear optics. *Phys. Rev. Lett.*, 83:2930–2933, 1999.

[106] S. C. Rae and K. Burnett. Detailed simulations of plasma-induced spectral blueshifting. *Phys. Rev. A*, 46:1084–1090, 1992.

[107] E. Priori, G. Cerullo, M. Nisoli, S. Stagira, S. De Silvestri, P. Villoresi, L. Poletto, P. Ceccherini, C. Altucci, R. Bruzzese, and C. de Lisio. Nonadiabatic three-

dimensional model of high-order harmonic generation in the few-optical-cycle regime. *Phys. Rev. A*, 61:063801, 2000.

[108] A. Börzsönyi, Z. Heiner, M. P. Kalashnikov, A. P. Kovács, and K. Osvay. Dispersion measurement of inert gases and gas mixtures at 800 nm. *Appl. Opt.*, 47:4856–4863, 2008.

[109] P. J. Leonard. Dispersion measurement of inert gases and gas mixtures at 800 nm. *At. Data Nucl. Data Tables*, 14:21–37, 1974.

[110] H. J. Lehmeier, W. Leupacher, and A. Penzkofer. Nonresonant third order hyperpolarizability of rare gases and N_2 determined by third harmonic generation. *Opt. Commun.*, 56:67–72, 1985.

[111] X. F. Li, A. L'Huillier, M. Ferray, L. A. Lompré, and G. Mainfray. Multiple-harmonic generation in rare gases at high laser intensity. *Phys. Rev. A*, 39:5751–5761, 1989.

[112] J. K. Koga, N. Naumova, M. Kando, L. N. Tsintsadze, K. Nakajima, S. V. Bulanov, H. Dewa, H. Kotaki, and T. Tajima. Fixed blueshift of high intensity short pulse lasers propagating in gas chambers. *Phys. Plasmas*, 7:5223–5231, 2000.

[113] R. W. Boyd. *Nonlinear Optics*, volume 2nd Ed. Academic Press, San Diego, 2003.

[114] V. Tosa, H. T. Kim, I. J. Kim, and C. H. Nam. High-order harmonic generation by chirped and self-guided femtosecond laser pulses. I. spatial and spectral analysis. *Phys. Rev. A*, 71:063807, 2005.

[115] C. T. Chantler, K. Olsen, R. A. Dragoset, J. Chang, A. R. Kishore, S. A. Kotochigova, and D. S. Zucker. *X-ray Form Factor, Attenuation and Scattering Tables (version 2.1).* National Institute of Standards and Technology, Gaithersburg, MD, 2005.

[116] B. L. Henke, E. M. Gullikson, and J. C. Davis. X-ray interactions: Photoabsorption,

scattering, transmission, and reflection at E = 50-30,000 eV, Z = 1-92. *At. Data Nucl. Data Tables*, 54:181–342, 1993.

[117] M. Lein, R. De Nalda, E. Heesel, N. Hay, E. Springate, R. Velotta, M. Castillejo, P. L. Knight, and J. P. Marangos. Signatures of molecular structure in the strong-field response of aligned molecules. *J. Mod. Opt.*, 52:465–478, 2005.

[118] A. T. Le, R. R. Lucchese, and C. D. Lin. Polarization and ellipticity of high-order harmonics from aligned molecules generated by linearly polarized intense laser pulses. *Phys. Rev. A*, 82:023814, 2010.

[119] C. B. Madsen and L. B. Madsen. High-order harmonic generation from arbitrarily oriented diatomic molecules including nuclear motion and field-free alignment. *Phys. Rev. A*, 74:023403, 2006.

[120] C. Figueira de Morisson Faria and B. B. Augstein. Molecular high-order harmonic generation with more than one active orbital: Quantum interference effects. *Phys. Rev. A*, 81:043409, 2010.

[121] A. E. Siegman. *Lasers*. University Science, Mill Valley, CA, 1986.

[122] A. L'Huillier, Ph. Balcou, S. Candel, K. J. Schafer, and K. C. Kulander. Calculations of high-order harmonic-generation processes in xenon at 1064 nm. *Phys. Rev. A*, 46:2778–2790, 1992.

[123] V. Tosa, K. T. Kim, and C. H. Nam. Macroscopic generation of attosecond-pulse trains in strongly ionized media. *Phys. Rev. A*, 79:043828, 2009.

[124] H. J. Wörner, J. B. Bertrand, D. V. Kartashov, P. B. Corkum, and D. M. Villeneuve. Following a chemical reaction using high-harmonic interferometry. *Nature*, 466:604–607, 2010.

[125] V.-H. Le, A.-T. Le, R.-H. Xie, and C. D. Lin. Theoretical analysis of dynamic chemical imaging with lasers using high-order harmonic generation. *Phys. Rev. A*, 76:013414, 2007.

[126] M. B. Gaarde and K. J. Schafer. Space-time considerations in the phase locking of high harmonics. *Phys. Rev. Lett.*, 89:213901, 2002.

[127] H. J. Wörner, H. Niikura, J. B. Bertrand, P. B. Corkum, and D. M. Villeneuve. Observation of electronic structure minima in high-harmonic generation. *Phys. Rev. Lett.*, 102:103901, 2009.

[128] S. Minemoto, T. Umegaki, Y. Oguchi, T. Morishita, A. T. Le, S. Watanabe, and H. Sakai. Retrieving photorecombination cross sections of atoms from high-order harmonic spectra. *Phys. Rev. A*, 78:061402, 2008.

[129] J. P. Farrell, L. S. Spector, B. K. McFarland, P. H. Bucksbaum, M. Gühr, M. B. Gaarde, and K. J. Schafer. Influence of phase matching on the Cooper minimum in Ar high-order harmonic spectra. *Phys. Rev. A*, 83:023420, 2011.

[130] P. Colosimo, G. Doumy, C. I. Blaga, J. Wheeler, C. Hauri, F. Catoire, J. Tate, R. Chirla, A. M. March, G. G. Paulus, H. G. Muller, P. Agostini, and L. F. DiMauro. Scaling strong-field interactions towards the classical limit. *Nature Phys.*, 4:386–389, 2008.

[131] J. Higuet, H. Ruf, N. Thiré, R. Cireasa, E. Constant, E. Cormier, D. Descamps, E. Mével, S. Petit, B. Pons, Y. Mairesse, and B. Fabre. High-order harmonic spectroscopy of the Cooper minimum in argon: Experimental and theoretical study. *Phys. Rev. A*, 83:053401, 2011.

[132] J. Levesque, D. Zeidler, J. P. Marangos, P. B. Corkum, and D. M. Villeneuve. High harmonic generation and the role of atomic orbital wave functions. *Phys. Rev. Lett.*, 98:183903, 2007.

[133] P. Lan, E. J. Takahashi, and K. Midorikawa. Wavelength scaling of efficient high-order harmonic generation by two-color infrared laser fields. *Phys. Rev. A*, 81:061802, 2010.

[134] A. Gordon and F. Kärtner. Scaling of keV HHG photon yield with drive wavelength. *Opt. Express*, 13:2941–2947, 2005.

[135] K. Schiessl, K. L. Ishikawa, E. Persson, and J. Burgdörfer. Quantum path interference in the wavelength dependence of high-harmonic generation. *Phys. Rev. Lett.*, 99:253903, 2007.

[136] T. Popmintchev, M.-C. Chen, O. Cohen, M. E. Grisham, J. J. Rocca, M. M. Murnane, and H. C. Kapteyn. Extended phase matching of high harmonics driven by mid-infrared light. *Opt. Lett.*, 33:2128–2130, 2008.

[137] V. S. Yakovlev, M. Ivanov, and F. Krausz. Enhanced phase-matching for generation of soft X-ray harmonics and attosecond pulses in atomic gases. *Opt. Express*, 15:15351–15364, 2007.

[138] E. L. Falcão-Filho, V. M. Gkortsas, A. Gordon, and F. X. Kärtner. Analytic scaling analysis of high harmonic generation conversion efficiency. *Opt. Express*, 17:11217–11229, 2009.

[139] M.-C. Chen, P. Arpin, T. Popmintchev, M. Gerrity, B. Zhang, M. Seaberg, D. Popmintchev, M. M. Murnane, and H. C. Kapteyn. Bright, coherent, ultrafast soft X-ray harmonics spanning the water window from a tabletop light source. *Phys. Rev. Lett.*, 105:173901, 2010.

[140] M. Nisoli, S. De Silvestri, and O. Svelto. Generation of high energy 10 fs pulses by a new pulse compression technique. *Appl. Phys. Lett.*, 68:2793–2795, 1996.

[141] M. Nisoli, E. Priori, G. Sansone, S. Stagira, G. Cerullo, S. De Silvestri, C. Altucci, R. Bruzzese, C. de Lisio, P. Villoresi, L. Poletto, M. Pascolini, and G. Tondello. High-

brightness high-order harmonic generation by truncated bessel beams in the sub-10-fs regime. *Phys. Rev. Lett.*, 88:033902, 2002.

[142] J. A. R. Samson and W. C. Stolte. Precision measurements of the total photoionization cross-sections of He, Ne, Ar, Kr, and Xe. *J. Electron Spectrosc. Relat. Phenom.*, 123:265–276, 2002.

[143] L. E. Chipperfield, P. L. Knight, J. W. G. Tisch, and J. P. Marangos. Tracking individual electron trajectories in a high harmonic spectrum. *Opt. Commun.*, 264:494–501, 2006.

[144] S. Kazamias, S. Daboussi, O. Guilbaud, K. Cassou, D. Ros, B. Cros, and G. Maynard. Pressure-induced phase matching in high-order harmonic generation. *Phys. Rev. A*, 83:063405, 2011.

[145] T. Popmintchev, M.-C. Chen, P. Arpin, M. M. Murnane, and H. C. Kapteyn. The attosecond nonlinear optics of bright coherent X-ray generation. *Nature Photonics*, 4:822–832, 2010.

[146] F. Ferrari, F. Calegari, M. Lucchini, C. Vozzi, S. Stagira, G. Sansone, and M. Nisoli. High-energy isolated attosecond pulses generated by above-saturation few-cycle fields. *Nature Photonics*, 4:875–879, 2010.

[147] C. Vozzi, M. Negro, F. Calegari, S. Stagira, K. Kovács, and V. Tosa. Phase-matching effects in the generation of high-energy photons by mid-infrared few-cycle laser pulses. *New J. Phys.*, 13:073003, 2011.

[148] M. B. Gaarde and K. J. Schafer. Generating single attosecond pulses via spatial filtering. *Opt. Lett.*, 31:3188–3190, 2006.

[149] M. Kutzner, V. Radojević, and H. P. Kelly. Extended photoionization calculations for xenon. *Phys. Rev. A*, 40:5052–5057, 1989.

[150] X. M. Tong and S. I. Chu. Time-dependent approach to high-resolution spectroscopy and quantum dynamics of Rydberg atoms in crossed magnetic and electric fields. *Phys. Rev. A*, 61:031401, 2000.

[151] M. B. Gaarde, Ph. Antoine, A. L'Huillier, K. J. Schafer, and K. C. Kulander. Macroscopic studies of short-pulse high-order harmonic generation using the time-dependent Schrödinger equation. *Phys. Rev. A*, 57:4553–4560, 1998.

[152] M. B. Gaarde. Time-frequency representations of high order harmonics. *Opt. Express*, 8:529–536, 2001.

[153] V. S. Yakovlev and A. Scrinzi. High harmonic imaging of few-cycle laser pulses. *Phys. Rev. Lett.*, 91:153901, 2003.

[154] A. Zaïr, M. Holler, A. Guandalini, F. Schapper, J. Biegert, L. Gallmann, U. Keller, A. S. Wyatt, A. Monmayrant, I. A. Walmsley, E. Cormier, T. Auguste, J. P. Caumes, and P. Salières. Quantum path interferences in high-order harmonic generation. *Phys. Rev. Lett.*, 100:143902, 2008.

[155] G. Sansone, C. Vozzi, S. Stagira, and M. Nisoli. Nonadiabatic quantum path analysis of high-order harmonic generation: Role of the carrier-envelope phase on short and long paths. *Phys. Rev. A*, 70:013411, 2004.

[156] Y. Mairesse, A. de Bohan, L. J. Frasinski, H. Merdji, L. C. Dinu, P. Monchicourt, P. Breger, M. Kovacev, T. Auguste, B. Carré, H. G. Muller, P. Agostini, and P. Salières. Optimization of attosecond pulse generation. *Phys. Rev. Lett.*, 93:163901, 2004.

[157] V. Strelkov, E. Mével, and E. Constant. Isolated attosecond pulse generated by spatial shaping of femtosecond laser beam. *Eur. Phys. J. Special Topics*, 175:15–20, 2009.

[158] V. V. Strelkov, E. Mével, and E. Constant. Generation of isolated attosecond pulses by spatial shaping of a femtosecond laser beam. *New J. Phys.*, 10:083040, 2008.

[159] M. Hentschel, R. Kienberger, Ch. Spielmann, G. A. Reider, N. Milosevic, T. Brabec, P. Corkum, U. Heinzmann, M. Drescher, and F. Krausz. Attosecond metrology. *Nature*, 414:509–513, 2001.

[160] S. Haessler, J. Caillat, and P. Salières. Self-probing of molecules with high harmonic generation. *J. Phys. B*, 44:203001, 2011.

[161] E. W. Plummer, T. Gustafsson, W. Gudat, and D. E. Eastman. Partial photoionization cross sections of N_2 and CO using synchrotron radiation. *Phys. Rev. A*, 15:2339–2355, 1977.

[162] A. Hamnett, W. Stoll, and C. E. Brion. Photoelectron branching ratios and partial ionization cross-sections for CO and N_2 in the energy range 1850 eV. *J. Electron Spectrosc. Relat. Phenom.*, 8:367–376, 1976.

[163] B. K. McFarland, J. P. Farrell, P. H. Bucksbaum, and M. Gühr. High harmonic generation from multiple orbitals in N_2. *Science*, 322:1232–1235, 2008.

[164] Y. Mairesse, J. Higuet, N. Dudovich, D. Shafir, B. Fabre, E. Mével, E. Constant, S. Patchkovskii, Z. Walters, M. Yu. Ivanov, and O. Smirnova. High harmonic spectroscopy of multichannel dynamics in strong-field ionization. *Phys. Rev. Lett.*, 104:213601, 2010.

[165] W. Boutu, S. Haessler, H. Merdji, P. Breger, G. Waters, M. Stankiewicz, L. J. Frasinski, R. Taieb, J. Caillat, A. Maquet, P. Monchicourt, B. Carre, and P. Saliéres. Coherent control of attosecond emission from aligned molecules. *Nature Phys.*, 4:545–549, 2008.

[166] T. Kanai, E. J. Takahashi, Y. Nabekawa, and K. Midorikawa. Observing molecular structures by using high-order harmonic generation in mixed gases. *Phys. Rev. A*, 77:041402, 2008.

[167] N. Wagner, X. Zhou, R. Lock, W. Li, A. Wüest, M. Murnane, and H. Kapteyn. Extracting the phase of high-order harmonic emission from a molecule using transient alignment in mixed samples. *Phys. Rev. A*, 76:061403, 2007.

[168] X. Zhou, R. Lock, W. Li, N. Wagner, M. M. Murnane, and H. C. Kapteyn. Molecular recollision interferometry in high harmonic generation. *Phys. Rev. Lett.*, 100:073902, 2008.

[169] C. Vozzi, F. Calegari, E. Benedetti, J.-P. Caumes, G. Sansone, S. Stagira, M. Nisoli, R. Torres, E. Heesel, N. Kajumba, J. P. Marangos, C. Altucci, and R. Velotta. Controlling two-center interference in molecular high harmonic generation. *Phys. Rev. Lett.*, 95:153902, 2005.

[170] R. Torres, T. Siegel, L. Brugnera, I. Procino, J. G. Underwood, C. Altucci, R. Velotta, E. Springate, C. Froud, I. C. E. Turcu, M. Yu. Ivanov, O. Smirnova, and J. P. Marangos. Extension of high harmonic spectroscopy in molecules by a 1300 nm laser field. *Opt. Express*, 18:3174–3180, 2010.

[171] C. D. Lin, X. M. Tong, and Z. X. Zhao. Effects of orbital symmetries on the ionization rates of aligned molecules by short intense laser pulses. *J. Mod. Opt.*, 53:21–33, 2006.

[172] D. Pavičić, K. F. Lee, D. M. Rayner, P. B. Corkum, and D. M. Villeneuve. Direct measurement of the angular dependence of ionization for N_2, O_2, and CO_2 in intense laser fields. *Phys. Rev. Lett.*, 98:243001, 2007.

[173] M. Spanner and S. Patchkovskii. One-electron ionization of multielectron systems in strong nonresonant laser fields. *Phys. Rev. A*, 80:063411, 2009.

[174] S.-K. Son and S.-I. Chu. Multielectron effects on the orientation dependence and photoelectron angular distribution of multiphoton ionization of CO_2 in strong laser fields. *Phys. Rev. A*, 80:011403, 2009.

[175] M. Abu-samha and L. B. Madsen. Theory of strong-field ionization of aligned CO_2. *Phys. Rev. A*, 80:023401, 2009.

[176] S. Petretti, Y. V. Vanne, A. Saenz, A. Castro, and P. Decleva. Alignment-dependent ionization of N_2, O_2, and CO_2 in intense laser fields. *Phys. Rev. Lett.*, 104:223001, 2010.

[177] G. H. Lee, I. J. Kim, S. B. Park, T. K. Kim, Y. S. Lee, and C. H. Nam. Alignment dependence of high harmonics contributed from HOMO and HOMO-1 orbitals of N_2 molecules. *J. Phys. B*, 43:205602, 2010.

[178] H. J. Wörner, J. B. Bertrand, P. Hockett, P. B. Corkum, and D. M. Villeneuve. Controlling the interference of multiple molecular orbitals in high-harmonic generation. *Phys. Rev. Lett.*, 104:233904, 2010.

[179] B. K. McFarland, J. P. Farrell, P. H. Bucksbaum, and M. Gühr. High-order harmonic phase in molecular nitrogen. *Phys. Rev. A*, 80:033412, 2009.

[180] J. P. Farrell, B. K. McFarland, M. Gühr, and P. H. Bucksbaum. Relation of high harmonic spectra to electronic structure in N_2. *Chem. Phys.*, 366:15–21, 2009.

[181] D. A. Telnov and S.-I. Chu. Effects of electron structure and multielectron dynamical response on strong-field multiphoton ionization of diatomic molecules with arbitrary orientation: An all-electron time-dependent density-functional-theory approach. *Phys. Rev. A*, 79:041401, 2009.

[182] M. Tudorovskaya and M. Lein. High-order harmonic generation in the presence of a resonance. *Phys. Rev. A*, 84:013430, 2011.

[183] M. V. Frolov, N. L. Manakov, A. A. Silaev, N. V. Vvedenskii, and A. F. Starace. High-order harmonic generation by atoms in a few-cycle laser pulse: Carrier-envelope phase and many-electron effects. *Phys. Rev. A*, 83:021405, 2011.

[184] K. Kato, S. Minemoto, and H. Sakai. Suppression of high-order-harmonic intensities observed in aligned CO_2 molecules with 1300-nm and 800-nm pulses. *Phys. Rev. A*, 84:021403, 2011.

[185] Y. Mairesse, J. Levesque, N. Dudovich, P. B. Corkum, and D. M. Villeneuve. High harmonic generation from aligned moleculesamplitude and polarization. *J. Mod. Opt.*, 55:2591–2602, 2008.

[186] S. Haessler, J. Caillat, W. Boutu, C. Giovanetti-Teixeira, T. Ruchon, T. Auguste, Z. Diveki, P. Breger, A. Maquet, B. Carré, R. Taïeb, and P. Salières. Attosecond imaging of molecular electronic wavepackets. *Nature Phys.*, 6:200–206, 2010.

[187] R. Torres, T. Siegel, L. Brugnera, I. Procino, J. G. Underwood, C. Altucci, R. Velotta, E. Springate, C. Froud, I. C. E. Turcu, S. Patchkovskii, M. Yu. Ivanov, O. Smirnova, and J. P. Marangos. Revealing molecular structure and dynamics through high-order harmonic generation driven by mid-IR fields. *Phys. Rev. A*, 81:051802, 2010.

[188] O. Smirnova, S. Patchkovskii, Y. Mairesse, N. Dudovich, and M. Yu Ivanov. Strong-field control and spectroscopy of attosecond electron-hole dynamics in molecules. *Proc. Natl. Acad. Sci. USA*, 106:16556–16561, 2009.

[189] A. Stolow and J. G. Underwood. Time-resolved photoelectron spectroscopy of nonadiabatic dynamics in polyatomic molecules. *Adv. Chem. Phys.*, 139:497–584, 2008.

[190] K. L. Reid. Photoelectron angular distributions. *Annu. Rev. Phys. Chem.*, 54:397–424, 2003.

[191] D. M. Neumark. Time-resolved photoelectron spectroscopy of molecules and clusters. *Annu. Rev. Phys. Chem.*, 52:255–277, 2001.

[192] M. Tsubouchi and T. Suzuki. Photoionization of homonuclear diatomic molecules aligned by an intense femtosecond laser pulse. *Phys. Rev. A*, 72:022512, 2005.

[193] D. Dill. Fixed-molecule photoelectron angular distributions. *J. Chem. Phys.*, 65:1130–1133, 1976.

[194] M. Meckel, D. Comtois, D. Zeidler, A. Staudte, D. Pavicic, H. C. Bandulet, H. Pépin, J. C. Kieffer, R. Dörner, D. M. Villeneuve, and P. B. Corkum. Laser-induced electron tunneling and diffraction. *Science*, 320:1478–1482, 2008.

[195] V. Kumarappan, L. Holmegaard, C. Martiny, C. B. Madsen, T. K. Kjeldsen, S. S. Viftrup, L. B. Madsen, and H. Stapelfeldt. Multiphoton electron angular distributions from laser-aligned CS_2 molecules. *Phys. Rev. Lett.*, 100:093006, 2008.

[196] O. Geßner, A. M. D. Lee, J. P. Shaffer, H. Reisler, S. V. Levchenko, A. I. Krylov, J. G. Underwood, H. Shi, A. L. L. East, D. M. Wardlaw, E. t. H. Chrysostom, C. C. Hayden, and A. Stolow. Femtosecond multidimensional imaging of a molecular dissociation. *Science*, 311:219–222, 2005.

[197] D. W. Turner, C. Baker, A. D. Baker, and C. R. Brundle. *Molecular Photoelectron Spectroscopy: A Handbook of He 584 Å Spectra*. Wiley, London, 1970.

[198] E. Gagnon, P. Ranitovic, X.-M. Tong, C. L. Cocke, M. M. Murnane, H. C. Kapteyn, and A. S. Sandhu. Soft X-ray-driven femtosecond molecular dynamics. *Science*, 317:1374–1378, 2007.

[199] A. D. Bandrauk and J. Ruel. Charge-resonance-enhanced ionization of molecular ions in intense laser pulses: Geometric and orientation effects. *Phys. Rev. A*, 59:2153–2162, 1999.

[200] T. Seideman. Revival structure of aligned rotational wave packets. *Phys. Rev. Lett.*, 83:4971–4974, 1999.

[201] J. Ortigoso, M. Rodríguez, M. Gupta, and B. Friedrich. Time evolution of pendular states created by the interaction of molecular polarizability with a pulsed nonresonant laser field. *J. Chem. Phys.*, 110:3870–3875, 1999.

[202] J. O. Hirschfelder, C. F. Curtiss, and R. B. Bird. *Molecular Theory of Gases and Liquids*. Wiley, New York, 1954.

[203] NIST Chemistry WebBook, NIST Standard Reference Database No. 69, edited by P. J. Linstrom and W. G. Mallard (National Institute of Standards and Technology, Gaithersburg, MD, 2006), p. 20899.

[204] L. D. Landau and E. M. Lifshitz. *Quantum Mechanics: Nonrelativistic Theory*. Pergamon Press, New York, 1965.

[205] H.-J. Werner *et al.*, MOLPRO, Version 2002.6, A Package of *Ab Initio* Programs, Birmingham, UK, 2003.

[206] S. Wallace and D. Dill. Detector integrated angular distribution: Chemisorption-site geometry, axial-recoil photofragmentation, and molecular-beam orientation. *Phys. Rev. B*, 17:1692–1699, 1978.

[207] S. A. J. Collins. Lens-system diffraction integral written in terms of matrix optics. *J. Opt. Soc. Am. A*, 60:1168–1177, 1970.

[208] A. Yariv. Imaging of coherent fields through lenslike systems. *Opt. Lett.*, 19:1607–1608, 1994.

Publication list

[1] Guoli Wang, **Cheng Jin**, Anh-Thu Le, and C. D. Lin. Conditions of extracting photoionization cross sections from laser-induced high-order harmonic spectra. *Phys. Rev. A*, (submitted).

[2] **Cheng Jin** and C. D. Lin. Comparison of high-order harmonic generation of Ar using truncated Bessel and Gaussian beams. *Phys. Rev. A*, 85:033423, 2012.

[3] W. Cao, G. Laurent, **Cheng Jin**, H. Li, Z. Wang, C. D. Lin, I. Ben-Itzhak, and C. L. Cocke. Spectral splitting and quantum path study of high-harmonic generation from a semi-infinite gas cell. *J. Phys. B*, 45:074013, 2012.

[4] **Cheng Jin**, Julien B. Bertrand, R. R. Lucchese, H. J. Wörner, Paul B. Corkum, D. M. Villeneuve, Anh-Thu Le, and C. D. Lin. Intensity dependence of multiple-orbital contributions and shape resonance in high-order harmonic generation of aligned N_2 molecules. *Phys. Rev. A*, 85:013405, 2012.

[5] C. Trallero-Herrero, **Cheng Jin**, B. E. Schmidt, A. D. Shiner, J.-C. Kieffer, P. B. Corkum, D. M. Villeneuve, C. D. Lin, F. Légaré, and A. T. Le. Generation of broad XUV continuous high harmonic spectra and isolated attosecond pulses with intense mid-infrared lasers. *J. Phys. B (fast track communication)*, 45:011001, 2012.

[6] Guoli Wang, **Cheng Jin**, Anh-Thu Le, and C. D. Lin. Influence of gas pressure on high-order harmonic generation of Ar and Ne. *Phys. Rev. A*, 84:053404, 2011.

[7] **Cheng Jin**, Anh-Thu Le, Carlos A. Trallero-Herrero, and C. D. Lin. Generation of isolated attosecond pulses in the far field by spatial filtering with an intense few-cycle mid-infrared laser. *Phys. Rev. A*, 84:043411, 2011.

[8] **Cheng Jin**, Hans Jakob Wörner, V. Tosa, Anh-Thu Le, Julien B. Bertrand, R. R. Lucchese, P. B. Corkum, D. M. Villeneuve, and C. D. Lin. Separation of target structure and medium propagation effects in high-harmonic generation. *J. Phys. B*, 44:095601, 2011.

[9] **Cheng Jin**, Anh-Thu Le, and C. D. Lin. Analysis of effects of macroscopic propagation and multiple molecular orbitals on the minimum in high-order harmonic generation of aligned CO_2. *Phys. Rev. A*, 83:053409, 2011.

[10] Song-Feng Zhao, **Cheng Jin**, R. R. Lucchese, Anh-Thu Le, and C. D. Lin. High-order harmonic generation using gas-phase H_2O molecules. *Phys. Rev. A*, 83:033409, 2011.

[11] **Cheng Jin**, Anh-Thu Le, and C. D. Lin. Medium propagation effects in high-order harmonic generation of Ar and N_2. *Phys. Rev. A*, 83:023411, 2011.

[12] Song-Feng Zhao, Junliang Xu, **Cheng Jin**, Anh-Thu Le, and C. D. Lin. Effect of orbital symmetry on the orientation dependence of strong field tunneling ionization of nonlinear polyatomic molecules. *J. Phys. B*, 44:035601, 2011.

[13] Song-Feng Zhao, **Cheng Jin**, Anh-Thu Le, and C. D. Lin. Effect of an improved molecular potential on strong field tunneling ionization of molecules. *Phys. Rev. A*, 82:035402, 2010.

[14] Song-Feng Zhao, **Cheng Jin**, Anh-Thu Le, T. F. Jiang, and C. D. Lin. Determination of structure parameters in strong-field tunneling ionization theory of molecules. *Phys. Rev. A*, 81:033423, 2010.

[15] **Cheng Jin**, Anh-Thu Le, Song-Feng Zhao, R. R. Lucchese, and C. D. Lin. Theoretical study of photoelectron angular distributions in single-photon ionization of aligned N_2 and CO_2. *Phys. Rev. A*, 81:033421, 2010.

[16] Song-Feng Zhao, **Cheng Jin**, Anh-Thu Le, T. F. Jiang, and C. D. Lin. Analysis of angular dependence of strong field tunneling ionization for CO_2. *Phys. Rev. A*, 80:051402, 2009.

[17] **Cheng Jin**, Anh-Thu Le, and C. D. Lin. Retrieval of target photorecombination cross sections from high-order harmonics generated in a macroscopic medium. *Phys. Rev. A*, 79:053413, 2009.

[18] Van-Hoang Le, Ngoc-Ty Nguyen, **C. Jin**, Anh-Thu Le, and C. D. Lin. Retrieval of interatomic separations of molecules from laser-induced high-order harmonic spectra. *J. Phys. B*, 41:085603, 2008.

Appendix A

Abbreviations

HHG	High-order harmonic generation
MWP	Macroscopic wave packet
QRS	Quantitative rescattering
TDSE	Time-dependent Schrödinger equation
SFA	Strong-field approximation
SAE	Single-active electron
CM	Cooper minimum
ADK	Ammosov-Delone-Krainov
MO-ADK	Molecular Ammosov-Delone-Krainov
HOMO	Highest-occupied molecular-orbital
PRCS	Photorecombination cross section
PR	Photorecombination
PICS	Photoionization cross section
PI	Photoionization
PAD	Photoelectron angular distribution
MF-PAD	Molecular frame photoelectron angular distribution
LF-PAD	Photoelectron angular distribution in the laboratory frame
DCS	Differential cross section
IDAD	Integrated detector angular distribution
ITAD	Integrated target angular distribution

CASSCF	Complete-active-space self-consistent field
CI	Configuration interaction
IR	Infrared
MIR	Mid-infrared
NIR	Near-infrared
XUV	Extreme ultraviolet
UV	Ultraviolet
APT	Attosecond pulse train
IAP	Isolated attosecond pulse
TFR	Time-frequency representation
CEP	Carrier-envelope phase
FWHM	Full width at half maximum
3-D	Three-dimensional
TB	Truncated Bessel
TB-1	Type-1 Bessel
TB-2	Type-2 Bessel
HATI	High-energy above-threshold ionization
NSDI	Nonsequential double ionization
GDD	Group delay dispersion
RRPA	Relativistic random-phase approximation
RABITT	Reconstruction of attosecond beating by interference of two-photon transitions
COLTRIMS	Cold target recoil ion momentum spectroscopy
HCF	Hollow-core fiber

Appendix B

Theory of alignment for linear molecules

Theory of molecular alignment for linear molecules has also been presented in Publication [15]. When linear molecules are placed in a short laser field (pump laser), a rotational wave packet is excited. At later times when the wave packet undergoes "rotational revival" [199, 200], the molecules will be aligned or antialigned. To calculate the alignment, or the angular distribution of the molecules, each molecule can be treated as a rigid rotor [73, 201]. The time-dependent Schrödinger equation describing the evolution of rotational wave packet with initial state $\Psi_{JM}(\theta, \varphi, t = -\infty)$ in a linearly polarized laser field is given by

$$i\frac{\partial \Psi_{JM}(\theta,\varphi,t)}{\partial t} = \left[B\mathbf{J}^2 - \frac{E(t)^2}{2}(\alpha_{\parallel}\cos^2\theta + \alpha_{\perp}\sin^2\theta)\right]\Psi_{JM}(\theta,\varphi,t), \tag{B.1}$$

where $\mathbf{J}$ is the angular momentum operator, B is the rotational constant, $\alpha_{\parallel}$ and $\alpha_{\perp}$ are the anisotropic polarizabilities in parallel and perpendicular directions with respect to the molecular axis, respectively. These molecular properties for N_2, O_2 and CO_2 are shown in Table B.1. The electric field of pump laser, $E(t)$ in Eq. (B.1), is taken to have a Gaussian form:

$$E(t) = E_0 e^{-(2\ln 2)t^2/\tau_w^2}\cos(\omega_0 t), \tag{B.2}$$

where E_0 is the peak field, τ_w and ω_0 are the pulse duration (full width at half maximum, FWHM) and frequency of the pump laser, respectively. Eq. (B.1) is written in the molecular (or body-fixed) frame.

Table B.1: *Molecular properties for N_2, O_2 and CO_2. B is rotational constant, $\alpha_\parallel$ and $\alpha_\perp$ are parallel and perpendicular polarizability, respectively. The data are taken from [202, 203].*

Molecule	B (cm^{-1})	$\alpha_\parallel$ (Å^3)	$\alpha_\perp$ (Å^3)
N_2	1.989	2.38	1.45
O_2	1.438	2.35	1.21
CO_2	0.39	4.05	1.95

Eq. (B.1) is solved independently for each initial rotational state $|JM\rangle$ (up to $J = 40$) using the split-operator method [84, 150]. After the pump laser is turned off, the rotational wave packet will continue to propagate in the free space,

$$\Psi_{JM}(t) = \sum_{J'} a_{J'} e^{-iE_{J'}t} |J'M\rangle, \tag{B.3}$$

where $E_{J'}$ are the energy eigenvalues, $|J'M\rangle$ are spherical harmonics, and the coefficients of $a_{J'}$ can be determined at the moment when the pump laser is turned off.

Assuming a Boltzman distribution of the rotational levels at the initial time, the time-dependent alignment at a given temperature can be obtained by

$$\rho(\theta, t) = \sum_{JM} \omega_{JM} |\Psi_{JM}(\theta, \varphi, t)|^2, \tag{B.4}$$

where ω_{JM} is the weight according to the Boltzman distribution. The nuclear statistics and symmetry of the total electronic wave function must be taken into account properly in order to determine ω_{JM}. The angular distribution or alignment does not depend on the azimuthal angle φ in the frame attached to the pump laser field, and it only depends on the angle θ between the molecular axis and the polarization direction of the pump laser.

Appendix C

Photorecombination transition dipole

C.1 Photorecombination transition dipole of atomic targets

Photoionization transition dipole from an initial bound state Ψ_i to the final continuum state $\Psi_{\vec{k}}^-$ due to a linearly polarized light is [95]

$$d_{\vec{k},\vec{n}} = \langle \Psi_i | \vec{r} \cdot \vec{n} | \Psi_{\vec{k}}^- \rangle. \tag{C.1}$$

Here $\vec{n}$ is the direction of the light polarization and $\vec{k}$ is the momentum of the ejected photoelectron. The photoionization differential cross section (DCS) is proportional to the modulus square of this transition dipole (in the length form):

$$\frac{d^2\sigma^I}{d\Omega_{\vec{k}} d\Omega_{\vec{n}}} = \frac{4\pi^2 \omega k}{c} |\langle \Psi_i | \vec{r} \cdot \vec{n} | \Psi_{\vec{k}}^- \rangle|^2, \tag{C.2}$$

where $k^2/2 + I_p = \omega$ (atomic units) with I_p being the ionization potential, ω the photon energy, and c the speed of light. The continuum wave function $\Psi_{\vec{k}}^-(\vec{r})$ satisfies the stationary Schrödinger equation

$$\left[-\frac{\nabla^2}{2} + V(r) - \frac{k^2}{2} \right] \Psi_{\vec{k}}^-(\vec{r}) = 0 \tag{C.3}$$

where the spherically symmetric model potential $V(r)$ is also used in Eqs. (2.34) and (2.35).

The more relevant quantity to the HHG process is its time-reversed one-photon photorecombination process. The photorecombination DCS can be written as

$$\frac{d^2\sigma^R}{d\Omega_{\vec{n}} d\Omega_{\vec{k}}} = \frac{4\pi^2 \omega^3}{c^3 k} |\langle \Psi_i | \vec{r} \cdot \vec{n} | \Psi_{\vec{k}}^+ \rangle|^2. \tag{C.4}$$

In comparison with photoionization DCS in Eq. (C.2), the continuum state is taken as the outgoing scattering wave $\Psi^+_{\vec{k}}$ instead of an incoming wave $\Psi^-_{\vec{k}}$, and there is also a different overall factor. In fact, the photoionization and photorecombination DCS's are related by

$$\frac{d^2\sigma^R}{\omega^2 d\Omega_{\vec{n}} d\Omega_{\vec{k}}} = \frac{d^2\sigma^I}{c^2 k^2 d\Omega_{\vec{k}} d\Omega_{\vec{n}}}, \tag{C.5}$$

which follows the principle of detailed balancing for the direct and time-reversed processes [204].

C.2 Doubly differential photoionization cross section in the molecular frame

Theory of photoionization cross section (PICS) of linear molecules has also been presented in Publication [15]. Similar to Eq. (C.2), the doubly differential PICS in the molecular (or body-fixed) frame is [95, 99, 100]

$$\frac{d^2\sigma^I}{d\Omega_{\hat{k}} d\Omega_{\hat{n}}} = \frac{4\pi^2\omega}{c} |I_{\vec{k},\hat{n}}|^2. \tag{C.6}$$

Here the dipole matrix elements from an initial bound state Ψ_i to the continuum state $\Psi^{(-)}_{f,\vec{k}}$ due to the linearly polarized light in the dipole length approximation are

$$I_{\vec{k},\hat{n}} = (k)^{1/2} \langle \Psi_i | \vec{r} \cdot \hat{n} | \Psi^{(-)}_{f,\vec{k}} \rangle, \tag{C.7}$$

where $\hat{n}$ is the polarization direction of the light, and $\vec{k}$ the momentum of the photoelectron.

To treat the angular dependence of the PICS on the target orientation, the dipole matrix elements are expanded in terms of spherical harmonics

$$I_{\vec{k},\hat{n}} = (\frac{4\pi}{3})^{1/2} \sum_{lm\mu} I_{lm\mu} Y^*_{lm}(\Omega_{\hat{k}}) Y^*_{l\mu}(\Omega_{\hat{n}}). \tag{C.8}$$

The partial-wave matrix elements are given by

$$I_{lm\mu} = (k)^{1/2} \langle \Psi_i | r_\mu | \Psi^{(-)}_{f,klm} \rangle, \tag{C.9}$$

where

$$r_\mu = \begin{cases} \mp(x \pm iy)/2^{1/2} & \mu = \pm 1, \\ z & \mu = 0. \end{cases} \tag{C.10}$$

In the calculation, the initial bound state Ψ_i is obtained from the MOLPRO code [205] within the valence complete-active-space self-consistent field (CASSCF) method. Based on the frozen-core approximation the final state $\Psi^{(-)}_{f,\vec{k}}$ is then described in a single-channel approximation where the wave function of the ionic core is given by a valence complete active space configuration interaction (CI) wave function obtained using the same bound orbitals as in the initial state. It has the form

$$\Psi^{(-)}_{f,\vec{k}} = \mathbf{A}[\Phi\phi^{(-)}_{\vec{k}}(\vec{r})], \tag{C.11}$$

where Φ is the correlated $N-1$ electron ionic-core wave function, $\phi^{(-)}_{\vec{k}}(\vec{r})$ is the one-electron continuum wave function, and operator $\mathbf{A}$ performs the appropriate antisymmetrization of spin and spatial symmetry adaptation of the product of the ionic core and continuum wave functions. Note that it is possible to use ionic orbitals, however, we perform CI calculations in both the initial and final states, the choice of orbitals does not affect much the final results. For valence ionization, such as we are studying here, the position of one-electron continuum resonances has been reproduced quite well using the initial state orbitals. So starting with initial state orbitals and using CI wave functions give quite reliable results.

The Schrödinger equation for the remaining continuum electron is then (in atomic units)

$$\left[-\frac{1}{2}\bigtriangledown^2 - \frac{1}{r} + V(\vec{r}) - \frac{k^2}{2} \right] \phi^{(-)}_{\vec{k}}(\vec{r}) = 0, \tag{C.12}$$

where $V(\vec{r})$ is the short-range portion of the electron-molecular-ion interaction. Note that the potential is not spherically symmetric for molecules. Eq. (C.12) is then solved by using the iterative Schwinger variational method. The continuum wave function is expanded in terms of partial waves as

$$\phi^{(-)}_{\vec{k}}(\vec{r}) = (\frac{2}{\pi})^{1/2} \sum_{l=0}^{l_p} \sum_{m=-l}^{l} i^l \phi^{(-)}_{klm}(\vec{r}) Y^*_{lm}(\Omega_{\hat{k}}), \tag{C.13}$$

where an infinite sum over l has been truncated at $l = l_p$. In the calculation, we typically choose l_p=11. Once we obtain $\phi^{(-)}_{klm}(\vec{r})$, $\Psi^{(-)}_{f,klm}$ in Eq. (C.9) can be obtained straightforwardly through Eq. (C.11). Note that our continuum wave function is constructed to be orthogonal to the strongly occupied orbitals. This avoids spurious singularities which can occur when scattering from correlated targets is considered.

Here we describe the method used to compute the scattering potential $V(\vec{r})$ found in Eq. (C.12). First, the electronic Hamiltonian is written as

$$H = \sum_{i=1}^{N} h(i) + \sum_{i<j}^{N} \frac{1}{r_{ij}}, \tag{C.14}$$

with

$$h(i) = -\frac{\nabla_i^2}{2} - \sum_a \frac{Z_a}{r_{ia}}, \tag{C.15}$$

where the Z_a are the nuclear charges, and N is the number of electrons. Then the single-particle equation for the continuum electron is obtained from

$$\langle \delta\Psi^{(-)}_{f,\vec{k}} | H - E | \Psi^{(-)}_{f,\vec{k}} \rangle = 0, \tag{C.16}$$

where $\delta\Psi^{(-)}_{f,\vec{k}}$ is written as in Eq. (C.11), with $\phi^{(-)}_{\vec{k}}(\vec{r})$ replaced by $\delta\phi^{(-)}_{\vec{k}}(\vec{r})$. By requiring this equation to be satisfied for all possible $\delta\Psi^{(-)}_{f,\vec{k}}$ [or $\delta\phi^{(-)}_{\vec{k}}(\vec{r})$], one obtains a nonlocal optical potential that can be written in the form of a Phillips-Kleinman pseudopotential.

A single-center expansion approach is used to evaluate all required matrix elements. In other words, all functions, including the scattering wave function, occupied orbital, and potential are expanded about a common origin, which is the center of mass of the molecule, as a sum of spherical harmonics times radial functions

$$F(\vec{r}) = \sum_{l=0}^{l_{\max}} \sum_{m=-l}^{l} f_{lm}(r) Y_{lm}(\theta, \phi). \tag{C.17}$$

With this expansion, the angular integration can be done analytically and all three-dimensional integrals reduce to a sum of radial integrals, which are computed on a radial grid. Typically, we choose $l_{\max}$=60 to 85.

If we are dealing with electron ionization from inner molecular orbitals, i.e., not highest-occupied molecular-orbital (HOMO), but rather HOMO-1 and HOMO-2, it can still be done in the same manner, except that the ionic-core state Φ employed in Eq. (C.11) needs to be replaced by the excited ion state, which corresponds to electron ionization from the HOMO-1 or HOMO-2 orbital. Furthermore, the present single-channel formalism can be extended to coupled-multichannel calculations to account for additional electron correlation effects. The calculations in this thesis are limited to the single-channel approximation.

As mentioned in the quantitative rescattering (QRS) theory (see Sec. 2.2.3), the photorecombination transition dipoles are involved in the process of high-order harmonic generation. It only has a difference in the sign of the phase, but has the same magnitude as compared to the photoionization transition dipole [95]. To perform the QRS calculation, we usually obtain the returning electron wave packet by using the strong-field approximation for simplicity, where the photorecombination transition dipole is either a pure real or pure imaginary number. And then the exact photorecombination transition dipole is incorporated with the wave packet to obtain the induced dipole moment.

C.3 Alignment dependence of integrated photoionization cross section

Doubly differential PICS in the molecular frame is given in Eq. (C.6), but for a given application one may need averaged PICSs as suggested by Wallace and Dill [206]. One such averaged distribution is the integrated detector angular distribution (IDAD), which corresponds to experiments where target orientation is fixed in space and the PICS is integrated over all possible emission directions of photoelectron. For linear molecules, the integrated cross section depends only on the alignment angle θ due to the symmetry of the molecules and the IDAD can be expressed in the molecular frame as

$$\sigma(\theta,\omega) = \frac{d\sigma}{d\Omega_{\hat{n}}} = \int \frac{4\pi^2\omega}{c} |I_{\vec{k},\hat{n}}|^2 d\Omega_{\hat{k}}. \tag{C.18}$$

Eq. (C.18) can also be found in the form of [99, 206]

$$\frac{d\sigma}{d\Omega_{\hat{n}}} = \frac{\sigma_{\text{tot}}}{4\pi}[1 + \beta_{\hat{n}} P_2(\cos\theta)], \tag{C.19}$$

where σ_{tot} is the total PICS averaged over all alignments and photoelectron directions, $P_2(\cos\theta)$ is the Legendre polynomial of degree 2 and $\beta_{\hat{n}}$ is the asymmetry parameter.

In experiments, the pump laser is used to create transiently aligned molecular sample, and then the soft X-ray probe ionizes the molecules. The time dependent alignment distribution is obtained by solving the time-dependent Schrödinger equation (see Appendix B). If the polarizations of the pump and probe lasers are parallel, the detected experimental signal in terms of the pump-probe time delay τ can be written as

$$Y(\omega, \tau) \propto \int_0^\pi \sigma(\theta, \omega)\rho(\theta, \tau)\sin\theta d\theta. \tag{C.20}$$

Without the pump-probe scheme, the molecules are distributed randomly, and the angular distribution of $\rho(\theta, \tau)$ in Eq. (C.20) is a constant. Eq. (C.20) actually gives us the total cross section σ_{tot}.

C.4 Photoelectron angular distribution in the laboratory frame

PICS in the molecular frame is given in Eq. (C.6), and the doubly differential PICS in the laboratory frame can be expressed as

$$\frac{d^2\sigma}{d\Omega_{\hat{k}'} d\Omega_{\hat{n}'}} = \frac{4\pi^2\omega}{c}|I_{\vec{k}',\hat{n}'}|^2, \tag{C.21}$$

where $\hat{n}'$ and $\vec{k}'$ are the polarization direction of pump laser and the momentum of the photoelectron in the laboratory frame, respectively. Assuming that the molecular axis is aligned at an arbitrary angle $\hat{\mathbf{R}} \equiv (\theta, \varphi)$ with respect to the polarization direction of pump laser. In other words, $\hat{\mathbf{R}}$ is the Euler angle of the molecular frame with respect to the laboratory frame. The dipole matrix elements in Eq. (C.8) can be rewritten in the laboratory

frame as

$$I_{\vec{k}',\hat{n}'} = (\frac{4\pi}{3})^{1/2} \sum_{lm\mu} I_{lm\mu} \sum_{m'=-l}^{l} D^{l}_{mm'}(\hat{\mathbf{R}}) Y^{*}_{lm'}(\theta_{k'}, \varphi_{k'}) \sum_{\mu'=-l}^{l} D^{l}_{\mu\mu'}(\hat{\mathbf{R}}) Y^{*}_{l\mu'}(\theta_{n'}, \varphi_{n'}), \quad \text{(C.22)}$$

with $D^{l}_{mm'}(\hat{\mathbf{R}})$ and $D^{l}_{\mu\mu'}(\hat{\mathbf{R}})$ being the rotation matrices. In Eq. (C.22), $\theta_{k'}$ and $\varphi_{k'}$ are the polar and azimuthal angles of the photoelectron in the laboratory frame, respectively, $\theta_{n'}$=0° and $\varphi_{n'}$=0° in the laboratory frame. The PICS of Eq. (C.21) in the laboratory frame is an explicit function of $\theta_{k'}$ and $\varphi_{k'}$ for the alignment angle $\hat{\mathbf{R}}$.

In the laboratory frame, taking into account the molecular distribution with respect to the polarization direction of the pump laser described by the angle θ, the PICS in Eq. (C.21) must be integrated over the azimuthal angle φ. Finally, we obtain the PICS for all molecules with a fixed alignment angle θ, which depends on photoelectron emission angle $\theta_{k'}$,

$$\sigma'(\theta, \omega, \theta_{k'}) = \int_0^{2\pi} \frac{d^2\sigma}{d\Omega_{\hat{k}'} d\Omega_{\hat{n}'}}(\theta, \theta_{k'}, \varphi_{k'} - \varphi) d\varphi. \quad \text{(C.23)}$$

The actual experimentally observed photoelectron angular distribution in the laboratory frame (LF-PAD) corresponds to the average of the PICS in Eq. (C.23) accounting for the molecular distribution in space. The time dependent angular distribution of $\rho(\theta, \tau)$ can be calculated by Eq. (B.4), and the analytical form of the LF-PAD, which can be compared with experimental photoelectron spectra directly, is expressed as

$$Y'(\omega, \theta_{k'}, \tau) \propto \int_0^{\pi} \sigma'(\theta, \omega, \theta_{k'}) \rho(\theta, \tau) \sin\theta d\theta. \quad \text{(C.24)}$$

The polarizations of the pump and probe lasers are parallel in Eq. (C.24).

As suggested by Wallace and Dill [206], another averaged PICS is the integrated target angular distribution (ITAD), which corresponds to PI experiments where target orientation is not resolved. For the isotropically distributed molecules, the angular distribution of $\rho(\theta, \tau)$ is a constant, and Eq. (C.24) has the form [99, 206]

$$\frac{d\sigma}{d\Omega_{\hat{k}'}} = \frac{\sigma_{\text{tot}}}{4\pi}[1 + \beta_{\hat{k}'} P_2(\cos\theta_{k'})], \quad \text{(C.25)}$$

where $\beta_{\hat{k}'}$ is the photoelectron asymmetry parameter.

Appendix D

Spatial mode of laser beam: Gaussian beam vs truncated Bessel beam

Theory of Gaussian and truncated Bessel beams has also been presented in Publication [2] and [17].

D.1 Gaussian beam

In optics, a Gaussian beam is a beam of electromagnetic radiation whose transverse electric field and intensity distributions are well approximated by Gaussian functions. For a Gaussian beam, the complex electric field is given by

$$E_{\text{gau}}(r,z) = \frac{bE_0}{b+2iz}\exp(-\frac{kr^2}{b+2iz}) = |E_{\text{gau}}(r,z)|e^{i\phi_{laser}(r,z)}. \tag{D.1}$$

Here E_0 is the peak laser field at the focus, ω_0 is the central frequency, $k = \omega_0/c = 2\pi/\lambda_0$ is the wave vector. As shown in Fig. D.1, the geometry and behavior of a Gaussian beam are governed by a set of beam parameters. The spot size $w(z)$ is at a minimum value w_0 along the z-axis, which is known as beam waist. At a distance z, the variation of the spot size is given by

$$w(z) = w_0\sqrt{1+(\frac{z}{z_R})^2}, \tag{D.2}$$

where

$$z_R = \frac{\pi w_0^2}{\lambda_0}, \tag{D.3}$$

is called the Rayleigh range. b is the confocal parameter (depth of focus) given by twice the distance along z-axis for the beam to expand from its minimum cross sectional area at $z = 0$ to twice this area, i.e., $b = 2z_R$.

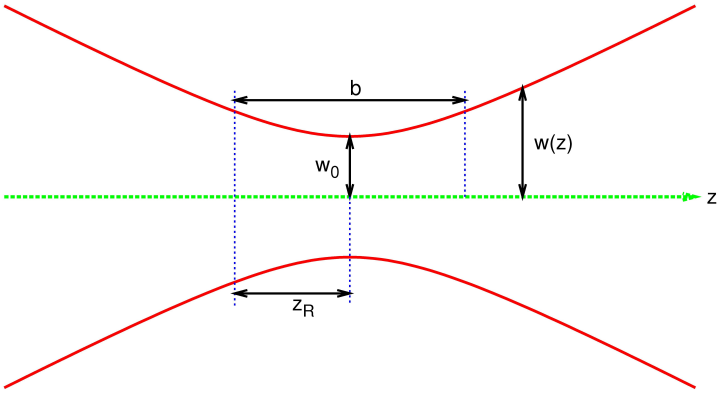

Figure D.1: *Schematic diagram of Gaussian beam. Beam width $w(z)$ as a function of the axial distance z; w_0: beam waist; b: confocal parameter, twice of Rayleigh range z_R. Reproduced from [113].*

From Eq. (D.1), we can also express the intensity and phase of a Gaussian beam explicitly

$$I(r,z) = |E_{\text{gau}}(r,z)|^2 = \frac{I_0}{1+(2z/b)^2} \cdot \exp[-(\frac{r}{w_0})^2 \cdot \frac{2}{1+(2z/b)^2}], \tag{D.4}$$

$$\begin{aligned} \phi_{\text{laser}}(r,z) &= -\tan^{-1}(\frac{2z}{b}) + \frac{2kr^2 z}{b^2+4z^2} \\ &= -\tan^{-1}(\frac{2z}{b}) + \frac{k\lambda_0}{2\pi} \cdot (\frac{r}{w_0})^2 \cdot \frac{(2z/b)}{1+(2z/b)^2}. \end{aligned} \tag{D.5}$$

Geometric phase due to focusing is given by ϕ_{laser}, and $\tan^{-1}(2z'/b)$ is the *Gouy phase*, which results in a phase shift of π relative to a plane wave as the laser passes through the focus from the far field on one side to the far field on the other side of the focus. As shown in Eq. (D.4) and (D.5), if the propagation distance z is scaled by the confocal parameter b, and the radial distance r is scaled by the beam waist w_0, the intensity and the phase stay the same.

D.2 Truncated Bessel beam

For an axial-symmetric lenslike system, the complex electric field on the output plane is related to the one on the input plane by an $ABCD$ ray matrix [207, 208]. Let the laser electric field on the input plane (the exit plane of a hollow-core fiber) be given by $\mathrm{E}(\rho)=\mathrm{E_0J_0}(2.405\rho/a)$ with $\rho \leq a$, where ρ is the radial coordinate, $\mathrm{E_0}$ the on-axis peak electric field, a the capillary radius, and $\mathrm{J_0}$ the zero-order Bessel function of the first kind. The transverse electric field on the output plane, according to the diffraction theory in the paraxial approximation, is

$$E_{\mathrm{TB}}(\xi, r) = E_0 \frac{-ik}{B(\xi)} \exp\left[ik(L+\xi+\frac{Dr^2}{2B(\xi)})\right] \int_0^a J_0(2.405\frac{\rho}{a}) J_0\left[\frac{kr\rho}{B(\xi)}\right] \exp\left[\frac{ikA(\xi)}{2B(\xi)}\rho^2\right] \rho d\rho, \tag{D.6}$$

where k=$2\pi/\lambda_0$, and λ_0 is the central laser wavelength. The meanings of the parameters in the equation will be defined explicitly below. We note that the integral in Eq. (D.6) becomes indeterminate if $B(\xi=\bar{\xi})$=0, where ξ=$\bar{\xi}$ is also the location of the focus plane. As discussed in Ref. [208], the electric field at $\bar{\xi}$ can be written as

$$E_{\mathrm{TB}}(\bar{\xi}, r) = \frac{E_0}{A} \exp\left[ik(L+\bar{\xi}+\frac{Cr^2}{2A})\right] J_0(2.405\frac{r}{aA}). \tag{D.7}$$

For a lossless system, AD-BC=1. In the following we will show two truncated Bessel (TB) beams from the different optical systems, which have been used by Nisoli *et al.* [141] and Wörner *et al.* [127], respectively.

D.2.1 Type-1 Bessel beam - - tightly focused beam

In the experiment of Nisoli *et al.* [141], the optical system setup is depicted in Fig. D.2. The radius of the capillary is a=0.25 mm, and the focal length of the focus mirror is f=250 mm. The ξ and the focus plane $\bar{\xi}$ are sketched in the figure. The laser pulse emerging from the hollow-core fiber propagates in free space for a distance d=2000 mm [or L in Eq. (D.6)] to the focusing mirror where it further propagates for a distance ξ after the mirror to the output

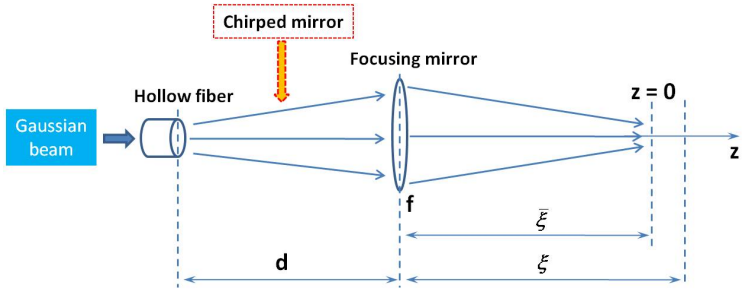

Figure D.2: *Sketch of the experimental setup for Type-1 Bessel beam generation [141]. Adapted from Publication [2].*

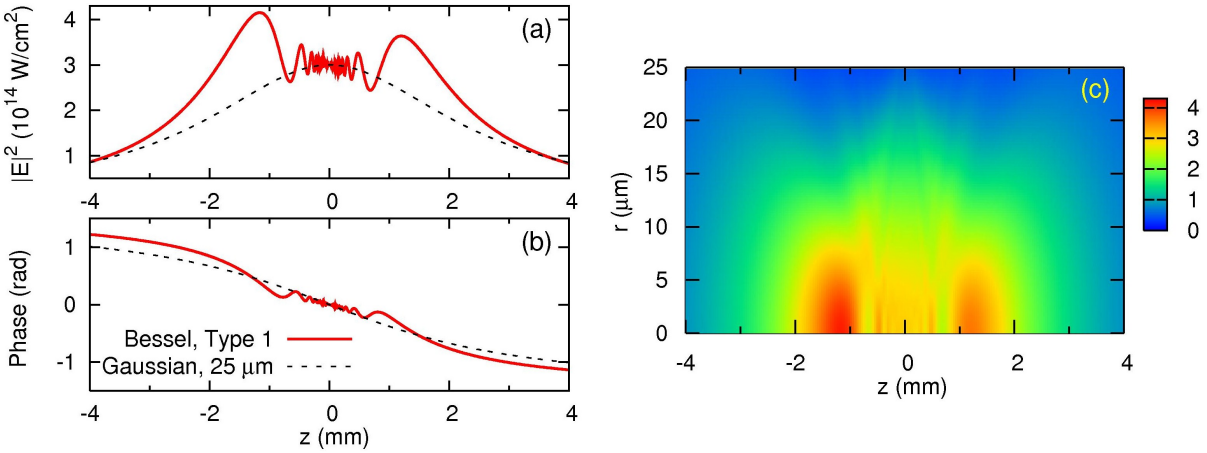

Figure D.3: *On-axis laser intensity (a) and phase (b) as a function of propagation distance z: Type-1 Bessel (solid lines) vs Gaussian (w_0=25 µm, dashed lines). (c) Spatial intensity distribution of Type-1 Bessel beam. The laser intensity at the focus is 3×10^{14} W/cm^2. Adapted from Publication [2].*

plane. The laser pulse is also compressed by chirped mirrors, but they are not included in the $ABCD$ matrix. For this optical system, the $ABCD$ matrix can be written as:

$$\begin{aligned} A(\xi) &= 1 - \xi/f, \\ B(\xi) &= d + \xi(1 - d/f), \\ C &= -1/f, \\ D &= 1 - d/f. \end{aligned} \tag{D.8}$$

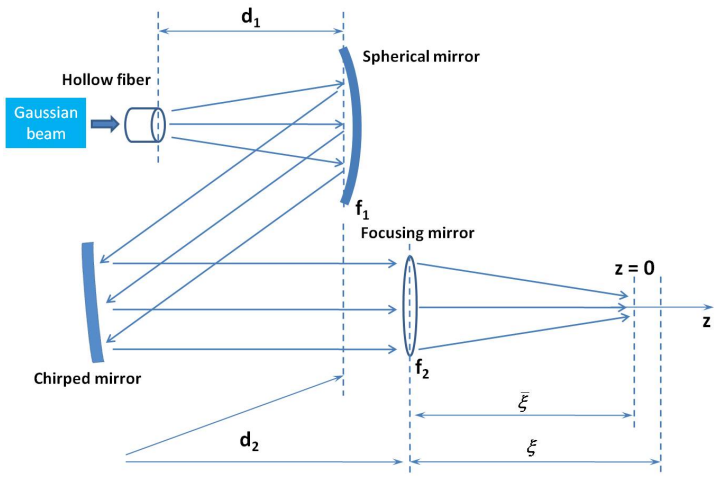

Figure D.4: *Sketch of the experimental setup for Type-2 Bessel beam generation. Adapted from Publication [2].*

The TB beam constructed by Eq. (D.8) is called Type-1 Bessel beam in this paper. We plot the intensity $|E_{\rm TB}|^2$ and the phase $\phi_{\rm TB}$ (red solid lines) as a function of z for r=0 (on-axis) in Figs. D.3(a) and (b), respectively. Here the coordinate ξ has been replaced by z=ξ-$\bar{\xi}$ for convenience, and the phase ϕ_{TB} is set as 0 at z=0 and r=0 (focusing point). In the present case, $\bar{\xi} > f$, where $B(\bar{\xi})$=0 with B defined in Eq. (D.8). Laser wavelength λ_0=780 nm, and laser intensity at the focus is 3×10^{14} W/cm^2. For comparison, we fix the laser intensity at the focus and plot the intensity and phase (dashed lines) of a Gaussian beam with the beam waist w_0=25 μm in Figs. D.3(a) and (b), respectively. In Fig. D.3(c), we plot the spatial distribution of the laser intensity for the TB beam.

D.2.2 Type-2 Bessel beam - - loosely focused beam

In the experiment of Wörner *et al.* [127], the setup is depicted in Fig. D.4. The hollow-core fiber (HCF) is similar to Nisoli *et al.*'s [141]. The beam comes out of the HCF (with radius a=0.125 mm) is divergent and. It is recollimated by a spherical mirror (focal length f_1=1000 mm) placed 1 m after the output of the HCF (d_1=1000 mm). The beam is then reflected 8 times on chirped mirrors and propagated a distance of 2 m from the spherical mirror (d_2=2000 mm) until a focusing mirror (focal length f_2=500 mm). It further propagates

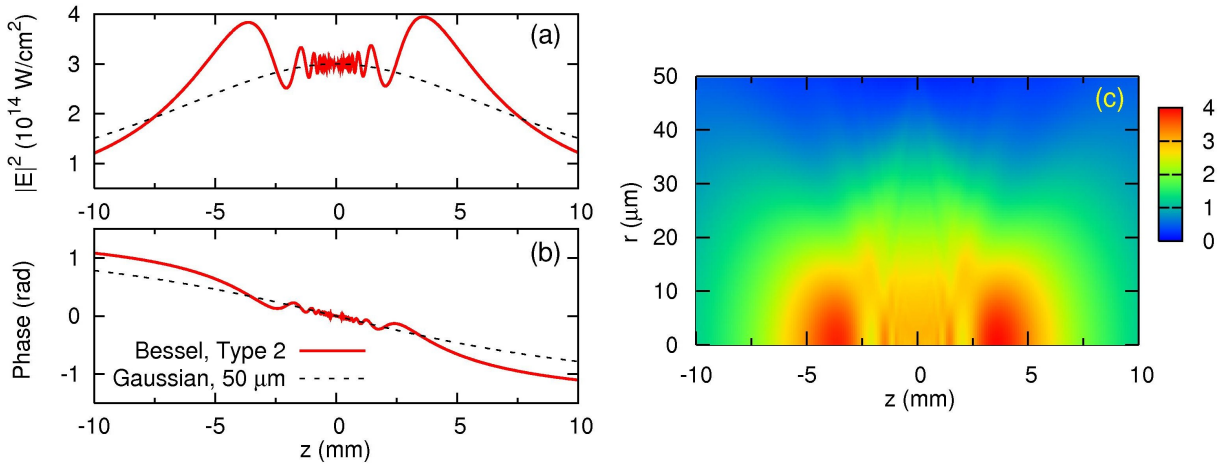

Figure D.5: *Same as Fig. D.3 except for loosely focused Type-2 Bessel and Gaussian (w_0=50 μm) beams. Adapted from Publication [2].*

through a distance ξ after the mirror to the output plane. L in Eq. (D.6) equals to $d_1 + d_2$. We then write down the $ABCD$ matrix for this optical system without considering the chirped mirrors,

$$
\begin{aligned}
A(\xi) &= (1 - \frac{d_2}{f_1})(1 - \frac{\xi}{f_2}) - \frac{\xi}{f_1}, \\
B(\xi) &= (d_1 + d_2 - \frac{d_1 d_2}{f_1})(1 - \frac{\xi}{f_2}) - \xi(\frac{d_1}{f_1} - 1), \\
C &= -\frac{1}{f_1} - \frac{1}{f_2} + \frac{d_2}{f_1 f_2}, \\
D &= -\frac{d_1}{f_2} + (1 - \frac{d_1}{f_1})(1 + \frac{d_2}{f_2}).
\end{aligned} \tag{D.9}
$$

To have the collimated laser beam before the focusing mirror f_2, it requires d_1=f_1, i.e., the output of the HCF is put at the focal plane of the spherical mirror f_1. In this case $\bar{\xi} = f_2$. The TB beam constructed by Eq. (D.9) is called Type-2 Bessel beam in this paper. Similar to Fig. D.3, we plot the on-axis intensity $|E_{\rm TB}|^2$ and the phase $\phi_{\rm TB}$ (red solid lines) as a function of z and the spatial distribution of intensity in Fig. D.5. In Figs. D.5(a) and (b), we also plot on-axis intensity and phase (dashed lines) of a Gaussian beam with the beam waist w_0=50 μm. The same laser wavelength and intensity (at the focus) are applied.

D.3 Ultrashort laser pulse and geometric phase

The spatial dependence of a laser field has been discussed above, we will write a laser field with complete spatial and temporal dependence in this section. In the moving coordinate frame (i.e., $z' = z$ and $t' = t - z/c$), the term of e^{-ikz} can be eliminated, and the electric field can be written as

$$E_1(r, z', t') = Re\Big[E_{\text{gau}}(r, z')A(r, z', t')e^{-i(\omega_0 t' + \varphi_{CE})}\Big], \tag{D.10}$$

where

$$A(r, z', t') = \cos^2\{\frac{\pi[t' - \phi_{laser}(r, z')/\omega_0]}{\tau_p}\}. \tag{D.11}$$

Here we assume spatial beam is Gaussian (i.e., E_{gau}), it can be replaced by truncated Bessel or other beams straightforwardly. Carrier-envelope phase is represented by φ_{CE}, and τ_p in the envelope function $A(r, z', t')$ is the total duration of the laser pulse, which equals to 2.75 times τ_w, the full width at half maximum (FWHM) of the laser's intensity. If we apply Gaussian envelope in time domain, and then

$$A(r, z', t') = \exp\Big[-(2\ln 2)\frac{(t' - \phi_{laser}(r, z')/\omega_0)^2}{\tau_w^2}\Big]. \tag{D.12}$$

We also introduce the pulse energy W_{pulse} for the laser beam:

$$W_{pulse} = \int\int I(r, z', t')2\pi r dr dt', \tag{D.13}$$

where $I(r, z', t')$ is the spatial- and temporal-dependent laser intensity (assuming cylindrical symmetry). For a Gaussian beam, we have an explicit expression of $I(r, z', t') = |E_1(r, z', t')|^2$ in Eq. (D.10), and we can derive an analytical expression for the pulse energy assuming the Gaussian envelope of Eq. (D.12) in time (it is convenient to calculate pulse energy at the focal plane where z=0):

$$W_{\text{pulse}} = I_0\frac{\pi w_0^2}{2}\tau_w\sqrt{\frac{\pi}{4\ln 2}}, \tag{D.14}$$

where I_0 is the laser peak intensity at the focus. We choose $\tau_{\rm p}$ to be 3 cycles (7.8 fs), I_0=3×10^{14} W/cm^2, then $\rm W_{pulse}$ obtained by Eq. (D.14) is 24.45 μJ for Gaussian beam in Fig. D.3. While $\rm W_{pulse}$ is 27.24 μJ for Type-1 Bessel beam in Fig. D.3 calculated numerically using Eq. (D.13).

If the fundamental laser field can be considered as propagating in the vacuum, its electric field can be expressed as an analytical form approximately by using Eq. (D.10). And then the propagation of the harmonic field in the gas medium can be simplified. Let

$$t'' = t' - \varphi_{laser}(r, z')/\omega_0, \tag{D.15}$$

then

$$E_1(r, z', t'') = |E_{\rm gau}(r, z')| \cos^2(\frac{\pi t''}{\tau_p}) \cos(\omega_0 t'' + \varphi_{CE}), \tag{D.16}$$

where we assume the cosine square envelope, and it can be changed as Gaussian envelope easily.

In order to solve Eqs. (2.55) and (2.60), the nonlinear polarization in the moving coordinate frame needs to be calculated. First we can compute $P_{nl}(r, z', t'')$ since in the time frame t'' the spatial component and temporal part are separated. In other words, the fundamental laser field only depends on the peak field $|E_{\rm gau}(r, z')|$. Using the Fourier transformation, we then obtain

$$\widetilde{P}_{nl}(r, z', \omega) = \widehat{F}[P_{nl}(r, z', t')] = \widehat{F}[P_{nl}(r, z', t'')]e^{-i(\frac{\omega}{\omega_0})\phi_{laser}(r,z')}. \tag{D.17}$$

From the expression above, it can be seen that there are two contributions to the phase of the nonlinear polarization: the first one is atomic phase, which depends only on the laser peak intensity; the second is geometric phase multiplied by the harmonic order. It is known that the most time-consuming job is the calculation of the spatial dependent nonlinear polarization for atoms inside the medium as the harmonic field is propagated. It is the separation of atomic phase and geometric phase that allows one to simplify the calculation. Using a batch of laser peak intensities, the nonlinear polarizations in the time frame t'' are

calculated and then stored. When it comes to solve the propagation equations for each value of ω, the nonlinear polarization in t'' for atoms (or molecules) inside the medium are obtained by interpolation. Meanwhile the geometric phase is added up in order to transform the nonlinear polarization to the moving coordinate frame. The use of interpolation method greatly improves the efficiency of harmonic field propagation. This approach is valid only for multi-cycle laser pulse (FWHM, 10 optical cycles) applied.

Appendix E

Copyright approval from the publishers

Cheng, Jin

From: lamanca@aps.org on behalf of Associate Publisher [assocpub@aps.org]
Sent: Friday, January 27, 2012 8:41 AM
To: Cheng, Jin
Subject: Re: Copyright questions

Dear Cheng Jin,

Thank you for your email. As the author, you have the right to use the article or a portion of the article in a thesis or dissertation without requesting permission from APS, provided the bibliographic citation and the APS copyright credit line are given on the appropriate pages.

Best wishes,

Eileen LaManca
Publications Marketing Coordinator
American Physical Society

On Thursday, January 26 2012 "Cheng, Jin" <cjin@phys.ksu.edu> wrote :
(Original included CC: to "Cheng, Jin" <cjin@phys.ksu.edu>)

>Dear editor,
>
>My name is Cheng Jin from Kansas State University. I am writing my Ph. D thesis now, and in my thesis I would like to include the contents (some paragraphs and figures) of my articles (I am the first author in these articles), which have been published in Physical Review A. Could you tell me what policy or procedure I need to follow?
>
>The articles I want to use are listed below:
>
>1. Cheng Jin, Anh-Thu Le, and C. D. Lin, Retrieval of target photorecombination cross sections from high-order harmonics generated in a macroscopic medium, Phys. Rev. A 79, 053413 (2009).
>
>2. Cheng Jin, Anh-Thu Le, Song-Feng Zhao, R. R. Lucchese, and C. D. Lin, Theoretical study of photoelectron angular distributions in single-photon ionization of aligned N2 and CO2, Phys. Rev. A 81, 033421 (2010).
>
>3. Cheng Jin, Anh-Thu Le, and C. D. Lin, Medium propagation effects in high-order harmonic generation of Ar and N2, Phys. Rev. A 83, 023411 (2011).
>
>4. Cheng Jin, Anh-Thu Le, and C. D. Lin, Analysis of effects of macroscopic propagation and multiple molecular orbitals on the minimum in high-order harmonic generation of aligned CO2, Phys. Rev. A 83, 053409 (2011).
>
>5. Cheng Jin, Anh-Thu Le, Carlos A. Trallero-Herrero, and C. D. Lin, Generation of isolated attosecond pulses in the far field by spatial filtering with an intense few-cycle mid-infrared laser, Phys. Rev. A 84, 043411 (2011).
>
>6. Cheng Jin, Julien B. Bertrand, R. R. Lucchese, H. J. Wörner, Paul B. Corkum, D. M. Villeneuve, Anh-Thu Le, and C. D. Lin, Intensity dependence of multiple-orbital contributions and shape resonance in high-order harmonic generation of aligned N2 molecules, Phys. Rev. A 85, 013405 (2012).
>
>I will appreciate your help!
>
>
>
>Best regards,
>
>Cheng Jin
>

RE: Copyright questions
Cheng, Jin
to:
'Permissions'
06/02/2012 16:11
Show Details

Dear Sarah,

I probably need to use Fig. 1, Fig. 2, and Fig.3 in J. Phys. B 44, 095601 (2011), and Fig.2 and Fig.3 in J. Phys. B 45, 011001 (2012) in my Ph.D. thesis.
Best regards,
Cheng Jin

From: Sarah Ryder [mailto:Sarah.Ryder@iop.org] **On Behalf Of** Permissions
Sent: Wednesday, February 01, 2012 7:44 AM
To: Cheng, Jin
Subject: RE: Copyright questions

Dear Dr Jin

Thank you for your permission request to the IOP. We however require more information of the figures/paragraphs you wish to reproduce. Please can you reply to the following email address with further details, so that your request can be processed.

Best Wishes

Sarah Ryder

Publishing Administrator
Email: permissions@iop.org

Copyright questions

Cheng, Jin to: 'jphysb@iop.org' 26/01/2012 16:06

Cc: "Cheng, Jin"

From: "Cheng, Jin" <cjin@phys.ksu.edu>
To: "'jphysb@iop.org'" <jphysb@iop.org>
Cc: "Cheng, Jin" <cjin@phys.ksu.edu>

Dear editor,

My name is Cheng Jin from Kansas State University. I am writing my Ph. D thesis now, and in my thesis I would like to include the contents (some paragraphs and figures) of my articles, which have been published in Journal of Physics B. Could you tell me what policy or procedure I need to follow?

The articles I want to use are listed below:

1. **Cheng Jin**, Hans Jakob Wörner, V. Tosa, Anh-Thu Le, Julien B. Bertrand, R. R. Lucchese, P. B. Corkum, D. M. Villeneuve, and C. D. Lin, Separation of target structure and medium propagation effects in high-harmonic generation, J. Phys. B 44, 095601 (2011).
2. C. Trallero-Herrero, **Cheng Jin,** B. E. Schmidt, A. D. Shiner, J-C. Kieffer, P. B. Corkum, D. M. Villeneuve, C. D. Lin, F. Légaré, and A. T. Le, Generation of broad XUV continuous high harmonic spectra and isolated attosecond pulses with intense mid-infrared lasers, J. Phys. B (fast track communication) 45, 011001 (2012).

I will appreciate your help!

Best regards,
Cheng Jin

PERMISSION TO REPRODUCE AS REQUESTED IS GIVEN PROVIDED THAT:

~~(a) the consent of the author(s) is obtained~~
(b) the source of the material including author, title of article, title of journal, volume number, issue number (if relevant), page range (or first page if this is the only information available), date and publisher is acknowledged.
(c) for material being published electronically, a link back to the original article should be provided (via DOI).

IOP Publishing Ltd
Temple Circus
Temple Way
BRISTOL
BS1 6BE

7/2/2012 .....
Date

..... Rights & Permissions